Fortress Mountain Resort
#1 Fortress Mountain Road, Kananaskis, AB
Box 8173, Canmore, AB T1W 2T9

Supplementary Information Package For Change In Purpose Application November 2018

In reference to dispositions: Water License File #12562, Priority # 1968-10-30-01

Submission Date: November 21, 2018

Submitted to:
Alberta Environment and Parks – Aster Wang
Team Lead – Water Approvals

Submitted by:
Fortress Mountain Resort Ltd - Chris Chevalier
President
Box 8173, Canmore, AB T1W 2T9
wk. 403 591-0320 cl. 403 688-3099
chris.chevalier@skifortress.com

Table of Contents

1.0	Introduction		3
2.0	Change In Purpose Request Details		3
	2.1	Forecasted Use	4
	2.2	Withdrawal and Usage	4
3.0	Closing		5

Appendices

A. Alberta Licence to Divert and Use Water
B. EPEA Approval Letter
C. KID & AEP approvals for Construction
D. Creek Water Flows
E. Craig Christensen Master Thesis

1.0 Introduction

Fortress Mountain Holdings has applied for a change in use on its domestic/potable water licence. This will allow for the commercial sale of a quantity of water from an existing allocation to support numerous re-development and sustainability initiatives. The annual quantity of water to be sold represents a very small percentage of the total water flow in the study area.

History

Fortress Mountain Ski Resort is located adjacent to the Continental Divide in the Canadian Rockies 1.5 hours west of Calgary Alberta.

Fortress Mountain Holdings Ltd. (FMH) holds two water licences totaling 155 acre feet/yr: 80 acre feet for Municipal use (approx. 100 million litres.) and 75 acre feet/yr for snowmaking (approx. 92 million liters).

The water licences were originally issued in 1968 and will renew in 2036 (see Appendix A)

The chairlifts and Daylodge at Fortress have been closed to the public since approximately December 2004 and as such there has been no water usage. The Government of Alberta (through AEP) knew and understood that there would be no (or limited) use until the new chair lifts and new Daylodge are completed. The "Phase 1" plan is described in detail in the Ecosign Mountain Resorts Master Plan that AEP has on file.

Fortress Mountain Holdings Ltd obtained the dispositions for the land leases and the water licences in July 2010. Since that time FMH has been working towards the re-opening of the ski resort as a fully lift-serviced resort and in fact must do so by December 2020 per clauses in the dispositions.

As a first step towards this re-opening, FMH was granted approval to rebuild/replace its potable water treatment plant and install the associated piping to the various future facilities, i.e. daylodge, future staff quarters, shops, fire hydrants, etc. This work was undertaken in summer 2018 and is well along the path to its completion which is expected in spring/summer 2019. The water treatment plant is on-property and will be positioned in the spring of 2019. This project had a capital spend of over $4.5 million and represents FMH's commitment to the re-opening of Fortress for the Alberta Public and associated use of water as permitted in the held licenses. This investment represents the largest single capital expenditure at Fortress since 1978.

FMH expects to have limited water use for staff and construction crews commencing Spring/Summer 2019. The commissioning requirement date of the functioning Water Treatment System (EPEA approval #370469-00-00) is December 31, 2019 (See Appendix B). Full re-opening of the resort and associated increased water usage is expected by December 2020.

2.0 Change In Purpose Request Details

During the summer of 2018 FMH discussed with AEP and KID the ability to add a raw water spur line to the already approved and under construction potable water works system. This request was approved by both parties (see Appendix C). Concurrently FMH applied to AEP for this current amendment in use from municipal to "municipal and commercial". As Fortress has been closed to public use and therefor no water could be used, FMH did not want to "waste" water to demonstrate use. As Fortress has shown significant investment and progress towards a position of municipal water use, it is requested that consideration in regard to 'point D' in the *Water Licence Change of Purpose Administrative Licensing Criteria* be provided.

2.1 Forecasted Use

The FMH potable water license allocation is for 98,678,547 litres. Current ski industry water usage averages are approximately 14.6 litres per skier. This accounts for staff, cooking, toilets etc. FMH anticipates having 120,000 skier visits in its opening season therefore requiring 1,752,000 litres. As Fortress grows its visits over future seasons to what is anticipated to be approx. 200,000 this will require 2,920,000 litres. Accommodations for staff and skier visit growth will add to the demand, potentially up to approximately 5 million litres. For local comparison, at Sunshine Village, the potable usage is approximately 6-7 million litres per annum with an 80 room hotel, staff accommodation and over 500,000 skier visits. Forecasted immediate and future potable water use at Fortress leaves over 93 million litres available within the current allocation.

FMH has a signed MOU with a Calgary based company seeking to purchase FMH raw water with bottling to be done in Southern Alberta. Initial sales and marketing will occur in Alberta and then regionally as the business develops.

As the ski industry sees significant fluctuations in skier visits from season to season as a weather/snow dependant business, water use will also naturally fluctuate somewhat. FMH proposes to utilize up to 50 million litres per annum of the allocation for potential resale leaving a 43-million-liter buffer. With approx. 5 million required for the resort operation this will leave approx. 44% of the allotted volume unused. Essentially if skier visits go up, water use for bottling will go down and vice versa. This will provide financial assistance and stability to the spikes and troughs of a weather-and-snow dependent business.

2.2 Withdrawal and Usage

The source of the water (coulee tributary to Galatea creek) has flows that have been and continue to be measured by the University of Saskatchewan Centre for Hydrology (Dr. John Pomeroy supervising). (See Appendix D for water flow chart. It should be noted for clarity that what is referred to as 'Bonsai Creek' is the flow outlet just below the source and what is referred to as 'Fortress Creek' is the same watercourse just above the potable water pick up). In summary however: the source creek produces 1.7-1.9 billion liters per annum from what is referred to as the Bonsai Basin, with 50 million liters representing 2.78% of this flow. This annual flow total does not include other drainage volumes from what is referred to as the 'Northern Outlet Spring' that enters below the Bonsai Basin study plot but above the reservoir in which the pick-up pumps are located. This knowledge would allow for assumptions of higher water flows that what is used in calculations contained in this document. In relation to this creek, Golder & Associates has also confirmed it as being a non-fish bearing stream through its currently being developed Fortress Redevelopment Environmental Overview.

For raw water withdrawals, the water will be pumped from the creek to a 33,000-liter reservoir tank immediately above the filling station located in what is referred to as the Condo Parking Lot (an already existing lot). This allows for very gradual withdrawal from the creek while also providing quick truck filling from the reservoir tank. Pumping rates at the creek are rated at a maximum of 8.8 liters/second and most often 4.4 liters/second. At a potential maximum annual withdrawal of approx. 50 million liters this represents 136,986 liters/day. Transport of this volume is achieved by moving an average of nine water truckloads of 15,000 liters each/day, on a year-round basis. This maximum usage will take a number of years to achieve however, and first year withdrawals are estimated to be significantly less (<25 million liters).

FMH believes this amount of an existing allocation represents a relatively small volume percentage of the annual creek flow and will not adversely impact the watershed. FMH also understands that withdrawals in times of extreme low flows are not good for the environmental health of the stream. FMH will monitor and reduce withdrawals in times of low flows ensuring stream viability and constant flows. Minimizing impact to the creek flow has also been designed into the entire water system to have low withdrawal flow rates from the creek supplying a high flow filling reservoir.

In relation to the greater drainage, that being the Kananaskis River, the 19 year average discharge has been calculated using Barrier Lake Dam flow rates as obtained through www.rivers.alberta.ca at being approximately 443 billion liters/yr. The proposed sales volume of water is approximately 0.0113% of this total average flow of the Kananaskis River, with the entire current potable license representing 0.0223%.

In addition, beginning in 2014, The University of Calgary has conducted hydrogeological studies within an area in FMH's leasehold named Bonsai Lake Basin. These recent studies culminated in a Master's Thesis published by Craig Christensen in November 2017 (see Appendix E)

This study characterizes the hydrogeology of the Bonsai Lake Basin. Three different geophysical methods (electrical resistivity tomography, seismic refraction tomography, and ground penetrating radar) imaged structures such as thick, heterogeneous talus, permafrost, and a buried over deepening. Bedrock topography, overburden heterogeneity, and overburden thickness are the most important controls on groundwater flow paths and storage which may explain anomalously high winter base flows at the site. (See Appendix E, Fig. 5.9

This study further confirmed that the Bonsai Lake Basin discharges 1.7-1.9 billion litres annually into Galatea Creek. (See Appendix E, section 6.1 - Streamflow Comparisons with Nearby Headwater Basins)

3.0 Closing

Fortress Mountain Resort occupies a very special Crown leasehold within the Kananaskis Valley. It is a very memorable place for many Albertans, and the re-opening is keenly anticipated.

The Government of Alberta has expressed its desire that Fortress remain a ski area for the enjoyment of the public, however the current restrictions placed on traditional ski resort developments are onerous and highly unlikely to change. This causes significant financial challenges along with difficulty in remaining competitive with other regional competitors (i.e. real estate development controls, four season tourist activities, permitted offerings, etc.)

To accomplish this mutual re-development goal, Fortress came up with a novel solution that addresses some of the existing challenges: Selling a portion of the already existing water allocation will provide for the successful and competitive re-development of the resort and achieve providing the Fortress lands for future generations to enjoy

New ways to sustainably develop while still protecting the environment requires new ways of thinking. We feel this approach achieves the Fortress re-development and environmental goals, and is compatible with the values of Kananaskis Country, AEP, and the Alberta public.

Supplementary Information Package For Change In Purpose Application
November 2018

APPENDIX A

Alberta Licence to Divert and Use Water

Alberta

ENVIRONMENT

LICENCE
to DIVERT AND USE WATER

Pursuant to Sections 11 and 33
THE WATER RESOURCES ACT

File No 12562

Priority No 1968-10-30-01

Purpose Municipal

Drainage Basin Bow River

First Issued 1982 23

Fortress Mountain Resorts Ltd.
c/o Howard, Mackie
Barristers and Solicitors
300, One Calgary Place
330, 5th Avenue, S.W.
Calgary, Alberta
T2P 0L4

TRANSFER RECORDED
CONTROLLER OF WATER RESOURCES
SEE LETTER DATED 1987-05-11

HAVING COMPLIED with the applicable provisions of The Water Resources Act and the regulations thereunder and Interim Licence No 6298 a copy of which is attached hereto and incorporated herein

IS HEREBY GRANTED LICENCE to divert and use the quantities of water prescribed in the Interim Licence in accordance with and subject to all other applicable provisions of that Act and the regulations thereunder, and the terms and conditions attached hereto and incorporated herein at locations described in the Interim Licence

BY MEANS AND THROUGH works and undertakings described in the Interim Licence

1982 23

WR 4 (July 8

Alberta
ENVIRONMENT

UPDATED AND RE-ISSUED

INTERIM LICENCE

Pursuant to Section 18
THE WATER RESOURCES ACT

Issued to: Fortress Mountain Resorts Ltd.
c/o Howard, Mackie
Barristers and Solicitors
300, One Calgary Place
330, 5th Avenue S.W.
Calgary, Alberta T2P 0L4

No. 6298

File No. 12562

Priority No. 1968-10-30-01

This updated and re-issued Interim Licence particularizes the rights, privileges and obligations embodied in and associated with the original Interim Licence as numbered above, or with any other form of authorization or approval issued in connection with the project identified herein under any former applicable Act or regulation, and updates same to conform to and comply with the current Act, regulations and standards.

In particular this Interim Licence provides for the right to

A. Construct, maintain and operate works as shown on current plans and reports filed, approved and identified in departmental records as:

12562-1 General and Detail Plan
12562-2 Key Plan and Water Supply Layout

B. Divert and use water as hereinafter specified and described subject to the terms and conditions attached hereto and incorporated herein:

PURPOSE: Municipal (Urban Water Supply)

SOURCE OF SUPPLY: Coulee tributary to Galatea reek

POINT OF DIVERSION: NE 32-21-9-5

GROSS DIVERSION: Up to 80.0 acre-feet annually consisting of:

1. Estimated Consumptive Use 80.0 acre-feet

2. Estimated Losses Ni

3. Estimated Return Flow: Nil

RESERVOIR CAPACITY 0.54 acre-feet

Date first issued 1968 12 05

Date re-issued 1982 11 23

First issued to Kanaka Holdings Lt

Original—Department
Copy—Licensee
WR 2A (Aug/82)

File: 12562

TERMS AND CONDITIONS INTERIM LICENCE NO. 6298

1 The licensee shall provide facilities for the release of water to riparians and prior licensees when requested to do so by the Controller of Water Resources.

2. The licensee is responsible for the operation and maintenance of the works and for any damages that may result therefrom.

3. The licensee shall submit an annual water use return to the Controller of Water Resources, Alberta Environment on or before January 31st in each year for the preceding calendar year showing:

periods and rates of diversion;

the total annual quantity of water diverted;

(c) the total annual quantity of water returned;

4. The rights and privileges hereby granted are subject to periodic review and to modification to ensure the most beneficial use of the water in the public interest and more particularly to ensure preservation of the rights of other water users.

5. The rights and privileges hereby granted can only be extended or modified with the approval of the Controller of Water Resources and are subject to cancellation or modification as provided in the Water Resources Act.

6. Following completion of the works herein authorized this interim licence and its terms and conditions shall be attached to and become part of the licence to use water issued under the provisions of Section 33 of the Water Resources Act.

1982 11 23
Dated at Edmonton

Supplementary Information Package For Change In Purpose Application
November 2018

APPENDIX B

EPEA Approval Letter

Alberta Environment and Parks

Provincial Programs
Regulatory Approvals Centre
5th Floor, South Petroleum Plaza
9915 – 108 Street
Edmonton, Alberta T5K 2G8
Canada
Telephone: (780) 427-6311
Fax: (780) 422-0154
www.aep.alberta.ca

December 19, 2017

Chris Chevalier
Fortress Mountain Holdings Ltd.
PO BOX 8173
CANMORE, AB T1W 2T9

Dear Mr. Chevalier:

Re: Fortress Mountain Resort Waterworks System
Application No. 001-370469

Your application for an approval under the *Environmental Protection and Enhancement Act* (EPEA) has been reviewed and enclosed is Approval No. 370469-00-00.

It is your responsibility to obtain any approvals, permits or licences that are required from other agencies.

The *Environmental Protection and Enhancement Act* regulations that pertain to your approved facility include at least the following:

- *Activities Designation Regulation*, Alberta Regulation 276/2003, as amended.
- *Approvals and Registrations Procedure Regulation*, Alberta Regulation 113/93, as amended.
- *Environmental Protection and Enhancement (Miscellaneous) Regulation*, Alberta Regulation 118/93, as amended.
- *Potable Water Regulation*, Alberta Regulation 277/2003, as amended.

Other regulations and legislation may apply.

A copy can be obtained, for a small fee, by contacting the Queen's Printer Bookstore in Edmonton at (780) 427-4952, or in Calgary at (403) 297-6251, or on-line at http://www.gov.ab.ca/qp.

It is recommended that you have the regulations above available, as you need to be aware of the requirements applicable with your facility.

The Act may provide the approval holder a right of appeal against any term or condition contained in the approval to the Alberta Environmental Appeals Board. You should note that there are strict time lines for filing an appeal dependent on the type of appeal. If you choose to appeal, please contact the office of the Registrar of Appeals, Environmental Appeals Board of Alberta, 3rd Floor, 10011 - 109 Street, Edmonton, Alberta, T5J 3S8, telephone (780) 427-6207.

If you have any questions, please contact me at (780) 427-6311.

Yours truly,

Tanya Berube,
Applications Coordinator

Enclosure

cc: Kate Vasicek - South Saskatchewan Region - Calgary
Darin Langhorst - McElhanneyConsulting Services Ltd.

Supplementary Information Package For Change In Purpose Application
November 2018

APPENDIX C

KID & AEP Approvals for Construction

KANANASKIS IMPROVEMENT DISTRICT

DEVELOPMENT PERMIT
REQUEST FOR REVISION(S) OR ADDITION(S)

Government of Alberta
Tourism, Parks and Recreation

18-05	Development -	Waterworks System Redevelopment
	Location -	Fortress Mountain Resort Sec 32 & Sec 33 Twp 21 Rg 9 WS
	Street Address -	1 Fortress Mountain Road

Disposition Holder

Title of Disposition Holder		
Fortress Mountain Holdings Ltd		
Mailing Address		
Box 8173, Canmore, Alberta T1W 2T9		
Email Address	Phone #	Alt Phone #
chris.mueller@skifortress.com	403-688-4421	403-591-0320

Applicant Contact Information (all correspondence and notifications will be sent to this address)

Name of Applicant		
Chris Mueller - Director of Operations & Maintenance		
Mailing Address		
Box 8173, Canmore, Alberta T1W 2T9		
Email Address	Phone #	Alt Phone #
chris.mueller@skifortress.com	403-688-4421	403-591-0320

Land Manager

Name of Land Owner	Name of Ministry Contact	
Alberta Environment and Parks	Geoff Smith	
Mailing Address		
8660 Bearspaw Dam Road, Calgary, Alberta T3L 1S4		
Email Address	Phone #	Alt Phone #
geoff.smith@gov.ab.ca	403-297-8591	

***ALL fields shall be completed**

REVISION(S) OR ADDITION(S) BEING REQUESTED FOR APPROVAL:

The system as approved stays essentially unchanged save the addition of a 150mm raw water line sharing the potable water line trench down the FrontSide, separating its burial to contour around to an outlet station at the existing quonset. Approximate length of separated burial line is 100m. Installation of a small (estimated to be around 30,000l) above ground holding tank and outlet station (approx 10'x10') to be installed next to existing Quonset on our already existing parking lot. See updated drawing booklet: https://www.dropbox.com/s/lwvq9kx8gi8smui/Waterworks%20drawing%20set%2C%20Aug%202018.pdf?dl=0 . Final as builts to be provided upon completion. Fee value doesn't change as permit has already surpassed the $20,000 maximum.

Please provide updated copies of all items from the Master Checklist which are affected by your request.
Response may take up to 45 days for items requiring approval by the SDA.

For Office Use Only:

[X] **APPROVED**

CONDITION(S) OF REVISION(S) OR ADDITION(S):

Following details to be provided prior to final build and install of additional components:
- Drawing set for outlet station including dimensions, color palette and base details.
- Final specification of holding tank, including location and base details.
- KID reserves the right to request additional screening once components of revision are installed.

Date of Approval: October 9th, 2018

[ ] **DENIED**

REASON FOR DENIAL:

Signature of Development Officer:

From: Geoff Smith <Geoff.Smith@gov.ab.ca>
Sent: Tuesday, September 4, 2018 9:46 AM
To: chris.mueller@skifortress.com
Cc: 'Thomas Heath' <thomas.heath@skifortress.com>; chris.chevalier@skifortress.com
Subject: RE: update on water install

Sorry for the delay Chris.

Yes, please use this e-mail, as no concerns from our office (Lands approvals, Environment and Parks) for an additional water line into the parking area, utilizing mostly the same trenching and construction methods

Thanks

Geoff Smith RPFT
Land Management Specialist
Alberta Environment and Parks
South Sask. Region
(403) 297-8591

Supplementary Information Package For Change In Purpose Application
November 2018

APPENDIX D

Creek Water Flows

Bonsai Creek 2014	
Date	Flow(L/s)
29-May-14	37
11-Jun-14	97
18-Jun-14	156
11-Jul-14	166
18-Jul-14	56
23-Jul-14	70
1-Aug-14	36
12-Aug-14	3
18-Aug-14	10
23-Aug-14	26
16-Sep-14	4

Bonsai Creek 2015	
Date	Flow(L/s)
11-Jun-15	324
18-Jun-15	75
14-Jul-15	48
28-Jul-15	55

Bonsai Creek 2016	
Date	Flow(L/s)
22-Apr-16	4
13-May-16	21
27-May-16	96
15-Jun-16	108
14-Jul-16	67
17-Aug-16	14
9-Sep-16	24
30-Sep-16	17

Bonsai Creek 2017	
Date	Flow(L/s)
1-Jun-17	223
6-Jun-17	196
26-Jun-17	167
14-Jul-17	103
28-Jul-17	59
15-Aug-17	39

Fortress Creek 2016	
Date	Flow(L/s)
2-Aug-16	63
17-Aug-16	39
9-Sep-16	33
30-Sep-16	32

Fortress Creek 2017	
Date	Flow(L/s)
1-Jun-17	618
6-Jun-17	527
25-Jun-17	283
14-Jul-17	170
28-Jul-17	77
15-Aug-17	41

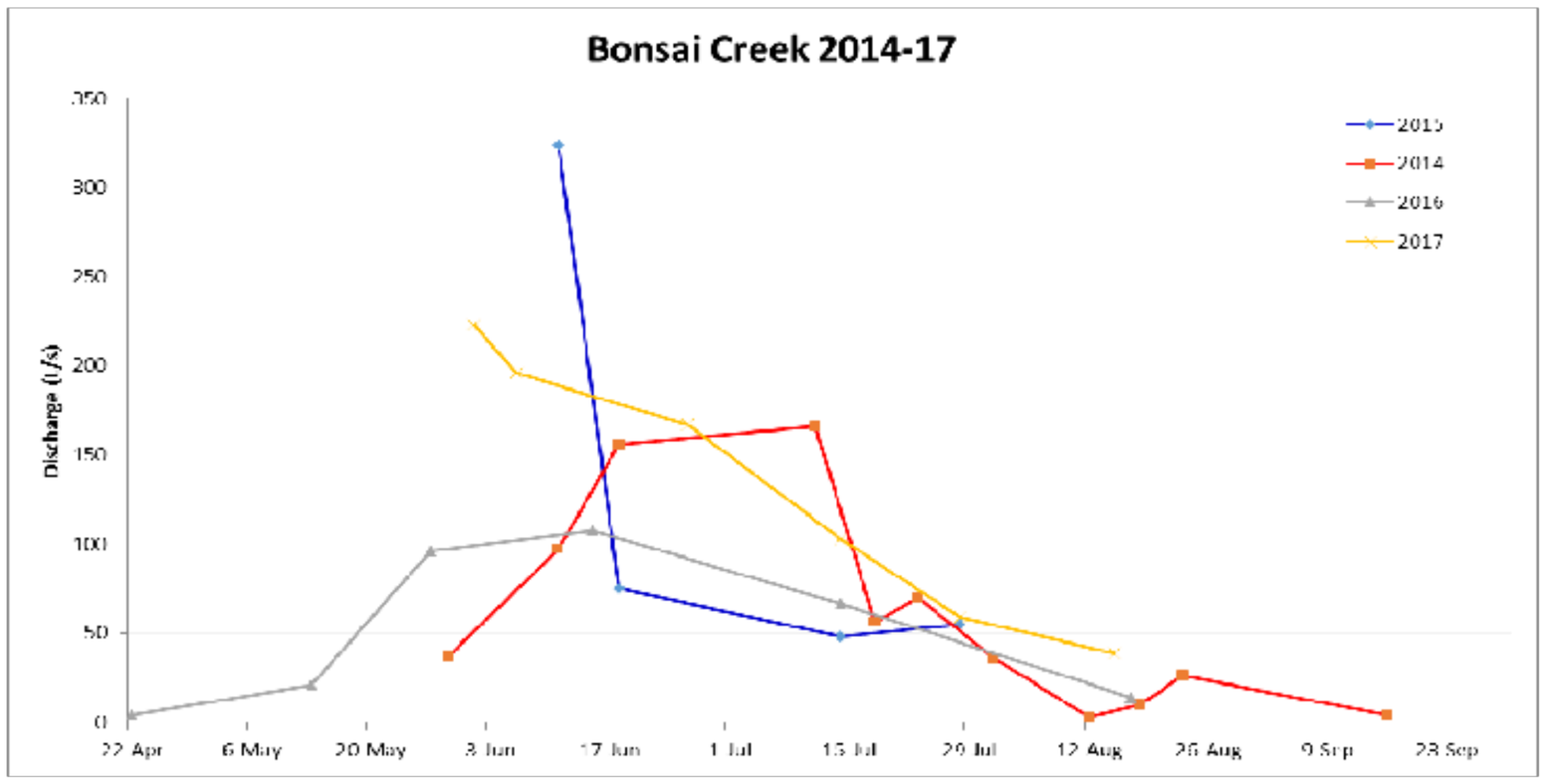

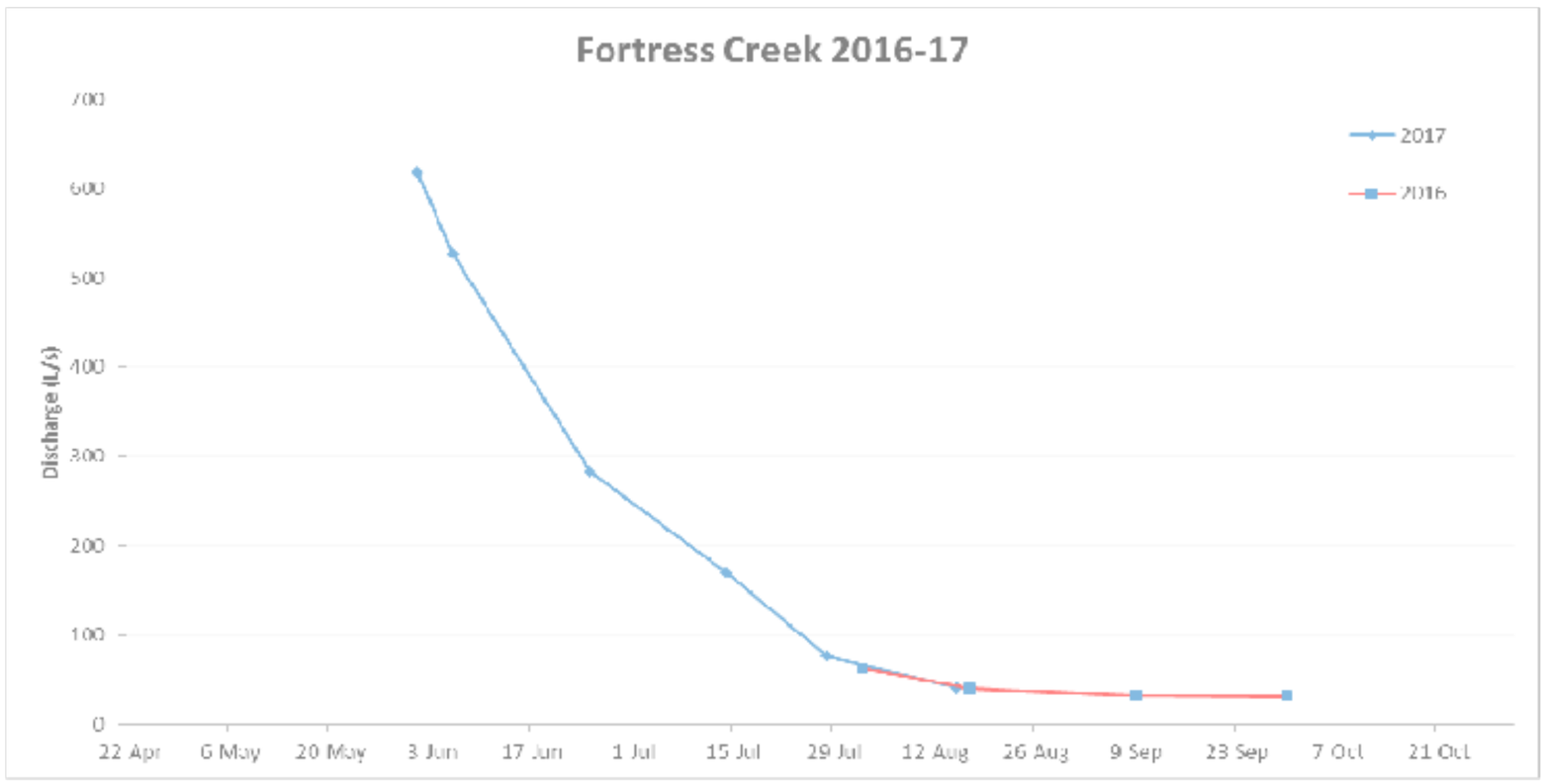

Supplementary Information Package For Change In Purpose Application
November 2018

APPENDIX E

Craig Christensen Master Thesis

UNIVERSITY OF CALGARY

A geophysical study of alpine groundwater processes and their geologic controls in the southeastern Canadian Rocky Mountains

by

Craig William Christensen

A THESIS

SUBMITTED TO THE FACULTY OF GRADUATE STUDIES

IN PARTIAL FULFILMENT OF THE REQUIREMENTS FOR THE

DEGREE OF MASTER OF SCIENCE

GRADUATE PROGRAM IN GEOLOGY AND GEOPHYSICS

CALGARY, ALBERTA

July 2017

© Craig William Christensen 2017

Abstract

Groundwater storage is essential for maintaining steady stream flows and temperatures in mountain watersheds, yet catchment-scale hydrogeological processes remain poorly understood. This study characterizes the hydrogeology of a new site in Kananaskis Valley of southeastern Canadian Rocky Mountains. Three different geophysical methods (electrical resistivity tomography, seismic refraction tomography, and ground penetrating radar) imaged structures such as thick, heterogenous talus, permafrost, and a buried overdeepening. Bedrock topography, overburden heterogeneity, and overburden thickness are the most important controls on groundwater flow paths and storage, and may explain anomalously high winter base flows at the site. Comparing the talus deposits to those at a contrasting site in Yoho National Park points to a causal link between hydrogeological characteristics and physiographic variables, hinting at possible spatial patterns in groundwater storage potential. These results will help water resource and ecosystem managers in adapting to stream flow changes resulting from climate change.

Preface

Some figures are tables within this thesis (and earlier versions thereof) have previously been published in Christensen et al. (2017), an industry magazine article of which I am lead author. These specifically are Figure 1-1, Figure 3-2, Figure 5-2, Figure 5-5, Table 4-6, and Table 5-3, adapted from Figure 1, Figure 7, Figure 8B, Figure 4, Table 2, and Table 1, respectively, from Christensen et al. (2017). Refer to Appendix H for the permission letters to reprint these materials.

Acknowledgements

First and foremost, this study would not have been without the support of many of friends and colleagues who assisted me in field, especially on those two long and challenging geophysics campaigns in July 2015 and July 2016. My thanks go to Polina Adbrakhimova, Laura Beamish, Jenna Christensen, Cody Good, Jennifer Hanlon, Jordan Harrington, Jesse He, Brandon Hill, Yu Hu, Feodora Ivaniuk, Chris Jackson, Luke Kary, Kristina Kublik, Barret Kurylyk, Matthew Lennon, Andrius Paznekas, Anna Pekinasova, Saskia Schaelicke, Kim Sena, Shelby Snow, Ben Stevenson, Kelsey Tillapaugh, Jenna Trofin, Calista Yim, and Scarlett Zhu. Big thanks go out especially to Polina for working late into the night to help me with preparing ERT sequence files on an unfamiliar instrument that I was woefully underprepared to use.

I also owe my gratitude to several faculty members for mentoring me, offering valuable technical advice regarding data acquisition, processing, and interpretation, as well as joining me in the field. Thank you to Masaki Hayashi, Larry Bentley, Jerry (Gerald) Osborn, and Rachel Lauer. My thanks also go to Ty Ferré, who offered some helpful comments on his brief visit to Calgary.

I have many collaborators at University of Saskatchewan to thank. John Pomeroy and his team at the Coldwater Hydrology laboratory introduced us to the site, assisted with field work and logistics, and shared valuable hydrometric and meteorological data that greatly enhanced the interpretation of my geophysical results. Special thanks go to May Guan, Angus Duncan, Michael Schirmer, and Logan (Xing) Fang. Additionally, I thank Cherie Westbrook and Hongye Wu, who were concurrently studying the water balance and chemistry of the Bonsai Lake basin, for sharing some of their preliminary results, which helped with planning my own hydrogeological study and with interpreting some of my own results.

Logistical support for field campaigns was provided by the folks at the Fortress Mountain Resort and at the Biogeoscience Institute (particularly from Adrienne Cunnings). The Norwegian Geotechnical Institute (namely Andreas Aspmo Pfaffhuber and Asgeir Olaf Kydland Lysdahl) also generously shared code for displaying ERT images.

On a more personal level, I thank my colleagues in the physical hydrology lab who I have not yet mentioned (Qixin Chang, Anna Leuteritz, Aaron Mohammed, Laura Morgan, Saskia Noorduijn, Igor Pavlovskii, and Kabir Rasouli) for offering good technical advice when I needed it and for

making this a congenial place to work and study. I thank my mentors Brian Schulte and Trevor Borden for helping me keep a healthy perspective on life, career, and the future when the going got tough. Similarly, thank you to my fellow scholars in the Graduate College for making my last year at the University of Calgary an especially enriching, energizing, and engaging experience.

Funding for this project was provided by a grant from the National Science and Engineering Research Council (NSERC), and by the following scholarships: NSERC Canadian Graduate Scholarship, Canadian Society of Exploration Geophysicists (CSEG) Foundation Scholarship, Canadian Exploration Geophysical Society (KEGS) Foundation Geological Survey of Canada (GSC) Pioneers Scholarship, Alberta Graduate Student Scholarship, and University of Calgary Graduate College Admission Scholarship.

Dedication

To my loving family,

Mom (Ann), Dad (Kevin), Jenna, and Allison,

for being with me for all these years no matter how far away from home I inevitably find myself.

Table of Contents (Abridged)

Abstract ii
Preface iii
Acknowledgements iv
Dedication vi
List of Figures x
List of Tables xix
List of Abbreviations xx
Chapter 1 Introduction 1
Chapter 2 Site Description 5
Chapter 3 Methods 13
Chapter 4 Talus Hydrogeology 30
Chapter 5 Hydrogeology of Low-Lying Features 64
Chapter 6 Synthesis 106
Chapter 7 Conclusions 121
References 124
Appendix A List of Field Site Visits 140
Appendix B Petrophysics of Alpine Deposits 142
Appendix C Optimization Equations for Geophysical Inversion 144
Appendix D Electrical Resistivity Tomography Images 146
Appendix E Seismic Refraction Tomography Images 178
Appendix F Ground Penetrating Radar Images 198
Appendix G Literature Review of Links Between Mountain Topography and Geomorphology of Mountain Landforms 209
Appendix H Copyright Permission Letters 212

Table of Contents

Abstract ii
Preface iii
Acknowledgements iv
Dedication vi
List of Figures x
List of Tables xix
List of Abbreviations xx
Chapter 1 Introduction 1

1.1 Review of Key Literature *1*
1.1.1 Mountains and River Hydrology: A Global and Regional Context 1
1.1.2 Catchment-Scale Groundwater Processes in Mountainous Headwater Basins 2
1.2 Research Objectives and Thesis Organization *3*
1.3 Figures *4*

Chapter 2 Site Description 5

2.1 General Overview *5*
2.2 Geological Setting: Bedrock Geology and Glacial History *5*
2.3 Precipitation Trends *6*
2.4 Tables *8*
2.5 Figures *10*

Chapter 3 Methods 13

3.1 Preliminary Site Reconnaissance *13*
3.2 Geophysical Methods *13*
3.2.1 Electrical Resistivity Tomography 15
3.2.2 Seismic Refraction Tomography 17
3.2.3 Ground Penetrating Radar 19
3.3 Supplementary Data Collection *19*
3.4 Tables *21*
3.5 Figures *25*

Chapter 4 Talus Hydrogeology 30

4.1 Literature Review: Hydrogeology of Alpine Talus *30*
4.2 Site Description *33*
4.2.1 Topographic Characteristics 33
4.2.2 Hydrological Features 34
4.2.3 Grain Size Differences 34
4.2.4 Summary and Classification by Formation Processes 35
4.3 Results *35*
4.3.1 General Trends in Geophysical Images 36
4.3.1.1 ERT 36
4.3.1.2 GPR 37
4.3.1.3 SRT 38
4.3.2 Other Results 38
4.3.2.1 Upper East Cone Anomaly 38
4.3.2.2 Bottom Temperature of Snowpack 39
4.3.2.3 Petrophysical Surveys Along Eastern Ridge 39
4.4 Discussion *40*
4.4.1 Geomorphology of the Talus Slope 40
4.4.2 Hydrologic Flow Paths 42
4.4.3 Permafrost Occurrence 43
4.5 Summary of Findings *44*
4.6 Tables *45*
4.7 Figures *48*

Chapter 5 Hydrogeology of Low-Lying Features 64

5.1 Literature Review: Hydrogeology of Low-Relief Alpine Deposits *64*
5.2 Detailed Site Description *66*
5.2.1 Meadow 66
5.2.2 Moraines 67
5.2.3 Hydrology 68
5.3 Results *69*
5.3.1 Meadow 70
5.3.1.1 ERT 70
5.3.1.2 SRT 71
5.3.1.3 GPR 71
5.3.1.4 Piezometric Data 72

5.3.2 Moraine and Outlet Springs 72
5.3.2.1 SRT 72
5.3.2.2 ERT 73
5.4 Discussion 74
5.4.1 Geophysics Interpretations 74
5.4.1.1 Geological Conceptual Model 74
5.4.1.1.1 Meadow 74
5.4.1.1.2 Moraines, Lake, and Springs 75
5.4.1.2 Hydrogeological Conceptual model 76
5.4.1.2.1 Summer Conditions 76
5.4.1.2.2 Fall and Winter Fluctuations 78
5.4.2 Controls on Storage and Flow Paths 79
5.4.3 Comparison of Results to Previous Studies 81
5.5 Summary of findings 82
5.6 Tables 82
5.7 Figures 85

Chapter 6 Synthesis 106
6.1 Streamflow Comparisons with Nearby Headwater Basins 106
6.2 Physiographic Controls on Groundwater Processes 108
6.2.1 Comparison of Talus Slopes Opabin Versus Bonsai Lake Basins 109
6.2.2 Emplacement of Fines in Talus Deposits 109
6.2.3 Thickness of Talus Deposit 110
6.2.4 Comparison to Previous Studies and Upscaling of Results 111
6.3 Implications for Alpine Hydrology 112
6.4 Other Limitations 113
6.5 Priorities for Future Study 114
6.6 Tables 116
6.7 Figures 117

Chapter 7 Conclusions 121
References 124
Appendix A List of Field Site Visits 140
Appendix B Petrophysics of Alpine Deposits 142
Appendix C Optimization Equations for Geophysical Inversion 144
C.1 Electrical Resistivity Tomography 144
C.2 Seismic Refraction Tomography 144

Appendix D Electrical Resistivity Tomography Images 146
D.1 ERT1 148
D.2 ERT2 151
D.3 ERT3 153
D.4 ERT4 155
D.5 ERT5 158
D.6 ERT6 160
D.7 ERT7 162
D.8 ERT8 164
D.9 ERT9 166
D.10 ERT10 168
D.11 ERT11 170

D.12 ERT12 ..... *172*
D.13 ERT13 ..... *174*

Appendix E Seismic Refraction Tomography Images 178

E.1 SEIS1-2-4 ..... *178*
E.2 SIES3 ..... *180*
E.3 SEIS5 ..... *182*
E.4 SEIS6 ..... *184*
E.5 SEIS7-8 ..... *186*
E.6 SEIS9 ..... *188*
E.7 SEIS10 ..... *190*
E.8 SEIS11 ..... *192*
E.9 SEIS12 ..... *194*
E.10 SEIS13 ..... *196*

Appendix F Ground Penetrating Radar Images 198

F.1 GPR1 ..... *198*
F.2 GPR2 ..... *202*
F.3 GPR3 ..... *203*
F.4 GPR4 ..... *206*
F.5 GPR5 ..... *207*
F.6 GPR6 ..... *208*

Appendix G Literature Review of Links Between Mountain Topography and Geomorphology of Mountain Landforms 209

G.1 Climatic Controls on Glacier and Talus Development *209*
G.2 Controls on Moraine and Overdeepening Geomorphology *210*

Appendix H Copyright Permission Letters 212

H.1 Letter from Publisher of Christensen et al. (2017) *212*
H.2 Letter from Co-Authors of Christensen et al. (2017) *214*

List of Figures

Figure 1-1: The extent of the South Saskatchewan River Basin in western Canada. Major sub-watersheds are shown, as are major cities, previous alpine sites studied by the Physical Hydrology group at the University of Calgary, and the site presented within this study (Fortress Mountain). The Oldman River, which is a major tributary flowing upstream of the City of Lethbridge, is grouped with the Upper South Saskatchewan catchment area in this dataset. Watershed data source: (PFRA / Agriculture and Agri-Food Canada 2008). Adapted from Christensen et al. (2017). 4

Figure 2-1: A) Topographic map showing major settlements, waterways, and the extent of panel B) in red; B) 2008 Aerial orthophoto of the study site, with 50 m elevation contours and the locations of The Fortress summit shown. Also shown are the catchment areas of Bonsai Lake and the northern outlet spring; C) Oblique view (facing southwest) of a 3D

terrain model with 1976 imagery draped on top. Data sources: (Alberta Energy and Natural Resources 1976; Alberta Sustainable Resource Development 2008; Natural Resources Canada 2016) 10
Figure 2-2: Geological map of study site. Bedrock data source: (McMechan 2012) 11
Figure 2-3: Historical precipitation data interpolated from nearby weather stations at T021R09W5, the township covering the current study area (Bonsai Lake). Data source: (Alberta Agriculture and Forestry 2017) 12
Figure 3-1: Map showing the locations of all geophysical surveys conducted. Panel A shows the full view of the survey area and the extent of Panel B and of Panel C (the largest panel). Note that CMP4 (not labelled) is coincident with CMP5. 25
Figure 3-2: An illustration, using data from SEIS 03, of how successive levels of band-pass filtering were used to assist with making first arrival picks (red x's). The original stacked section (A) was filtered using a plateau frequency range of 20-40 Hz and cut-off values of 0-200 Hz (B), and again with an upper cut-off of 80 Hz (C). The first arrival picks illustrate that the leading edge of a pulse as it appears in (C) was not used; rather, the filtered data assisted in picking the appropriate pulse in the unfiltered data (A). Adapted from Christensen et al. (2017). 26
Figure 3-3: A) An example of co-located vertical logs of EM velocity (blue) and resistivity (orange) from CMP9. EM-velocities are taken from the 1D-velocity models resulting from semblance analysis of CMP captures, while resistivity is interpolated from the ERT models at those locations. B) Scatter plot showing collocated pairs of resistivity and EM-velocity from all nine CMP captures. Colours of the data points indicate which CMP location they are from. The modeled correlation above in black was used to produce a 2D EM-velocity model and to convert GPR reflection sections from time domain to depth domain. See Figure 3-1 for the location of CMP measurements. 27
Figure 3-4: Coloured diamonds indicate the locations where bottom temperature of snowpack (BTS) sensors were installed from October 2015 to June 2016. Colours of the diamonds correspond to the colours used in Figure 4-19. Grid coordinates are in Universal Transverse Mercator (UTM), Zone 11 North, WGS 1984 Datum. 28
Figure 3-5: Map showing the locations where piezometers, stilling wells, and a barometer (blue hexagons) were installed. The red rectangle on the left indicates the extent of the right-hand panel. ERT survey lines are shown as pink or red lines. Grid coordinates: UTM, Zone 11 WGS 1984 Datum 29
Figure 4-1: An oblique photo (facing southwest) of the talus deposits in the study area taken on June 14, 2016. The four talus cones are outlined in orange, though the Lower East cone is partially obscured by trees in the foreground. Approximate locations of important springs and waterfalls are indicated in blue, while notable couloirs above the Upper East and Central Cones are outlined with red arrows. 48
Figure 4-2: Surficial geology map with the different talus deposits labelled. Abbreviations refer to: [WC] West Cone; [CC] Central Cone; [UEC] Upper East Cone; [LEC] Lower East Cone; and [ETS] Eastern Talus Slope. The coloured lines traversing the length of talus deposits indicate the alignment of the topographic profiles in Figure 4-3. Grid coordinates are in Universal Transverse Mercator, Zone 11 North WGS 1984 Datum. 49

Figure 4-3: The elevation and slope profiles of the talus deposits. A) shows the elevation as a function of distance from bottom of the slope, while B) shows the slope angle. 50
Figure 4-4: A lunate moraine ridge located on the Eastern Talus Slopes. Photo taken from the northwest shore of Bonsai Lake on June 18, 2015. 50
Figure 4-5: Levees related to debris flow events deposited on top of the grassy meadow at the toe of the Lower East Cone. Photo dated June 18, 2015. 51
Figure 4-6: Photos showing important surface water features on the talus cone. A) SP1 on the West Cone on July 8, 2015. View is oriented downhill to the northeast. B) An annotated photo of important hydrologic features on the Central Cone, including: the location of SP3 (blue dot), surface water filling ephemeral streams (white arrows), and the alignment of large channels scoured into the surface of the talus (blue dashed line). The boulder circled in red is the same as that seen in Figure 4-8D. Photo faces south and was taken June 28, 2016. 51
Figure 4-7: Channel features (annotated with white arrows) are visible in air photo on the Western Cone (WC). Extent of Central Cone (CC) is shown with dashed black line. Photo number 171 from roll number AS1486 (Alberta Energy and Natural Resources 1976). 52
Figure 4-8: A sample of photos highlighting the differences in grain sizes and packing on the talus cones within the study area: A) large, loosely packed boulders with little infill on the eastern side of the Central Cone, located at approximately 375 m on ERT3; B) small cobbles and coarse gravel filled in with soil at the start of ERT2 on the West Cone; C) tightly packed grains of many sizes near the apex of the Central Cone; D) on the west half of the Central Cone near the apex, there is a linear depression that has minimal fine-grained sediments (in the foreground) and is less densely packed and less vegetated than the surrounding deposits outside the channel (seen in the background). The boulder circled in red at the edge of the channel is the same as that circled in Figure 4-6B. Photos are dated July 22, 2015 (A), July 20, 2015 (B), and July 8, 2015 (C and D). 53
Figure 4-9: Composite of the P-wave velocity and resistivity models along ERT1. Annotations indicate the locations of: BTS sensors (diamonds), springs (blue circle), tie points with other lines (grey boxes), and convergent flow paths (black ellipses). Only the second half of ERT1's and SEIS1-2-4's full lengths (shown here) intersect the talus. See Figure 3-1 for the location of the survey line. 54
Figure 4-10: Co-located GPR reflection and electrical resistivity images with corresponding features emphasized. These include: very high-amplitude GPR reflectors at locations of strong resistivity contrast, and reduced radar wave penetration where sediments at surface have lower resistivity. See Figure 3-1 for the location of the survey line. See Section 3.2.3 for notes on the GPR color scale..... 55
Figure 4-11: A sample of GPR data showing the differences in texture near the base of the Central Cone (A) and between the west and Central Cone (B). See Figure 3-1 for the location of the survey line and Section 3.2.3 for notes on the GPR color scale. 56
Figure 4-12: P-wave velocity and resistivity models for SEIS7-8 and ERT3. Annotations indicate the locations of: BTS sensors (diamonds), springs (blue circle), tie points with other lines (grey boxes), convergent flow paths (black ellipses, solid line). See Figure 3-1 for the location of the survey line..... 57

Figure 4-13: Reflection images from GPR4 corresponding to the anomaly at the end of ERT3 and SEIS7-8 (Figure 4-12). Annotations emphasize: high-amplitude reflectors between 350-360 m, a zone of lower amplitude reflectors within the anomaly, and the direct air wave that obscures real geologic structures in the upper few metres of the ground. See Figure 3-1 for the location of the survey line, and Section 3.2.3 for notes on the GPR color scale. 58
Figure 4-14: Composite of the P-wave velocity and resistivity models along ERT5. Annotations indicate the locations of: BTS sensors (diamonds), tie points with other lines (grey boxes), and convergent flow paths (black ellipses). See Figure 3-1 for the location of the survey line..... 59
Figure 4-15: Composite of the P-wave velocity and resistivity models along ERT2. Annotations indicate the locations of: BTS sensors (diamonds), tie points with other lines (grey boxes), convergent flow paths (black ellipses), and the inferred locations of geological contacts from McMechan (2012) (dashed tan lines). See Figure 3-1 for the location of the survey line..... 60
Figure 4-16: Composite of the P-wave velocity and resistivity models along ERT12 and SEIS13. Annotations include: descriptions of surface cover (grey lines), estimated location of the thrust fault from McMechan 2012 (dashed tan line), a spring (blue circle), and the estimated location of intact Fernie Formation (dashed black line). See Figure 3-1 for the location of the survey line..... 61
Figure 4-17: Resistivity image from ERT10, with annotations pointing to typical and anomalous resistivity values within the Fernie Formation. See Figure 3-1 for the location of the survey line..... 62
Figure 4-18: Fence diagram of resistivity images with superimposed surface imagery. Resistivity scale has units of Ωm. Locations of springs are indicated with blue spheres. Cones are labelled UEC (Upper East Cone), CC (Central Cone), and WC (West Cone). Note the anomalously high resistivities in the sections of the Upper East Cone that are more well-shaded than the headwall. 62
Figure 4-19: Temperature data recorded by BTS sensors and corrected using spring melt zero curtain. Note that the sensors have a lower detection limit of -5.0 °C. Sensor locations are shown in Figure 3-4. 63
Figure 5-1: Map showing the areal extent of various surficial units and the locations of important hydrologic features. The blue line within Bonsai Lake indicates location of the stream when the lake is dry in late summer. The two branches of the stream in the meadow are labelled “EMS” for “East Meadow Stream” and “WMS” for the “West Meadow Stream.” Small white arrows indicate the direction of the streams. Uncoloured areas were not mapped or are transitional zones between units. 85
Figure 5-2: A view of the meadow as seen from the Central Cone looking east. Approximate alignments of ERT1 and ERT4 are shown, along with distance markers in metres. The locations of the streams and SP4 are highlighted in blue. The two branches of the stream in the meadow are labelled “EMS” for “East Meadow Stream” and “WMS” for the “West Meadow Stream.” Small, light blue arrows indicate the flow direction of the streams. Adapted from Christensen et al. (2017)..... 86
Figure 5-3: Moraine ridges shown along a hill-shaded DEM used to help delineate their locations. Yellow circles indicate linear depressions that may be the results of alluvial erosion. A

photo of the moraine on the Eastern Talus Slopes is shown in Figure 4-4. The more heavily forested NE corner of the image contains N-S oriented linear artefacts that do not represent real terrain and that might be the result of processing of the LiDAR. 87
Figure 5-4: Rock fragments on moraines like that located on (A) the southern talus slope show more rounding and have a more uniform size distribution compared to (B) undisturbed talus material. Hence, cases like (A) have been interpreted as push moraines. Some moraines, like (C) on the north side of Bonsai Lake, have more angular boulders, have multiple fragments in excess of 3 m wide, and less uniform rock size distribution. These moraines have been interpreted as recessional moraines. Photo dates are: A) June 18, 2015; B) and C) June 28, 2015 88
Figure 5-5: Elevation cross-section showing the main hydrologic features at the study site. See Figure 5-10 for the alignment of this line. Adapted from Christensen et al. (2017). 88
Figure 5-6: Temperature measurements taken from low-lying features in 2015. Refer to Figure 5-1 for the locations of hydrologic features listed..... 89
Figure 5-7: Views of important lakebed features A) A panorama from the north side of the lake. Annotations include compass directions (white letters), locations of B and C (coloured rectangles), flow direction of the small lakebed stream (blue arrows), and location of inlet stream from the meadow. B) One of the sink features (LMK14) where pooled water cascades into void spaces of rocky material that is not covered by lakebed muds. C) A view of groundwater discharge (GWD) at the south shore that supply water (along with the meadow inlet stream) to the small lakebed stream. Photo dates: September 19, 2016. 90
Figure 5-8: Panorama showing the northern outlet spring draining from the base of the moraines. Annotations show the locations of points named “SP6” and “SP7” and compass directions (white letters). Photo date: June 28, 2015. 91
Figure 5-9: Streamflow data from the northern outlet spring. Stream level data courtesy of J. Pomeroy, and rating curve courtesy of H. Wu and C. Westbrook..... 92
Figure 5-10: Overview map of the geophysical lines and main hydrologic features at the study site. The green line indicates the alignment of the cross sections in Figure 5-5 and Figure 5-21. Note that the line labeled “SEIS1” includes roll-along surveys that were combined for the image “SEIS1-2-4.”..... 93
Figure 5-11: P-wave velocity (A) and electrical resistivity (B) models of the meadow, and the interpretation of these results (D). A zoomed view of the meadow with a modified colour scale is also shown in C) to emphasize the thin 1-3 m layer of unsaturated sediments in the meadow above the water table. The black rectangle in A) and B) indicates the extent of the GPR image in Figure 5-13A. Annotations in B) include: important resistivity boundaries (black, dashed lines), Deep Layer 1 and 2 (DL1, DL2), thickness variations in the top layer of the meadow (white lines), and the tie point with ERT4 in Figure 5-12 (grey label). Note that only the first half of ERT1, which is the only portion that interests the meadow, is shown here; portions covering the talus are shown in Chapter 4. See Figure 5-10 for the location of this line. 94
Figure 5-12: P-wave velocity (A) and electrical resistivity (B) models of the meadow, and the interpretation of these results (C). The black rectangle in A) and B) indicates the extent of the GPR image in Figure 5-13B. Annotations in B) include: important resistivity boundaries (black, dashed lines), Deep Layer 1 and 2 (DL1, DL2), resistivity changes in

the moraine, and the tie point with ERT4 in Figure 5-11 (grey label). See Figure 5-10 for the location of this line. 95
Figure 5-13: Radar reflection sections crossing the meadow. Annotations in A) and B) indicate tie-points with intersecting lines (grey boxes), notable flat reflectors (white arrows), and changes in GPR texture (black and blue text). Panel C) is a close-up of B) where changes in texture are emphasized with a blue dashed line, indicating a transition from fine-grained meadow sediments to moraine material. See Figure 5-10 for the line locations and Section 3.2.3 for notes on the color scale. 96
Figure 5-14: Oblique view (facing northwest) focusing on the tie point between ERT1 and ERT4 where resistivity boundary depths of deeper layers differ by as much as 5 m. 97
Figure 5-15: Piezometric data collected in the meadow and lake, shown over the whole field season (A) and during a short period in September 2016 (B). Dashed lines indicate the elevation of (and hence lower detection limit of) the sensors. The stream measurements are taken from the stilling well labelled "HWW" in Figure 3-5 and Figure 5-10. 98
Figure 5-16: Geophysical models from the moraine along the south side of Bonsai Lake. Annotations note the elevation of GWD on the south shore of Bonsai Lake (dashed black line), the minimum elevation of the lakebed (dot-dashed line), the interpreted depth to bedrock (solid black line), and the location of the inlet stream from the meadow to the lake. See Figure 5-10 for the location of this line. 99
Figure 5-17: Resistivity image (in Ωm) along ERT9. The elevation of the lake at the time of survey (2088.5 masl), the lowest point in the lake (2086 masl), and outlet springs SP6 and SP7 (2082 masl), and indicated with horizontal lines. See Figure 5-10 for the location of this line. 100
Figure 5-18: Geophysical models near the northern outlet spring along ERT11. Annotations note the elevation of the interpreted depth to saturation (WT, dashed line), the intersection with ERT8 (grey box), a low-resistivity anomaly at depth (black ellipse), and the elevation of Bonsai Lake (2088.5 masl) at the time of survey. See Figure 5-10 for the location of this line. 100
Figure 5-19: Geophysical models near the northern outlet spring along ERT7. Annotations note the elevation of the interpreted depth to bedrock (BR, solid black line), the interpreted depth to saturation (WT, dashed line), the location of the outlet springs SP6 and SP7, the intersection with ERT8 (grey box), low-resistivity anomalies at depth (black ellipses), and the elevation of Bonsai Lake (2088.5 masl) at the time of survey (dot-dash line). See Figure 5-10 for the location of this line. 101
Figure 5-20: Geophysical models near the northern outlet spring along ERT8. Annotations note the elevation of the interpreted depth to bedrock (BR, solid black line), the interpreted depth to saturation (WT, dashed line), the location of the outlet springs SP6 and SP7, the intersection with ERT7 and ERT11, (grey boxes) and low-resistivity anomalies at depth (black ellipses). See Figure 5-10 for the location of this line. 102
Figure 5-21: A conceptual model showing the geology and water table fluctuations of the study site. Geophysical survey lines parallel to (ERT4) or perpendicular to (ERT1, 6, 9, and 7) this cross-section are noted above. See Figure 5-10 for the alignment of this cross-section. 103

Figure 5-22: Forward modeling exercise with the aim of showing how resistivity of overburden material may affects the interpreted depth to the saturated zone: (A) the known resistivity distribution; (B) the inverted resistivity model based on simulated surface measurements of the known resistivity distribution. 104
Figure 5-23: Map showing all the low-resistivity anomalies (triangle symbols) imaged around the outlet springs in ERT surveys (Figure 5-18B, Figure 5-19B, and Figure 5-20B). 105
Figure 6-1: Map showing the whole cirque southwest of The Fortress. The yellow polygon indicates catchment area (as derived from surface topography) upstream of an important stream confluence. Thicker arrows indicate groundwater flow lines in areas that may plausibly drain into the Northern Outlet Spring (purple) or the northwestern stream branch (yellow) due to unknown bedrock topography. The exact demarcation between the two zones is not exactly known, as suggested by the green arrows. 117
Figure 6-2: A model summarizing how topographic and geologic variables (in green) affect the geomorphologic processes (orange) and hence the geomorphology of talus deposits (red) and in turn their hydrogeological characteristics (blue). 118
Figure 6-3: Comparisons of the headwall characteristics at Bonsai Lake (A) above the Central Cone, and Opabin (B) above the talus studied by Muir et al. (2011). Elevation profiles (C) and calculated slopes (D) are shown along the solid blue and dashed red lines in in A) and B). The second panel on the right in C) shows the same data but with a 1:1 horizontal to vertical aspect ratio. 119
Figure 6-4: Map showing a proposed site for future study. The talus slopes present in the yellow box are also below a north-facing headwall, but differ in that there are no shales from the Exshaw and Banff formations present in the headwall, and the headwall lacks deeply incised gullies..... 120
Figure D-1: Measured apparent resistivities (top) versus those calculated from the final resistivity model (middle) on ERT1. 148
Figure D-2: Comparison of inverted models resulting from different starting models on ERT1. 149
Figure D-3: Forward modeling exercise showing (A) a known resistivity distribution loosely based on the meadow section of ERT1 in Figure 5-11B and (B) the inverted resistivity model based on simulated surface measurements of the known resistivity distribution. 150
Figure D-4: Measured apparent resistivities (top) versus those calculated from the final resistivity model (middle) on ERT2. 151
Figure D-5: Comparison of inverted models resulting from different starting models on ERT2. 152
Figure D-6: Measured apparent resistivities (top) versus those calculated from the final resistivity model (middle) on ERT3. 153
Figure D-7: Comparison of inverted models resulting from different starting models on ERT3. 154
Figure D-8: Measured apparent resistivities (top) versus those calculated from the final resistivity model (middle) on ERT4. 155
Figure D-9: Comparison of inverted models resulting from different starting models on ERT4. 156

Figure D-10: Forward modeling exercise showing (A) a known resistivity distribution loosely based on ERT4 (Figure 5-12B), and (B) the inverted resistivity model based on simulated surface measurements of the known resistivity distribution. 157
Figure D-11: Measured apparent resistivities (top) versus those calculated from the final resistivity model (middle) on ERT5. 158
Figure D-12: Comparison of inverted models resulting from different starting models on ERT5 159
Figure D-13: Measured apparent resistivities (top) versus those calculated from the final resistivity model (middle) on ERT6. 160
Figure D-14: Comparison of inverted models resulting from different starting models on ERT6. 161
Figure D-15: Measured apparent resistivities (top) versus those calculated from the final resistivity model (middle) on ERT7. 162
Figure D-16: Comparison of inverted models resulting from different starting models on ERT7. 163
Figure D-17: Measured apparent resistivities (top) versus those calculated from the final resistivity model (middle) on ERT8. 164
Figure D-18: Comparison of inverted models resulting from different starting models on ERT8. 165
Figure D-19: Measured apparent resistivities (top) versus those calculated from the final resistivity model (middle) on ERT9. 166
Figure D-20: Comparison of inverted models resulting from different starting models on ERT9. 167
Figure D-21: Measured apparent resistivities (top) versus those calculated from the final resistivity model (middle) on ERT10. 168
Figure D-22: Comparison of inverted models resulting from different starting models on ERT10. 169
Figure D-23: Measured apparent resistivities (top) versus those calculated from the final resistivity model (middle) on ERT11. 170
Figure D-24: Comparison of inverted models resulting from different starting models on ERT11. 171
Figure D-25: Measured apparent resistivities (top) versus those calculated from the final resistivity model (middle) on ERT12 172
Figure D-26: Comparison of inverted models resulting from different starting models on ERT1. 173
Figure D-27: Resistivity sections for each layer of the ERT13 resistivity model. 175
Figure D-28: Oblique view of the ERT13 resistivity model 176
Figure D-29: Oblique view of the ERT13 resistivity model along with intersecting 2D models. 177
Figure E-1: P-wave velocity models (A) and ray path density (B) along SEIS1-2-4 178
Figure E-2: Modeled versus measured first arrival times on SEIS1-2-4. 179
Figure E-3: P-wave velocity models (A) and ray path density (B) along SEIS3. 180

Figure E-4: Modeled versus measured first arrival times on SEIS3..... 181
Figure E-5: P-wave velocity models (A) and ray path density (B) along SEIS5 182
Figure E-6: Modeled versus measured first arrival times on SEIS5..... 183
Figure E-7: P-wave velocity models (A) and ray path density (B) along SEIS6 184
Figure E-8: Modeled versus measured first arrival times on SEIS6..... 185
Figure E-9: P-wave velocity models (A) and ray path density (B) along SEIS7-8. 186
Figure E-10: Modeled versus measured first arrival times on SEIS7-8 187
Figure E-11: P-wave velocity models (A) and ray path density (B) along SEIS9 188
Figure E-12: Modeled versus measured first arrival times on SEIS9..... 189
Figure E-13: P-wave velocity models (A) and ray path density (B) along SEIS10. 190
Figure E-14: Modeled versus measured first arrival times on SEIS10..... 191
Figure E-15: P-wave velocity models (A) and ray path density (B) along SEIS11. 192
Figure E-16: Modeled versus measured first arrival times on SEIS11..... 193
Figure E-17: P-wave velocity models (A) and ray path density (B) along SEIS12 194
Figure E-18: Modeled versus measured first arrival times on SEIS12..... 195
Figure E-19: P-wave velocity models (A) and ray path density (B) along SEIS13 196
Figure E-20: Modeled versus measured first arrival times on SEIS13..... 197
Figure F-1: Full view of GPR1. 198
Figure F-2: Excerpt of GPR 1 from 28 to 180 m. 198
Figure F-3: Excerpt from GPR1 from 160 m to 300 m. 199
Figure F-4: Excerpt from GPR1 from 280 m to 400 m. 200
Figure F-5: Excerpt of GPR1 from 380 m to 580 m. 201
Figure F-6: Full view of GPR2. 202
Figure F-7: Full view of GPR3 at rendered at two different illuminations. 203
Figure F-8: Excerpt of GPR3 from 0 to 200 m 204
Figure F-9: Excerpt of GPR3 from 180 to 340 m. 204
Figure F-10: Excerpt of GPR from 300 to 410 m. 205
Figure F-11: Full view of GPR4. 206
Figure F-12: Full view of GPR5 207
Figure F-13: Full view of GPR6 208
Figure G-1: An illustration showing how differences in lithology may lead to vertical heterogeneities in a paraglacial talus deposit. The cirque headwall has a uniform profile during glaciation (A), but the weaker rock unit recedes more quickly to a shallower equilibrium slope angle compared to the stronger one (B). After the units recede at a more uniform rate (C), the relative proportion of each unit in the talus (expressed as the weighted colour average between red and blue) changes, which may have implications for the hydrology of the deposit. 211

List of Tables

Table 2-1: Lithological descriptions of the bedrock formations on site 8
Table 2-2: Summary of precipitation data at the nearest public weather station with long-term records. Data source: (Environment and Climate Change Canada 2017) 9
Table 3-1: Listings of air photos covering the study site that available through the Government of Alberta's Aerial Photographic Record System (Alberta Environment and Parks 2017).. 21
Table 3-2: A summary of typical ranges of geophysical parameters for alpine deposits. A full listing of sources is available in Appendix B..... 21
Table 3-3: Listings of all geophysical lines showing which lines are coincident and the main targets of each. Refer to Figure 3-1 for the locations of each..... 22
Table 3-4: Key survey parameters of all electrical resistivity tomography (ERT) lines collected. 23
Table 3-5: Key parameters regarding the seismic data collected 23
Table 3-6: Summary of acquisition parameters for ground-penetrating radar (GPR) data collected. 24
Table 3-7: Important installation parameters for the piezometers, stilling wells, and barometric pressure logger. 24
Table 4-1: A summary of hydrogeological properties of talus slopes from previous studies. 45
Table 4-2: The attributes used by White (1981) to identify the dominant formation process for talus slopes. 45
Table 4-3: Summary of the main hydrologic features on the talus deposits..... 46
Table 4-4: Summary of the main attributes of the talus slope and the inferred formation process following the classification scheme by White (1981)..... 47
Table 4-5: Average midwinter temperatures measured by the BTS sensors in 2016. Locations that are below the -3°C defined by Hoelzle et al. (1999) are bolded and italicized. 47
Table 4-6: Summary of the physical properties of the two most important rock formations as measured by ERT and SRT surveys directly at known bedrock locations. Adapted from Christensen et al. (2017). 48
Table 5-1: A summary of hydrological features observed at surface 82
Table 5-2: Discharge measurements in the creek fed by the northern outlet spring (SP6 and SP7). 83
Table 5-3: A summary of the petrophysical units and their interpreted geology. DL1 and DL2 stand for "Deep Layer 1" and "Deep Layer 2", the tentative names used when discussing resistivity images of the meadow in Section 5.3.1. Adapted from Christensen et al. (2017). 84
Table 6-1: Summary of important hydrometric and climatic characteristics of alpine streams previously studied in the southeastern Canadian Rocky Mountains. Bracketed numbers indicate years measured 116
Table D-1: Summary of error statistics of the inverted ERT images. 147
Table D-2: The depth range of each layer in the 3D resistivity model from ERT13. 174

List of Abbreviations

2D	two-dimensional
3D	three-dimensional
Bonsai	Bonsai Lake Basin
BTS	bottom temperature of snow
CMP	common mid-point
DEM	digital elevation model
DGPS	differential global positioning system
DLX	deep layer (X = number)
EM	electromagnetic
EMS	east meadow stream
ERT	electrical resistivity tomography
Fm	formation (unit of bedrock)
GPR	ground penetrating radar
GWD	groundwater discharge
HVSR	horizontal-to-vertical spectral ratio
LiDAR	light detection and ranging
masl	metres above sea level
Opabin	Opbain sub-basin
SPX	spring (X = number)
SRT	seismic refraction tomography
SSRB	South Saskatchewan River Basin
UTM	universal transverse Mercator
WGS84	World Geodetic System 1984
WMS	west meadow stream

Chapter 1 **Introduction**

1.1 Review of Key Literature

1.1.1 Mountains and River Hydrology: A Global and Regional Context

Mountainous regions of the world play a larger role in surface hydrology than other terrain types. Despite covering only approximately 25% of the world's land surface area, they account for somewhere between 32% (Meybeck et al. 2001) and 60% (Bandyopadhyay et al. 1997) of surface runoff. For this reason, mountains are popularly referred to as the "water towers of the world" (Bandyopadhyay et al. 1997). Locally, their importance varies; the drier lowland areas are, the more important mountain inputs become (Viviroli and Weingartner 2004). Globally, 7% of mountain regions provide essential water resources to downstream populations, and another 37% provide an important supporting supply in regions prone to shortages (Viviroli et al. 2007).

The South Saskatchewan River Basin (SSRB) in western Canada is one such basin where mountain inputs play a strong supporting role (Figure 1-1). Estimates vary between studies, but mountain zones contribute on average 38% of annual flow, varying ±20% seasonally (Ashmore and Church 2001; Viviroli and Weingartner 2004). The SSRB has a semi-arid, cold, continental climate (Martz et al. 2007). Like most river systems in western North America, snowmelt is the dominant input, and effectively delays release of winter precipitation to the summer when it is most needed (Gray and Landine 1988; Mote et al. 2005). In contrast, summer rain is not as important for groundwater and streamflow due to evapotranspiration losses (Sauchyn et al. 2002; Fernandes et al. 2007; Jasechko et al. 2017). Likewise, glacier meltwater plays only a minor role. In the Bow River at Calgary, it accounts for only 3% of average annual flow and at most 8-20% of flow in August (Bash and Marshall 2014).

Being a watershed dominated by snow inputs makes the SSRB especially sensitive to climatic changes. Researchers have documented earlier spring freshet and decreasing fall and winter flows since the mid-twentieth century in both mountainous and prairies areas of the SSRB and have attributed these to increases in temperature and decreases in winter precipitation (Burn et al. 2008; Rood et al. 2008; DeBeer et al. 2016). Climatic modeling studies suggest that these trends will likely continue (Barnett et al. 2005; Tanzeeba and Gan 2012), but there is still substantial uncertainty in forecasting the consequences of climate change on river stream flow. Tanzeeba

and Gan (2012), for instance, do not account for small-scale heterogeneity of alpine zones that Bonsal and Shabbar (2008) and DeBeer et al. (2016) argued are necessary to make accurate stream flow predictions. Hence, understanding catchment-scale hydrological processes in alpine zones is imperative for making more accurate and precise predictions of streamflow changes in the South Saskatchewan River Basin.

This goal is one of broader societal importance. The SSRB is the most populous river basin on the Canadian Prairies, with current population of 2.4 million (Statistics Canada 2016). As of 2009, 30% of the SSRB's median natural flow was being consumed, mostly for agriculture and municipal water (Martz et al. 2007; AMEC 2009). One-sixth of the world's population lives in snowmelt-dominated watersheds in mid- to high latitude regions like the SSRB (Barnett et al. 2005). Hence, improving regional forecasting of streamflow by way of studying underlying processes is important for the sake of the populations living both in the SSRB and similar basins.

Moreover, mountain regions have greater biodiversity and ecosystems that are more sensitive to climatic changes than flatlands (Steinbauer et al. 2016). This is especially true of alpine aquatic species, which are confined to a small, stream habitats (Hannah et al. 2007; Brown et al. 2009; Finn et al. 2013). However, recent data from Isaak et al. (2016) suggest that headwater streams so far have not been as sensitive to air temperature changes as predicted, indicating that water temperature is influenced by other subsurface processes too. Hence, a better understanding of catchment-level groundwater processes is key for not only managing human water consumption, but also developing better ecological management strategies.

1.1.2 Catchment-Scale Groundwater Processes in Mountainous Headwater Basins

Groundwater plays a more significant role in storage and streamflow regulation than previously thought. In the past, workers assumed that alpine catchments behave like "Teflon® basins," where snowmelt becomes streamflow shortly after release (Clow et al. 2003). However, research since the mid-1990's has demonstrated that even thin, coarse sediments in alpine zones constitute an important flow path and reservoir (e.g. Campbell et al. 1995; Mast et al. 1995). Several cases studies have demonstrated that in some catchments, talus slopes are the main contributors to streamflow and have a storage capacity that exceeds total annual surface discharge (Davinroy 2000; Clow et al. 2003). Moreover, given that snowmelt is released over a period of weeks, subsurface storage reservoirs are recharged efficiently (Williams et al. 2015). In one example,

Hood and Hayashi (2015) found that 60-100 mm of all snowfall inputs (representing roughly 10-20% of the annual total snowfall) was retained as groundwater, helping maintain streamflow year-round. Furthermore, interannual storage of water as ground ice may be critical in some catchments (Caine 2010).

In the southeastern Canadian Rocky Mountains, nearly a decade of research has focussed on understanding the role of groundwater in one location: the Lake O'Hara basin in Yoho National Park. Often, these focussed on the Opabin sub-basin, a hanging valley within the larger Lake O'Hara basin. Studies have employed either hydrological monitoring (Hood et al. 2006; Roy and Hayashi 2008, 2009; Roy et al. 2011; Langston et al. 2013; Hood and Hayashi 2015), detailed geophysical surveys (McClymont et al. 2010, 2011, 2012; Langston et al. 2011; Lehmann-Horn et al. 2011; Muir et al. 2011), or basin-scale numerical modeling (Paznekas 2016). These efforts have revealed that in this area, flow in coarse-grained deposits like talus and moraines is confined to a thin saturated layer at the bedrock interface. Similarly, storage is in part controlled by bedrock characteristics, namely topography and fracture connectivity. Furthermore, ground ice may be an important control on flow paths and storage.

While these studies at Lake O'Hara basin and the Opabin sub-basin have revealed important insights, their utility in understanding groundwater processes elsewhere is limited in two ways. With no other studies of similar level of detail, it is difficult to assess whether the processes identified are ubiquitous and widespread, or instead novel and unique to this site. Similarly, with no other case studies available for comparison, an understanding of spatial trends in groundwater dynamics remains elusive. This new study hence aims to understand groundwater processes in a new, contrasting headwater basin to address these two shortcomings.

1.2 Research Objectives and Thesis Organization

The aim of this thesis is to image the subsurface structures that affect hydrogeological processes in alpine headwaters and hence determine the main controls on storage and flow processes at a new study site. Doing so in a variety of different surficial landforms will help characterize the varying role of each in a basin's hydrogeology. Comparing these new findings with those of previous studies will hence reveal links between geomorphology and groundwater processes at a larger scale.

This thesis is divided into seven chapters. Chapter 1 summarizes important literature on alpine hydrology and the motivation for this study. Chapter 2 gives a broad overview of the chosen study site located in the Front Ranges of the Canadian Rocky Mountains, and Chapter 3 describes the research methods used. Chapter 4 presents information relating to talus slopes at the study site. It includes a short literature review, a detailed site description, geophysical results, and a preliminary discussion. Chapter 5 does the same for the other landscape units at the site, including meadows, a lake, moraines, and a large perennial spring. Chapter 6 synthesizes these results, discussing their broader implications, and Chapter 7 presents a succinct summary of this study's findings.

1.3 Figures

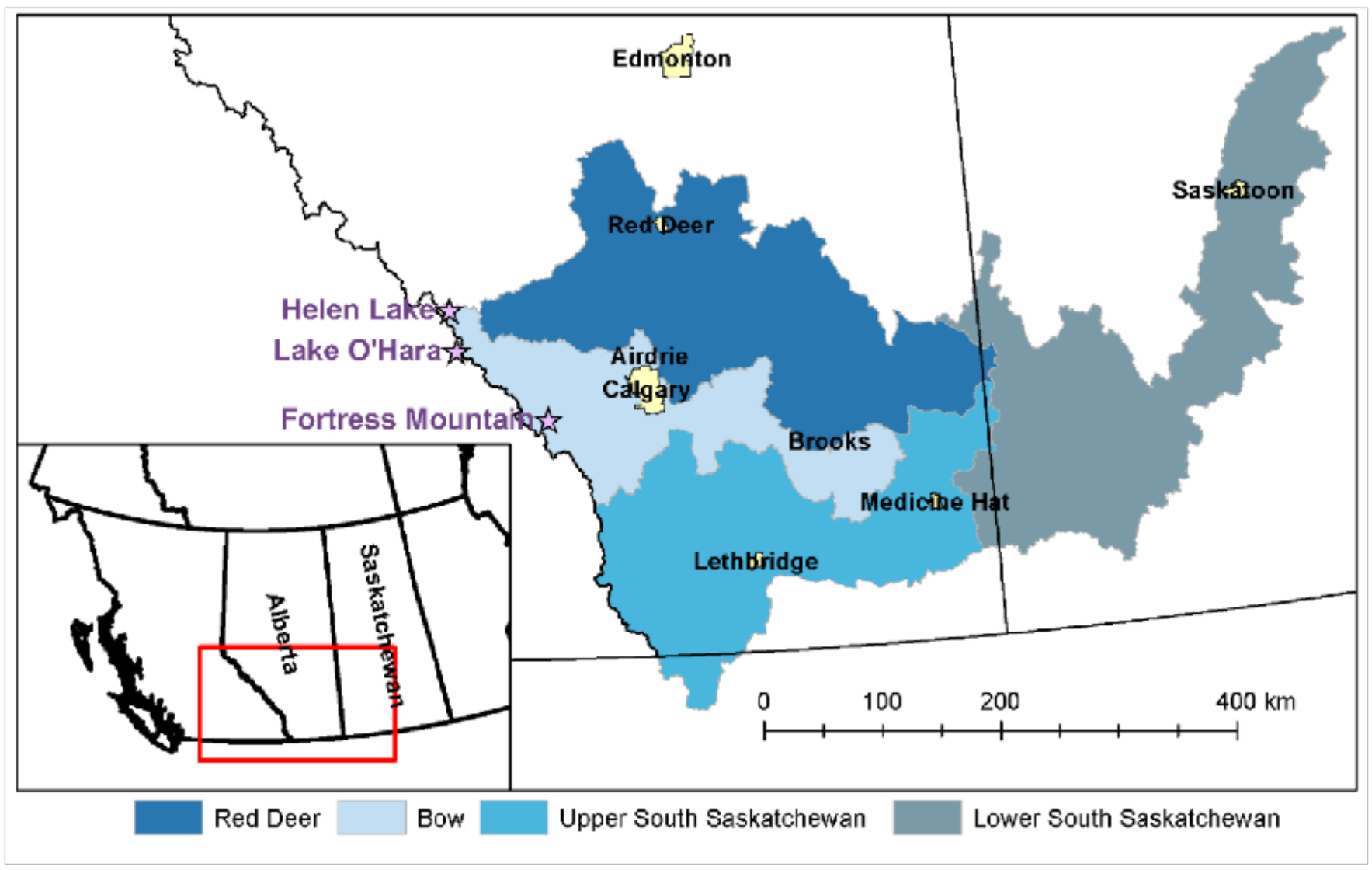

Figure 1-1: The extent of the South Saskatchewan River Basin in western Canada. Major sub-watersheds are shown, as are major cities, previous alpine sites studied by the Physical Hydrology group at the University of Calgary, and the site presented within this study (Fortress Mountain). The Oldman River, which is a major tributary flowing upstream of the City of Lethbridge, is grouped with the Upper South Saskatchewan catchment area in this dataset. Watershed data source: (PFRA / Agriculture and Agri-Food Canada 2008). Adapted from Christensen et al. (2017).

Chapter 2 **Site Description**

2.1 General Overview

This study focuses on a north-facing cirque adjacent to the Kananaskis Valley in the Front Ranges of the Canadian Rocky Mountains (Figure 2-1A). The site, which is immediately east of *The Fortress* (a mountain summit), is located on a former downhill ski resort (Fortress Mountain). It is approximately 80 km west of Calgary, Alberta. A tall headwall, which extends up to 400 m above the valley (Figure 2-1C), borders southern edge of the watershed, while the east and west drainage divides are defined by ridges with more subdued topography (Figure 2-1B). Surface water drains into Galatea Creek, which in turn drains into the Kananaskis River.

This study's scope is limited to the southeast portion of the cirque, specifically the portion draining into a tarn (unofficially called *Bonsai Lake*) and feeding an adjacent, perennial spring. This sub-basin covers 0.87 km^2, or 0.92 km^2 when including additional areas contributing to the perennial spring but not directly to the Bonsai Lake (Figure 2-1B). This 0.92 km^2 is herein referred to as the *Bonsai Lake basin* (or simply *Bonsai*). Elevations range from 2082 metres above sea level (masl) at the northern outlet spring to 2900 masl at the southern summits.

This site was chosen for a groundwater investigation in part to complement ongoing surface hydrology work by researchers at the University of Saskatchewan. More importantly, it was selected for its contrasts with Lake O'Hara. Bedrock here is more heterogeneous, younger, and less competent compared to the Cambrian quartzite and limestone of the Gog Group and Cathedral Formation at Lake O'Hara (Price et al. 1980). There is also a wide variety of surficial units in a relatively small area (Figure 2-2). This allows one to more easily study hydrological role of many different landscape units (moraines, meadows, and talus). Furthermore, there are obvious signs that groundwater plays a major role in this system, given that Bonsai Lake has no outlet stream and that are multiple springs both upstream and downstream of the lake (Figure 2-2). Section 2.2 summarizes the bedrock geology and glacial history of this site, and more detailed descriptions of surface hydrology and geology are given in Chapter 4 and Chapter 5.

2.2 Geological Setting: Bedrock Geology and Glacial History

The bedrock geology of the basin is shown in Figure 2-2. Most of the Bonsai Lake basin is underlain by the highly recessive Jurassic-age Fernie Formation comprised mostly of highly fissile shale, but with some sandstone strata (Stockmal 1979; McMechan 2012). The headwall of

the basin is a fault scarp corresponding to the Suphur Mountain Thrust and is made up of older rocks. The Palliser Formation is the thickest of these. This competent, Devonian-age carbonate rock makes up the core of many larger peaks in the Canadian Rocky Mountains (Stockmal 1979). Above this (2500-2900 masl) are the Carboniferous Exshaw and Banff Formations, which include dark black and incompetent shales, calcareous shale, and argillaceous lime wackestone. There are two other Devonian units in the western portion of the basin that are buried by talus. These are the Alexo Formation, which is also called the Sassenach Formation by some practitioners (Mallamo 1995), and the Southesk Formation. Properties of these units are given in Table 2-1.

Large portions of western Canada were covered by continental glaciers in the late Pleistocene. The most important advance of Rocky Mountain glaciers, the so-called *Crowfoot Advance*, occurred in the Younger Dryas (Menounos et al. 2009). Regionally, ice coverage reached its peak 14.0 ka (Clague 1989), and the lower Kananaskis Valley was ice free, at the latest, by 10.4 ka (±110 a) (Jackson and Pawson 1984). Several fluctuations in alpine cirque glacier movements have occurred during the Holocene. The most significant was the *Little Ice Age*, a period that began in 12th or 13th century and ended in the late 19th century. Moraine studies indicate that the Little Ice Age and Crowfoot glacial advances were generally of similar magnitudes in the Southern Rocky Mountains, with the Little Ice Age moraines often indicating a slightly larger ice extent (Osborn and Luckman 1988; Menounos et al. 2009). In the Kananaskis area, there is evidence of multiple phases of moraine-building: one preceding the 15th century, one in the late 16th to 17th century, one in the early 18th century, and one corresponding to the maximal glacier extent in the mid to late 19th century (Smith et al. 1995). Recessional moraines were rare at the sites studied by Smith et al. (1995), suggesting that glaciers retreated continuously with few periods of stagnation during the Little Ice Age in this locality.

2.3 Precipitation Trends

Total annual precipitation in the basin ranged between 890 to 1500 mm from 2014 to 2016 (J. Pomeroy and X. Fang, personal communication). However, earlier meteorological data are not available at this site to characterize the years in which this study was conducted as wetter or drier than average. The closest weather station with at least 30 years of data is located at the north end of the Kananaskis Valley, approximately 25 km NNW of Bonsai Lake. The data in Table 2-2

show that total annual precipitation in 2015 and 2016 was below the 1971-2010 average at that station, but calculated standard deviations are not included in the published data set. A similar data set from Alberta Agriculture and Forestry provides annual precipitation amounts from 1971 to 2017 on townships (i.e. legal land divisions measuring approximately 10 km x 10 km) across the province. Values were estimated from an inverse distance weighting interpolation of data from the eight closest weather stations that were no more than 60 km from the midpoint of each township. Figure 2-3 shows the values for the township containing Bonsai Lake. This second data set shows that precipitation in 2015 and 2016 was either slightly above (709 mm) or somewhat below (625 mm) the 1970-2016 average (695 mm), but both years were within one standard deviation (130 mm). Therefore, these data suggest that 2015 and 2016 were not unusually wet years at Bonsai Lake, and they may have been somewhat drier than normal.

2.4 Tables

Table 2-1: Lithological descriptions of the bedrock formations on site

Period	Formation	Lithological description
Jurassic	Fernie Formation	"Dark brown to black shale interbedded with argillaceous sandstone units. Sandstones are finely bedded, dark grey on fresh surfaces, and weather dark grey to brown. Extremely recessive and incompetent" (Stockmal 1979)
Carboniferous (Mississippian)	Upper-Middle Banff Formation	"Medium to fine grained, light to dark grey argillaceous lime wackestone. […] Characteristically quite variable in lithology over short stratigraphic intervals. Recessive and incompetent, but less so than the Lower Banff Formation" (Stockmal 1979)
	Lower Banff Formation	"Generally calcareous shale, weathering light grey to tan to occasionally orange-brown. Bedding is distinct and finely laminated though often irregular. […] Pyrite nodules […]Very recessive and incompetent; in some locations, it may form a décollement zone with the Exshaw Formation above the Palliser Formation." (Stockmal 1979)
	Exshaw Formation	"Black, very finely bedded fissile shale. Orange weathered surfaces. Sharp upper and lower contacts. Extremely recessive and incompetent. " (Stockmal 1979)
Devonian	Palliser Formation	"Medium to dark grey, fossiliferous limestone and dolomitic limestone. […] Bedding is often poor to nonexistent; breaks irregularly. Characterized by light tan mottling and irregular tracery on weathered surface. Upper contact sharp; lower contact not observed. Competent and resistant." (Stockmal 1979)
	Alexo (Sassenach) Formation	"Sandstone and siltstone: quartz, dolomitic, calcareous, siliceous; minor carbonate: silty; shale"(McMechan 2012)
	Southesk Formation	"Dolostone: light and medium grey-weathering, massive, fine to coarse crystalline."(McMechan 2012)

Table 2-2: Summary of precipitation data at the nearest public weather station with long-term records. Data source: (Environment and Climate Change Canada 2017)

Station Name	**KANANASKIS**
Station Number ("Climate ID")	3053600
Latitude	51°01'39.080" N
Longitude	115°02'05.060" W
Elevation (m)	1391.1
Mean Annual Precipitation 1981-2010 (mm)	639.4
Total precipitation 2015 (mm)	594.3
Total Precipitation 2016 (mm)	487.2

2.5 Figures

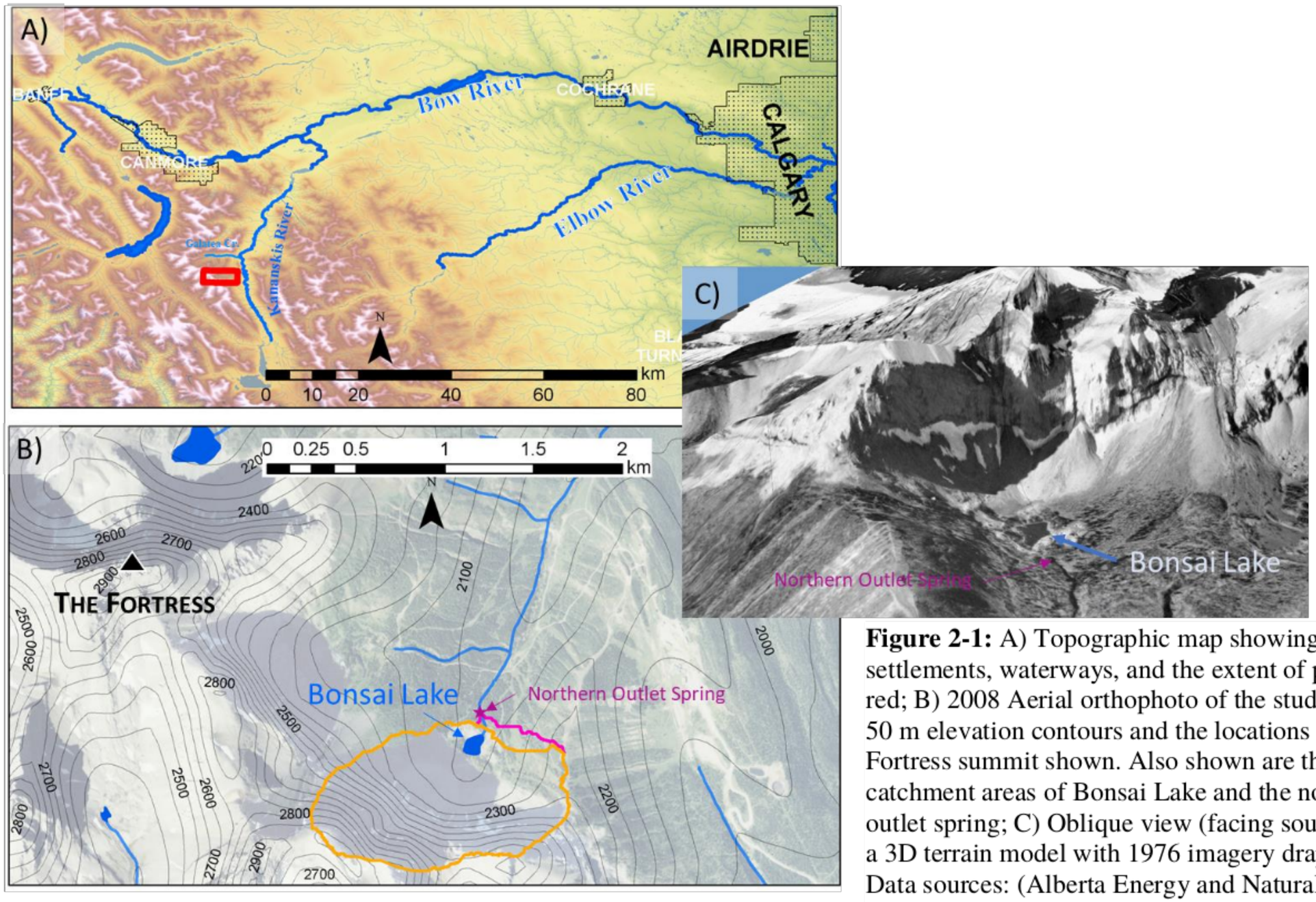

Figure 2-1: A) Topographic map showing major settlements, waterways, and the extent of panel B) in red; B) 2008 Aerial orthophoto of the study site, with 50 m elevation contours and the locations of The Fortress summit shown. Also shown are the catchment areas of Bonsai Lake and the northern outlet spring; C) Oblique view (facing southwest) of a 3D terrain model with 1976 imagery draped on top. Data sources: (Alberta Energy and Natural Resources 1976; Alberta Sustainable Resource Development 2008; Natural Resources Canada 2016)

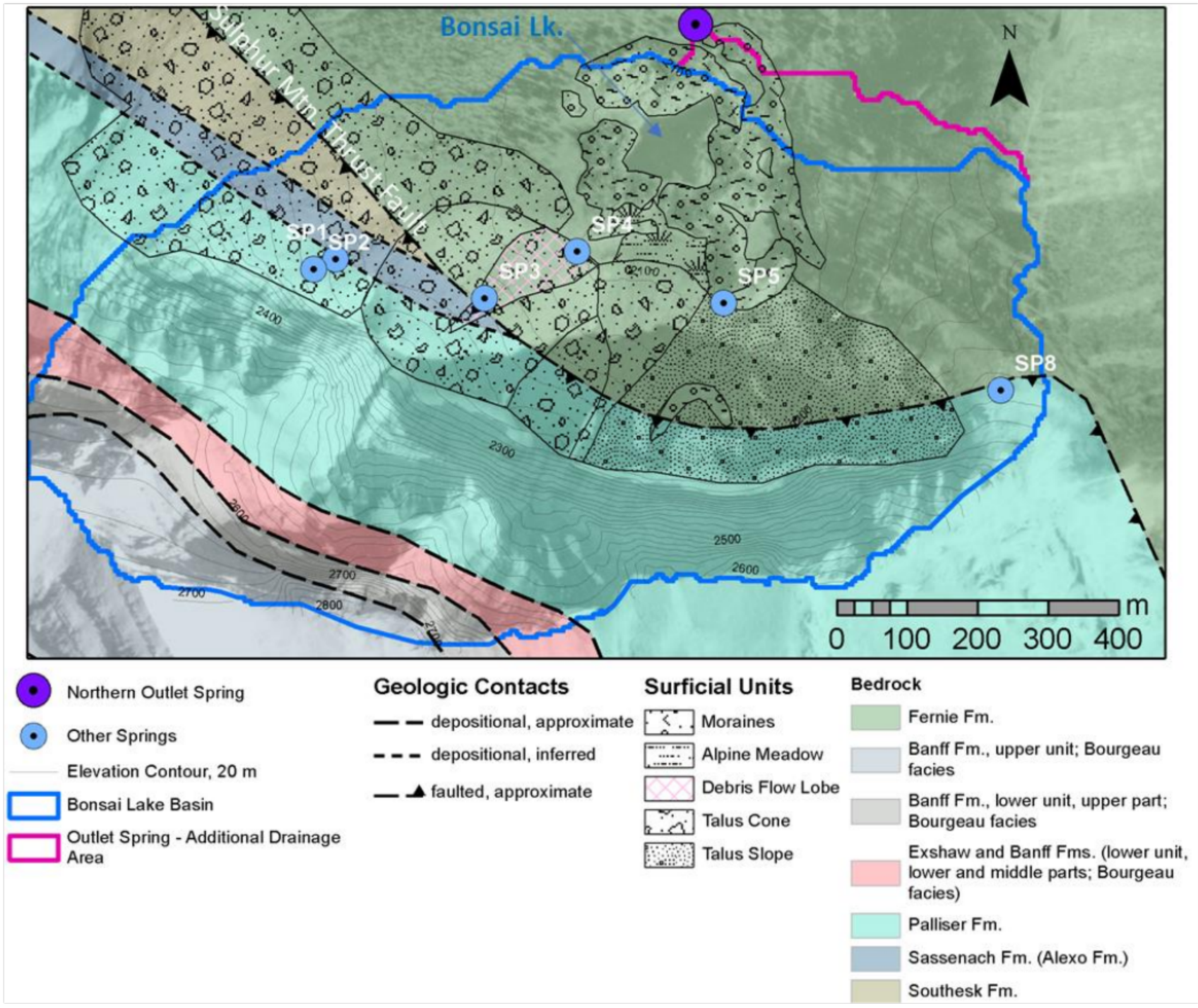

Figure 2-2: Geological map of study site. Bedrock data source: (McMechan 2012)

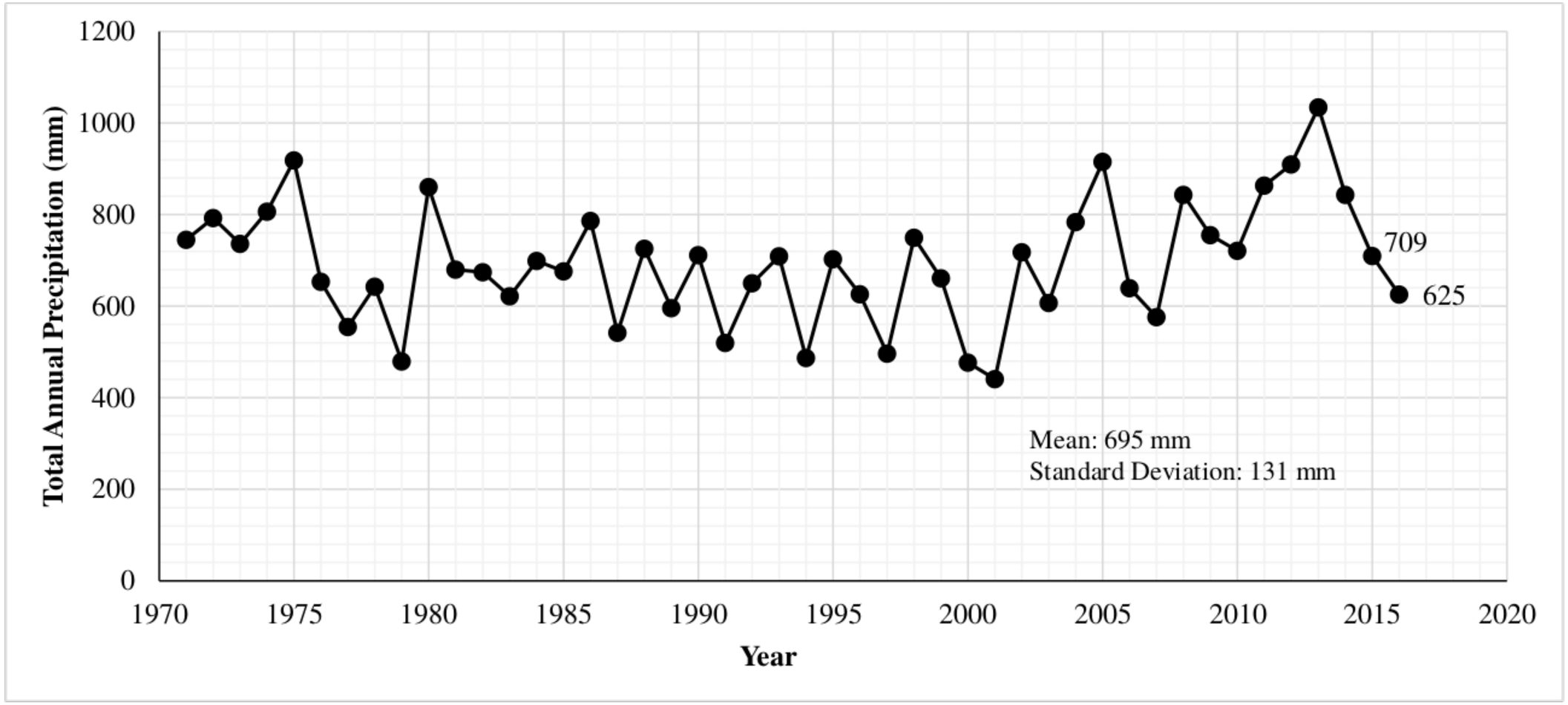

Figure 2-3: Historical precipitation data interpolated from nearby weather stations at T021R09W5, the township covering the current study area (Bonsai Lake). Data source: (Alberta Agriculture and Forestry 2017)

Chapter 3 **Methods**

3.1 Preliminary Site Reconnaissance

Several data sets were employed for desktop study prior to early site visits. At least three air photo sets (Table 3-1) cover the study area. Generally, orthorectified photos from 1976 are used rather than those 2008 for map overlays in this thesis because the former were captured at a time of day when shadows from the headwall obscured a smaller fraction of the site. A high-resolution digital elevation model (DEM) with 2 m grid cell resolution, derived from light detection and ranging (LiDAR) data collected by a private contractor, was provided by collaborators at the University of Saskatchewan (M. Schirmer and J. Pomeroy, personal communication). Together, these data were used to delineate drainage divides, map surficial landforms, and analyze the relief of the southern headwall. This desktop study and the site visits catalogued in Appendix A are the basis of the detailed site descriptions in Sections 4.2 and 5.2.

3.2 Geophysical Methods

Geophysical methods were the main tools used in this study. Like in earlier alpine groundwater studies in the Rocky Mountains, there are significant constraints on using direct sampling methods normally employed by hydrogeologist. Drilling in remote, rugged terrain is logistically challenging, and non-invasive methods are preferred in tightly regulated parkland. Moreover, this was the first study of groundwater at this location, and little existing information of the subsurface was available. Hence having inexpensive methods to map a large area with high-resolution data was preferred to drilling costly wells with limited spatial coverage.

Employing geophysical methods to study hydrogeology has several pitfalls that Linde (2014) articulates succinctly. First, the coarse resolution of the measurements can obscure small-scale heterogeneities that may have important hydrogeological consequence. Second, there are nuisance parameters other than the hydrologic parameters of interest that can affect the petrophysics of earth materials, complicating the interpretations. Furthermore, indirect geophysical methods often measure a large volume of earth material at once, so to produce an image, one must use an optimization algorithm to find a parameter model whose simulated (forward modeled) response is adequately close to the measured data. This process, called *inversion*, produces models that are non-unique. This ambiguity as well as errors that may be introduced in the forward model computations both contribute to uncertainty in the final image.

Some of these shortcomings can be addressed in alpine settings using appropriate data collection strategies. First, multiple methods help reduce ambiguity. As Langston et al. (2011) demonstrated, a layer of saturated sediment can mask the presence of (even highly resistive) bedrock, making the use of seismic methods important for locating bedrock. Similarly, direct observations and ground truth data, like measurements at outcropping ice and bedrock, are very important in interpreting results (Langston et al. 2011; McClymont et al. 2011). Where direct measurements like these are not possible, indirect measurements can at least offer partial if not definitive support of one's interpretation. This is often the case with mapping permafrost, where temperature sensors may be used to map zones where its occurrence is likely (e.g. Mozil 2016).

Three geophysical methods were used in this study: electrical resistivity tomography (ERT), seismic refraction tomography (SRT), and ground penetrating radar (GPR). These three were chosen because they are some of the most widely used and robust methods in applied alpine geophysics and have complementary strengths (Hauck and Kneisel 2008). ERT, is good at locating frozen material, saturated zones, and fine-grained sediments. SRT is the most reliable method for locating bedrock. GPR helps with identifying sedimentary textures by mapping contrasts in dielectric permittivity, a value that is strongly controlled by water content in earth systems. The petrophysical responses of common alpine deposits are summarized in Table 3-2, based on a compilation of multiple studies and sources catalogued in Appendix B.

The locations of all geophysical surveys performed for this study are shown in Figure 3-1. Data were acquired over two summer field seasons, the first and main campaign occurring July 13 to 31, 2015, and the second on July 19 to 23, 2016. The motivation and alignment for each survey line is summarized in Table 3-3. In two-dimensional (2D) surveys, geophones, electrodes, and antennae were evenly spaced along the surface using survey chain, and the locations of electrodes and geophones were measured with a differential global positioning system (DGPS) unit (Leica Geosystems AG, Leica Viva CS15). In the case of a three-dimensional (3D) ERT survey, electrodes were placed at a specific location using the DGPS rover unit to maintain a fixed horizontal spacing. An official Alberta Survey Control Marker (no. 486340) was used as a base station throughout the campaign. Generally, location uncertainty was less than 3 cm, though errors were higher in densely forested areas (especially at the north end of the study site) due to poor signal reception. Such instances were usually isolated, so spurious values were removed

and a more realistic position interpolated from surrounding points or, in the worst cases, the LiDAR-derived DEM.

Only the results needed to describe the most important trends are included in the main body of the text. The reader is referred to the appendices for the complete collection: Appendix D for ERT images, Appendix E for SRT images, and Appendix F for GPR images.

3.2.1 Electrical Resistivity Tomography

Resistivity data were collected using the IRIS Instruments Syscal Pro data acquisition system. Key statistics regarding these surveys are given in Table 3-4. In all, twelve 2D surveys, and one 3D survey (ERT 13) were performed.

A modified dipole-dipole sequence was used for most survey lines. This custom sequence used an n-spacing of up to 6 and included partial reciprocals (roughly 40%). In a full 72 electrode array, 2819 quadripoles were collected using this sequence. In some locations where extra depth information was important for a target (specifically ERT7 and ERT9), some large-offset, Wenner quadripoles were added at the end of the sequence. In the case of the 3D survey, a custom sequence that included in-line dipole-dipole with an n-spacing up to 9, cross-line dipole-dipole, equatorial dipole-dipole, and diagonal dipole were all employed for a total of 4221 quadripoles.

A consistent challenge with acquiring resistivity data was poor electrode contact. This was especially true in the unvegetated portion of the talus, where there were very little fine-grained surface sediments to improve contact. Poor electrode contact was diagnosed with a resistance check before starting each survey. In cases where there was sediment present but it was dry, saltwater was poured immediately adjacent to the electrode to decrease contact resistance. In talus or moraine material where there were large air gaps, saltwater-soaked sponges or a mixture of cat litter (i.e. impure bentonite clay) and saltwater was applied to the electrode. In most cases, contact resistance was reduced below 20 kΩ, but some electrodes that proved difficult to remedy were accepted with a contact resistance of 20-50 kΩ. Those above 50 kΩ were excluded from the survey. There may be some noise in the data attributable to the frequent theft of saltwater sponges by wildlife. Injections were repeated (i.e. stacked) two to four times, only advancing to the next set of quadripoles if measured values deviated on average less than 1% or if the maximum number of repetitions was reached.

Before inversion, data were subject to a consistent quality control protocol. All negative resistances and potential measurements with only one significant digit recorded were discarded. Measurements that exceeded a 1% standard deviation between stacked measurements were also rejected. (ERT2, where data noise was a more severe issue, used a 5% maximum instead). Finally, any remaining, isolated outliers (as viewed in pseudo depth versus resistivity semi-log plots) were removed manually.

Inverse modelling was done using RES2DINV or RES3DINV (Geotomo Software 2012a, 2012b). By default, the program uses a smoothness-constrained least-squares optimization. However, using the square of the data misfit (the L_2 norm) tends to make the inversion scheme more sensitive to bad data points (Farquharson and Oldenburg 1998) which is an issue in areas on the talus or moraine with poor electrode contact. Hence, the absolute values of data misfit (the L_1 norm) was employed instead. Detailed explanations of the optimization equations are given in Appendix C. RES2DINV and RES3DINV use the mean absolute difference in logarithm between observed and measured resistivity values as their error metric (M. Loke, personal communication):

$$\%AbsoluteError = \frac{100\%}{N}\sum_{i=1}^{N}\left|\ln\left(\frac{\rho_{obs_i}}{\rho_{calc_i}}\right)\right| \quad (3\text{-}1)$$

where

N	number of measurements
ln	natural logarithm (logarithm of base *e*)
ρ_{obs}	observed (measured) apparent resistivity
ρ_{calc}	calculated apparent resistivity calculated based on the resistivity model

Other non-default inversion parameters were tested or used consistently. Applying slightly more horizontal than vertical smoothing (i.e. a 0.7 vertical to horizontal smoothing ratio) tended to produce models with lower data misfit and were deemed more geologically plausible given the depositional environment. A model grid cell width equal to half the unit electrode spacing was employed to reduce the influence of high-resistivity anomalies in the thin, dry, uppermost layers of the ground.

The depth of investigation (DOI) index developed by Oldenburg and Li (1999) is often employed to assess which parts of a resistivity model are reliable, but their method did not yield useful

results in this case. Instead, the inversion process was repeated twice using very different reference models (constant values of 100 Ωm and 10,000 Ωm), and the results were directly compared.

Forward modeling was used in three instances to assist with interpretation of some resistivity images. RES2DMOD (Geotomo Software 2014) is a program that allows one to input a known resistivity distribution and then simulate ERT measurements using the same survey parameters as those used in the field. That simulated data can then be inverted in RES2DINV to produce a model. By comparing the inverted model to the original, known model, one can evaluate how certain resistivity distributions may be distorted during an inversion process and hence asses how reliable the images produced from inverted ERT measurements may be. One such exercise is discussed in Chapter 5, and two others are shown in Appendix D.

3.2.2 Seismic Refraction Tomography

Seismic data were collected using the Geometrics Geode data acquisition system. Each Geode unit can collect 24 channels of data, and up to four were connected at a time for 96 channels. Two different types of geophone were used: spike geophones where there was sufficient fine-grained sediment to support them, and plate geophones on talus and moraine deposits where there were no fine-grained sediments. As noted by Mozil (2016), vibrations of the cable and survey chain caused by the wind can be a significant source of noise. Care was given to ensure there was no contact between the survey chain and geophone cable, and small rocks were stacked on the geophones to both minimize wind-induced movement and help improve coupling.

A 5-kg sledgehammer was used as the seismic energy source. The hammer was equipped with an automatic accelerometer trigger and was struck on a cylindrical aluminum plate measuring 13 cm in diameter, 14 cm in height, and 22 kg in mass. Shots were spaced every six stations (i.e. every 12 m when 2 m geophone spacing was used). Hammer blows were repeated (i.e. stacked) seven to thirteen times until there was no noticeable change in the stacked signal.

Table 3-5 shows the key survey parameters for each of the 13 lines collected. Geophone spacing ranged from 1 to 2.5 m, and total line length varied from 71 m to 190 m. Note however that several lines were overlapping and merged during data processing as roll-along surveys; SEIS1, SEIS2, and SEIS4 were grouped together, as were SEIS7 and SEIS8.

First arrival times were manually picked in ReflexW software (Sandmeier Software 2005). Given the low energy of the source, first breaks were often difficult to pick at far-offset geophones, especially in loose talus material. To assist with picking first breaks in these cases, band-pass filtering was used. As Figure 3-2 shows, the highest-frequency noise was removed first with a relatively wide band-pass filter (B), and then with a second, narrower one (C). Removing the high-frequency content tended to push the first arrival earlier in time. However, first arrival times were not directly picked from these filtered sections; rather, they helped in identifying the correct pulse in the unfiltered dataset.

P-wave velocity models were produced using an inversion scheme developed by Lanz et al. (1998). This program uses a fast finite-difference eikonal solver, which typically produces more accurate simulations of wave propagation in highly heterogeneous media, in its forward model. The optimization routine uses standard regularization criteria on the inverted model: minimize high spatial gradients and deviations from an input reference model. (The mathematical formulation of these is given in Appendix C). Two grids of differing resolutions are used in these series of computations. A coarser one is used for defining the slowness model, while a finer one is used in the forward modelling. Zhi (2013) tested a wide range of grid setups using this same inversion scheme and found that the optimal model grid has cells between 75 to 100% of the nominal geophone spacing; smaller values led to unstable inversion results. The optimal computational grid used 16 cells (a 4x4 grid) per model parameter cell.

P-wave velocity tomograms were produced using a standard workflow. First, a simple straight-line analysis (e.g. Lowrie 1997, p. 145-147) was used to estimate the depth to major velocity boundaries and guide selection of an appropriate starting model for inversion. With this software, using initial models that favour shallower ray paths usually leads to more accurate models because they help detect shallow layers and ensures that ray paths enter model cells from many different angles (Musil et al. 2002). In the first run of the inversion, a high dampening ratio (relative to the starting model) and a model with a linearly increasing velocity with depth was used. The result of this first run was then used as the new starting model in the second and final run, and the dampening ratio reduced.

3.2.3 Ground Penetrating Radar

GPR data were acquired using the Sensors & Software PulseEkko Pro system. In this setup, one transmitting antenna emits an electromagnetic (EM) wave pulse, and the other receiving antenna records the amplitude of the returning EM wave. Low frequency (50 MHz) antennae were used to favour a greater depth of penetration and to avoid excessive diffractions from large boulders in talus slopes. Data were only collected in open (i.e. unforested) areas because shielded antennae, which can block reflected signals from trees, were not available. Six reflection surveys were conducted using a 0.25 m step size with a 2-m antenna separation. Dates of acquisition and total length are given in Table 3-6. Signals were digitized at a 0.8 ns sampling interval, and 32 stacks were used per capture. In addition, nine common midpoint (CMP) surveys were performed to acquire velocity information. Each began with a 2-m antenna separation and had a step size of 0.2 m (i.e. 0.1 m movement away from the midpoint for each antenna) between captures.

Data were processed in ReflexW (Sandmeier Software 2005) using a standard workflow: dewow filtering, static correction, and an exponential gain function. As a result, the pixel brightnesses in the GPR images shown in this thesis do not represent the intensity of the received signal in W/m^2, but instead show the relative amplitude of an EM wave in arbitrary units when correcting for geometric signal attenuation. Note also that radargrams in this thesis use a non-standard colour scheme, where red and yellow show high- and low-amplitudes, while black indicates no signal. Noisy channels, likely caused by interference from intermittent use of short-range radios by the crew, were manually removed. Semblance analysis was used to develop 1D velocity models from the CMP data. A strong correlation between resistivity and EM wave velocity was noted (Figure 3-3). This correlation was used to develop a 2D EM velocity model and thus convert GPR reflection sections from time to depth sections.

3.3 Supplementary Data Collection

Several additional datasets were acquired to reduce ambiguity in the geophysical measurements. Mid-winter bottom temperatures of snowpack (BTS) is an indicator of the likelihood of permafrost occurrence. Hoelzle et al. (1999) found that mid-winter temperatures of -3°C or less correspond to zones where permafrost is likely to occur, while those above -2°C are zones where it is unlikely to occur. For these rules of thumb to be valid, however, snow cover must be sufficiently thick (around 1 m) for the air temperature not to have an influence on BTS. While

this condition was likely met, one cannot confirm this with direct snow depth measurements because of the extreme avalanche hazard in most locations south of Bonsai Lake. Nevertheless, the data do provide some additional support in identifying permafrost where the geophysical signal may be ambiguous. BTS was recorded at ten different locations from October 22, 2015 to June 14, 2016 (Figure 3-4). The “zero-curtain”, the period during spring melt where temperatures remain a constant 0°C, was used to calibrate sensors (Outcalt et al. 1990; Staub et al. 2015).

Piezometers were also installed at several locations (Figure 3-5) to document seasonal changes in hydraulic head. Most of these are in the meadow, including a nested pair (P05 and P06) intended to examine possible vertical head gradients. These were constructed from PVC pipes with a 2.5 cm inner diameter wherein the bottom 20 to 30 cm was perforated then wrapped with a fine wire mesh to serve as a screen. Hand-augered holes of 5 cm diameter housed these piezometers, and the annulus space was filled with coarse sand over the screened interval and bentonite clay from the top of the screen up to surface. Automatic water level data loggers (a Solinst Levelogger, model no. 3001) were placed at these locations, as well as in two stilling wells: one in the meadow stream installed by H. Wu (University of Saskatchewan) and another installed by the author in Bonsai Lake. A barometric pressure logger (Solinst Barologger, model no. 3001) was used to track changes due to atmospheric pressure fluctuations. It was installed just below surface at a shaded location to reduce instrument drift caused by diurnal temperature variations. Coordinates and elevations of these instruments are given in Table 3-7. Loggers measured pressure at 15-minute intervals, and water levels in piezometers were measured by hand with a measuring tape periodically during summer 2016 site visits to correct for instrument drift.

Some measurements of volumetric discharge were taken at the creek exiting from the northern outlet spring. A propeller flow meter (Global Water FP101) was used to measure average flow velocity within a vertical column at 10 cm horizontal intervals. Discharge was calculated using the velocity-area method (Dingman 2002, p. 609). Using the method, measurement error is in the range of 4 to 9% (Hood et al. 2006). These measurements are mainly discussed in Section 6.1.

Finally, where possible, some ground truth data were collected. Holes up to 4 m deep were dug with a hand auger in the meadow to install piezometers. Qualitative changes in soil characteristics and water content with depth were noted. Moreover, additional geophysical data was collected on the eastern ridge of the basin atop outcrops of Palliser and Fernie Formation.

This included ERT data at two locations (ERT10 and ERT12) and SRT data at one location (SEIS13) (Figure 3-1). Resulting values are discussed in Section 4.3.2.3. The temperature and electrical conductivity of springs and water features were also measured on most site visits.

3.4 Tables

Table 3-1: Listings of air photos covering the study site that available through the Government of Alberta's Aerial Photographic Record System (Alberta Environment and Parks 2017).

Date	Series name	Image numbers	End-references listing
2008-08-15	AS545ON	65-67	Alberta Sustainable Resource Development (2008)
1976-08-31	AS1486	169-172	Alberta Energy and Natural Resources (1976)
1947	A11102	72, 73, 128, 129, 130	National Air Photo Library (1947)

Table 3-2: A summary of typical ranges of geophysical parameters for alpine deposits. A full listing of sources is available in Appendix B.

Sediment type	Velocity ($m\ s^{-1}$)	Resistivity (kΩ m)		EM velocity ($m\ ns^{-1}$)
		dry	wet	
Bedrock (shale, gneiss, schist)	2000 to 6000	0.1 to 10	-	-
Bedrock (other)	2000 to 6000	5 to 20	-	0.12 to 0.13
Talus	550 to 2500	20 to 100	0.5 to 3	0.09 to 0.14
Meadow	300 to 700	2	-	0.065
Moraine	300 to 1500	2 to 30	0.3 to 3	0.13
Ice	3000 to 4500	1000 to 10,000	-	0.168
Permafrost	2400 to 3400	1 to 1000	-	
Till	600 to 2700	0.5 to 3	-	0.09 to 0.10

Table 3-3: Listings of all geophysical lines showing which lines are coincident and the main targets of each. Refer to Figure 3-1 for the locations of each.

ERT line	Collinear seismic lines(s)	Collinear GPR lines	Target(s)
ERT 1	SEIS 1-2-4 SEIS 5	GPR 1	• East-west profile of meadow • Toe spring (SP4) of talus
ERT 2	SEIS 6	GPR3	• Downslope profile of West Cone • SP1 and SP2
ERT 3	SEIS 7-8	GPR4	• Cross-profile of Centre Cone • SP3
ERT 4	SEIS 3	GPR2	• Longitudinal profile of East Cone, meadow, and moraines
ERT 5	SEIS 9	GPR5	• Longitudinal profile of Centre Cone
ERT 6	SEIS 10		• Moraine on south edge of tarn, particularly location of bedrock and saturated zone
ERT 7	SEIS 11		• North outlet spring, • Bedrock, and saturated zone beneath moraine
ERT 8	SEIS 12		• North outlet spring, • Bedrock, and saturated zone beneath moraine
ERT 9			• Depth of saturation beneath moraine
ERT 10			• Petrophysical information on Fernie Formation
ERT 11			• Improved 3D information on north outlet spring
ERT 12	SEIS 13	GPR6	• Improved petrophysical information on Fernie and Palliser Formations
ERT 13			• Improved 3D information on north outlet spring

Table 3-4: Key survey parameters of all electrical resistivity tomography (ERT) lines collected.

Line name	Total length (m)	Nominal electrode spacing (m)	Orientation	Date measured	Number of electrodes
ERT1	572	4	E to W	2015-07-18	144
ERT2	188	4	S to N	2015-07-20	48
ERT3	424	8	W to E	2015-07-21	54
ERT4	236	4	S to N	2015-07-22	60
ERT5	284	4	N to S	2015-07-23	72
ERT6	142	2	E to W	2015-07-26	72
ERT7	177.5	2.5	W to E	2015-07-28	72
ERT8	71	1	W to E	2015-07-29	72
ERT9	142	2	W to E	2015-07-30	72
ERT10	92	4	N to S	2015-07-31	24
ERT11	213	3	E to W	2016-07-20	72
ERT12	213	3	S to N	2016-07-21	72
ERT13		4 (in line) 8 (between lines)		2016-07-22	72

Table 3-5: Key parameters regarding the seismic data collected

Line name	Total length (m)	Nominal geophone spacing (m)	Orientation	Date acquired	Sampling interval (ms)	Acquisition time (s)
SEIS1	142	2	E to W	2015-07-15	0.5	5
SEIS2	142	2	E to W	2015-07-15	0.5	5
SEIS3	190	2	S to N	2015-07-18	0.25	2
SEIS4	142	2	E to W	2015-07-19	0.25	2
SEIS5	96	2	E to W	2015-07-20	0.25	2
SEIS6	96	2	S to N	2015-07-21	0.25	2
SEIS7	142	2	W to E	2015-07-23	0.25	2
SEIS8	96	2	W to E	2015-07-24	0.25	2
SEIS9	142	2	N to S	2015-07-25	0.25	2
SEIS10	142	2	E to W	2015-07-28	0.25	2
SEIS11	177.5	2.5	W to E	2015-07-29	0.25	2
SEIS12	71	1	N to S	2015-07-30	0.25	2
SEIS13	190	2	S to N	2016-07-21	0.125	0.5

Table 3-6: Summary of acquisition parameters for ground-penetrating radar (GPR) data collected.

Line name	Date of acquisition	Total length along surface (m)	Comment
GPR1	2015-07-14 and 2015-07-15	590	3 segments collected over two consecutive days
GPR2	2015-07-16	167.5	
GPR3	2015-07-18	188	collected in two segments
GPR4	2015-07-22	420	
GPR5	2015-07-24	224	collected in two segments
GPR6	2016-07-23	104	

Table 3-7: Important installation parameters for the piezometers, stilling wells, and barometric pressure logger.

Name	Coordinates (UTM 11N, WGS 1984, m)		Date installed	Surface elevation (masl)			Logger elevation (masl)		
	Easting	Northing							
Baro	625661.4	5631196.9	2016-06-24	2103.552	±	0.019	2103.39	±	0.03
HWE	625770.3	5631097.5	Unknown	2094.124	±	0.014	2092.86	±	0.03
HWN	625769.6	5631097.7	Unknown	2094.061	±	0.014			
HWS	625769.6	5631097.2	Unknown	2094.104	±	0.014			
HWW	625768.2	5631098.1	Unknown	2094.035	±	0.013	2093.58	±	0.03
Lake Stilling	625838.1	5631304.7	2016-06-28	2088.500	±	0.050	2088.59	±	0.07
P01	625775.6	5631086.7	2016-06-24	2094.927	±	0.014	2092.38	±	0.03
P02	625735.4	5631073.5	2016-06-24	2096.151	±	0.020			
P03	625736.9	5631139.6	2016-06-24	2093.569	±	0.013			
P04	625655.6	5631205.0	2016-06-24	2102.458	±	0.013			
P05	625766.8	5631086.2	2016-07-27	2095.107	±	0.015	2091.17	±	0.03
P06	625766.1	5631086.1	2016-07-27	2095.147	±	0.015	2092.48	±	0.03

3.5 Figures

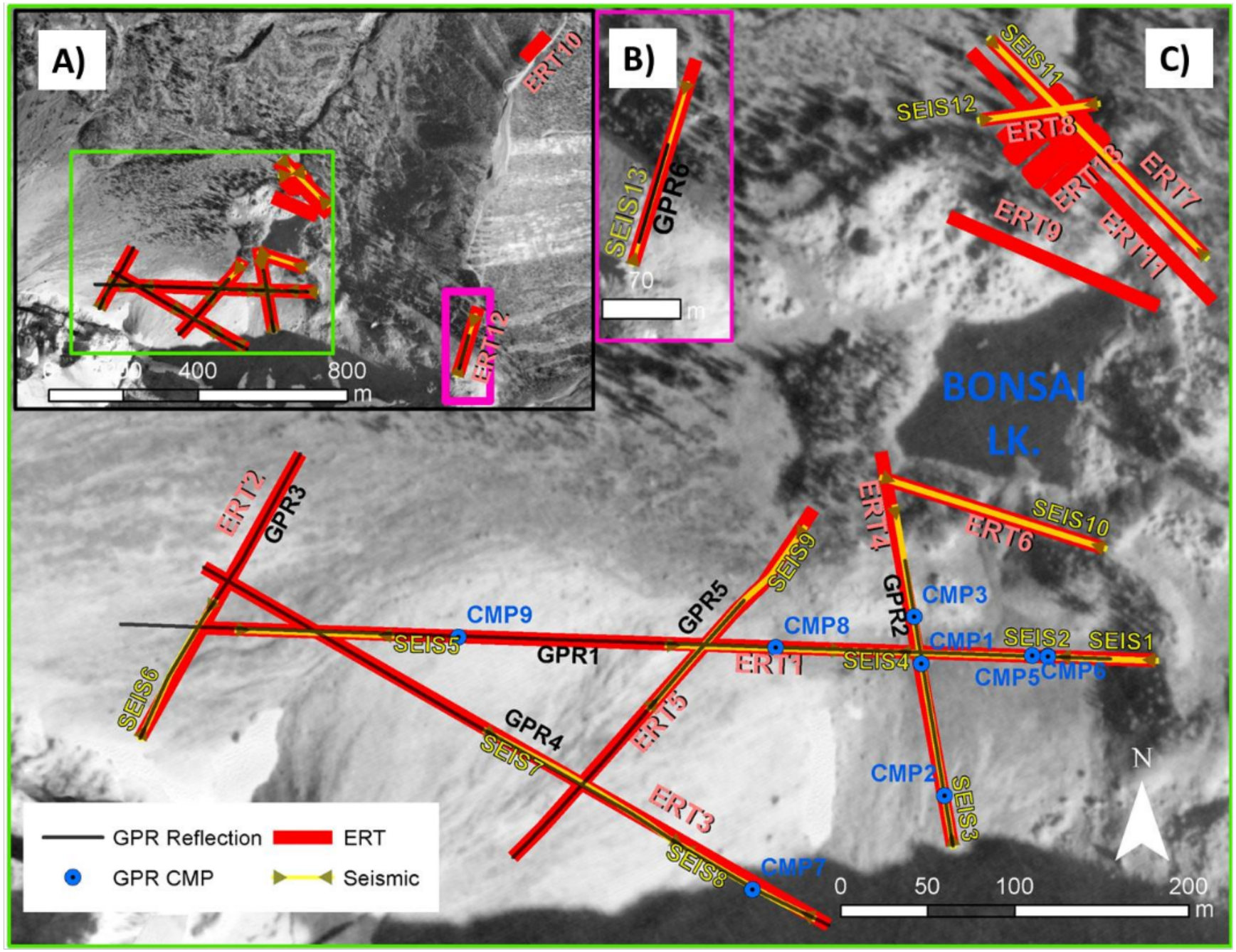

Figure 3-1: Map showing the locations of all geophysical surveys conducted. Panel A shows the full view of the survey area and the extent of Panel B and of Panel C (the largest panel). Note that CMP4 (not labelled) is coincident with CMP5.

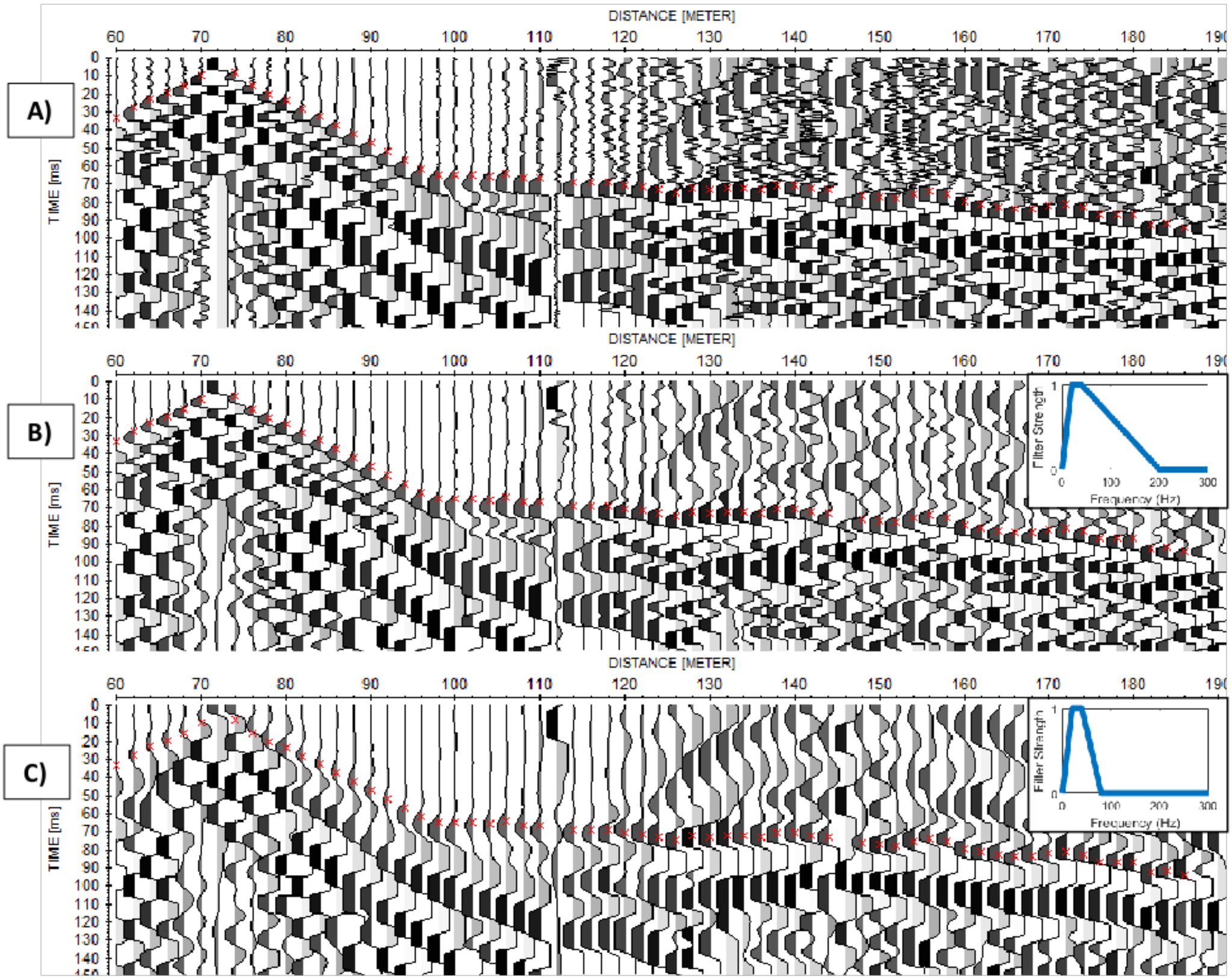

Figure 3-2: An illustration, using data from SEIS 03, of how successive levels of band-pass filtering were used to assist with making first arrival picks (red x's). The original stacked section (A) was filtered using a plateau frequency range of 20-40 Hz and cut-off values of 0-200 Hz (B), and again with an upper cut-off of 80 Hz (C). The first arrival picks illustrate that the leading edge of a pulse as it appears in (C) was not used; rather, the filtered data assisted in picking the appropriate pulse in the unfiltered data (A). Adapted from Christensen et al. (2017).

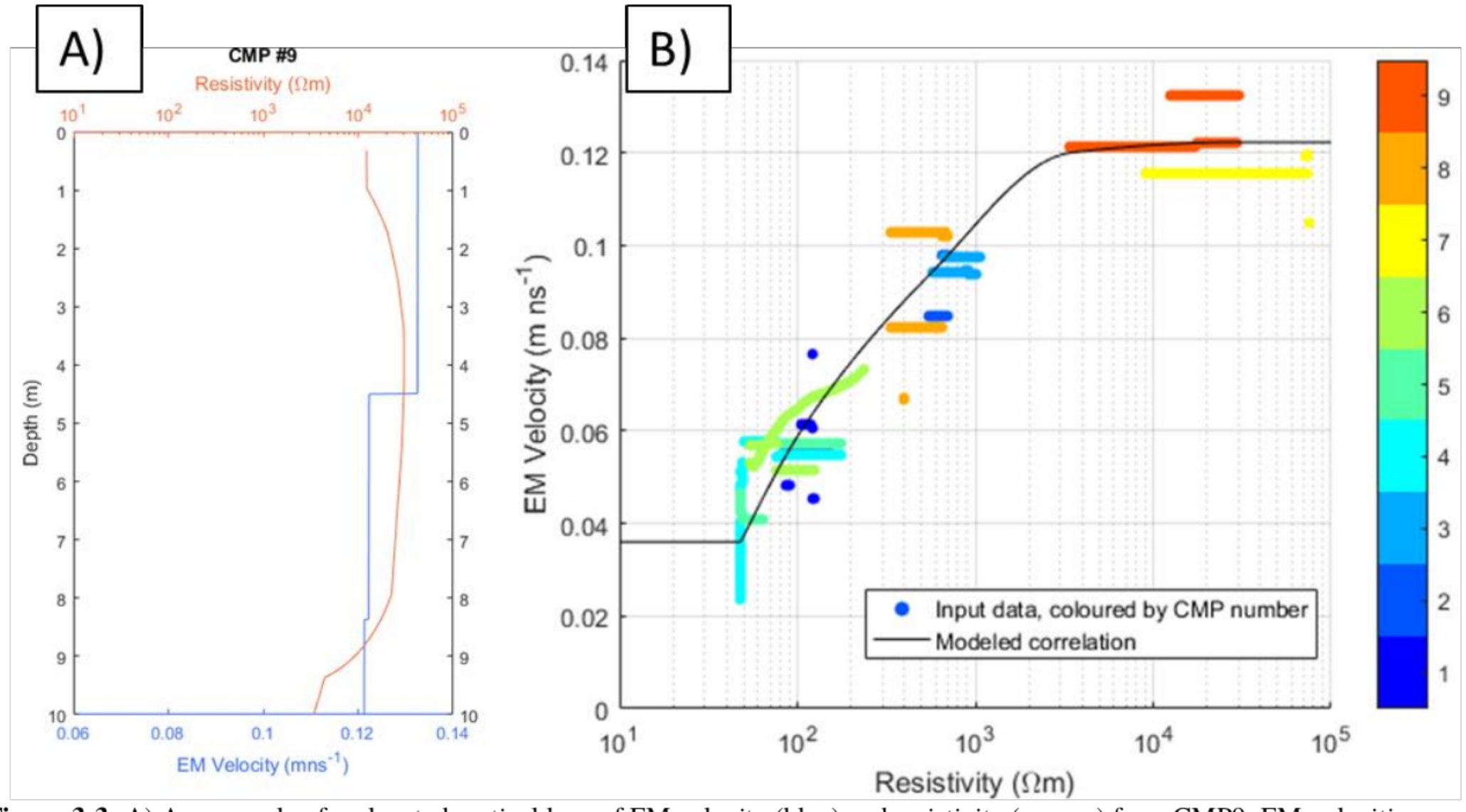

Figure 3-3: A) An example of co-located vertical logs of EM velocity (blue) and resistivity (orange) from CMP9. EM-velocities are taken from the 1D-velocity models resulting from semblance analysis of CMP captures, while resistivity is interpolated from the ERT models at those locations. B) Scatter plot showing collocated pairs of resistivity and EM-velocity from all nine CMP captures. Colours of the data points indicate which CMP location they are from. The modeled correlation above in black was used to produce a 2D EM-velocity model and to convert GPR reflection sections from time domain to depth domain. See Figure 3-1 for the location of CMP measurements.

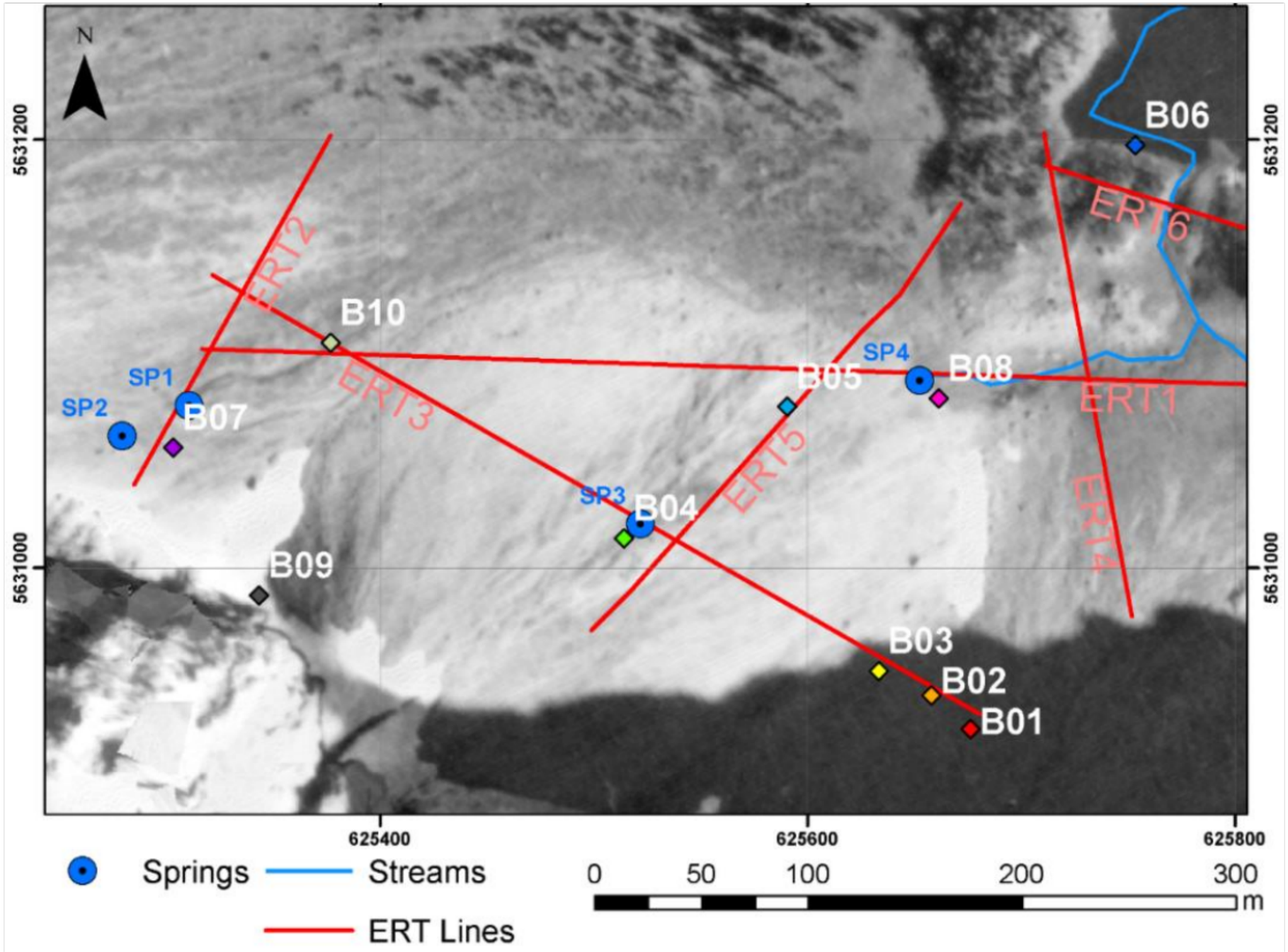

Figure 3-4: Coloured diamonds indicate the locations where bottom temperature of snowpack (BTS) sensors were installed from October 2015 to June 2016. Colours of the diamonds correspond to the colours used in Figure 4-19. Grid coordinates are in Universal Transverse Mercator (UTM), Zone 11 North, WGS 1984 Datum.

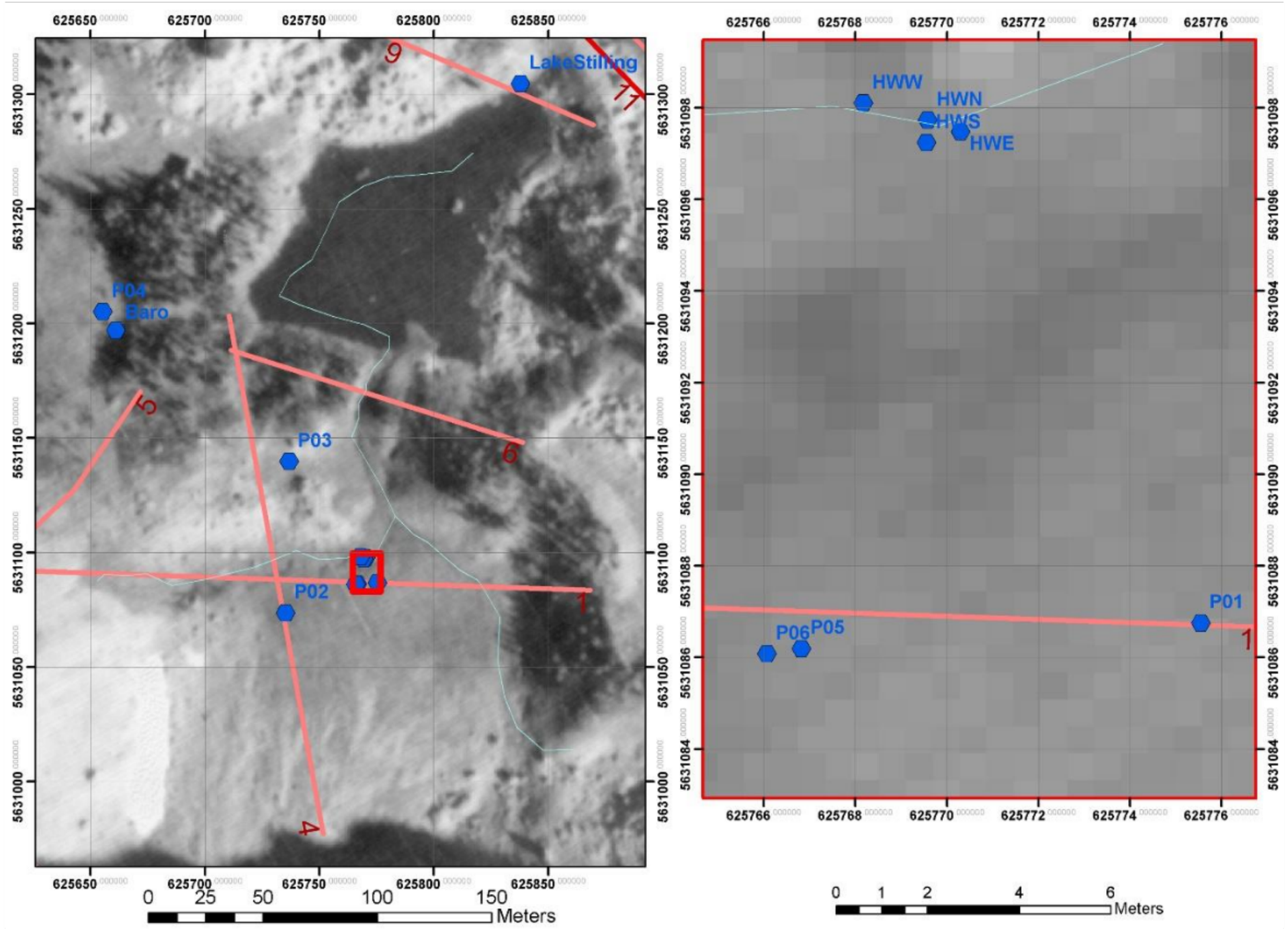

Figure 3-5: Map showing the locations where piezometers, stilling wells, and a barometer (blue hexagons) were installed. The red rectangle on the left indicates the extent of the right-hand panel. ERT survey lines are shown as pink or red lines. Grid coordinates: UTM, Zone 11 WGS 1984 Datum.

Chapter 4 **Talus Hydrogeology**

The scope of this chapter is to present findings about the hydrogeology of talus deposits present in the Bonsai Lake basin. Results from other areas of the basin are discussed in Chapter 5. Sections herein include: a literature review of alpine talus hydrogeology (4.1), a detailed site description and classification of the talus slopes (4.2), geophysical survey results and other data (4.3), and an interpretation of results and comparison to previous studies (4.4). The reader is referred to Chapter 2 for a broader introduction to the field site, Chapter 3 for a description of the methods used, and to Chapter 6 for a synthesis of results in both this chapter and Chapter 5.

4.1 Literature Review: Hydrogeology of Alpine Talus

Talus is defined as "accumulations of loose, coarse, usually angular rock debris at the foot of steep rock slopes". These deposits are long-lasting landscape features because their coarseness makes them resistant to erosion (Luckman 2004). They are common landforms in alpine environments both because of the presence of oversteepened terrain and because of rapid rockfall rates following glacial retreat since the early Holocene (Ballantyne 2002; Hoffman et al. 2013). While dominated by rockfall deposits, many different sediment redistribution processes act on them, including (but not limited to) avalanching, debris flow, dry grain flows, supranival sliding, and creep (Lowe 1976; Bertran et al. 1993; van Steijn et al. 1995; Luckman 2004). "Talus" is used interchangeably with "scree," though the latter is more commonly used in Europe (Luckman 2004).

Several studies have characterized the role of talus slopes in alpine watersheds. For example, Clow et al. (2003) used tracer tests to show that talus slopes are the primary storage reservoir in the headwater basin studied, having a potential storage exceeding the annual discharge of the basin's outlet stream. Similarly, Davinroy (2000) showed that after spring snowmelt, talus discharge accounts for 68% percent of streamflow exiting from the valley studied. Both studies focused on basins in the Colorado Front Ranges of the Rocky Mountains. Similar patterns have been observed in the Cordillera Blanca in Peru, where talus slopes (and related debris fans) are important recharge features and offset meltwater for later discharge during the dry season (Baraer et al. 2015; Gordon et al. 2015). Hence, across many localities, talus has been shown to be an important landscape unit in the hydrology of mountain headwater basins.

In addition to watershed-scale studies, several workers have attempted to characterize the hydrogeological properties of individual slopes. The hydraulic conductivity, storage time, and saturated zone thicknesses of multiple studies are summarized in Table 4-1. In short, talus slopes have a relatively high hydraulic conductivity, low mean residence time, and in some cases, can have very thick saturated zones. However, these measurements highlight the wide variability of these properties between sites.

Some of this variability can be explained by differences in proportion of fine-grained material in talus slopes. Filling the air-filled voids between cobbles and boulders with fine grains decreases hydraulic conductivity and decreases total porosity (Davinroy 2000; Caballero et al. 2002). This has implications for not just underground conveyance of water, but also infiltration. Coarse grains with high porosity permit rapid infiltration of water (Sosedov 1974) while fine, low-permeability materials on top of coarser grains can prevent it (Pierson 1982). Moreover, stony covers on talus help prevent the capillary motion of water up to surface, thus reducing losses due to evaporation (Pérez 1998). In short, adding fine-grained sediment to coarse talus decreases the bulk porosity but increases the residence time of groundwater in talus slopes, and coarse-grained covers enhances the retention of water.

Grain size distribution is not the only control on flow paths and storage in talus slopes. For one, bedrock may play an important role. Muir et al. (2011) found that groundwater flow in a talus deposit was concentrated in a thin layer at the talus-bedrock interface, and that depression in bedrock were a likely storage mechanism. Frozen ground plays a similar role. At the pore scale, interstitial ice is an important seasonal store of water. It continues to slowly melt after spring snow cover is gone, and redirects flow, mostly by limiting infiltration of snowmelt (Davinroy 2000). There are also several examples of large bodies of permafrost, which is defined as ground that remains below 0°C for at least two years (Permafrost Subcommittee 1988), detected in talus (e.g. Sass 2006; Hauck and Kneisel 2008, p. 153-164). While the effect these large bodies of ice have on flow paths in talus are unknown, studies of permafrost in coarse-grained proglacial moraines have shown that ice acts as an impermeable barrier to flow in the subsurface and as an important interannual and seasonal store of water (Langston et al. 2011). Hence, beyond grain size distribution, bedrock properties and the thermal regime may affect the hydrological role talus slopes play in a watershed.

While no classification schemes currently exist to describe how the hydrological role of talus slopes may differ between basins, several that highlight geomorphological differences have been proposed. White (1981) proposed classifying those they observed in New Zealand based on the three most important redistribution processes: rockfall, avalanche, and alluvial talus. Their scheme, which relies on differences in slope, grain attributes, and surficial landforms to differentiate the three categories, is summarized in Table 4-2. Selby (1982), in contrast, emphasized clast fabric, using four categories in their scheme: (1) coarse and openwork with large void spaces; (2) partially infilled with fines; (3) clast-supported with all voids filled; and (4) matrix supported. Note that both schemes describe natural phenomena that occur on a continuum. More than one redistribution phenomenon may act on a talus slope, and there is no strictly defined threshold for when a talus slope becomes a regular, soil-covered hillslope. Nonetheless, they capture features, such as grain size distribution and microtopography, that are important for the hydrology of talus slopes.

Many researchers have used geophysics to understand the internal structures of talus deposits. Some of these focused on mapping their internal fabric, often with the explicit aim of developing genetic models (Sass 2006, 2007; Sass and Krautblatter 2007; Onaca et al. 2016). Most of these rely on GPR texture to detect changes in fabric and very deep structures, while SRT and ERT more easily detect lateral variations. Geophysical prospecting has also been used on talus to map permafrost (Hauck and Kneisel 2008, p. 153-164; Stiegler et al. 2014) and for engineering investigations (Brody et al. 2015). Hydrogeophysical studies are much rarer. Studies at Lake O'Hara in the Canadian Rocky Mountains showed that talus deposits were no more than 20 m thick, generally very coarse-grained, and harboured groundwater only in thin layers above a stepped bedrock surface (McClymont et al. 2010; Muir et al. 2011). Investigations of a similar nature are ongoing in the Cordillera Blanca of Peru (R.L. Glas, personal communication). Hence, while geophysics has often been used on talus deposits, this study adds to the limited set of hydrogeophysical investigations of talus slopes.

This literature review shows that while it is conceptually understood how talus sedimentology affects its hydrogeology, such insights have largely been from tracer tests and other geochemical means rather than more detailed geophysical surveys. Likewise, while some studies have looked at how different talus formation and sediment redistribution processes affect deposit

geomorphology, few document how these in turn affect hydrogeological processes. Both these gaps in knowledge regarding catchment-scale hydrological processes must be addressed to reach the goal of more accurate and precise predictions of streamflow. This thesis addresses these knowledge gaps by both documenting in detail the geomorphic, sedimentological, and hydrological characteristics of the talus and by imaging the subsurface with geophysical methods.

4.2 Site Description

There are four main talus cones at the study site along the southern headwall of the basin, each of which are pictured in Figure 4-1 and Figure 4-2. These are referred to herein as the Upper East Cone, Lower East Cone, Central Cone, and West Cone. Both the Upper East and Central Cones occur below a narrow couloir, while the West Cone is below a much broader incised valley. At the southeast margin of the basin, there is also a talus slope (referred to herein as the Eastern Talus Slopes) with no obvious convex transverse profile nor a couloir concentrating rockfall. The key hydrological, topographic, and sedimentological aspects of these deposits are summarized in this subsection, with the aim of identifying differences in formation processes.

4.2.1 Topographic Characteristics

Longitudinal elevation profiles of each cone (Figure 4-3) show similar shapes at a large scale, with some notable differences. All cones are upwards concave, with a decreasing slope moving down and a maximum steepness of 30° or greater at the apex. The Upper East and Central Cones differ in that their slopes are relatively constant in the upper half (Figure 4-3B), only being curved in their lower halves. The Lower East Cone has the shallowest gradient of all, and has an abrupt change of slope at 200 m right at the northeast margin of the Upper East Cone. Unlike the other cones, the Eastern Talus Slope has a kink in its profile at 75-100 m. This is related to a moraine near the transect (Figure 4-2 and Figure 4-4) that, based on similar cases in the Canadian Rocky Mountains, likely formed during the Little Ice Age (G. Osborne, personal communication).

At a smaller scale, there are many notable microtopography features. All slopes have pronival ramparts where late-lying snow forms a small ridge between the talus deposit and headwall. There are prominent levees related to debris flow extending from the Lower East Cone onto the meadow (Figure 4-5). The Central Cone has two large channels, approximately 1 m deep and 3-8

m wide branching away from the apex of the talus cone (Figure 4-6B). Similarly, the West Cone has several linear channel features visible in air photos (Figure 4-7).

4.2.2 Hydrological Features

The two couloirs above the Upper East and Central Cones are both important hydrological features of the basin. Each one concentrates water inputs into a single waterfall. Flow from the Upper East Couloir is only obvious during the snowmelt season and storm events, or in midwinter when an icefall highlights its presence. In contrast, the Central Couloir has persistent flow nearly year-round. Late-lying snowpack is visible well into August on the shaded, high-elevation slopes above each couloir, which may play a role in maintaining waterfall discharge in the Central Couloir.

Several springs and streams are also observed on the talus deposits. The locations of the springs are shown in Figure 4-1 and Figure 4-2, and key attributes are summarized in Table 4-3. SP1 and SP2, on the West Cone near the headwall, have flow until late summer (Figure 4-6A) but run dry thereafter. In contrast, SP3, which is located on the Central Cone, has visible flow to late October, and it may or may not run later in to the winter. There are also several ephemeral streams where there is visible flow at surface in late spring and early summer. These occur along the margin of the West and Central Cones and downslope of the waterfall and SP3 on the Central Cone (Figure 4-6B). Discharge from none of these springs reaches the toe of the talus cones, even during the highest flow period. However, at the base of the Central Cone and the Eastern Talus Slopes, there are springs (SP4 and SP5) that feed small streams flowing into the meadow.

4.2.3 Grain Size Differences

There are considerable heterogeneities in grain size distribution and porosity throughout the talus deposits, some of which are illustrated in Figure 4-8. Generally, fine-grained sediment is more proximal, with coarsening of grain sizes moving downslope. Beyond longitudinal changes, there are also lateral variations in fraction of fine-grained sediment. Using Selby's (1982) parlance, size distributions range from "clast-supported with all voids filled" to "coarse, openwork matrix with large void spaces," but completely matrix-supported deposits were not observed. Areas of higher fine-grained fraction is normally easily identified by the presence of vegetation.

There are also discernable differences between each of the talus cones. The West Cone is generally uniform, where coarse gravel is mixed in with small amounts of organic soil. Yet, large

carbonate boulders (>2 m) are scattered around sporadically. In contrast, the Central Cone shows large lateral variation. Fine-grained material is more common along the path of steepest descent from the apex of the cone, whereas the western half of the cone is very coarse, blocky, and very loosely packed. The Upper East Cone tends to have high porosity and low fines content compared to the Lower East Cone.

4.2.4 Summary and Classification by Formation Processes

Table 4-4 summarizes key features of each talus cone, and shows that all cones do not fit neatly into any of the categories proposed by White (1981). All cones start with slope > 30 degrees (indicative rockfall and alluvial talus) at apex, but are also concave upward at the base (alluvial and avalanche). There appear to be fines washed in between coarser material into areas proximal to the apex of cones (alluvial), yet a fringe of coarser debris at the toe of each (rockfall, avalanche). Some areas lack vegetation and have angular fragments (rockfall) yet others have clear fluvial microtopography features, are vegetated, and are below a couloir which concentrates flow (alluvial). Moreover, large cornices develop along the upper ridges, posing a severe avalanche risk during the winter months. For this reason, some combination of avalanche, rockfall, and fluvial process all contributed to the formation of most these talus deposits.

There are two cases where one or more of these processes played a less important role. The Lower East Cone is distinct from the others because it is not directly under a couloir, has a long run-out length, and has a much shallower surface gradient. Moreover, in contrast to the other cones, it has a downward fining of grain sizes, and is more heavily vegetated. While it is difficult to assess whether avalanche or alluvial redistribution was more important in its formation, the deposit lacks the features of rockfall talus, and has been classified as such in Table 4-4. Similarly, on the Central Cone, the region downslope of the water with greater fine content, more vegetation, and ephemeral streams is distinct from the rest of the cone. In plan view and in stereophotos, it is a convex protrusion that extends beyond the rest of the cone. For this reason, it is classified as a “debris flow lobe” in Figure 4-2.

4.3 Results

Geophysical data were collected along four different orientations along the talus slope:

- An oblique line starting from the meadow, crossing SP4 and the Central Cone, and ending on the West Cone (ERT1, SEIS1-2-4, SEIS5, and GPR1 in Figure 4-9, Figure 4-11, and Figure 4-10)
- A cross-section of the Central Cone that also covers portions of the Upper East and West Cones and crosses SP3 (ERT3, SEIS7-8, and GPR4 in Figure 4-12 and Figure 4-13)
- A longitudinal line along the debris flow lobe of the Central Cone (ERT5 and SEIS9 in Figure 4-14)
- A line on the West Cone that crosses SP1 and SP2 (ERT2 and SEIS6 in Figure 4-15).

In addition, two lines along the eastern ridge of the basin at known bedrock locations were collected to obtain petrophysical information about the Fernie and Palliser Formations (ERT12 and SEIS13 in Figure 4-16 and ERT10 in Figure 4-17). Small inset maps are included in all geophysical image figures in this chapter, with the green line highlighting the location of the current survey line. The reader is referred to Figure 3-1 for the full-sized map.

General trends in the results (Section 4.3.1) are organized according to method: ERT, GPR, and SRT. Separate subsections are used to describe a notable anomaly in the Upper East Cone (4.3.2.1), the bottom temperature of snowpack data (4.3.2.2), and surveys along bedrock outcrops along the eastern ridge of the basin (4.3.2.3).

4.3.1 General Trends in Geophysical Images

4.3.1.1 ERT

The resulting resistivity images for ERT1, ERT2, ERT3, and ERT5 (Figure 4-9B, Figure 4-12B, Figure 4-14B, Figure 4-15B) show that there are three main units in the talus with distinct resistivities: a high-resistivity group (15,000-65,000 Ωm, corresponding to red or deep brown in the images), an intermediate resistivity one (3,000-10,000 Ωm; yellow or orange), and one of low resistivity (500-3,000 Ωm; light green to dark green). The high-resistivity unit is only present within the upper 15 m of the talus deposits, and tends to present in large, contiguous bodies (e.g. Figure 4-9B, 300 to 450 m). In contrast, both the intermediate- and low-resistivity units may be present at depth, and in places are intermixed, as seen at the toe of the Central Cone (Figure 4-9B, 280 to 350 m, circled in black).

These transitions in resistivity correspond closely with transitions in surface cover. On the west side of the Central Cone, there is a large area where the talus lacks fine-grained material and is made of only coarse blocks with large air gaps. This unit appears as a high-resistivity zone on ERT1 (Figure 4-9B, 300-450 m) and ERT3 (Figure 4-12B, 100-230 m) and is also visible in the 3D fence diagram in Figure 4-18. Similarly, on ERT2, the high-resistivity unit between 100 and 160 m corresponds to less vegetation and more rocky cover (Figure 4-15B) compared to the rest of the line.

The lowest resistivity unit usually corresponds to hydrological features seen at surface. SP4, the spring at the base of the Central Cone, corresponds to the location at surface along ERT1 (Figure 4-9B, 220 m) where resistivities decrease sharply along a relatively flat boundary (indicated with a black, dashed line). Similarly, SP3 corresponds to a low-resistivity anomaly on ERT3 (Figure 4-12B, 231 m, black ellipse). The location and elevation of SP1, which is just out of plane of ERT2, corresponds to the low-resistivity feature at 44 m and 2193 masl (Figure 4-15B, black ellipse). Moreover, channel features at surface also correspond to some low-resistivity anomalies. These include the ephemeral streams at the margin of the Central and West Cones imaged in ERT1 and ERT3 (Figure 4-9B, 460 m; Figure 4-12, 60 m), and a relict debris flow channel on ERT3 (Figure 4-12B, 340 m).

4.3.1.2 GPR

The GPR data corroborate several aspects of the geologic structures imaged by resistivity images (Figure 4-10). In general, areas with greater signal attenuation (indicated by the dotted white line) usually correspond to lower resistivities. Locations in Figure 4-10A where the high-resistivity unit is in close contact with the low-resistivity unit have the highest-amplitude reflectors (Figure 4-10B).

Changes in EM velocity correspond closely to changes in resistivity. The EM velocity in the low-resistivity unit ranges between 0.06-0.10 m/ns (Figure 3-3B, CMP8), whereas that in the intermediate and high-resistivity units have velocities of 0.11-0.13 m/ns (Figure 3-3B, CMP7 and CMP9). This correlation is more obvious in the cross-plot of co-located resistivity and EM velocity data in Figure 3-3.

Furthermore, the radar images also highlight changes in fabric within the upper zone of the talus, as illustrated with data from GPR1 (Figure 4-11). The reflectors within high-resistivity bodies

(indicated with the dashed white line) are more discordant compared to the intermediate- and low-resistivity zones. Where reflectors are more concordant, they are in general surface parallel (e.g. 520-580 m). The exception are reflectors along GPR1 at the toe of the debris lobe on the Central Cone, where they are acute angled and surface-terminating (250-300 m).

4.3.1.3 SRT

Images of P-wave velocity are shown in Figure 4-9A, Figure 4-12A, Figure 4-14A, and Figure 4-15A. Areas with no ray path (i.e. areas where no wave signal passes through them) are omitted in these figures, which leads to variable maximum depth and some large gaps in some images.

The images show that there are three distinct layers in the talus. The uppermost layer, with velocities no more than 500 m/s, is approximately 10 m thick throughout the talus. Most small-offset ray paths travel along the lower boundary of this layer. The deepest layer is a high-velocity unit with velocities ranging from 2300-3500 m/s, the depth of which varies throughout the study site. It is up to 60 m deep (an elevation of approximately 2090 masl) below the Central Cone on SEIS7-8 (Figure 4-12A), yet only 20 m deep (2190 masl) below the West Cone near the headwall (Figure 4-15A, 0-30 m). This high-velocity layer is not detected in some areas, including SEIS5 (Figure 4-9A) and past 32 m along SEIS6 where it drops off precipitously (Figure 4-15A). Between the shallowest, slow layer and the deepest, fast layer, there is an intermediate zone of variable thickness. Due to low ray path coverage (e.g. Figure 4-12A, 200-250 m), its velocity is not very well constrained, ranging between 500 and 1500 m/s.

4.3.2 Other Results

4.3.2.1 Upper East Cone Anomaly

There is large anomaly within the Upper East Cone that is visible at the east end (350-410 m) of ERT3 (Figure 4-12B), SEIS7-8 (Figure 4-12A), and GPR4 (Figure 4-13). It has a resistivity (65,000-75,000 Ωm) higher than anything observed elsewhere in the talus (Figure 4-12B). It also has a much higher velocity (3500-5500 m/s) and is much shallower (between 3 and 6 m depth) than the high-velocity zones detected elsewhere under the talus (Figure 4-12A). In the GPR data, though reflectors are generally surface parallel yet discordant as they are elsewhere along this line (Figure 4-13, up to 340 m), the amplitudes are more subdued within the anomaly 350 to 410 m (Figure 4-13, 350 to 410 m). There are also high-energy reflectors between 350-360 m (Figure 4-13A). The direct (air) wave obscures the upper few metres of the subsurface, however, so a

reflector corresponding to the upper boundary in the seismic image is not visible in the GPR reflection section. Nevertheless, all three images indicate that there is a shallow unit with something petrophysically distinct from the rest of the talus.

4.3.2.2 Bottom Temperature of Snowpack

Figure 4-19 shows the full time series from bottom temperature of snowpack loggers installed at locations shown in Figure 3-4, and mid-winter averages (February 1 to March 31) are given in Table 4-5. All points above the anomaly in the Upper East Cone (B01, B02, and B03) are below the -3°C boundary for probable permafrost occurrence suggested by Hoelzle et al. (1999). Moreover, there is an increasing trend in temperature moving from the centre to the west margin of the anomaly.

4.3.2.3 Petrophysical Surveys Along Eastern Ridge

Two locations on Bonsai Lake basin's eastern ridge were imaged to obtain petrophysical information on the Fernie and Palliser Formations. ERT12 and SEIS13 (Figure 4-16) straddle the contact between the two formations (i.e. the Sulphur Mountain Thrust Fault) mapped by McMechan (2012). A heavily weathered shale occurs in a treeless gully (Figure 4-16, 80-120 m). Upslope and south of this gully, talus deposits comprised of carbonate boulders covers the surface. Gaps between these boulders are partly or fully filled with soil between 20 and 80 m but are largely air-filled from -10 to 20 m. Between 0 and 20 m, the line orthogonally crosses a bedrock ridge. Although it is difficult to distinguish between car-sized boulders and outcropping bedrock at this location, intact bedrock is expected to be shallow in this location regardless.

The second location surveyed (ERT10) is approximately 700 m further north (Figure 4-17). A service road has exposed the Fernie Formation, and sediment of no more than 0.5 m thick intermittently covers the bedrock. Unlike the other location, bedrock here is more intact.

The resulting image from SEIS13 (Figure 4-16A) shows that the P-wave velocities for the Palliser and Fernie Formation differ significantly. Whereas the Palliser Formation is between 3500-5000 m/s when intact, the Fernie Formation only reaches a maximum of 3800 m/s. The image also shows that the zone of weathered Fernie Formation (like the material seen at surface) is up to 20 m thick, as indicated by the low velocities.

The resistivity images from ERT10 (Figure 4-17) and ERT12 (Figure 4-17B) show that resistivities of the Fernie Formation typically range between 130-370 Ωm, but extreme values between 70-600 Ωm are possible. There is no ERT data in Figure 4-16B that overlaps with zones of intact Palliser Formation mapped by the seismic data in Figure 4-16A. Hence, in the table summarizing the petrophysical properties of these bedrock units (Table 4-6), the resistivity of the Palliser Formation has been left undefined.

4.4 Discussion

4.4.1 Geomorphology of the Talus Slope

The petrophysical variations in the talus can largely be explained by variations in grain sizes and water content. The high resistivity unit (15,000-65,000 Ωm) maps areas with coarse talus boulders, minimal fines content, and high porosity. The intermediate resistivity unit (3,000-10,000 Ωm Ωm) corresponds to talus with air gaps between coarse rubble filled with fine-grained content and with increased vegetation cover. The low resistivity unit (500-3,000 Ωm) is like the intermediate resistivity unit, except that it has high water content. These interpretations are informed largely by the correspondence between transitions in resistivity and either water features or surface cover changes. The changes in EM velocity are consistent with this interpretation given the decrease in bulk porosity and an increase in water content that cause lower bulk resistivities can also explain an increase in bulk dielectric permittivity.

The ranges of resistivities, P-wave velocities, and EM velocities observed are similar to literature values summarized in Table 3-2 and listed in Appendix B. Earlier studies found talus to have P-wave velocities of 500-2500 m/s, resistivities of 20,000-100,000 Ωm when dry and 500-3,000 Ωm when wet, and EM velocities of 0.09 to 0.14 m/ns (Hauck and Kneisel 2008, Tables A2, A3, A4; McClymont et al. 2010; Muir et al. 2011). The P-wave velocities and EM velocities from this study (400-1500 m/s and 0.06-0.14 m/ns, respectively) extend somewhat below the minimum extent of the published ranges. The resistivity of the wet, soil-bearing talus (500-3,000 Ωm) and the dry, bouldery talus (15,000-65,000 Ωm) largely overlap with the “wet” and “dry” categories of talus resistivity from Table 3-2. This comparison further supports the interpreted meaning of the different petrophysical units within the talus.

The radar reflection images further reveal how different weathering processes may have led to these variations. Such interpretations are based heavily on work by O. Sass whose geophysical

studies of talus in the Alps have led to a set of identifiable GPR "fingerprints" (i.e. diagnostic textures) for a deposit's formation processes (e.g. Sass 2006, 2007; Sass and Krautblatter 2007). Rockfall talus and debris flow talus can be distinguished by having either surface-parallel or acute-angled, surface-terminating reflectors, respectively (Sass 2007). This can explain the different texture observed in the toe of the Central Cone in the debris flow lobe, which tends to have surface-terminating reflectors (Figure 4-11, 270 m), versus the rest of the talus which tends to have surface-parallel reflectors. He interprets crude bedding seen in radargrams as resulting from variation in fine-grained content; areas lacking this bedding therefore lack fine-grained material (Sass 2007). This in turn explains why, in the present study at Bonsai Lake, areas with discordant reflectors often correspond to areas of very high resistivity with less fine-grained material (Figure 4-11). The addition of fine-grained material to rockfall deposits is normally explained by downwashing of sediment into gaps between coarse grains (White 1981; Sass 2006; Sass and Krautblatter 2007), implying that these rockfall deposits with fewer concordant reflectors might be deposits from more recent events.

In addition to lateral changes in grain size and water content, vertical variations are important as well. First, the loose, high-porosity deposits seen at surface do not extend below 10 m, as suggested by the extent of zones with higher resistivity (15,000-65,000 Ωm) and low seismic velocity (<500 m/s). This interpretation is consistent with other geophysical studies in the Austrian Alps where deeper zones are more densely packed due to the deposition of fine grains into pore space (Sass 2006; Götz et al. 2013).

The results also indicate that the talus deposits are generally very thick. The deepest, high P-wave velocities are best interpreted as bedrock. Hence, the talus is generally 20-40 m thick, and as thick as 60 m in some places. Similar thicknesses above 30 m have been observed at sites in the Sierra Nevada and European Alps (e.g. Sass and Krautblatter 2007; Götz et al. 2013; Brody 2015). Bedrock is unusually shallow at one point below the West Cone, where there is a "shelf" of bedrock detected at the south end of SEIS6 (Figure 4-15A, 0-32 m). This shelf likely occurs because of lithological changes. While the Fernie Formation underlies most of the talus slopes, the more competent Palliser Formations is expected at this location near the headwall. Approximate locations of geologic contacts from McMechan (2012) are indicated in Figure

4-15A with tan-coloured dashed lines. Given that this rock formation is not as weak and recessive as the Fernie Formation, it is plausible that it would not be weathered as far down.

These results contrast with hydrogeophysical studies of talus slopes at Lake O'Hara, specifically McClymont et al. (2010) and Muir et al. (2011). McClymont et al. (2010) studied a talus slope lapping onto a small meadow on the northeastern slope of the Obapin sub-basin. They estimated that the talus was at most 6 m thick. In a more detailed study of talus, Muir et al. (2011) focussed on a different slope on the southwestern side of the sub-basin. Like the Eastern Talus Slopes in the Bonsai Lake Basin, there was a moraine forming a small depression on the talus slope, but this area was not covered by geophysical lines. Results showed that the talus in no more than 20 m thick, and that there were several large bedrock steps below the talus. In both studies, the talus slopes were found to be made up almost entirely of boulders of mostly carbonate and quartzite with only a minor fraction of fine-grained sediments, unlike the slopes at Bonsai that have a larger fraction of fine-grained material and significant vertical heterogeneity.

4.4.2 Hydrologic Flow Paths

These results show that flow paths in these talus deposits are largely controlled not by bedrock location, but rather sediment distribution. For example, SP3 lies more than 30 m above bedrock, and is separated from deeper saturated zones (Figure 4-12, 240 m), indicating that it is a perched flow path. These imaging results are consistent with geochemical studies like Davinroy (2000) and Roy and Hayashi (2009), the former of which showed two distinct flow systems in the talus: a fast one in the coarse overburden, and one that is more sustained in deeper parts with lower bulk porosity. The pockets of low-resistivity material in the toe of the Central Cone debris flow lobe seem to also indicate convergent flow paths in pockets of higher-permeability material. Geomorphologically, this interpretation is plausible with talus deposits shaped by fluvial processes because they exhibit lateral heterogeneity due the difference between beds and banks of erosional channels (e.g. van Steijn et al. 1995, Fig. 15), a differentiation that is visible at surface presently (Figure 4-8D).

Hydrologically, the talus deposits at this site contrasts in two key ways with those studied at Lake O'Hara. This prominent role of grain size contrasts in controlling talus flow differs from McClymont et al. (2010) and Muir et al. (2011). In both of those studies, flow was concentrated in a thin saturated layer at the bedrock-talus interface. Muir et al. (2011) estimated that this layer

was on the order of 0.01 to 0.1 m thick. While bedrock location was important in controlling groundwater flow paths in those Lake O'Hara talus deposits, this only seems to occur in one location survey at Bonsai: in the West Cone at SP1 and SP2. There, the elevation of the closest spring (SP1) matches the elevation at the interpreted bedrock in SEIS6 (Figure 4-15A, 30 m and 2194 masl). Moreover, given that talus deposits at Bonsai much thicker (<20 m versus 20-60 m), these slopes can presumably store a larger volume of water in following snowmelt. Additionally, with a greater proportion of fines, the talus slopes at Bonsai have a presumably lower hydraulic conductivity can hence delay the release of stored water for longer. Consequently, the talus slopes at these sites will arguably play a greater role in water storage in the Bonsai Lake basin than at Lake O'Hara. Despite this thick zone of lower porosity, these talus deposits still have a stony cover in some areas to help with infiltration and prevention of capillary rise and evaporation as suggested by Pérez (1998), further enhancing longer-term retention of groundwater.

4.4.3 Permafrost Occurrence

The anomaly at the end of the Upper East Cone is best explained as a large body of permafrost. Referring to Table 3-2, the resistivity of the anomaly (65,000-75,000 Ωm) is likely too high to be bedrock (100-20,000 Ωm) and too low to be pure ice (1 MΩm to 10 GΩm). While resistivities of 20,000-100,000 are plausible for talus, the seismic velocities of the anomaly (3500-5500 m/s) are well above the maximum 2500 m/s measured in talus in other alpine geophysics studies (Table 3-2). Furthermore, the GPR reflection image (Figure 4-13) does not have the features that would be expected from a bedrock survey of GPR: continuous bedding planes or hyperbolae related to fractures (Sass 2006, 2007; Sass and Krautblatter 2007). Rather, the reflectors in the upper 10 m from 350 m to 410 m in Figure 4-13 are discordant and somewhat stratified like the reflectors seen elsewhere along the talus at this depth. Hence, by process of elimination, the anomaly is most likely talus material with interstitial ice.

There are other observations and data that individually cannot exclude other interpretations, but they are still consistent with the assertion that the anomaly is a talus-ice mixture. The mid-winter averages are both below the -3°C threshold for probable permafrost occurrence suggested by Hoelzle et al. (1999), and temperatures decrease moving towards the western edge of the anomaly. The location has geomorphic characteristics that are consistent with this interpretation.

It is well-shaded by the cliffs above (Figure 4-18), and the moraine immediately to the east of the anomaly (Figure 4-4) also suggests a colder microclimate. Furthermore, the Upper East Cone (especially at its fringes) has coarse blocky material which favours ground ice development (Harris and Pedersen 1998; Rödder and Kneisel 2012; Harrington 2017). Lastly, the GPR reflection image indicates that there is a change in bulk dielectric permittivity between 350-360 m along the line. As Figure 4-13 shows, there are high-energy reflectors both near surface and at depth at this span. Moreover, the shallow reflectors within the anomaly (360-410 m) are of a lower amplitude than in the talus to the west (300-340 m). This reduction in reflectivity and high-amplitude reflector at 350 m might be due to a difference in sedimentology between the Central and East Cones or due to the substitution of air in interstitial spaces with ice.

Unfortunately, the full role of permafrost is not fully understood in this particular basin. Large bodies of ice have been shown to be important for routing groundwater in proglacial moraines and for storing water interannually (Langston et al. 2011). It is possible that the imaged body of permafrost may extend further into the Eastern Talus Slope past the east end of ERT3, given that there was a sufficiently cold microclimate that sustained a small glacier atop the talus that formed the moraine 130 m to the east. If that is the case, permafrost may play a larger role in the hydrology of this catchment than is apparent from this initial study's data.

4.5 Summary of Findings

The goal of this study is to understand the groundwater flow processes in talus deposits. More specifically, it aims to address the lack of hydrogeophysical studies of talus and the poorly understood link between talus sedimentology, formation processes, and hydrogeology. Observations at surface indicate that some amount of rockfall, fluvial, and avalanche processes all contribute to some degree to the formation of these deposits at the Bonsai Lake basin. Geophysical surveys further indicate that there are significant lateral and vertical heterogeneities in grain-size distribution related to differences in which sediment redistribution dominates. These heterogeneities in turn are the most important control on groundwater flow paths, leading to the occurrence of springs at surface, perched water tables, and convergent flow paths at depth. This contrasts with previous studies of talus at Lake O'Hara (specifically, the Opabin sub-basin) where bedrock topography was the more important control on flow paths. Furthermore, the talus in the Bonsai Lake basin is quite thick, ranging between 20-60 m thick, with the upper 10 m

being more loosely packed. This layering and thickness again contrasts with Lake O'Hara, where talus was less than 20 m and lacked this vertical differentiation. Additionally, there is a large permafrost body occurring at one well-shaded location (at the Upper East Cone). The full extent of ice is unknown and may extend further into the Eastern Talus Slope.

4.6 Tables

Table 4-1: A summary of hydrogeological properties of talus slopes from previous studies.

Source	Location	Hydraulic conductivity ($m\ s^{-1}$)	Estimate of storage time	Thickness of saturated zone (m)
Muir et al. 2011	Lake O'Hara, Canada	0.01 to 0.03	exponential decay coefficient for storm peaks ~1 day^{-1}	0.01 to 0.1
Davinroy 2000	Upper Green Lakes Valley, Colorado Front Range, USA	0.018 to 0.026		
Clow et al. 2003	Loch Vale, Colorado Front Range, USA	0.0065 to 0.0094		1.5 to 11.2
Caballero et al. 2002	Rio Zongo Valley, Cordillera Real, Bolivia		a delay of at least 24 h	

Table 4-2: The attributes used by White (1981) to identify the dominant formation process for talus slopes.

	Slope angle	Grain attributes	Other attributes
Rockfall talus	• 35° to 45°	• Small rocks near the top • Large ones with enough energy to flow down to toe of slope	• Angular rocks • Usually lack vegetation
Alluvial talus	• 35° to 38° near the top • ≤28° at the bottom and concave up	• Large rocks at top deposited where water loses energy with slope change • Fines wash down in between coarser	• Fed by a couloir with sufficient source of water • Vegetation • Heavy storms or snowmelt may leave slush/debris flows, plus levees
Avalanche talus	• < 25°, concave up	• Any size, usually angular • Often a fringe of coarser debris (Potter 1969) • Rocks balanced in precarious positions at the bottom of the slope (Gardner 1970)	• Usually on lee-side slopes • There can be scour strips

Table 4-3: Summary of the main hydrologic features on the talus deposits.

Description	Nomenclature in this thesis	Timing and relative flow volume
Waterfall above Centre Cone		Strongest during snowmelt, small trickle persists in early fall
Springs on talus cones	*SP1, SP2, SP3, SP8*	SP1, SP2, SP8* are dry after main snowmelt (late summer) SP3 persists into early fall, possibly later
Ephemeral streams on talus cone		Only visible in early snowmelt season, not visible by mid-July
Talus toe springs	SP4, SP5	Flow much greater during snowmelt; SP4 persists into early fall, but SP5 is seasonal

*SP8 is outside the view of Figure 4-2. Refer to Figure 2-2 for its location.

Table 4-4: Summary of the main attributes of the talus slope and the inferred formation process following the classification scheme by White (1981).

	Associated hydrological features	Topography	Sediment	Dominant formation process
West Cone	SP1, SP2, ephemeral springs at east margin	>30° at top, upward concave, channel and levees	Generally uniform, clasts partly filled with fines and organic soil, some large boulders, vegetated	Combination of avalanche, fluvial redistribution, and rockfall, with lateral variations within a single cone
Central Cone	SP3, SP4, ephemeral springs at west margin, waterfall	>30° at top, upward concave, prominent channels near apex	Strong lateral variation. Vegetated and clasts-supported sediment with filled pore spaces along path of steepest descent below waterfall. West half has coarse, blocky, no fines between clasts.	
Upper East Cone	waterfall	>30° at top, upward concave	Blocky, partly filled with fines	
Lower East Cone		Shallow slope, mostly < 15°, upward concave, debris flow features at toe	Vegetated, clasts with most gaps filled with fines.	Fluvial or avalanche

Table 4-5: Average midwinter temperatures measured by the BTS sensors in 2016. Locations that are below the -3°C defined by Hoelzle et al. (1999) are bolded and italicized.

Sensor Name	Mid-winter average temperature (Feb 1 to Mar 31) (°C)
B01	***-3.9***
B02	***-3.5***
B03	***-3.0***
B04	-0.6
B05	*-2.7*
B06	***-4.9***
B07	-0.3
B08	-0.7
B09	-1.9
B10	-0.1

Table 4-6: Summary of the physical properties of the two most important rock formations as measured by ERT and SRT surveys directly at known bedrock locations. Adapted from Christensen et al. (2017).

Parameter	Fernie Formation (Jurassic shale)	Palliser Formation (Devonian carbonates)
Electrical resistivity (Ωm)	70 - 600	N/A
P-wave velocity (m/s)	400-3800	3500-5000

4.7 Figures

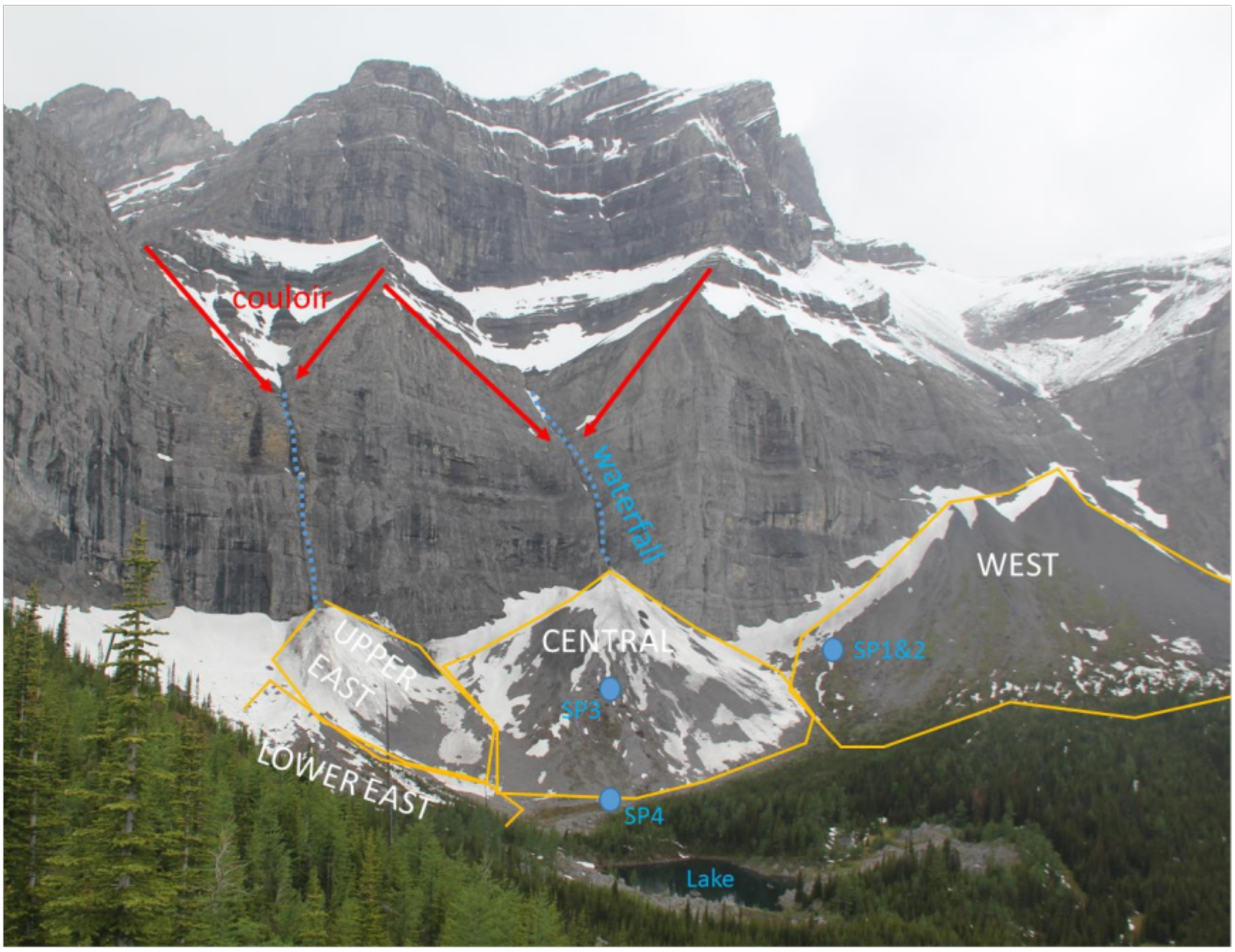

Figure 4-1: An oblique photo (facing southwest) of the talus deposits in the study area taken on June 14, 2016. The four talus cones are outlined in orange, though the Lower East cone is partially obscured by trees in the foreground. Approximate locations of important springs and waterfalls are indicated in blue, while notable couloirs above the Upper East and Central Cones are outlined with red arrows.

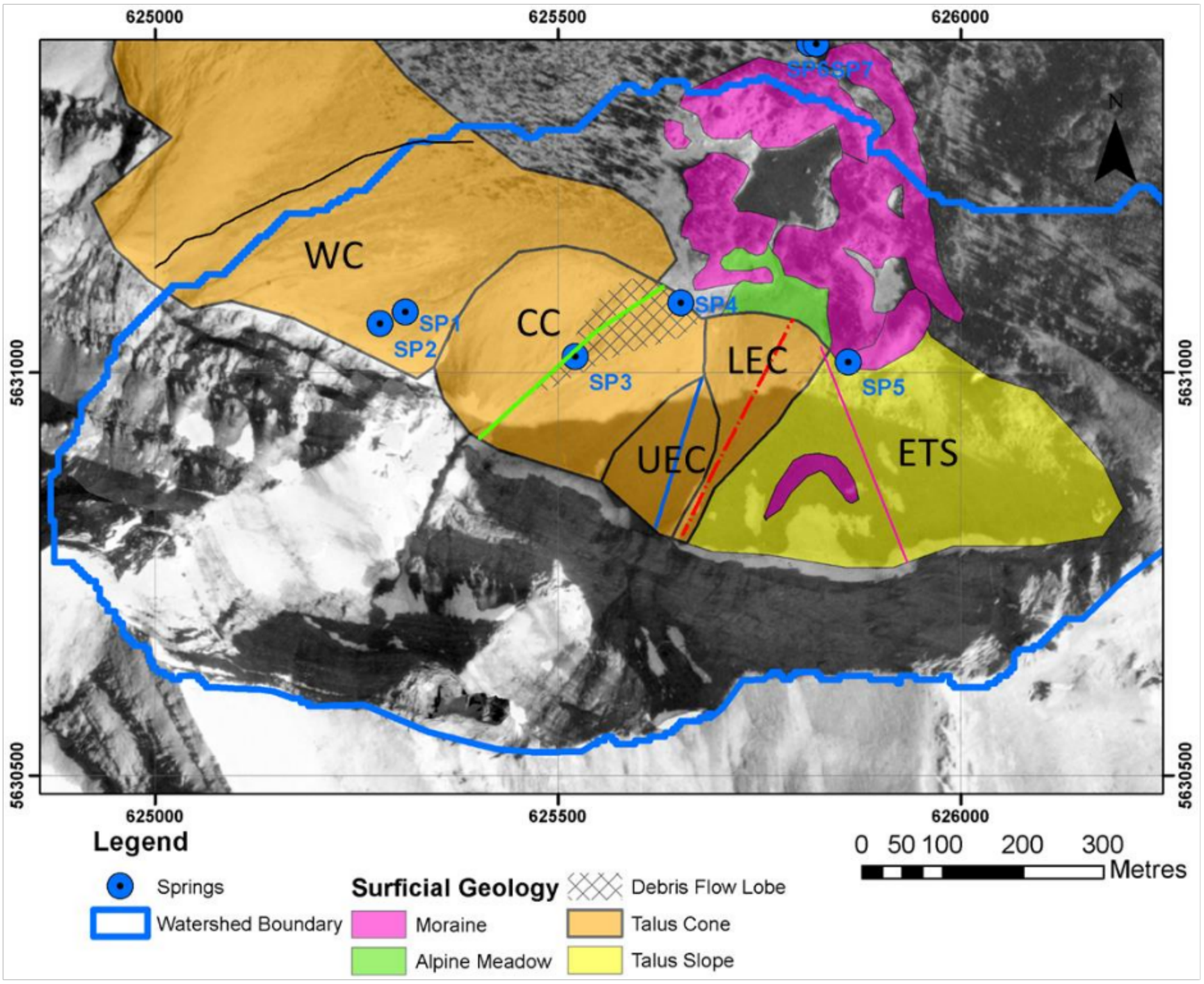

Figure 4-2: Surficial geology map with the different talus deposits labelled. Abbreviations refer to: [WC] West Cone; [CC] Central Cone; [UEC] Upper East Cone; [LEC] Lower East Cone; and [ETS] Eastern Talus Slope. The coloured lines traversing the length of talus deposits indicate the alignment of the topographic profiles in Figure 4-3. Grid coordinates are in Universal Transverse Mercator, Zone 11 North WGS 1984 Datum.

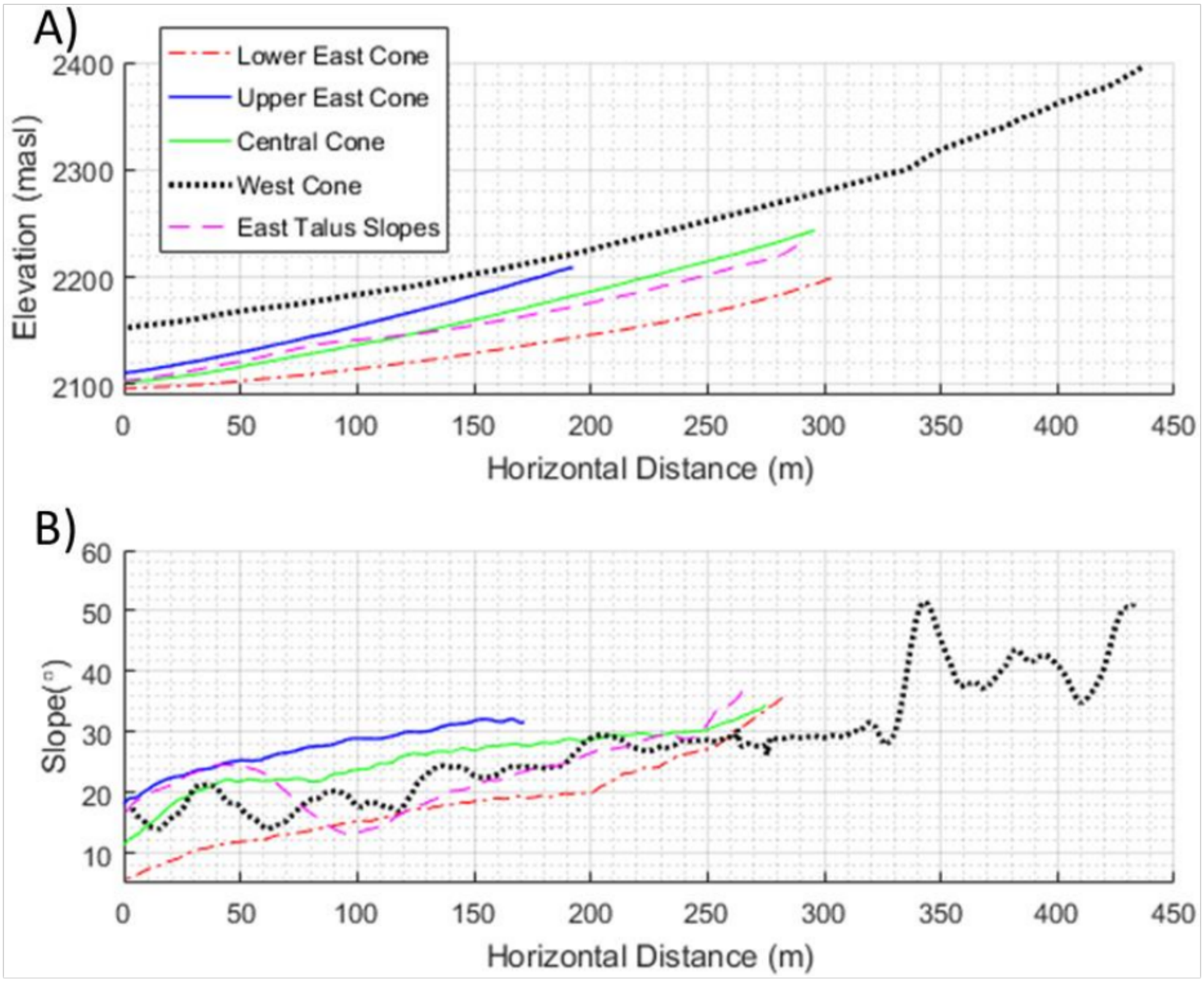

Figure 4-3: The elevation and slope profiles of the talus deposits. A) shows the elevation as a function of distance from bottom of the slope, while B) shows the slope angle.

Figure 4-4: A lunate moraine ridge located on the Eastern Talus Slopes. Photo taken from the northwest shore of Bonsai Lake on June 18, 2015.

Figure 4-5: Levees related to debris flow events deposited on top of the grassy meadow at the toe of the Lower East Cone. Photo dated June 18, 2015.

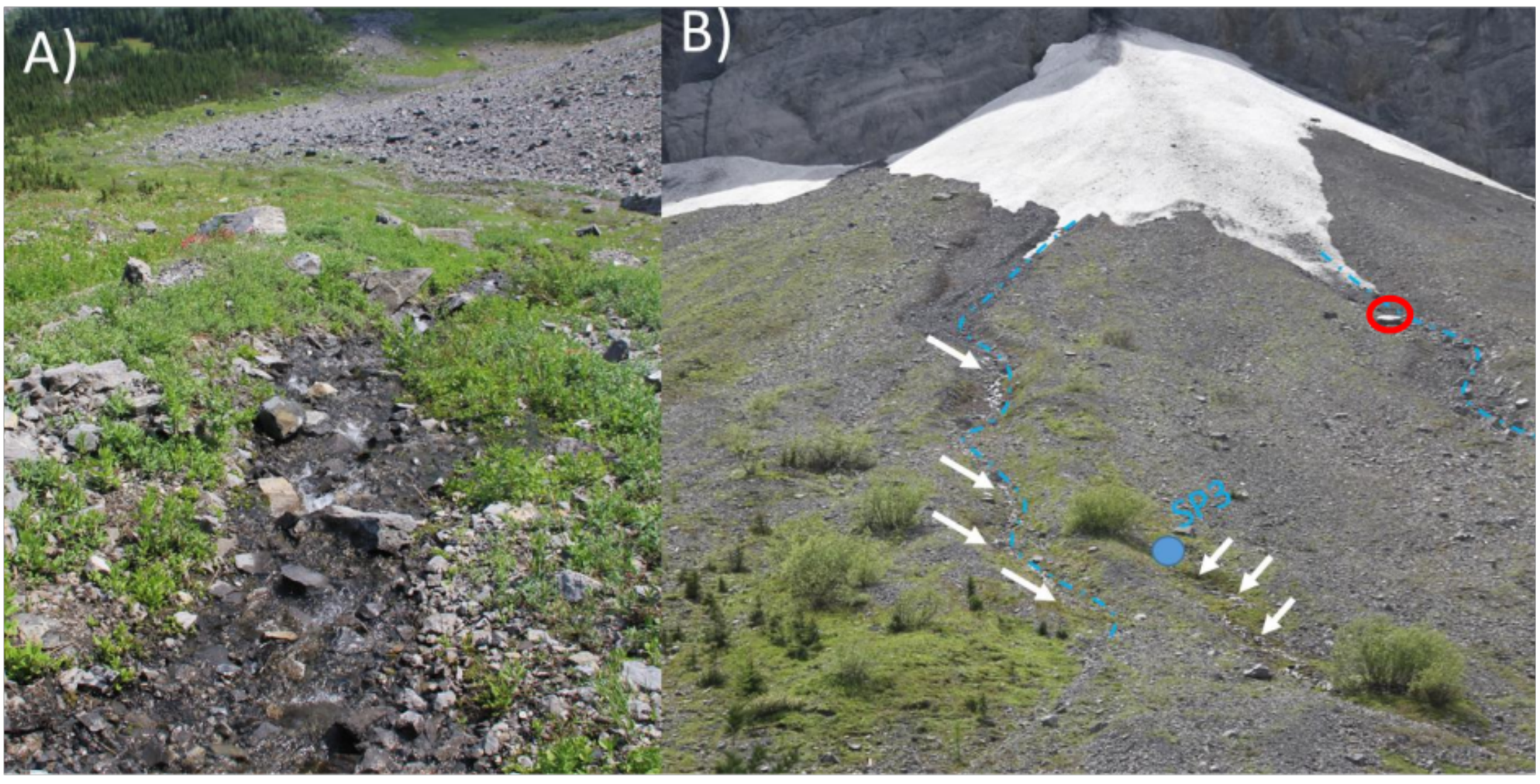

Figure 4-6: Photos showing important surface water features on the talus cone. A) SP1 on the West Cone on July 8, 2015. View is oriented downhill to the northeast. B) An annotated photo of important hydrologic features on the Central Cone, including: the location of SP3 (blue dot), surface water filling ephemeral streams (white arrows), and the alignment of large channels scoured into the surface of the talus (blue dashed line). The boulder circled in red is the same as that seen in Figure 4-8D. Photo faces south and was taken June 28, 2016.

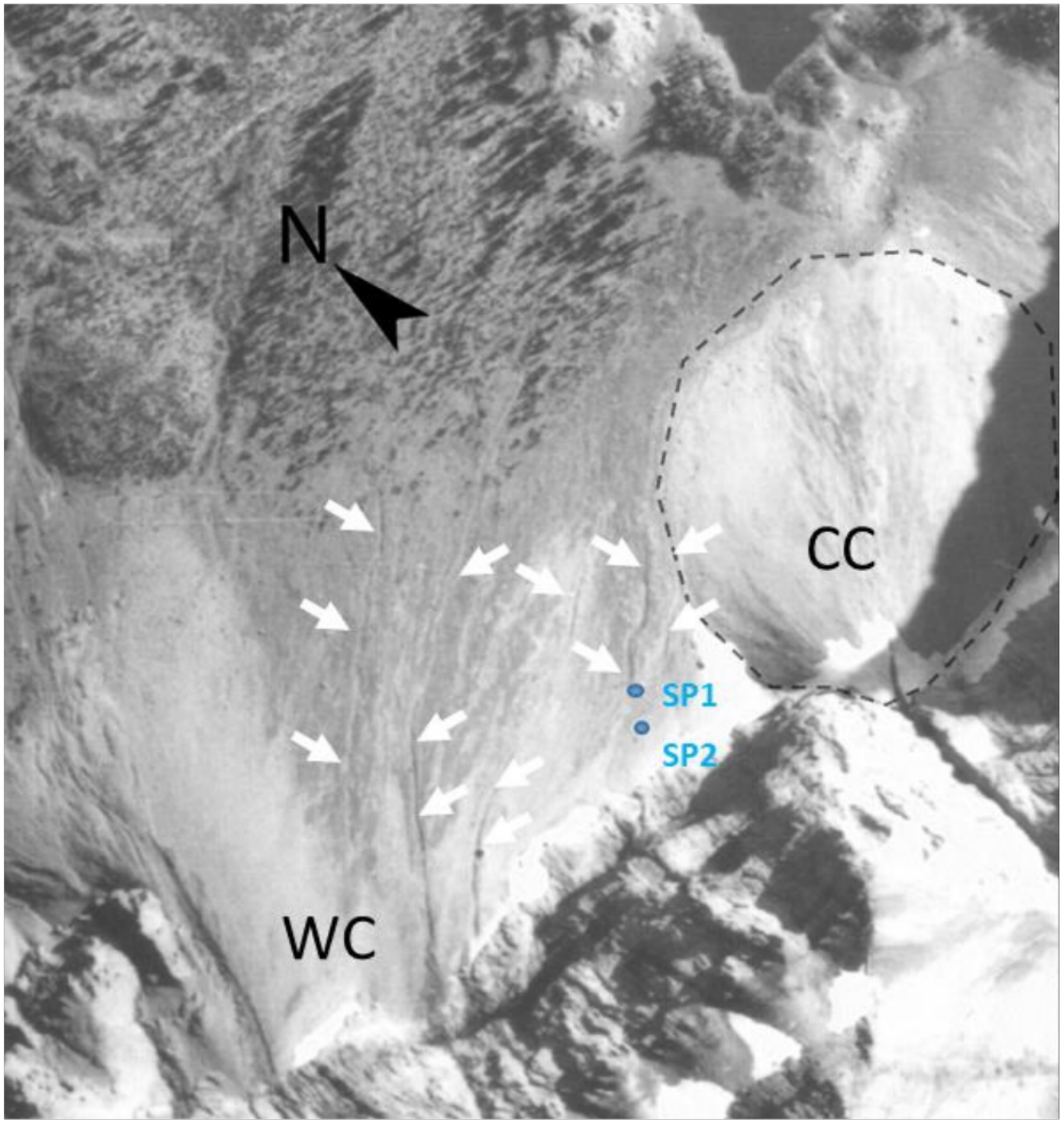

Figure 4-7: Channel features (annotated with white arrows) are visible in air photo on the Western Cone (WC). Extent of Central Cone (CC) is shown with dashed black line. Photo number 171 from roll number AS1486 (Alberta Energy and Natural Resources 1976).

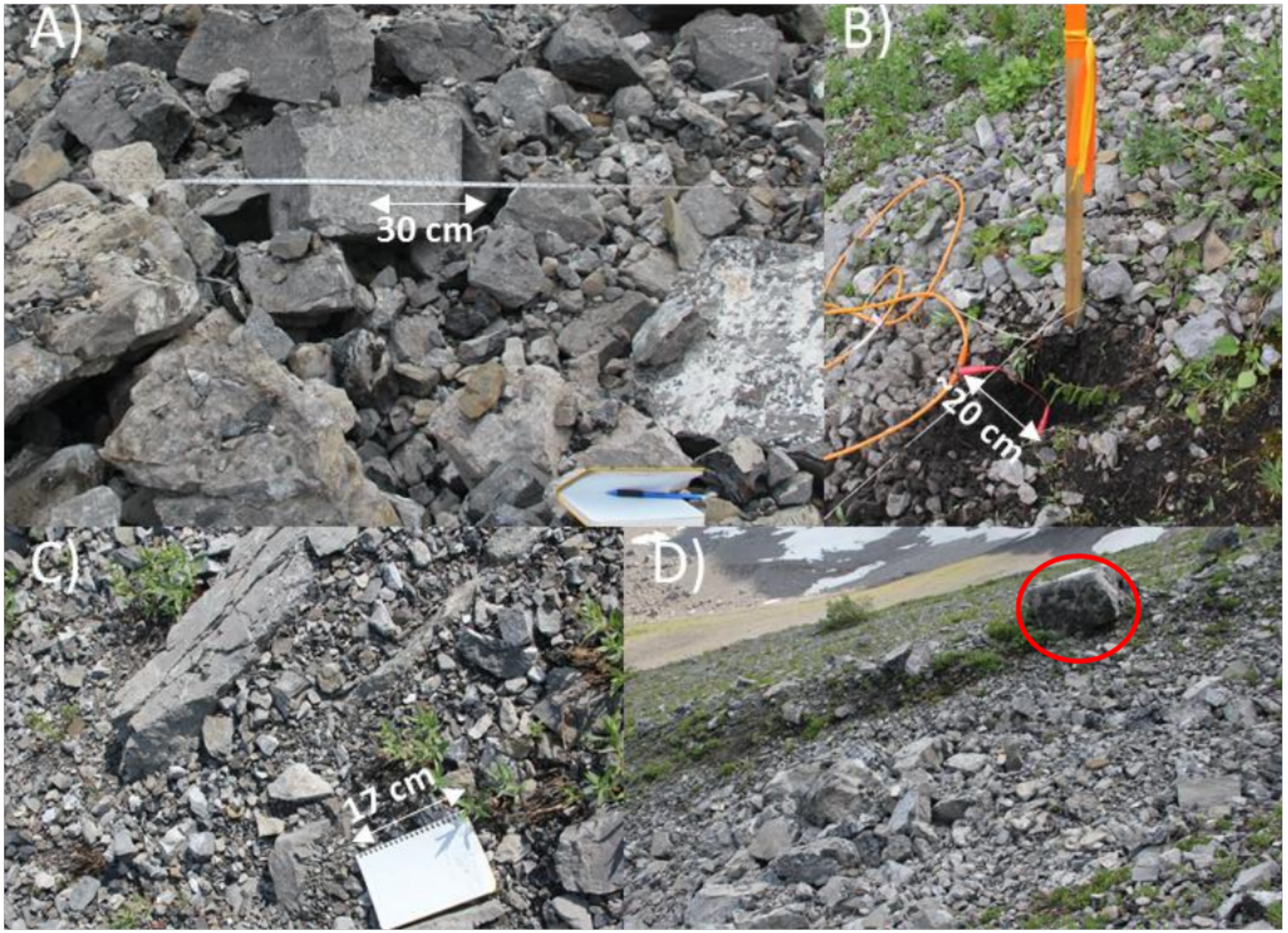

Figure 4-8: A sample of photos highlighting the differences in grain sizes and packing on the talus cones within the study area: A) large, loosely packed boulders with little infill on the eastern side of the Central Cone, located at approximately 375 m on ERT3; B) small cobbles and coarse gravel filled in with soil at the start of ERT2 on the West Cone; C) tightly packed grains of many sizes near the apex of the Central Cone; D) on the west half of the Central Cone near the apex, there is a linear depression that has minimal fine-grained sediments (in the foreground) and is less densely packed and less vegetated than the surrounding deposits outside the channel (seen in the background). The boulder circled in red at the edge of the channel is the same as that circled in Figure 4-6B. Photos are dated July 22, 2015 (A), July 20, 2015 (B), and July 8, 2015 (C and D).

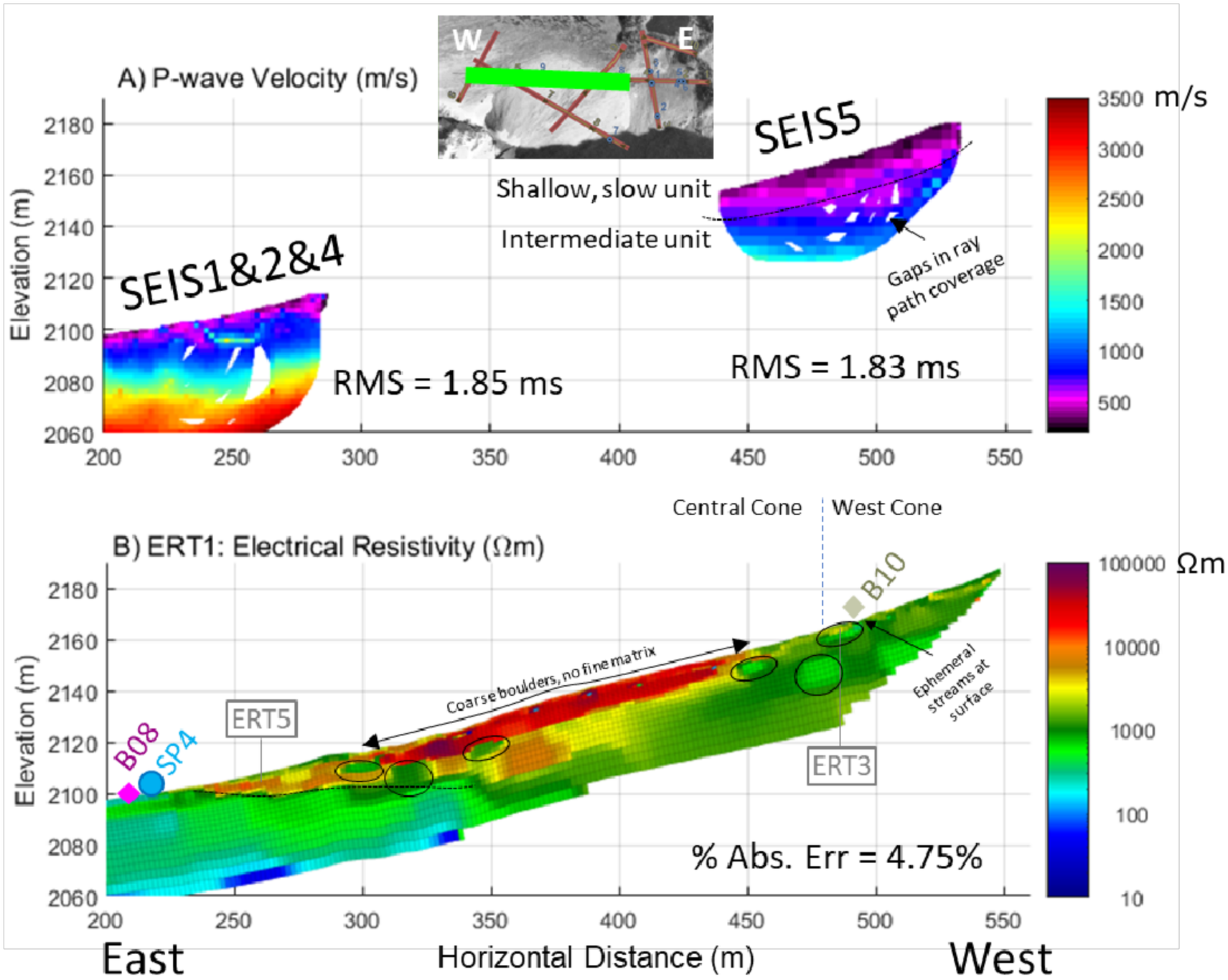

Figure 4-9: Composite of the P-wave velocity and resistivity models along ERT1. Annotations indicate the locations of: BTS sensors (diamonds), springs (blue circle), tie points with other lines (grey boxes), and convergent flow paths (black ellipses). Only the second half of ERT1's and SEIS1-2-4's full lengths (shown here) intersect the talus. See Figure 3-1 for the location of the survey line.

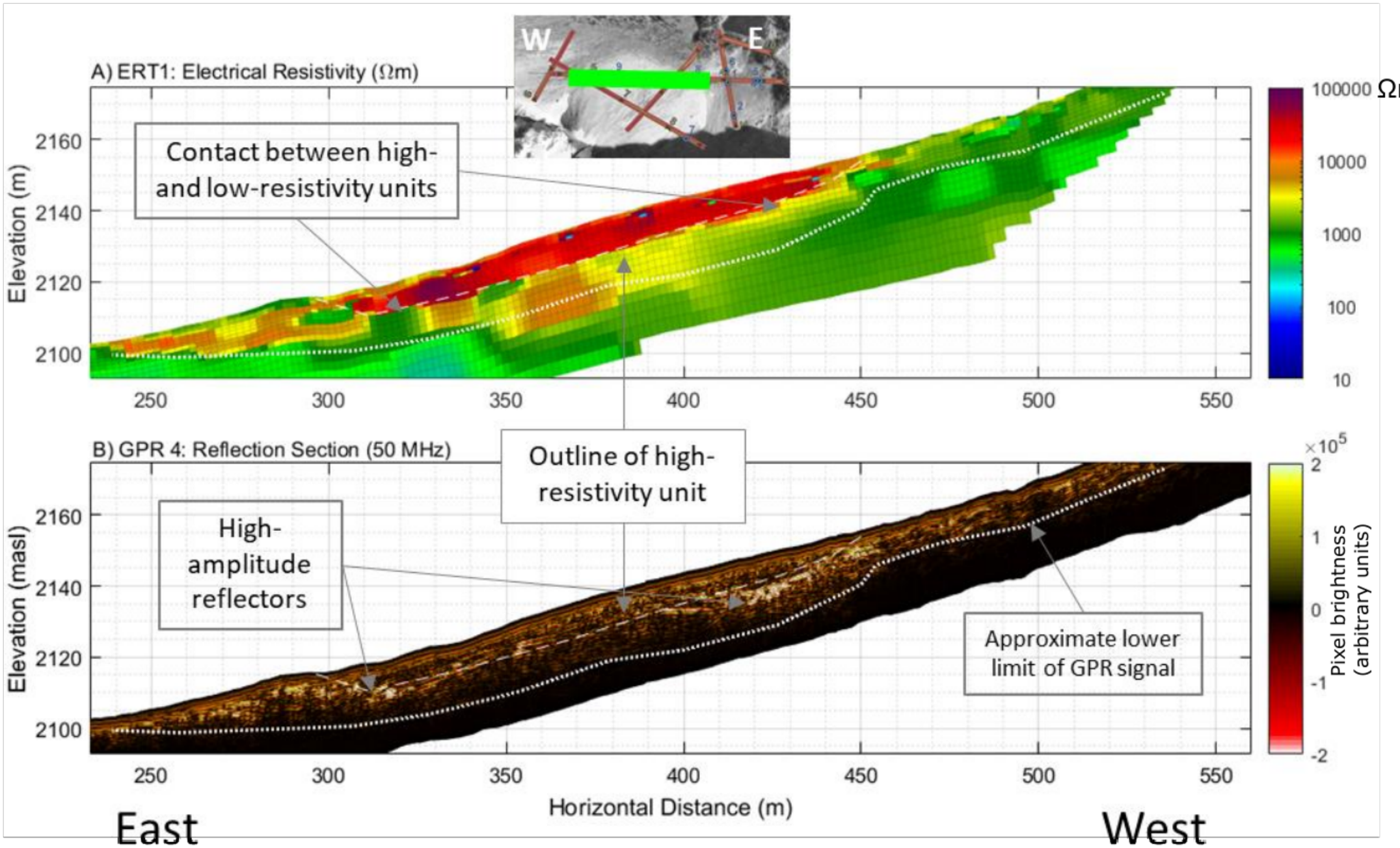

Figure 4-10: Co-located GPR reflection and electrical resistivity images with corresponding features emphasized. These include: very high-amplitude GPR reflectors at locations of strong resistivity contrast, and reduced radar wave penetration where sediments at surface have lower resistivity. See Figure 3-1 for the location of the survey line. See Section 3.2.3 for notes on the GPR color scale.

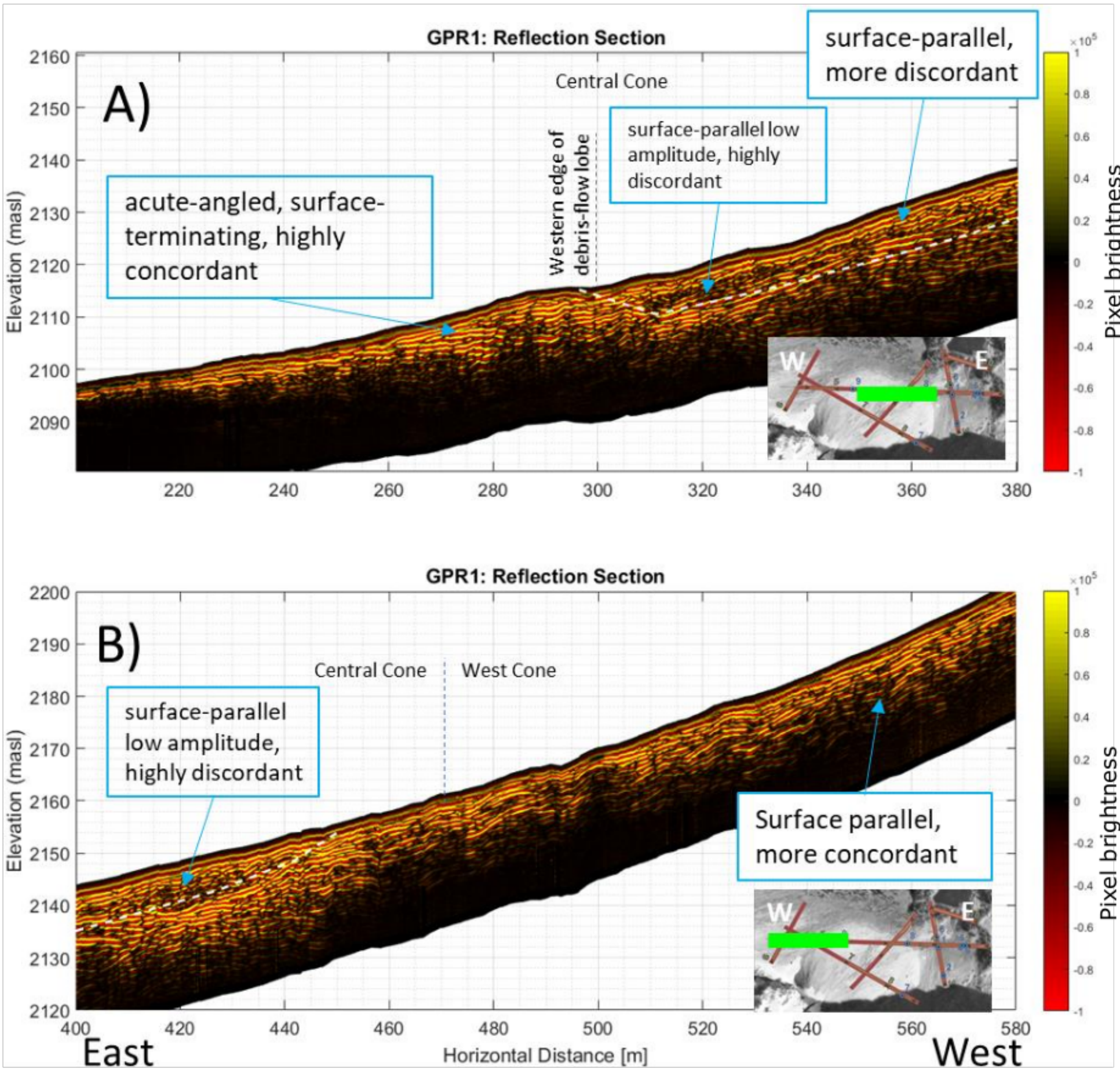

Figure 4-11: A sample of GPR data showing the differences in texture near the base of the Central Cone (A) and between the west and Central Cone (B). See Figure 3-1 for the location of the survey line and Section 3.2.3 for notes on the GPR color scale.

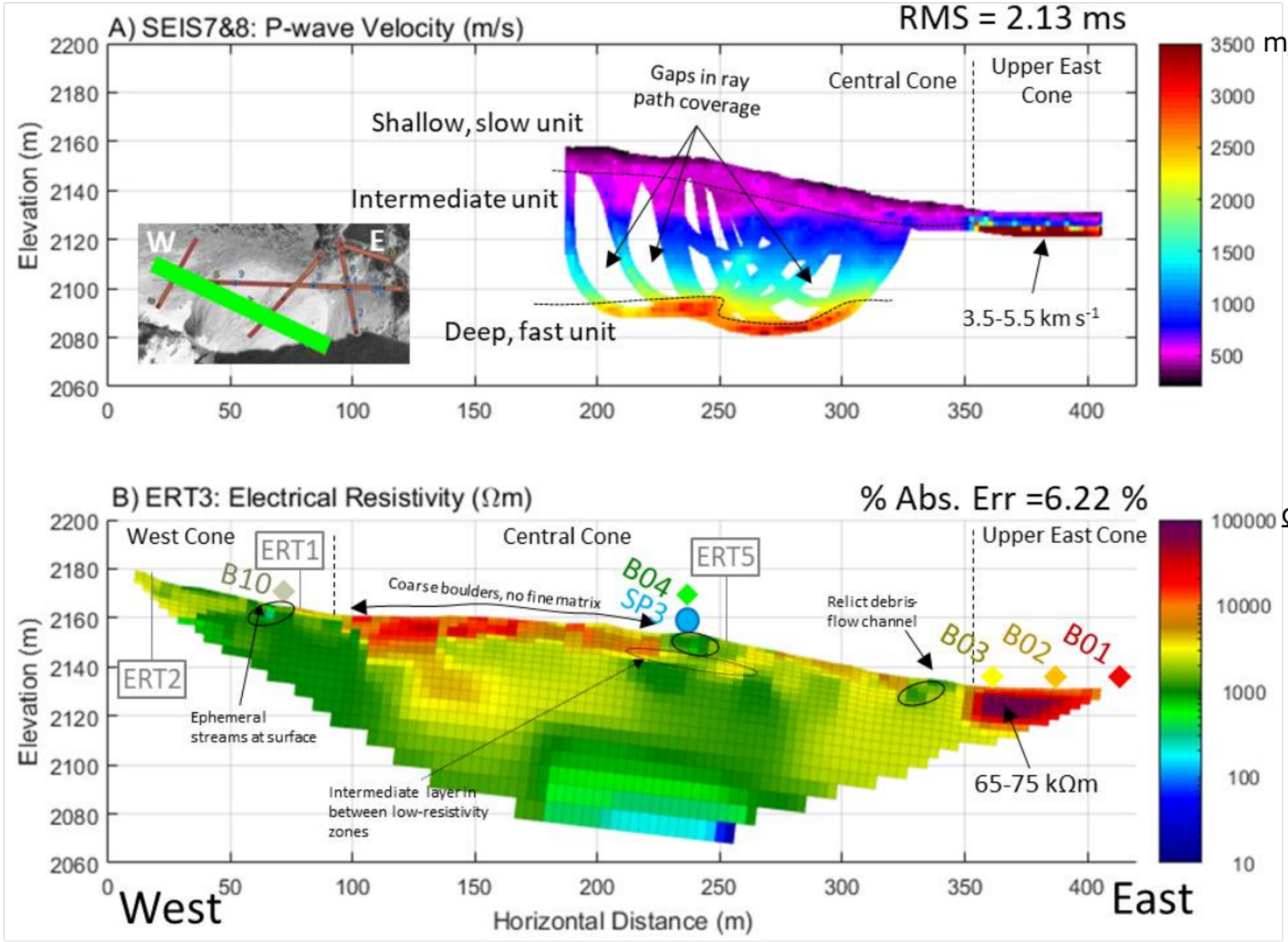

Figure 4-12: P-wave velocity and resistivity models for SEIS7-8 and ERT3. Annotations indicate the locations of: BTS sensors (diamonds), springs (blue circle), tie points with other lines (grey boxes), convergent flow paths (black ellipses, solid line). See Figure 3-1 for the location of the survey line.

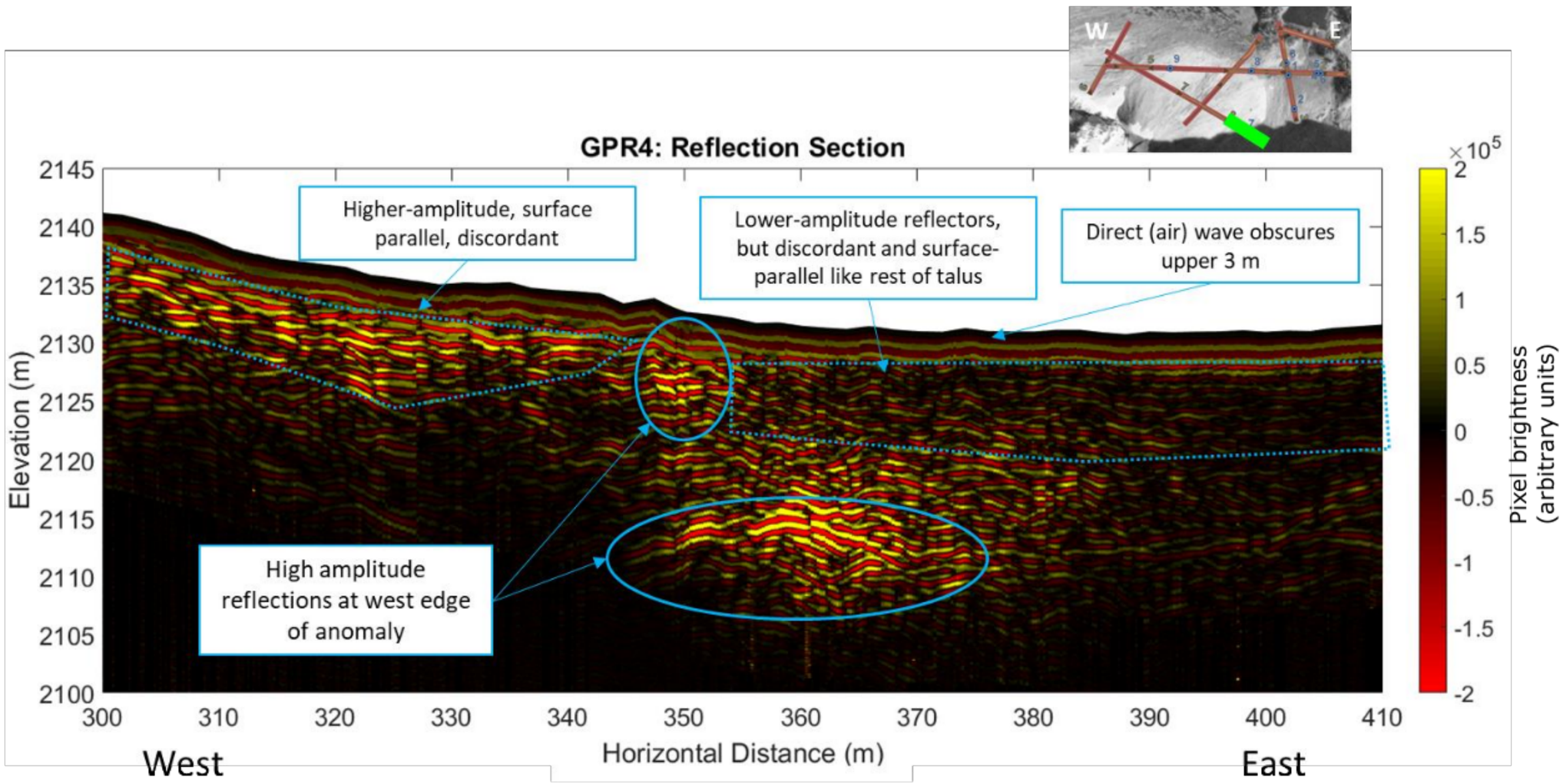

Figure 4-13: Reflection images from GPR4 corresponding to the anomaly at the end of ERT3 and SEIS7-8 (Figure 4-12). Annotations emphasize: high-amplitude reflectors between 350-360 m, a zone of lower amplitude reflectors within the anomaly, and the direct air wave that obscures real geologic structures in the upper few metres of the ground. See Figure 3-1 for the location of the survey line, and Section 3.2.3 for notes on the GPR color scale.

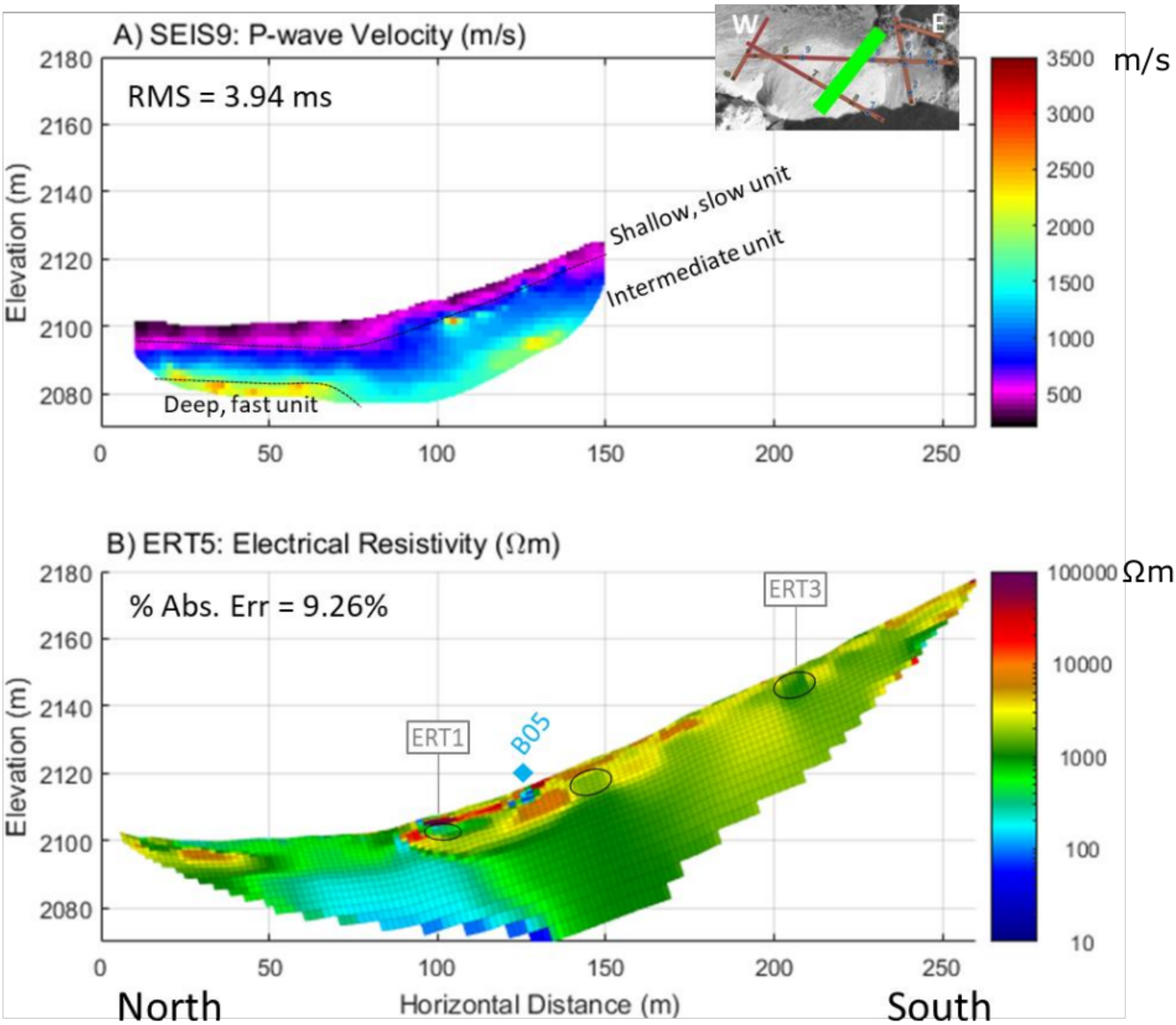

Figure 4-14: Composite of the P-wave velocity and resistivity models along ERT5. Annotations indicate the locations of: BTS sensors (diamonds), tie points with other lines (grey boxes), and convergent flow paths (black ellipses). See Figure 3-1 for the location of the survey line.

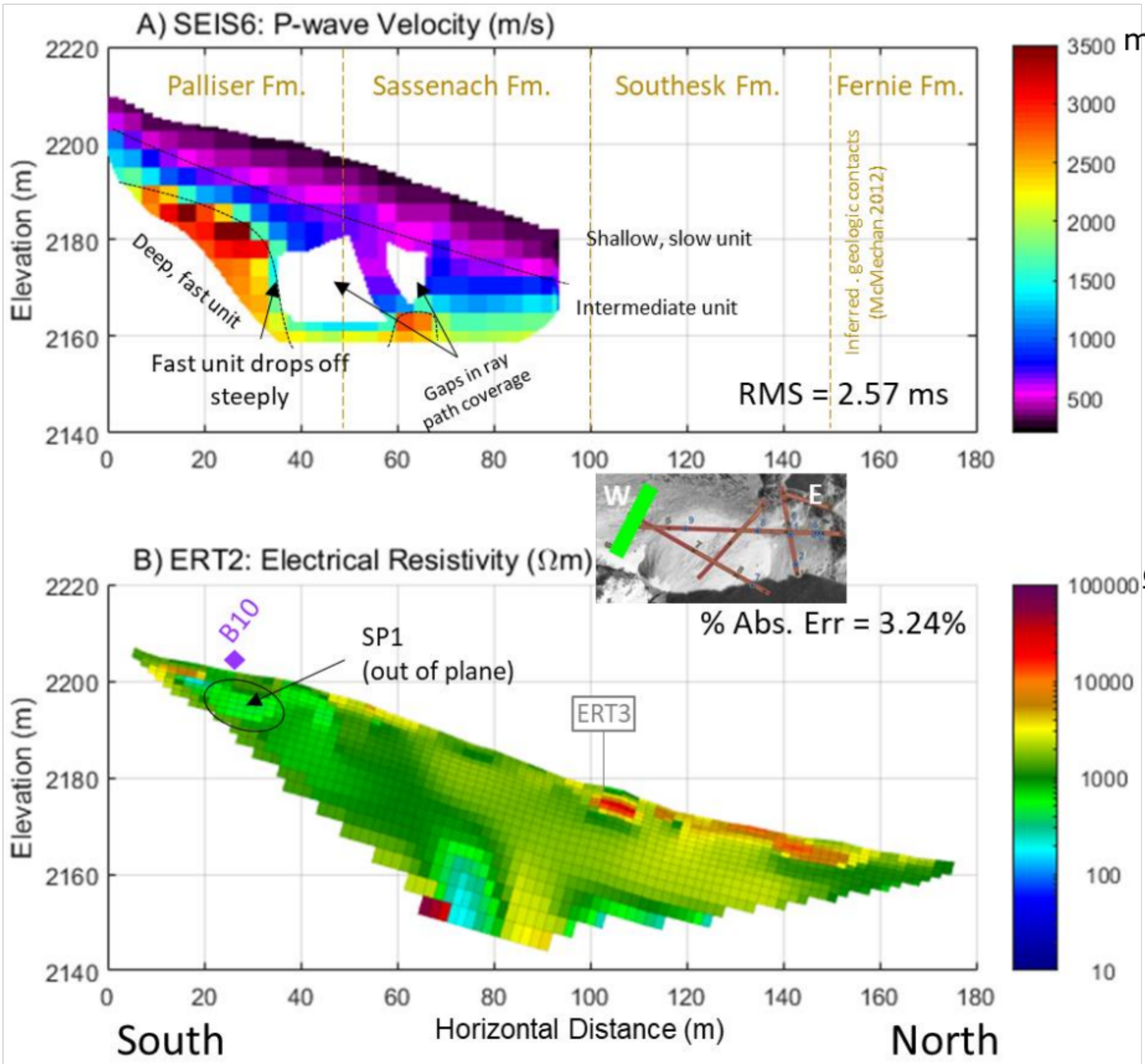

Figure 4-15: Composite of the P-wave velocity and resistivity models along ERT2. Annotations indicate the locations of: BTS sensors (diamonds), tie points with other lines (grey boxes), convergent flow paths (black ellipses), and the inferred locations of geological contacts from McMechan (2012) (dashed tan lines). See Figure 3-1 for the location of the survey line.

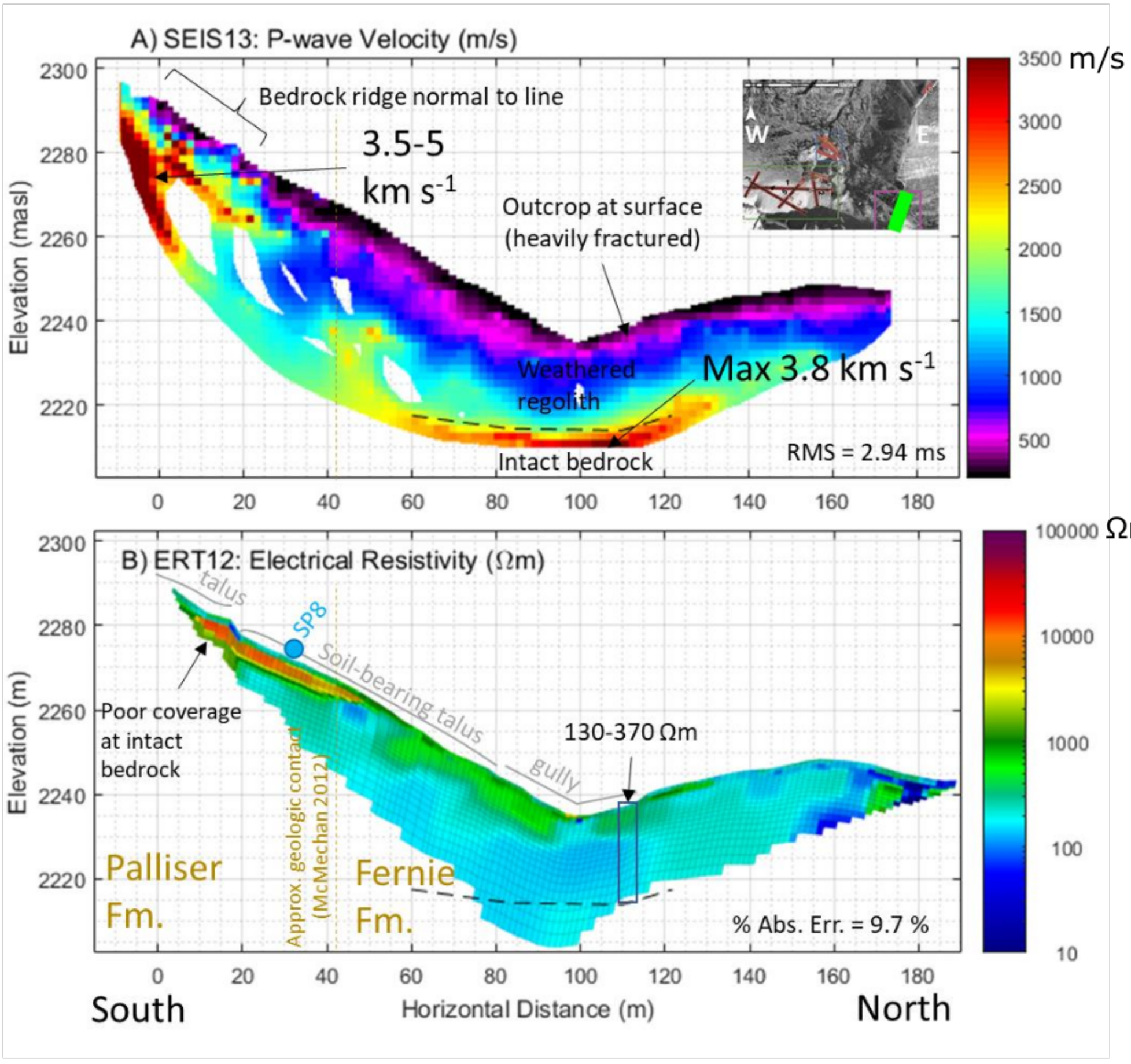

Figure 4-16: Composite of the P-wave velocity and resistivity models along ERT12 and SEIS13. Annotations include: descriptions of surface cover (grey lines), estimated location of the thrust fault from McMechan 2012 (dashed tan line), a spring (blue circle), and the estimated location of intact Fernie Formation (dashed black line). See Figure 3-1 for the location of the survey line.

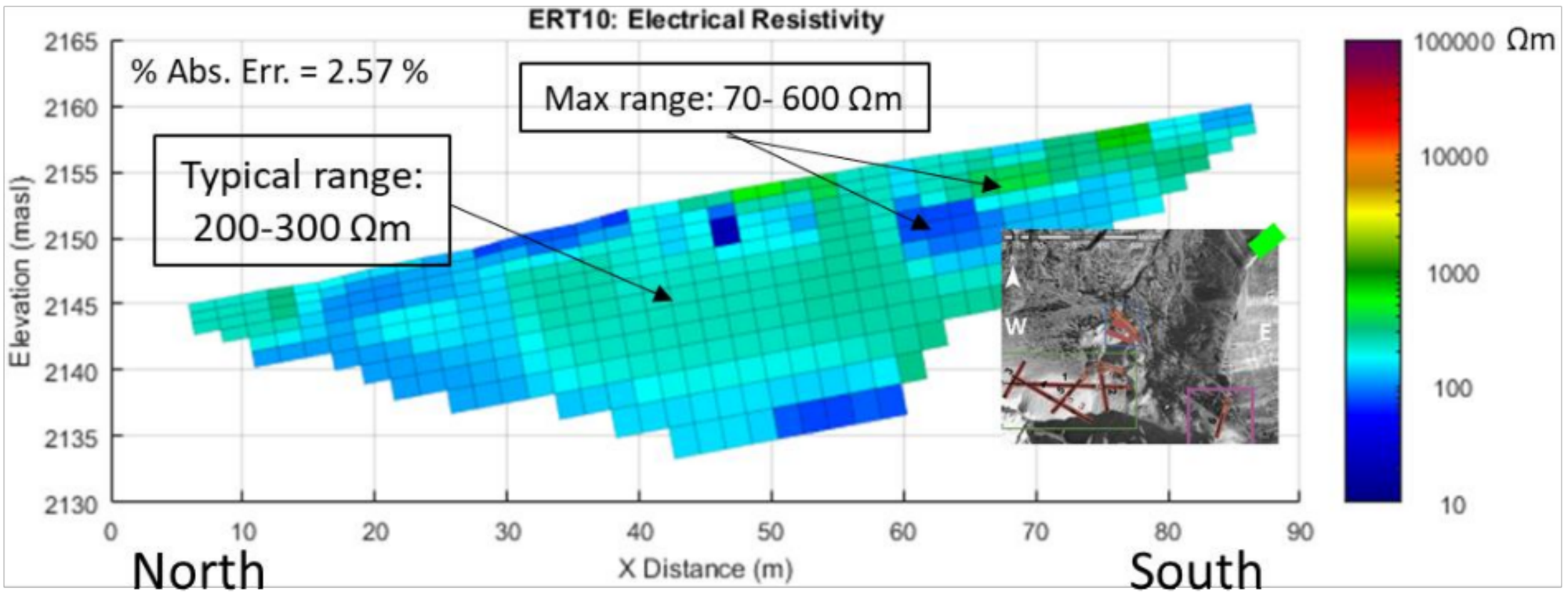

Figure 4-17: Resistivity image from ERT10, with annotations pointing to typical and anomalous resistivity values within the Fernie Formation. See Figure 3-1 for the location of the survey line.

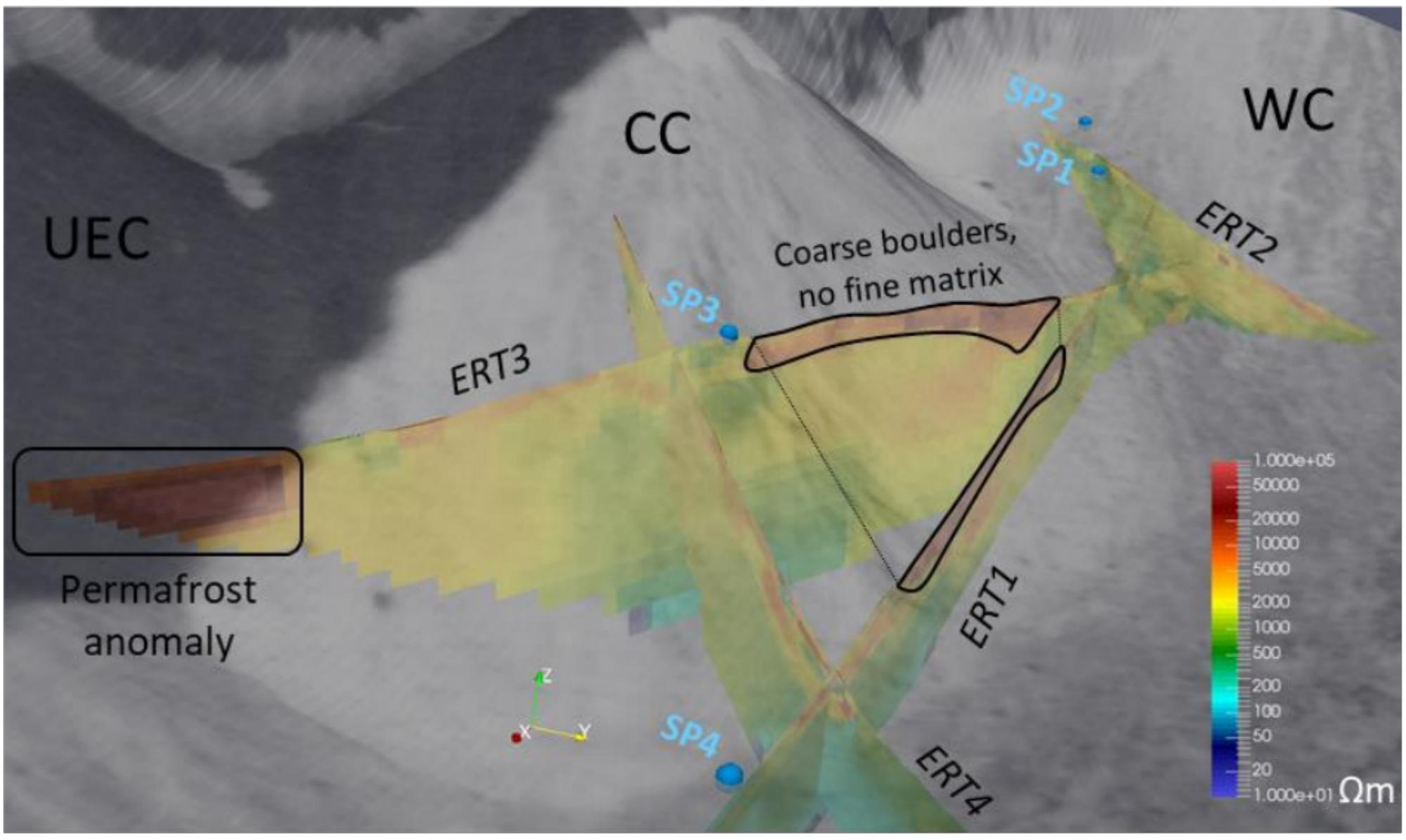

Figure 4-18: Fence diagram of resistivity images with superimposed surface imagery. Resistivity scale has units of Ωm. Locations of springs are indicated with blue spheres. Cones are labelled UEC (Upper East Cone), CC (Central Cone), and WC (West Cone). Note the anomalously high resistivities in the sections of the Upper East Cone that are more well-shaded than the headwall.

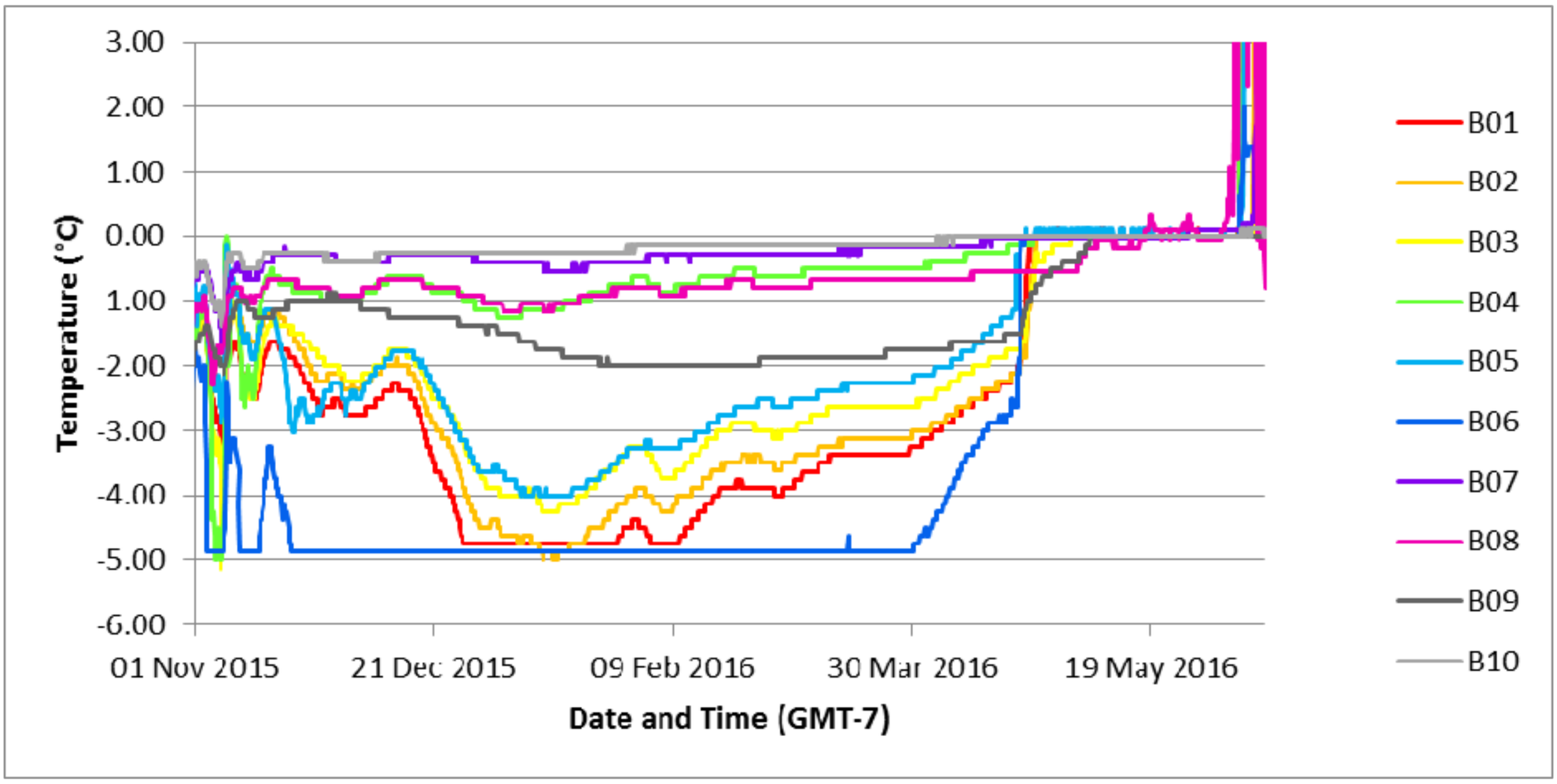

Figure 4-19: Temperature data recorded by BTS sensors and corrected using spring melt zero curtain. Note that the sensors have a lower detection limit of -5.0 °C. Sensor locations are shown in Figure 3-4.

Chapter 5 **Hydrogeology of Low-Lying Features**

The scope of this chapter is to present findings in locations downstream of the talus slopes, herein referred to as the "low-lying features". More specifically, the chapter discusses the role of unconsolidated sediments (moraine and meadow sediments), important hydrological features (lake, steams, springs), and bedrock. Subsections herein include: a literature review of hydrogeology of these features in alpine headwaters (5.1), a detailed site description (5.2), geophysical images and other data (5.3), an interpretation of results and a comparison to past studies (5.4), and a summary of key findings (5.5).

5.1 Literature Review: Hydrogeology of Low-Relief Alpine Deposits

While outcropping bedrock is often the most extensive geologic unit in alpine headwaters, low-lying, unconsolidated material is nevertheless an important flow path in such basins and, in some cases, may be the more important storage unit (Roy and Hayashi 2007). In some cases, groundwater flow in low-relief areas of a basin may account for the largest water fluxes in a system, even where there is substantial flow in surface streams (e.g. Gordon et al. 2015). For this reason, they are important targets of study for understanding the full picture of a watershed's hydrology.

Both the hydraulic conductivity and spatial arrangement of sedimentary units are an important control on flow paths and storage. For one, heterogeneity in sedimentary units may contribute to rapid, channelized flow in the subsurface (Roy and Hayashi 2009; McClymont et al. 2011). Moreover, the connectivity of high-permeability units is important. For example, in studies from the Cordillera Blanca of Peru, Baraer et al. (2015) and Gordon et al. (2015) compared two different catchments: Llanganuco and Quilcayhuanca. Both sites have large talus deposits bordering the valleys and glaciolacustrine sediments underlying meadows in low-lying areas. The talus deposits at Quilcayhuanca differ in that they connect to deep, rockfall deposits below the meadows (Gordon et al. 2015). Consequently, groundwater fluxes do not play as large of a role at Llanganuco because they are in contact only with sediments having low hydraulic conductivities (Baraer et al. 2015). Finally, while low-conductivity sediments like alpine meadows may not contribute much to total fluxes in a basin (e.g. Fischer et al. 2015), they are important for storing water longer and buffering seasonal variations in freshwater supplies (Clow et al. 2003; Roy and Hayashi 2007; Weekes et al. 2015). Therefore, while the hydraulic

conductivity of sediment is an important control on flow paths and storage, the spatial variability and geometry of sedimentary units is likely as important.

Groundwater storage potential of low-relief areas of alpine headwaters may be linked to some common glacial landforms. Ubiquitous in glacierized mountain terrain, moraines are important in directing surface water flow (Barr and Lovell 2014). Similarly, overdeepenings (i.e. closed, sub-glacial basins), are widespread, and measure anywhere from hundreds to thousands of metres long and tens of metres deep (Cook and Swift 2012). These landforms help with the retention of both syn-glacial and post-glacial sediments at high elevations, leading to the formation of thick sedimentary packages that can, in some cases, be important sources of drinking water (e.g. Seiler 1990). This ability is partly related to the fact that moraines and overdeepenings lead to the formation of proglacial lakes, which are common and well-documented sediment traps (Carrivick and Tweed 2013). Hence, the presence of certain glacial landforms affects sediment fluxes in a watershed and in turn affects its groundwater storage potential.

While the overburden material in alpine headwaters may store most groundwater, bedrock still plays an important role in controlling flow paths. Multiple geophysical studies have demonstrated that bedrock is an important, impermeable layer in alpine hydrologic systems and that flow is often concentrated in a thin saturated layer above bedrock (Langston et al. 2011; Muir et al. 2011; Lehmann-Horn et al. 2011). Like heterogeneity in sedimentary units, channelized flow in the subsurface may too be the result of bedrock topography (Roy and Hayashi 2009; Muir et al. 2011; McClymont et al. 2011). These results agree with earlier observations that bedrock topography and depth to bedrock are some of the most important parameters determining shallow groundwater contributions to streamflow (Freer et al. 2002; Detty and McGuire 2010).

Beyond controlling flow paths, bedrock can also be an important store of water at the scale of headwater basins. One mechanism of storage is the “fill and spill” hypothesis, wherein water collects into closed depressions at the bedrock-sediment interface (Spence and Woo 2003; Tromp-van Meerveld and McDonnel 2006). Several researchers have explained the stability of water tables below meadows (McClymont et al. 2010; Gordon et al. 2015) and heterogeneous distributions of water storage in moraines (Langston et al. 2011; McClymont et al. 2012) using

this model. Beyond just topography, the degree of fracturing can affect storage and transmission of water in the subsurface. Onda et al. (2004) showed that weaker rock types (a shale versus a granite in their case) drain water in the overburden more quickly. In their statistical analysis of multiple headwater basins, Paznekas and Hayashi (2016) speculated that this mechanism in part explains why watersheds with younger rock, which generally have a higher porosity and greater storage potential, exhibited higher winter baseflows. Notwithstanding that trend, shallow bedrock fracture flow may be important even in competent, metamorphic rocks like the Cambrian quartzite of the Gog Group in the Main Ranges of the Canadian Rocky Mountains (McClymont et al. 2011). In response, Paznekas (2016) proposed a modified "fill, spill, and drain" model, wherein bedrock depressions are connected via fractures, to explain high baseflows that could not be numerically modelled with a "fill-and-spill" model alone. Hence, bedrock properties (specifically topography and fracturing) play an important role in storing and delaying the release of groundwater.

This portion of the thesis addresses the following knowledge gaps. First, it aims to image hydrogeological processes that have not previously been documented with geophysics, specifically the influence of heterogeneity and connectivity of sedimentary units and the possibility of convergent flow paths. Next, it aims to characterize the role of bedrock topography on flow paths, adding to the limited number of cases studies where geophysics was used to do so. Furthermore, while many studies have characterized the role of different landscape units in basin hydrology and measured the dimensions of post-glacial overdeepenings, this new case study adds detailed spatial information that will enhance current understanding of these topics.

5.2 Detailed Site Description

This section provides a detailed description of the surficial geology and hydrology of low-lying features in the Bonsai Lake basin. Figure 5-1 shows the extent and locations of these features.

5.2.1 Meadow

A small, grassy meadow of approximately 5000 m^2 is present at study site (Figure 5-1 and Figure 5-2). Bordered by moraines to the north and east and by talus to the south and west, this mostly flat expanse has an elevation range between 2094 and 2096 masl, sloping gently up with a concave curvature as it transitions gradually into the adjacent talus deposits. This smoothly varying topography is interrupted by current-day streams along the north margin that incise up to

1 m down below the surrounding meadow plain. At the north end of the meadow, where the two main branches of the stream meet, there are small, river terraces indicating past fluctuations in their flow volume.

There are some notable variations of grain size distribution within the meadow, as observed in hand-augured samples extracted while installing piezometers. (Locations of piezometers are shown in Figure 3-5). Deposits at the centre of the meadow are composed primarily of silt- and clay-sized sediments in the upper 3.5 m. Sediments near surface are moist but still plastic (*sensu* Seed 1964) and not fully saturated. Between 2 and 3 m depth, they surpass their liquid limit and are nearly or fully saturated. There is also a decreasing trend in intact plant material with depth. In contrast, hand auguring is difficult at the west and south margins of the meadow because of the high gravel fraction. In fact, gravelly debris flows originating from the talus cone is visible at surface, deposited atop the meadow (Figure 4-5). Lastly, some scattered boulders are present in the west end of the meadow.

5.2.2 Moraines

This site has extensive deposits of moraines with complex geometry. Their shapes are best visualized in the DEM (Figure 5-3). Most moraines at this site are located around Bonsai Lake, where there are several sets of concentric ridges with many different orientations. The exposed height of these varies dramatically, with the tallest and widest moraine located at the north side of Bonsai Lake. The moraines are often intersected by small, linear depressions (highlighted in yellow in Figure 5-3). The linear depression on the south side of Bonsai Lake corresponds to a current-day stream, suggesting that such depressions are likely caused by fluvial erosion following moraine-dam breeches, a common phenomenon in glacierized terrain (Carrivick and Tweed 2013). Thus, it is believed that many of these inter-moraine depressions previously held standing water.

The grain size characteristics of the moraines highlight possible genetic differences between them. Figure 5-4 highlights the differences between (a) moraines with (comparatively) well-sorted, subangular fragments (b) talus material with poorly-sorted, angular fragments, and (c) moraines with poorly-sorted, subangular fragments. Moraines with more uniform grain size distributions and more rounded cobbles and boulders have been interpreted as push moraines, while those with poorly-sorted, angular grains have been categorized as recessional moraines

(Knight 2004). This site hence contrasts strongly with those studied in the area by Smith et al. (1995), where recessional moraines were rather rare (Section 2.2). While the moraines may be covered by vegetation in some places, the soil cover in these areas is no more than 2 m thick.

5.2.3 Hydrology

This subsection describes surface water features visible in the low-lying areas of the Bonsai Lake Basin. Figure 5-1 shows the locations of all the important low-lying hydrologic features, and Figure 5-5 shows a cross-section highlighting the elevation of some features. Temperature readings from these are also included in Figure 5-6.

Starting upstream, there is a small stream network draining the surrounding hillslopes into the meadow. These are herein referred to as the "East Meadow Stream (EMS)" and the "West Meadow Stream (WMS)." The two main stream branches are fed by springs emerging from talus deposits (SP4 and SP5) at the west and southeast ends of the meadow, respectively. These springs emerge over a wide area about 10 m wide where flow between coarse ground cover is audible (but not visible) below surface. Over a few tens of metres, these converge into a few small channels and then concentrate into a single, main channel for the rest of its reach above the fine-grained sediments of the meadow. Flowing along the northerly margins of the meadow near the boundary with the moraines, the two branches of the meadow streams meet at a confluence in the north-central section of the meadow before flowing down into Bonsai Lake (Figure 5-1). While the WMS flows throughout summer and fall, the EMS often dries up by mid-summer.

Bonsai Lake is a seasonal lake. While water levels can be as high as 2091 masl during spring melt, the lake is dry by late summer, dropping to its minimum elevation of 2086 masl (Figure 5-7A). When lake levels are low, groundwater discharge (GWD) points all along the south shore of the lake become visible (Figure 5-7C). These are all at an elevation of 2090 masl, and discharge water that is between 2 to 5 °C throughout the summer, even when the rest of the lake water is as much as 10°C warmer (Figure 5-6). Moreover, when the lake level is at its minimum, important features of the lakebed are revealed. An alluvial fan formed of fine-grained sediment progrades onto the lakebed where the inlet stream from the meadow enters the lake. While most of the lakebed is covered in a layer of fine-grained sediment, its thickness is not uniform. In most areas, this bed, which separates the lake water from the coarse morainic material below, is only a few centimetres or decimetres thick.

Even at its minimum, however, Bonsai Lake is never completely dry. A small amount of water from the inlet stream and GWD supply water to a channel carved into the fine lakebed sediments. This channel roughly follows the south margin of the lake going west, then north following the west lakeshore, before pooling in a small depression at the north end of the lake. Along its course, water in this channel is lost to sink features on the west and northern parts of the lakebed, indicated by the red circles in Figure 5-1. These are locations where there are holes through the lakebed mud and where moraine cobbles (and occasionally, large void spaces) are exposed (Figure 5-7B). In some cases, water is cascading down below lakebed sediments without ponding, while in others, there is consistent flow entering yet no change in water level within these small depressions.

The outlet spring at the north end of the study area drains this basin (Figure 5-8). Located at 2082 masl in an area of loose cobbles and boulders where two moraines intersect (Figure 5-3), it is a diffuse-source spring (like SP4 and SP5) where flow is audible upstream of where it is first visible. The points labelled SP6 and SP7 in Figure 5-1 and Figure 5-8 are simply the westernmost and easternmost points where the springs discharge to surface. The spring complex has a discharge that far exceeds the other visible surface flows seen upstream, and unlike most springs upstream, this one flows perennially. Water level data and a rating curve for the northern outlet spring have been shared with the author by collaborators at the University of Saskatchewan (J. Pomeroy, H. Wu, C. Westbrook). Calculated discharge values for 2015 and 2016 are given in Figure 5-9. The author's own measurements from July 2015 indicate that discharge in the creek 20 m downstream from the springs is not detectably different from discharge 100 m further downstream (Table 5-2). This suggests that the spring is the dominant contributor to streamflow. Moreover, it is a cold-water spring. While not continuously monitored, with temperatures at the spring ranged between 1.2 and 3.0 °C from June to October 2015, a range that is smaller than other surface water features on site (Figure 5-6). Lastly, the electrical resistivity of the spring water is generally lower than those measured in Bonsai Lake (Table 5-1), suggesting that the water is sourced from a deeper, distinct flow system.

5.3 Results

The results in this section are discussed in two parts, starting with surveys performed in the meadow, and continuing with those from the moraines surrounding Bonsai Lake. Within each of

these halves, results are organized according to method used (i.e. ERT, GPR, SRT, or Piezometric Data). Locations of geophysical lines are shown in Figure 5-10.

5.3.1 Meadow

Geophysical data were collected along two different orientations around the meadow: either crossing east-west (ERT1, SEIS1-2-4, GPR1) or north-south (ERT4, SEIS3, GPR2). ERT and SRT images are shown in Figure 5-11 and Figure 5-12, while GPR data are shown in Figure 5-13.

5.3.1.1 ERT

There are considerable lateral and vertical variations of resistivity in the immediate subsurface of the meadow. The uppermost unit of sediments varies between 4 m thick at the east end (Figure 5-11B, 30m) and 11 m thick near the centre of the meadow (Figure 5-11B, 80m). Most of these sediments have a resistivity between 30 and 80 Ωm. However, there is a thin crust at surface with higher resistivities (100-200 Ωm) that is more clearly visible in Figure 5-11C. This layer is between 2 m and 3 m thick, and extends from the EMS to the west margin of the meadow (Figure 5-11C, 45 m to 230 m).

The sediments surrounding the meadow also see some lateral and vertical heterogeneity in resistivity. In the talus cone immediately west of the meadow (the Central Cone), there is a transition at 2100 masl where resistivities transitions from over 5000 Ωm to below 2000 Ωm. This boundary is shown in Figure 5-11B to the west of 230 m, and it corresponds to where SP4 daylights (Figure 5-11D). Similarly, the moraine bordering the meadow on the northwest side has resistivities between 500 and 1500 Ωm closest to the meadow (Figure 5-12B, 120-150 m), but sees values as high as 20,000 to 30,000 Ωm going north towards the lake along ERT4 (Figure 5-12B, 170-220 m).

The deeper parts of the resistivity images suggest that there are two main layers below the meadow sediments. Resistivities immediately below the meadow are similar to that of the talus and moraines seen at surface (greater than 500 Ωm). This is the layer labelled “Deep Layer 1 (DL1)” in Figure 5-11B. Below this is a layer of lower resistivities (<200 Ωm) with an upper boundary of 2070-2080 masl (Figure 5-11B, “DL2”). However, there is a poor match of the elevation of these boundaries when comparing the tie point of ERT1 and ERT4 (Figure 5-14). The upper boundary of DL1 is 2089 masl in ERT4 but 2084 masl in ERT 1. Similarly, the upper boundary of DL2 is 2075 masl in ERT4 but 2084 masl in ERT1.

5.3.1.2 SRT

The P-wave velocity models show lateral variations in the upper few metres of sediment similar to those observed in the resistivity images. Velocities in the meadow are usually less than 300 m/s (e.g. Figure 5-11A, 50-150m). Stream crossings in the meadow are the exception where velocities are closer to 500-600 m/s (e.g. Figure 5-11A, 38 m). This latter range is close to the shallow velocities (500-600 m/s) observed in the talus and moraines (e.g. Figure 5-11A, 230-300 m). There is a notable, shallow anomaly of 1500-2000 m/s at the toe of the talus present in both SEIS1-2-4 (Figure 5-11A, 250 m) and SEIS9 (Figure 4-14, 100 m and 2100 masl). These correspond closely to the resistivity boundary that corresponds to SP4 in Figure 5-11B.

There are also notable changes in P-wave velocity with depth visible in both Figure 5-11A and Figure 5-12A. Values of 500 m/s (as indicated with a white dot-dash line in both figures) are at a similar depth everywhere, roughly following surface topography. In contrast, values in the range of 800-1500 m/s (marked with blue dot-dash line) are at a similar elevation throughout the study area, at 2085 to 2090 masl. A deep zone of very high velocities (>3000 m/s) is present throughout, and has an upper elevation boundary anywhere between 2060 and 2070 masl below the meadow. The transition to the 3000 m/s zone is not sharp, but is instead a rather gradual zone that is up to 10 m thick.

5.3.1.3 GPR

There are some issues with radar signal attenuation, but GPR reflection images in Figure 5-13 reveal some important structures and textural variations. For one, the data can be used to distinguish between moraine and talus deposits. Whereas the talus deposits have largely continuous, surface-parallel reflectors of intermediate amplitude, material under moraines has many arched, discordant, chaotic reflectors with high amplitude. This helps remove some of the ambiguity where moraine and talus deposits are largely indistinguishable with ERT and SRT alone. Within most of the meadow, there is no signal below areas with resistivities less than 100 Ωm. However, at the west end of the meadow and below the adjacent talus slope, where resistivities are not as low (Figure 5-11B and Figure 5-13A, 100-140 m and 175-210 m), flat and continuous reflectors are detected. These flat, continuous reflectors are marked with white arrows in Figure 5-13A and Figure 5-13B. Considering the error in depth due to uncertainties in the EM velocity model in Figure 3-3 (approximately 10% or +/- 1 m depth), this reflector corresponds roughly to the top of DL1 in the resistivity images (e.g. Figure 5-11B).

5.3.1.4 Piezometric Data

Most of the piezometers installed were not installed deep enough to intersect the water table, but Figure 5-15 shows viable data that were collected in the Bonsai Lake stilling well and at three locations in the meadow: HWW, P05, and P01. (Note that the only the locations of these four sensors and the barometer are shown in Figure 5-10; all other locations are shown in Figure 3-5). There are long periods where the screens in some piezometers do not intersect the water table. Nonetheless, the data demonstrate that the head levels in the West Meadow Stream are consistently between 2093.5 and 2094 masl. Yet, 11 m to the south, head levels in P01 and P05 rarely exceed the elevation at which the piezometers are screened and at which the sensors installed (2088.59 masl in P01 and 2091.17 masl in P05). Though P01 is 9 m east of P05, they are equally close to the West Meadow Stream, and their screened intervals span the same type of material: fine-grained meadow sediments. These observations suggest that the West Meadow Stream is in a losing reach and that there is a downward, vertical hydraulic gradient in its vicinity.

5.3.2 Moraine and Outlet Springs

Geophysical data were collected along five lines on the moraines and near the northern outlet spring (Figure 5-10). Going in order from south to north, these include a line on the south side of Bonsai Lake (Figure 5-16), one on the north side of Bonsai Lake (Figure 5-17), two parallel, NW-SE oriented lines along the northernmost moraine near the outlet spring (Figure 5-18 and Figure 5-19), and an intersecting line also near the outlet spring (Figure 5-20). (An additional 3D ERT survey was conducted, but is only included in Appendix D due to the limited hydrogeological information provided by the low-resolution, resultant model.)

5.3.2.1 SRT

Like in the meadow area, the P-wave velocity images show that in the upper few metres of the ground, the velocity gradient is very similar throughout the study area. (Only three of the five survey lines have seismic data. These are shown in Figure 5-16A, Figure 5-19A, and Figure 5-20A.) In most places, velocities range between 300 and 500 m/s, reaching the higher end of this range within the upper 5 m of the subsurface. A notable exception is at the northern outlet spring along SEIS11 (Figure 5-19A, 45-60 m), where velocities at surface are around 800-1200 m/s. On the same line, there is also an unusually thick slow zone where velocities of over 500 m/s are not reached until a depth of 8 to 10 m (Figure 5-19A, 60-90 m).

There are two important velocity boundaries at depth. First, the transition to velocities above 800 or 900 m/s corresponds to the elevation of nearby water features. These include GWD at 2090 masl along SEIS10 (Figure 5-16A), the outlet springs at 2082 masl along both SEIS11 (Figure 5-19A, 45-60 m) and SEIS12 (Figure 5-20A, 45-60 m), and the lake level of 2086-2088 masl near the east end of SEIS11 (Figure 5-19A, 140-180 m). The other important boundary is the transition to velocities above 3000 m/s, marked with a solid black line in in Figure 5-16A, Figure 5-19A, and Figure 5-20A. It differs from that observed under the meadow in a few key ways. First, it occurs at higher elevations, varying between 2078 and 2082 masl in all the images. Second, there are anomalous, localized lows. SEIS11 indicates that it reached down to 2070 masl under the outlet spring and adjacent moraines (Figure 5-19A, 45-100 m). Moreover, unlike the gradual boundary seen under the meadow, this transition is a sharp one.

5.3.2.2 ERT

The resistivity images of moraine deposits show highly heterogenous, high-resistivity deposits lying atop more uniformly low-resistivity material. Values as high as 66,000 Ωm can be seen in the upper 10 m of the moraine (e.g. Figure 5-17, 35 m), with some patchy zones of low-resistivity material (600-3000 Ωm) occurring in the upper 3 m (e.g. Figure 5-17, 50-80 m). The transition to material below 2000 Ωm corresponds roughly to the 800-1500 m/s boundary in the seismic velocity models (e.g., see the dashed line from 10-30 m in ERT 8, Figure 5-20). However, unlike in the seismic velocity models, this resistivity transition is not flat. Where this transition occurs immediately below very high resistivity material (>20,000 Ωm), the boundary deflects downward. This occurs, for example, between 60 and 80 m along ERT9 (Figure 5-17). Resistivity transitions do not normally occur at elevations corresponding to the 3000 m/s velocity boundary, with the exception of ERT6 (Figure 5-16B). Resistivity values in the deepest part of these images at the edge of the model are poorly constrained by the data, and the P-wave velocity models are used instead, where available, to interpret deeper structures.

At the toe of the northern moraine, near the outlet spring, there are several anomalies with resistivities under 100 Ωm. These are marked in Figure 5-18, Figure 5-19B, and Figure 5-20B using the naming system of "Line Number – Anomaly Number." Most of these have elevations between 2085 and 2082 masl, with a decreasing trend approaching SP6 and SP7. On ERT7 (Figure 5-19B), many correspond to the depressions in the high-velocity layer (Figure 5-19A).

5.4 Discussion

5.4.1 Geophysics Interpretations

Figure 5-21 shows an integrated conceptual model of the subsurface geology and hydrology of the system. The following subsections discuss first the geologic interpretations, and then the hydrologic interpretations of the system.

5.4.1.1 Geological Conceptual Model

5.4.1.1.1 Meadow

Table 5-3 summarizes the properties and interpretations of the petrophysical units observed in and near the meadow. The boundaries between these petrophysical units are also annotated alongside geophysical images in Figure 5-11D and Figure 5-12D. The talus sediments are prograding onto meadow sediments, which is consistent with the observed debris flow deposits at surface that are encroaching upon the meadow (Figure 4-5). Similarly, unconsolidated materials extend tens of metres down, and their accumulation has been enhanced by the presence of a moraine dam on their north side. This is consistent to how fine-grained sediments have been accumulating in Bonsai Lake, and it explains why the fine-grained material laps onto the moraine in ERT4 (Figure 5-12B) and GPR2 (Figure 5-13C). Lastly, the seismic velocities and resistivities below 2070 masl are consistent with the resistivities and seismic velocities of the Fernie Formation observed at outcrops on the eastern ridge. (See Table 4-6 and Section 4.3.2.3).

The identity of Deep Layer 1 is less certain. Strong 3D effects may be affecting the geometry and resistivity in those geophysical images based on the mismatch between ERT1 and ERT4 at their tie point (Figure 5-14). The 2D ERT inversion algorithm assumes that the earth is uniform perpendicular to the survey alignment, meaning that off-line features can spuriously appear on a 3D line (e.g. Bentley and Gharibi 2004). This may explain why the moraine appears to have a resistivity as low as 500 Ωm in Figure 5-11B and Figure 5-12B; there is a large amount of low-resistivity meadow sediment out of plane, leading the inversion algorithm to compute a value that is an average of the meadow and moraine resistivities. Moreover, forward modeling from past studies shows that absolute resistivity values of deep, resistive layers below conductive overburden are misleading due to poor signal penetration (e.g. Langston et al. 2011).

Accounting for these limitations of the ERT method, classifying “Deep Layer 1” as moraine material is still reasonable. Like the moraine bordering the meadow in Figure 5-21, the moraine

on the north end of Bonsai Lake has a high crest, and a long, shallow-angle southern slope leading up to that crest. Noting this similarity, it is a geologically plausible interpretation, even though the thickness of this buried moraine is unclear south of the meadow.

Deep Layer 2 is similarly difficult to interpret. Given how recessive the Fernie Formation is, there may be a layer of regolith overlying intact bedrock. The erodibility of individual members of the Fernie Formation vary between observed outcrops (Sections 4.3.2.3), but the resolution of the most detailed geological map of the area (McMechan 2012) is too coarse to note these intra-formation heterogeneities. This might explain why the regolith unit occurs below the meadow but not below the moraines and the lake. Moreover, a decrease in resistivity at 2070 to 2080 masl (Figure 5-11B) can be explained by a change from moraine (composed primarily of limestone cobbles and boulders) to saturated shale. Alternatively, it may be till rather than in-situ regolith. Over-consolidated till can have velocities between 1500 and 2700 m/s (Hauck and Kneisel 2008), which is consistent with the P-wave velocity images (Figure 5-11A and Figure 5-12A). Moreover, this till may be absent below the moraines and lake because the glacier persisted longer to the south. Given this ambiguity, both possible interpretations are included in Figure 5-21.

Lastly, some areas of the images, which are labelled "???" in Figure 5-11D, Figure 5-12C, and Figure 5-21, have been left without a definitive interpretation. This is due to lack of GPR signal and to ambiguous P-wave and resistivity signals.

5.4.1.1.2 Moraines, Lake, and Springs

The geophysical images suggest that the geological variability within moraines, like with the talus (Section 4.4.1), are largely the result of heterogeneities in grain size distribution. Areas with lower resistivities (600-3000 Ωm) in the upper 3 m correspond often to areas with soil cover and vegetation. Yet, given that only high-resistivities are imaged at depths of between 3 and 10 m, such pockets of fine-grained materials are not present in the moraine beyond this thin veneer. This lack of vertical variability in resistivity suggests the vertical changes in seismic velocity can largely be attributed to changes in effective stress due to burial pressure. In this regard, the moraine deposits have largely uniform elastic properties, but the anomalously thick low-velocity zone in SEIS7 (Figure 5-19A, 60-90 m) shows that the moraine rubble immediately upslope of the outlet springs is more loosely packed.

The geophysical images indicate that bedrock characteristics of the meadow, as imaged in Figure 5-11A and Figure 5-12A, differ significantly from locations to the north (Figure 5-16A, Figure 5-19A, and Figure 5-20A). First, the transition from moraine material to bedrock (that is, where velocities transition to above 3000 m/s) is sharp north of the meadow, meaning there is little to no fractured bedrock or till. Second, the elevation of bedrock is higher, ranging between 2077 and 2082 masl. Lastly, there are significant variations in bedrock topography near the outlet springs where bedrock dips down as low as 2070 masl (Figure 5-19). The exact shape of these is poorly constrained because of the low signal to noise ratio in this loose rubble, but these so-called "bedrock channels" (Figure 5-19A, 45-100 m) are unique within the area studied.

5.4.1.2 Hydrogeological Conceptual model

This subsection first discusses the location of saturated zones under summer conditions (July 2015 and 2016), where there is the most geophysical data to constrain the interpretations. Seasonal fluctuations throughout the fall and winter are considered thereafter using other data.

5.4.1.2.1 Summer Conditions

Locating the water table in ERT images with strong lateral heterogeneity in overburden is not straightforward, as demonstrated by a forward modeling exercise (Figure 5-22). In the known resistivity distribution (Figure 5-22A), the lower layer of 200 Ωm representing the water table is fixed at a constant depth, while material above (representing unsaturated overburden) has resistivities spanning the range observed in the moraine: 10,000 to 100,000 Ωm. The inverted model (Figure 5-22B) shows that the interpreted depth to the water table is about 5 m lower under the higher-resistivity (100,000 Ωm) zone compared to the lower-resistivity (10,000 Ωm) zone if one uses just a single, constant threshold value to locate it. Hence, when choosing an appropriate threshold resistivity to interpret a boundary, one must consider not only smoothing effects but also that the magnitude of resistivity across a boundary will warp its apparent location.

Two separate approaches are used to interpret water table depths depending on location. In the moraines, the transition from 800-1100 m/s in moraines corresponds to the elevation of known water features like GWD, Bonsai Lake, SP6, and SP7, and is the threshold used throughout the images. This velocity range overlaps with the 1000-1200 m/s range employed by other studies to interpret saturated zones in inverted images (Watson et al. 2005; Zelt et al. 2006). Where seismic data are not available, the uppermost elevation where resistivities begin transitioning from >5,000 Ωm to 2000 Ωm is instead used to locate the water table, but used cautiously given

the aforementioned issues with ERT. In the meadow, ERT are relied upon more because the lithological changes in the meadow obscure the changes in P-wave velocity that are due to changes in water content. In both the meadow and the moraine, while the geophysical images help show general trends, the following interpretations rely on other hydrological observations to assign more precise water table elevations in Figure 5-21.

Starting in the talus, defining the water table at the west margin of the wetland (in the Central Cone) is more easily done than at the south margin (in the Lower East Cone). The resistivity boundary at 2100 masl in the Central Talus Cone (Figure 5-11B, 230 m) is clearly a water table given that it intersects surface at the same location as SP4. However, at the south margin of the meadow in the Lower East Talus Cone, there is no surface water discharge and no data before 40 m along ERT4 (Figure 5-12B). While the GPR image shows attenuation of the signal below 5m depth, there is not a single reflector or sudden change in signal energy corresponding to the water table in either the west or south side of the meadow. Hence, the water table within the talus in Figure 5-21 is a dashed as opposed to a solid line. The Lower East Talus Cone (the cone that Figure 5-21 intersects) has generally a lower porosity and a higher fraction of fine-grained content than the Central Cone (Section 4.2.3) and hence likely has a lower hydraulic conductivity. For this reason, the hydraulic gradient drawn in the talus in Figure 5-21 is steeper than that in the toe of the Central Cone (Figure 5-11D, 230-280 m).

Within the meadow, the water table is generally between 1.5 and 3 m below surface. This is based on readings from piezometer P01 (Figure 5-15), and on the observation that hand-augured sediments typically surpass their liquid limit at 2-3 m depth (Section 5.2.1). This agrees with the geophysical images. The data in SEIS1-2-4 (Figure 5-19A) and ERT1 (Figure 5-19B), show P-wave velocities below 300 m/s and resistivities above 100 Ωm in the upper few grid cells of the model, indicative of loose, unsaturated sediment (Kirsch 2006). Furthermore, the geophysical images show that the P-wave velocities and resistivities in the upper 2-3 m surrounding the East Meadow Stream (Figure 5-11, 38 m) are more like that of deeper locations. This suggests that these sediments surrounding the stream are saturated and the watercourse is in a losing reach. Similar patterns are not as obvious in the geophysical data at West Meadow Stream, where it crosses ERT1 and SEIS1-2-4 (Figure 5-11) at 173 m. This is because the stream crosses the survey alignment at an acute angle as opposed to a right angle (Figure 5-10) and because there

are grain size changes near the intersection that obscure the changes in water content. However, the piezometric data in Figure 5-15 show that there is a vertical hydraulic gradient near the stream, suggesting that the West Stream is also losing to the subsurface.

Moving north in Figure 5-21, hydraulic head decreases steadily moving from the meadow towards GWD. The resistivity image from ERT4 indicates sloping water table through the moraines between the meadow and Bonsai Lake (Figure 5-12B, 130-200 m). At the north end of Bonsai Lake, ERT9 shows that the water table does not exceed the elevation of the lake level (Figure 5-17), though the precise elevation is obscured by smoothing effects. All other geophysical lines in the northern moraine and spring area indicate that hydraulic head decreases from the lake to the toe of the moraine where there is loose rubble, and thus Bonsai Lake is losing water to the moraine.

5.4.1.2.2 Fall and Winter Fluctuations

In September and October, the West Meadow Stream, GWD, and northern outlet spring continue to output water, but at considerably lower rates. The gradient of the water table in the moraines and talus are reduced accordingly in Figure 5-21. While no flow gauge data is available for GWD or the meadow stream, there are two pieces of information available to estimate the water table between Bonsai Lake and the northern outlet spring. First, by early September, the lakebed is completely dry aside from a few small trickles of water that disappear into sinkholes in the lakebed (Figure 5-7), meaning that at its highest, the water table is immediately below the lakebed (2086 masl). Second, the discharge data from the northern outlet spring (Figure 5-10) can be used to approximate the water table's location. The discharge data indicate flow around September 15 is approximately 20-40% of the flow around July 15. Assuming that bedrock is at a consistent 2079 masl and that the flow between the lake and the spring is roughly horizontal as per the Dupuit Assumptions, one can model water table as (Schwartz and Zhang 2003, p. 125):

$$h(x) = \sqrt{\frac{2Qx}{K} + c^2} \tag{5-1}$$

where

- Q discharge per unit width of aquifer ($m^2 s^{-1}$)
- K hydraulic conductivity ($m\ s^{-1}$)
- h aquifer vertical thickness and hydraulic head (m)

x horizontal distance from discharge point (e.g. well, spring) (m).

c aquifer thickness at discharge point (m).

Since the location of the water table in July is known at the north end of the lake and at the outlet springs, one can solve for Q/K and c. Then, by reducing the value of Q/K to 30% of the July value, one can compute a new water table location (i.e. $h(x)$) between the lake and the outlet spring. This is how the September water table is defined between 250 and 450 m in Figure 5-21. This method makes a key assumption that the water table in this location responds uniformly and is not affect by a significant lag. For this short distance in relatively coarse-grained (and presumably high-hydraulic conductivity) moraine, the error from this assumption is likely not great. Indeed, the computed surface is no higher that the lakebed elevation, agreeing with the observed drying of the lakebed.

As for the winter time, the water table has very few data to constrain it. The features in the lake and meadow were not accessible from late November to late May due to thick snow cover or avalanche risk. The BTS sensor near SP4 indicates that the mid-winter temperature in 2016 averaged -0.7 °C (Table 4-5). However, this temperature reading is the average of a large spatial area, and the groundwater that feeds SP4 is sourced from depth and may be insulated from air temperature fluctuations. Hence, it is not clear whether the meadow streams are discharging water in winter. The discharge data in Figure 5-9 indicate that mid-winter discharge is roughly half the value in September. To define the February water table in Figure 5-21, Equation 5-1 was used in same way as it was to define the September one. The water table is simply left blank south of Bonsai Lake in the figure due to lack of data.

5.4.2 Controls on Storage and Flow Paths

Large-scale, bedrock topography appears to play an important role in controlling groundwater storage in this system. The package of unconsolidated material below the meadow is as thick as 30-40 m in places, compared to less than 10 m near the outlet springs. Bedrock below the meadow is 10 to 20 m lower than below the lake and springs, leading to this thick accumulation. Given that the bedrock depression is closer to the headwall where the former glacier persisted longest, this was likely a glacially carved overdeepening.

The large moraine deposits also play a role in the dynamics of the groundwater system. Like bedrock overdeepening, the moraines helped trap sediment. The depression would have been full

up to 2080 masl, but moraines on the south side of Bonsai Lake helped a further 15 m of sediment accumulate. Given the evidence of a dam breach at the moraine between the meadow and Bonsai Lake (Section 5.2.2), it is plausible that these fine-grained meadow sediments are glaciolacustrine in origin. Moreover, the moraines on the north and south side of the lake each help maintain a head difference of 4-6 m first between the meadow surface and Bonsai Lake and also between Bonsai Lake and northern outlet spring. Nonetheless, the conceptual model in Figure 5-21 indicates that that most of the storage in Bonsai Lake Basin is likely in upstream of Bonsai Lake. While the moraines surrounding Bonsai Lake may be up to 20 m thick, only a small portion of its volume is saturated is ever saturated, which is especially true of the moraine north of Bonsai Lake.

Hence, it is not only the thickness of the material south of the lake that allows it to be an important storage reservoir and flow path. First, there is a combination of coarse-grained, high-permeability units (bouldery talus and moraine) that can easily convey water and fine-grained, low-permeability units (meadow sediments, lakebed muds, and fine-grained talus) that delay the release of water that Roy and Hayashi (2007) argued were both key functions of alpine groundwater systems. Second, there is a consistent source of water (SP4) that maintains consistent head levels in the meadow and keeps meadow sediments saturated. This is confirmed by the piezometric data and resistivity model that indicate that the meadow is a losing reach for the stream. Third, as Baraer et al. (2014) and Gordon et al. (2015) observed in their studies, there may be a connection between the talus slopes and the high-permeability layers below the meadow, providing a flow path that can supply flow to the outlet spring well after Bonsai Lake is dry. While geophysical data is lacking to confirm this last item, it is plausible given how the meadow sediments seem to taper in thickness going south (Figure 5-21).

At the outlet spring, there seem to be several factors controlling the location of flow paths. To start, the low-resistivity anomalies from Figure 5-18B, Figure 5-19B, and Figure 5-20B have all been plotted in Figure 5-23. Those anomalies west of SP6 are all associated with a small, boulder-filled gully at the toe of the moraine with water flow that is audible (though not visible) at surface. This suggests that the other low-resistivity anomalies are also zones of convergent, rapid flow in coarse rubble. Those anomalies east of SP6 are not grouped around a single surface feature, but all occur either just below or in front of the central ridge of a moraine, in loose

material. In addition, some of them seem associated with bedrock lows observed in SEIS7. Overall, heterogeneities in grain packing, surface topography, and bedrock topography all seem to have some control on the location of this outlet spring.

5.4.3 Comparison of Results to Previous Studies

The geological model proposed in Figure 5-21 is consistent with what we know about overdeepenings. Cook and Swift (2012, Figure 3a) show a common form of overdeepening that is strikingly similar to Figure 5-21: a bedrock-scoured basin partly confined by a terminal moraine. The dimensions also agree with other studies. Haeberli et al. (2016), who analyzed the morphometric characteristics of overdeepened basins in the Swiss Alps, Himalaya-Karakoram region, and Peruvian Andes showed a wide spread over several orders of magnitude of basin depths, surface area, and length, with only weak and barely significant correlation between some of those variables. The length and depth of this basin (approx. 200-400 m and 30-40 m, respectively) are within the range they measured, though the depth is above the median for basin length of this range (Haeberli et al. (2016), Figure 8). Buried glacial overdeepenings with similar order of depth and surface area have been documented with detailed geophysics (e.g. Götz et al. 2013).

Similarly, this site has many of the features often associated with overdeepenings. Areas with weaker bedrock and tectonic structures (e.g. faults) and lithological boundaries where there is a contrast in rock properties more commonly have overdeepenings (Preusser et al 2010; Brückl et al. 2010; Jordan 2010). The overdeepening at Bonsai Lake likewise is associated with the Sulphur Mountain Thrust, which juxtaposes competent Palliser Formation limestone and very recessive Fernie Formation shale. Some authors have noted that large, numerous moraines with complex arrangements are often found alongside overdeepenings (e.g. Spedding and Evans 2002). This is an apt description of the moraines surrounding Bonsai Lake.

Moreover, this study corroborates the findings of others who emphasize the role of bedrock and sediment heterogeneity in alpine hydrogeology, but is notable for adding more detailed subsurface information to support these previous conclusions. As McClymont et al. (2010) and Gordon et al. (2015) did before, it documents another instance of bedrock depression coinciding with an alpine meadow that has very stable water levels. The bedrock depressions in the proglacial moraine studied by McClymont et al. (2012) serve a similar function in maintaining

stream flow, though their saturated thickness does not exceed 10 m. This study has also shown evidence that bedrock topography and sediment heterogeneity may play a role in concentrating flow into rapid, convergent flow paths, as proposed by Roy and Hayashi (2009) and McClymont et al. (2011). Bedrock fracture flow and storage is plausible based on these geophysical results and may be a significant flow path, but their relative importance in this basin is unknown without further geochemical sampling, numerical modeling, or drilling.

5.5 Summary of findings

This study has found that a thick package of unconsolidated sediment, bedrock topography, and sediment heterogeneity control flow paths and help maintain steady stream flow in this site. Below the meadow there is up to 40 m of overburden, up to 11 m of which is fine-grained sediment of (presumably) glaciolacustrine origin. Two different structures helped trap this sediment and led to its accumulation: a glacial overdeepening approximately 20 m deep and tall moraines between 15 and 30 m tall. Locally, at the northern outlet spring, there are rapid, convergent flow paths whose locations are controlled by heterogeneities in grain size, by anomalous bedrock lows, and by surface topography. Results further indicate that most of storage in the basin is in areas south and upland of Bonsai Lake.

This study contributes to the wider body of research in a few ways. While convergent flow paths in coarse, alpine sediments have been hypothesized, this study (along with the findings presented in Chapter 4) is the first time that they have been imaged with geophysics. It also adds to the limited set of detailed geophysical surveys that demonstrate that bedrock topography is an important control on storage and flow paths in alpine systems. However, while bedrock fracturing is expected to influence alpine headwater hydrology, the degree of bedrock fracturing remains poorly understood in the Bonsai Lake basin. Furthermore, few post-glacially filled bedrock overdeepenings have been documented, hence this newly discovered case will contribute to a better understanding of the spatial distribution and genesis of these landforms.

5.6 Tables

Table 5-1: A summary of hydrological features observed at surface

Description	Nomenclature in this thesis	Timing and relative flow volume	Elevation (masl)	Water resistivity (Ωm)
Talus toe springs	SP4, SP5	Flow much greater during snowmelt, but SP4 persists	2100	10 to 30 (SP4) ~70 (SP5)

		into early fall		
Meadow streams and lake inlet	West Meadow Stream, East Meadow Stream, Lake Inlet Stream	West stream larger flow than east, which is dry by late August.	2100 to lake level	30 – 35 (Lake inlet)
Groundwater inputs to lake	GWD	Not visible until lake levels are low, but cold-water discharge indicates their presence when lake is higher	2090	35 to 55
Seasonal Tarn	Bonsai Lake	>3 m deep in June, but dry by late summer	2086-2091	40 to 60
Lakebed sink features	LMK9, LMK11, LMK12, LMK13, LMK14	Not visible until lake levels are low	N/A	
Northern outlet spring	Northern Outlet Spring *OR* SP6 and SP7	Total flow much greater than all visible inputs to lake (GWD and lake inlet stream), and is also perennial	2082	35 to 55

Table 5-2: Discharge measurements in the creek fed by the northern outlet spring (SP6 and SP7).

Date	**Time (Mountain Time Zone)**	**Location**	**Discharge ($m^3 s^{-1}$)**
2015-July-08	14:30*	~20 m north of SP6 and SP7	0.089
2015-July-08	14:45*	~105 m downstream of SP6 and SP7	0.085
2017-February-21	*(Afternoon)*	~70 m north of SP6 and SP7	0.008
*Indicates that daylight savings time was in effect			

Table 5-3: A summary of the petrophysical units and their interpreted geology. DL1 and DL2 stand for "Deep Layer 1" and "Deep Layer 2", the tentative names used when discussing resistivity images of the meadow in Section 5.3.1. Adapted from Christensen et al. (2017).

	Resistivity (Ωm)	P-wave velocity (m/s)	GPR characteristics	Interpretation
	30 - 80	250 – 400	No signal	Fine-grained, meadow sediments
	80 - 160	500 – 600	Low amplitude, flat reflectors, poor depth penetration	Fine-grained, meadow sediments either mixed with boulders or unsaturated
	500 - 7000	500 – 1500	Mostly continuous, surface-parallel reflectors	Talus deposits. Transition of <2000 Ωm is high water content zone
(DL1)	500 - 30,000	500 – 2000	Discordant, arched, high-amplitude reflectors	Moraine material. Higher resistivities indicate low water content; near-surface variability (<3m deep) caused by presence of soil; seismic velocity increases with burial pressure and saturation
(DL2)	180 - 300	2300 – 3000	Signal obscured by conductive overburden	*Weathered regolith from Fernie Fm.? Over-consolidated till?*
	180 - 300	3000 – 3700		Competent shale (Fernie Fm.)

5.7 Figures

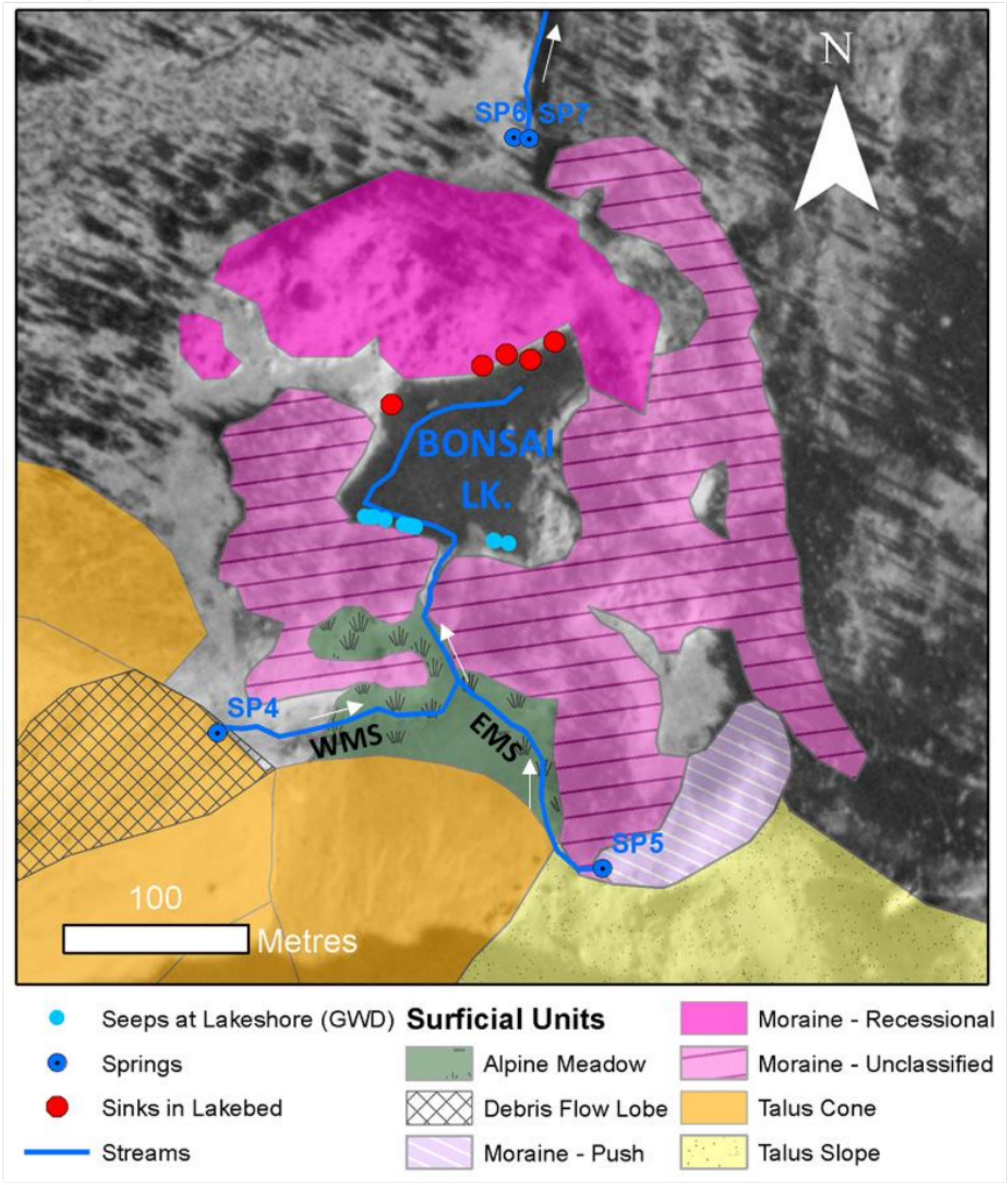

Figure 5-1: Map showing the areal extent of various surficial units and the locations of important hydrologic features. The blue line within Bonsai Lake indicates location of the stream when the lake is dry in late summer. The two branches of the stream in the meadow are labelled "EMS" for "East Meadow Stream" and "WMS" for the "West Meadow Stream." Small white arrows indicate the direction of the streams. Uncoloured areas were not mapped or are transitional zones between units.

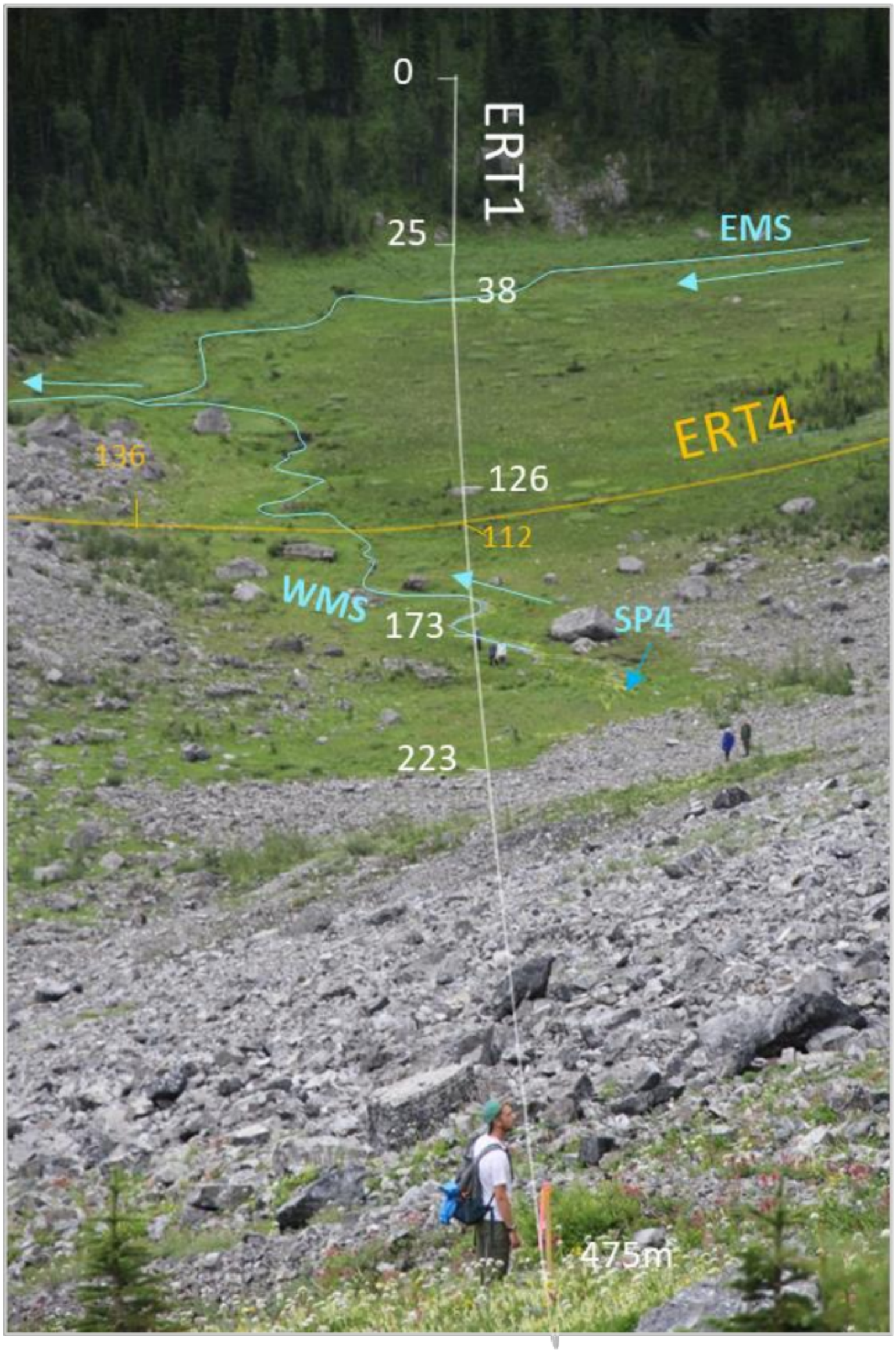

Figure 5-2: A view of the meadow as seen from the Central Cone looking east. Approximate alignments of ERT1 and ERT4 are shown, along with distance markers in metres. The locations of the streams and SP4 are highlighted in blue. The two branches of the stream in the meadow are labelled "EMS" for "East Meadow Stream" and "WMS" for the "West Meadow Stream." Small, light blue arrows indicate the flow direction of the streams. Adapted from Christensen et al. (2017).

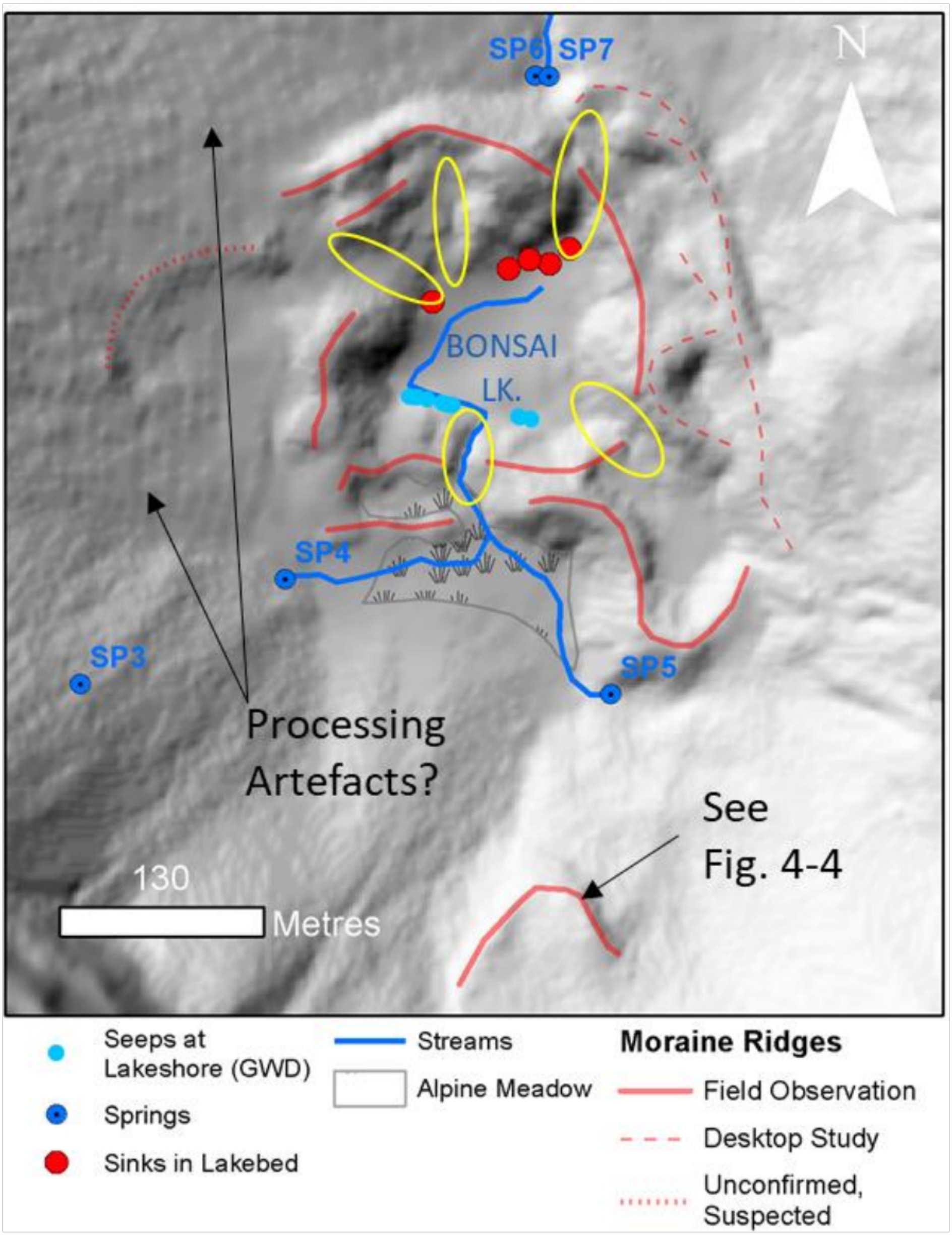

Figure 5-3: Moraine ridges shown along a hill-shaded DEM used to help delineate their locations. Yellow circles indicate linear depressions that may be the results of alluvial erosion. A photo of the moraine on the Eastern Talus Slopes is shown in Figure 4-4. The more heavily forested NE corner of the image contains N-S oriented linear artefacts that do not represent real terrain and that might be the result of processing of the LiDAR.

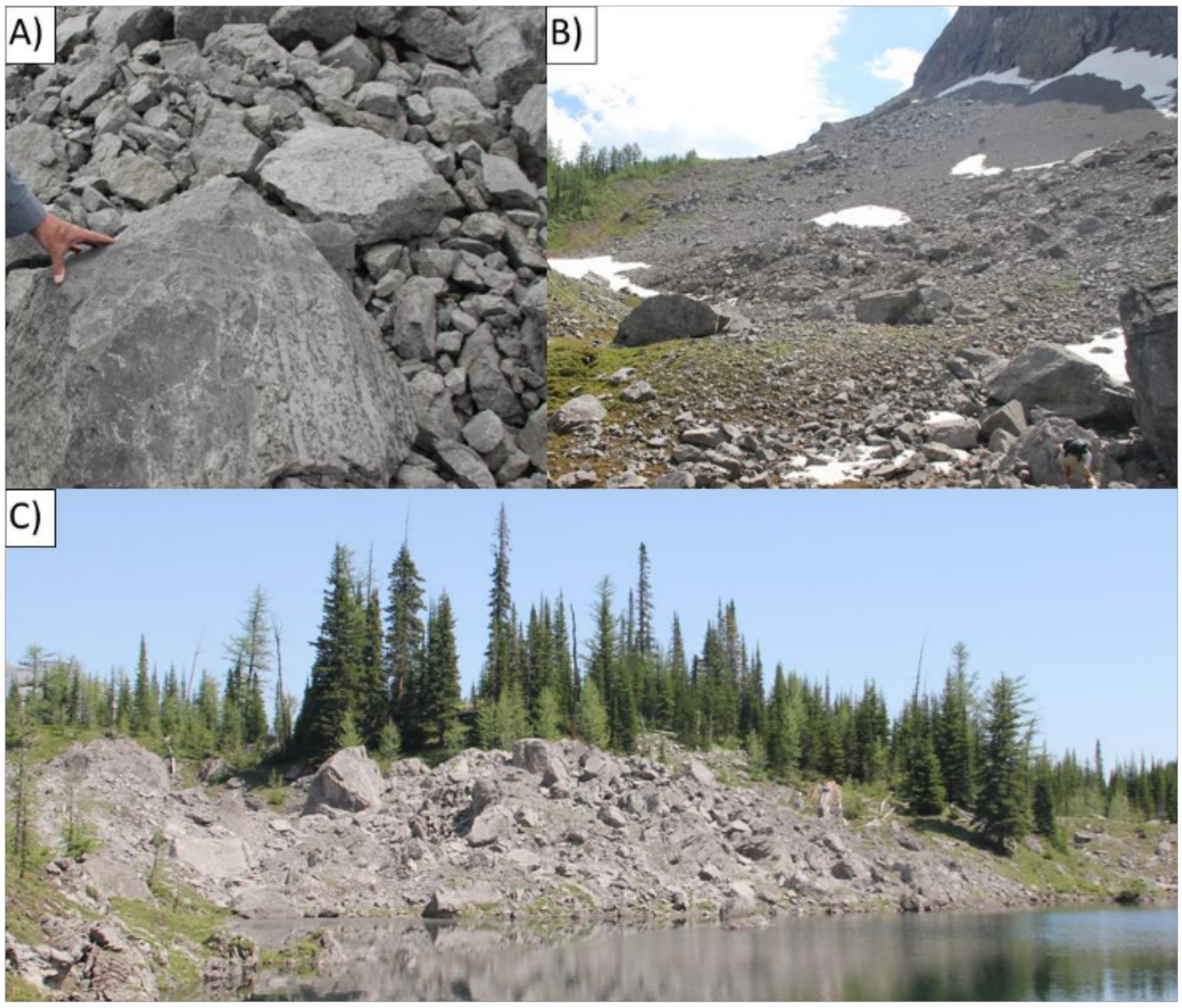

Figure 5-4: Rock fragments on moraines like that located on (A) the southern talus slope show more rounding and have a more uniform size distribution compared to (B) undisturbed talus material. Hence, cases like (A) have been interpreted as push moraines. Some moraines, like (C) on the north side of Bonsai Lake, have more angular boulders, have multiple fragments in excess of 3 m wide, and less uniform rock size distribution. These moraines have been interpreted as recessional moraines. Photo dates are: A) June 18, 2015; B) and C) June 28, 2015

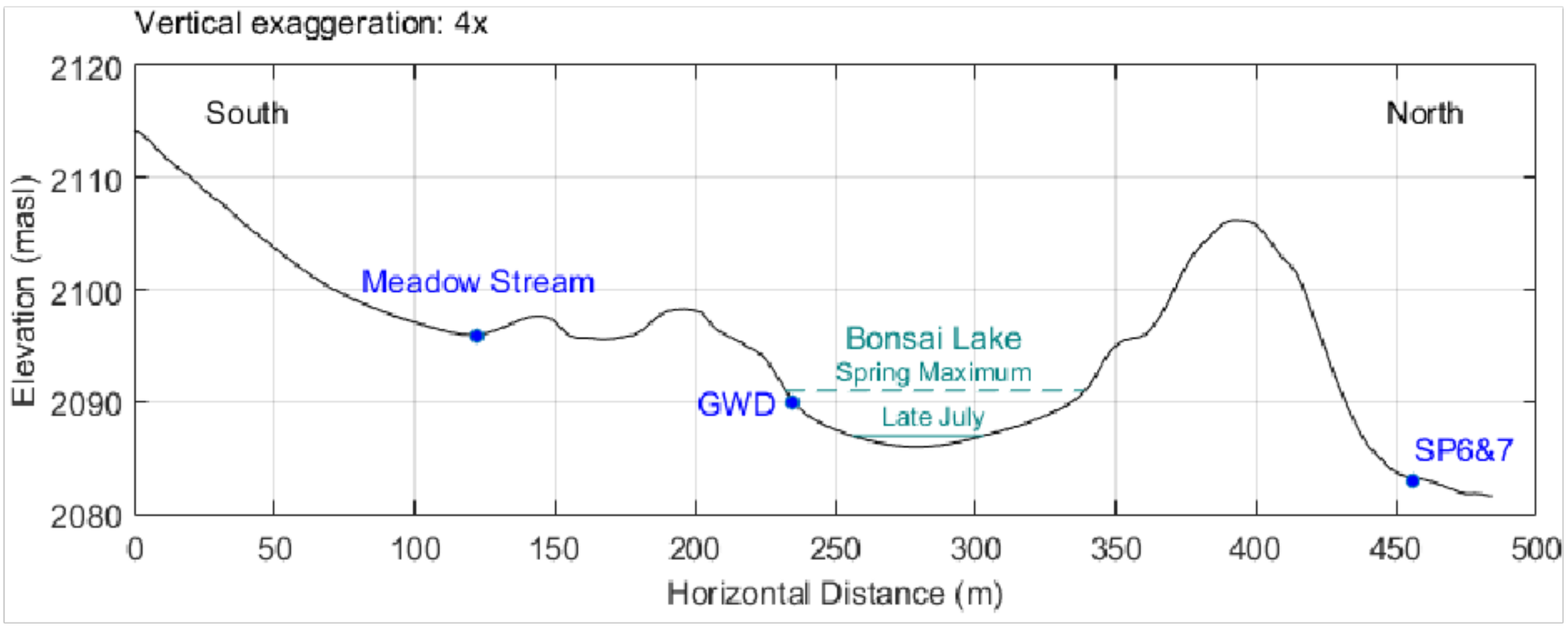

Figure 5-5: Elevation cross-section showing the main hydrologic features at the study site. See Figure 5-10 for the alignment of this line. Adapted from Christensen et al. (2017).

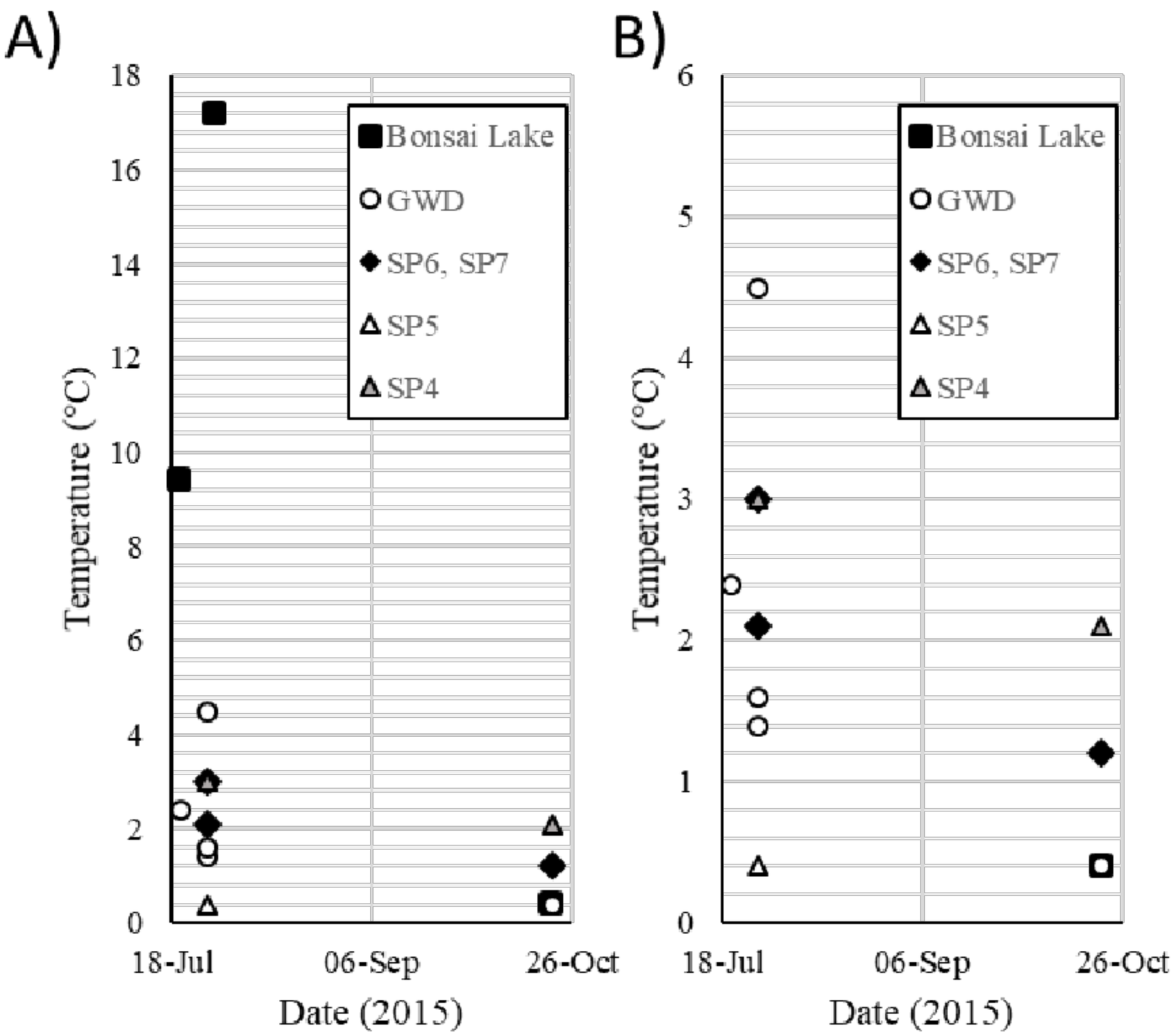

Figure 5-6: Temperature measurements taken from low-lying features in 2015. Refer to Figure 5-1 for the locations of hydrologic features listed.

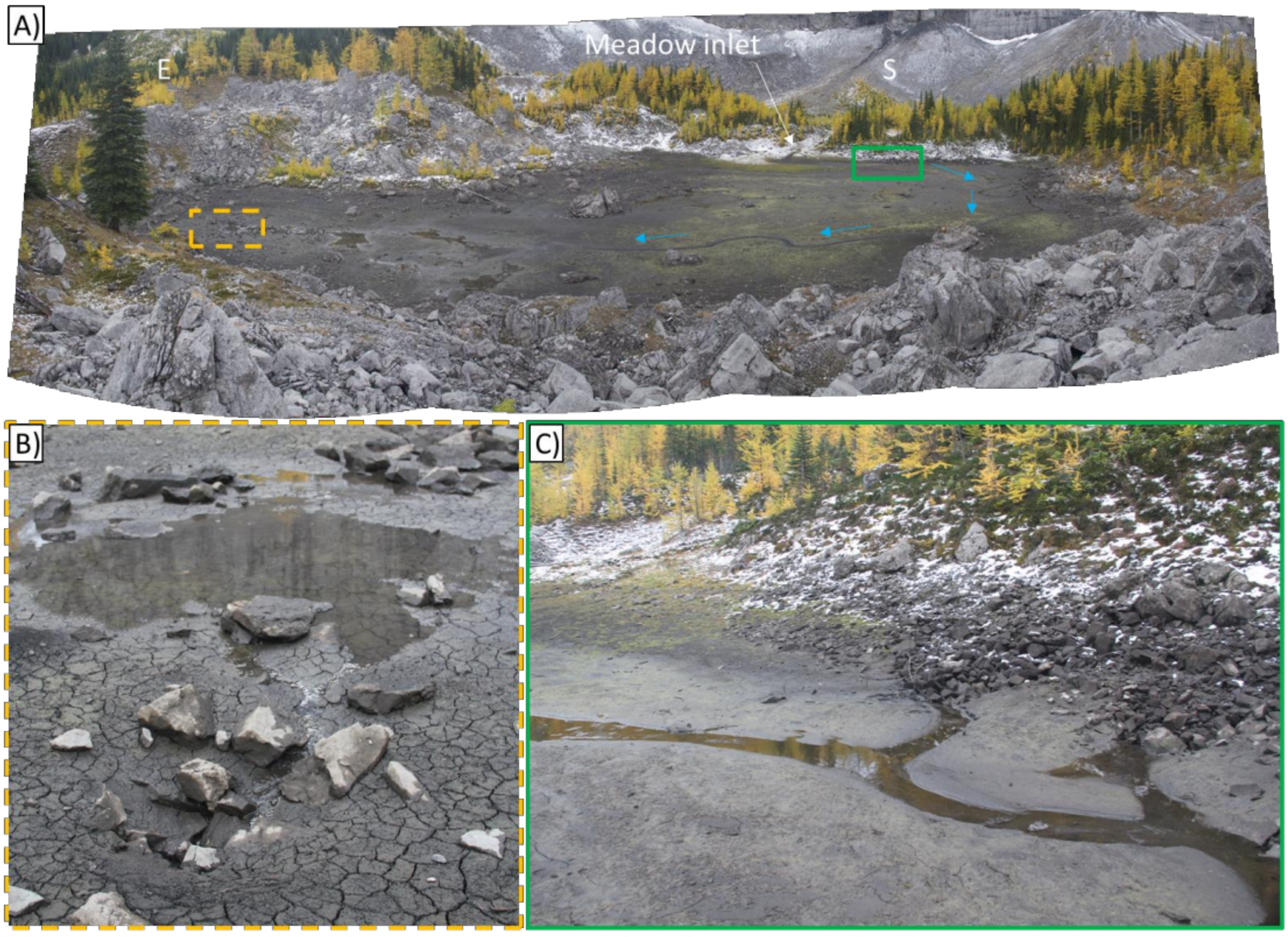

Figure 5-7: Views of important lakebed features A) A panorama from the north side of the lake. Annotations include compass directions (white letters), locations of B and C (coloured rectangles), flow direction of the small lakebed stream (blue arrows), and location of inlet stream from the meadow. B) One of the sink features (LMK14) where pooled water cascades into void spaces of rocky material that is not covered by lakebed muds. C) A view of groundwater discharge (GWD) at the south shore that supply water (along with the meadow inlet stream) to the small lakebed stream. Photo dates: September 19, 2016.

Figure 5-8: Panorama showing the northern outlet spring draining from the base of the moraines. Annotations show the locations of points named “SP6” and “SP7” and compass directions (white letters). Photo date: June 28, 2015.

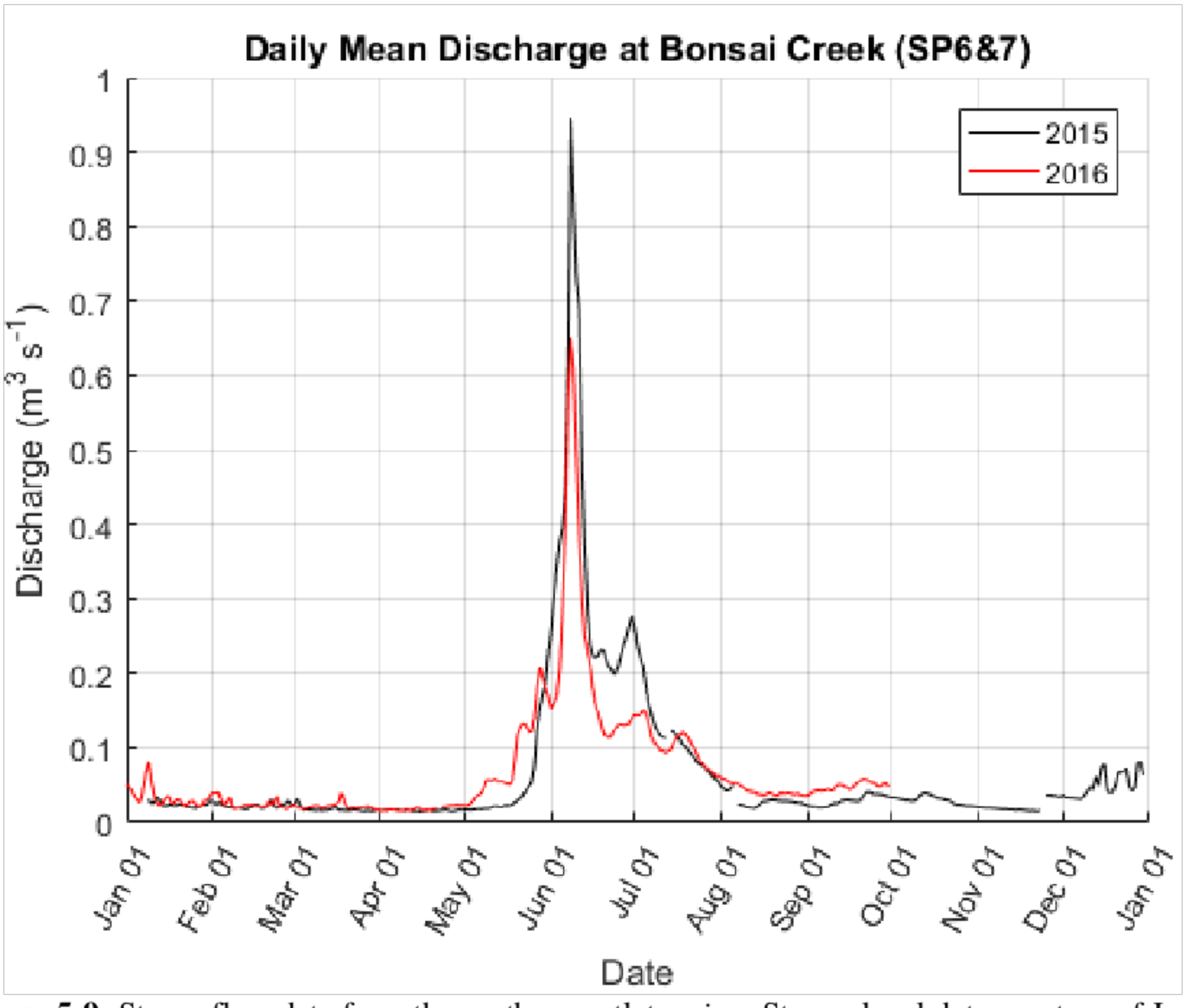

Figure 5-9: Streamflow data from the northern outlet spring. Stream level data courtesy of J. Pomeroy, and rating curve courtesy of H. Wu and C. Westbrook.

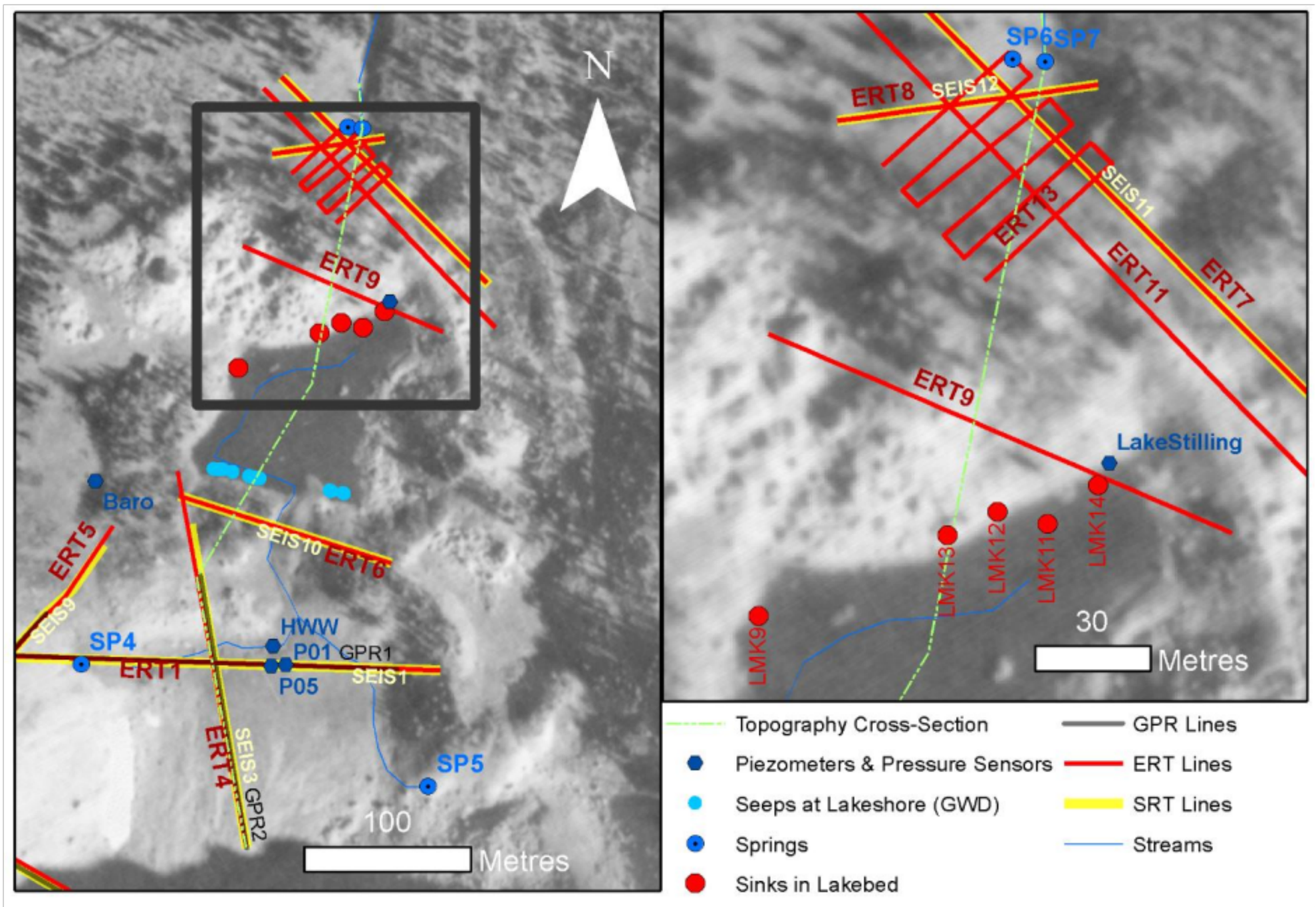

Figure 5-10: Overview map of the geophysical lines and main hydrologic features at the study site. The green line indicates the alignment of the cross sections in Figure 5-5 and Figure 5-21. Note that the line labeled "SEIS1" includes roll-along surveys that were combined for the image "SEIS1-2-4."

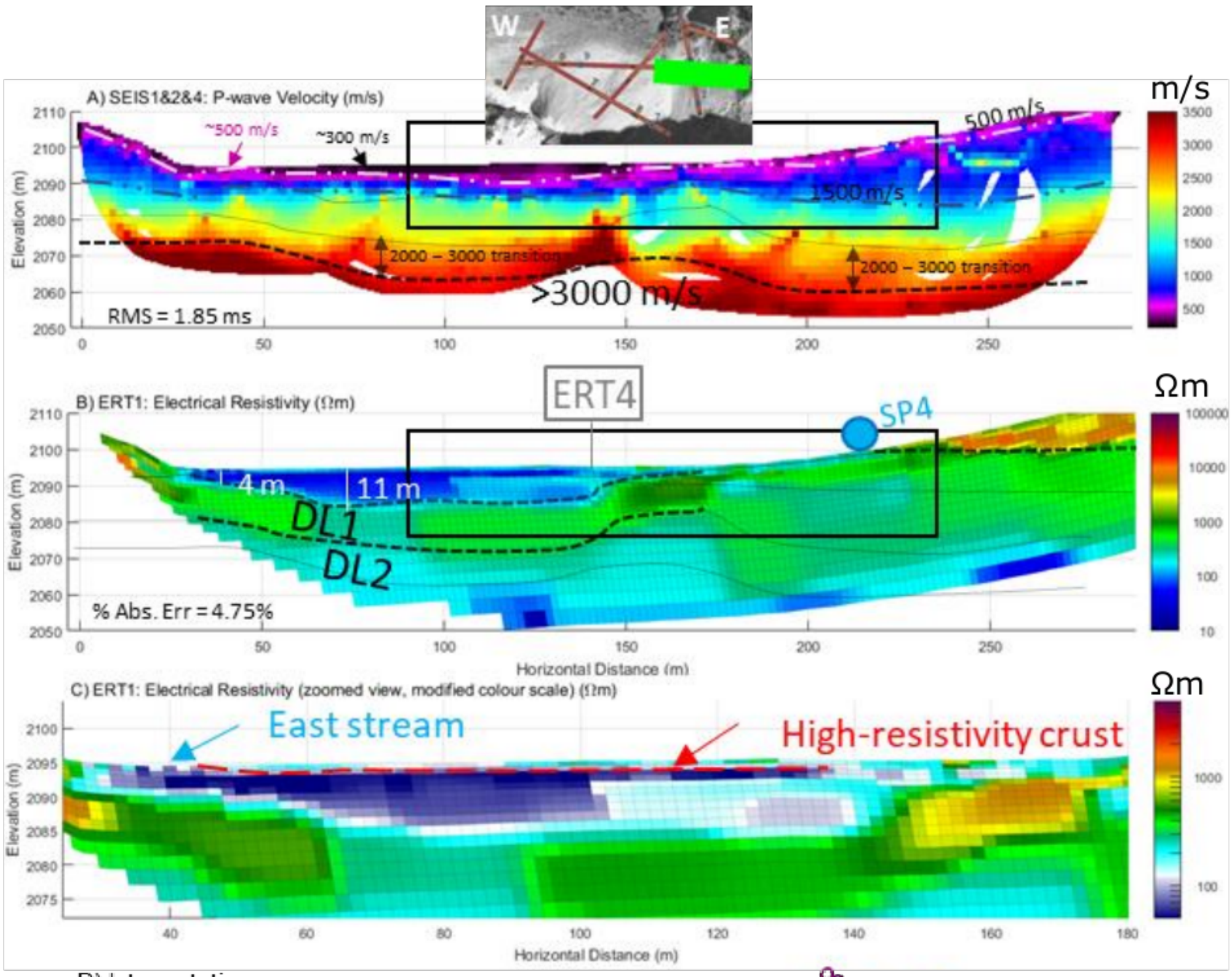

Figure 5-11: P-wave velocity (A) and electrical resistivity (B) models of the meadow, and the interpretation of these results (D). A zoomed view of the meadow with a modified colour scale is also shown in C) to emphasize the thin 1-3 m layer of unsaturated sediments in the meadow above the water table. The black rectangle in A) and B) indicates the extent of the GPR image in Figure 5-13A. Annotations in B) include: important resistivity boundaries (black, dashed lines), Deep Layer 1 and 2 (DL1, DL2), thickness variations in the top layer of the meadow (white lines), and the tie point with ERT4 in Figure 5-12 (grey label). Note that only the first half of ERT1, which is the only portion that interests the meadow, is shown here; portions covering the talus are shown in Chapter 4. See Figure 5-10 for the location of this line.

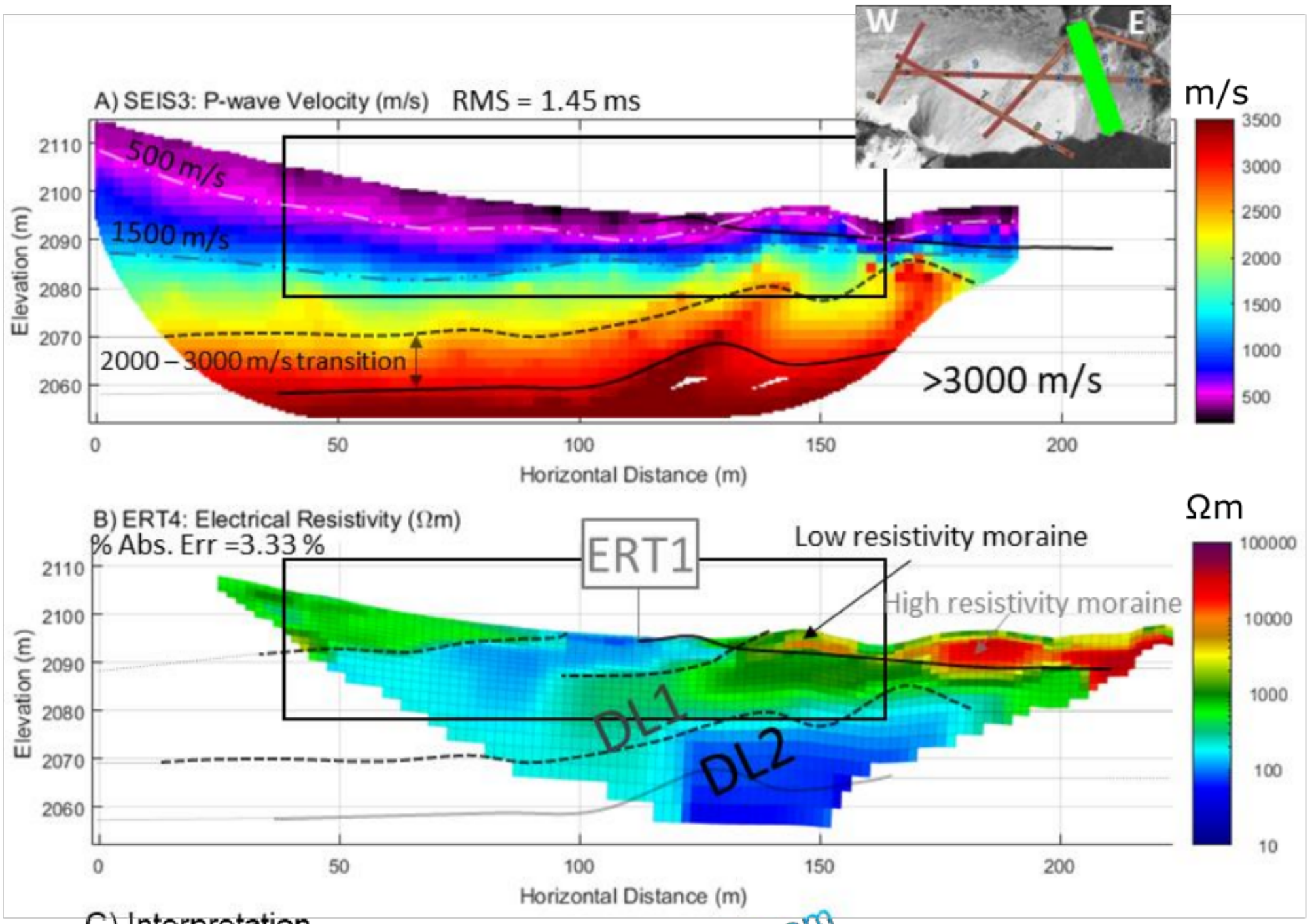

Figure 5-12: P-wave velocity (A) and electrical resistivity (B) models of the meadow, and the interpretation of these results (C). The black rectangle in A) and B) indicates the extent of the GPR image in Figure 5-13B. Annotations in B) include: important resistivity boundaries (black, dashed lines), Deep Layer 1 and 2 (DL1, DL2), resistivity changes in the moraine, and the tie point with ERT4 in Figure 5-11 (grey label). See Figure 5-10 for the location of this line.

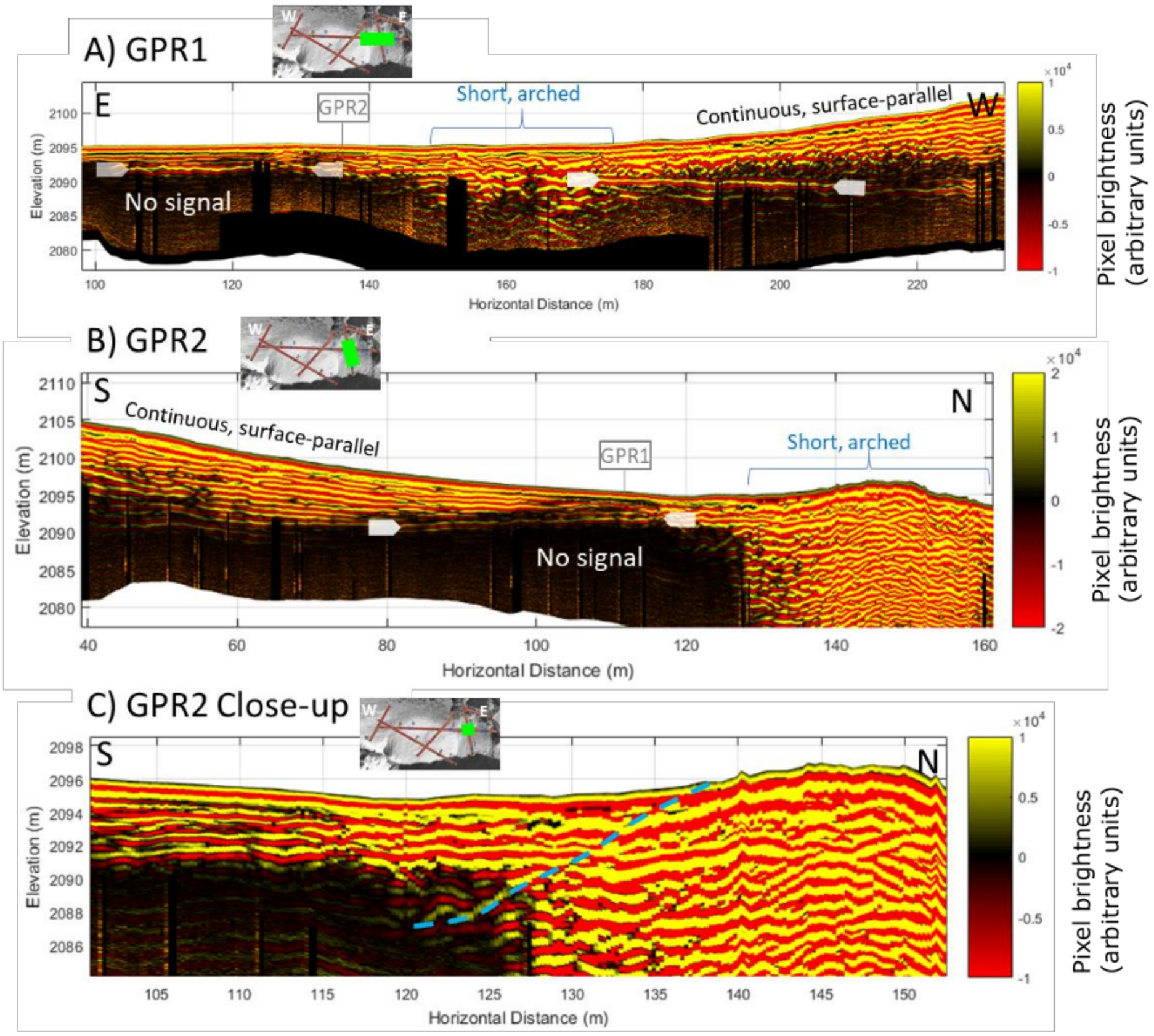

Figure 5-13: Radar reflection sections crossing the meadow. Annotations in A) and B) indicate tie-points with intersecting lines (grey boxes), notable flat reflectors (white arrows), and changes in GPR texture (black and blue text). Panel C) is a close-up of B) where changes in texture are emphasized with a blue dashed line, indicating a transition from fine-grained meadow sediments to moraine material. See Figure 5-10 for the line locations and Section 3.2.3 for notes on the color scale.

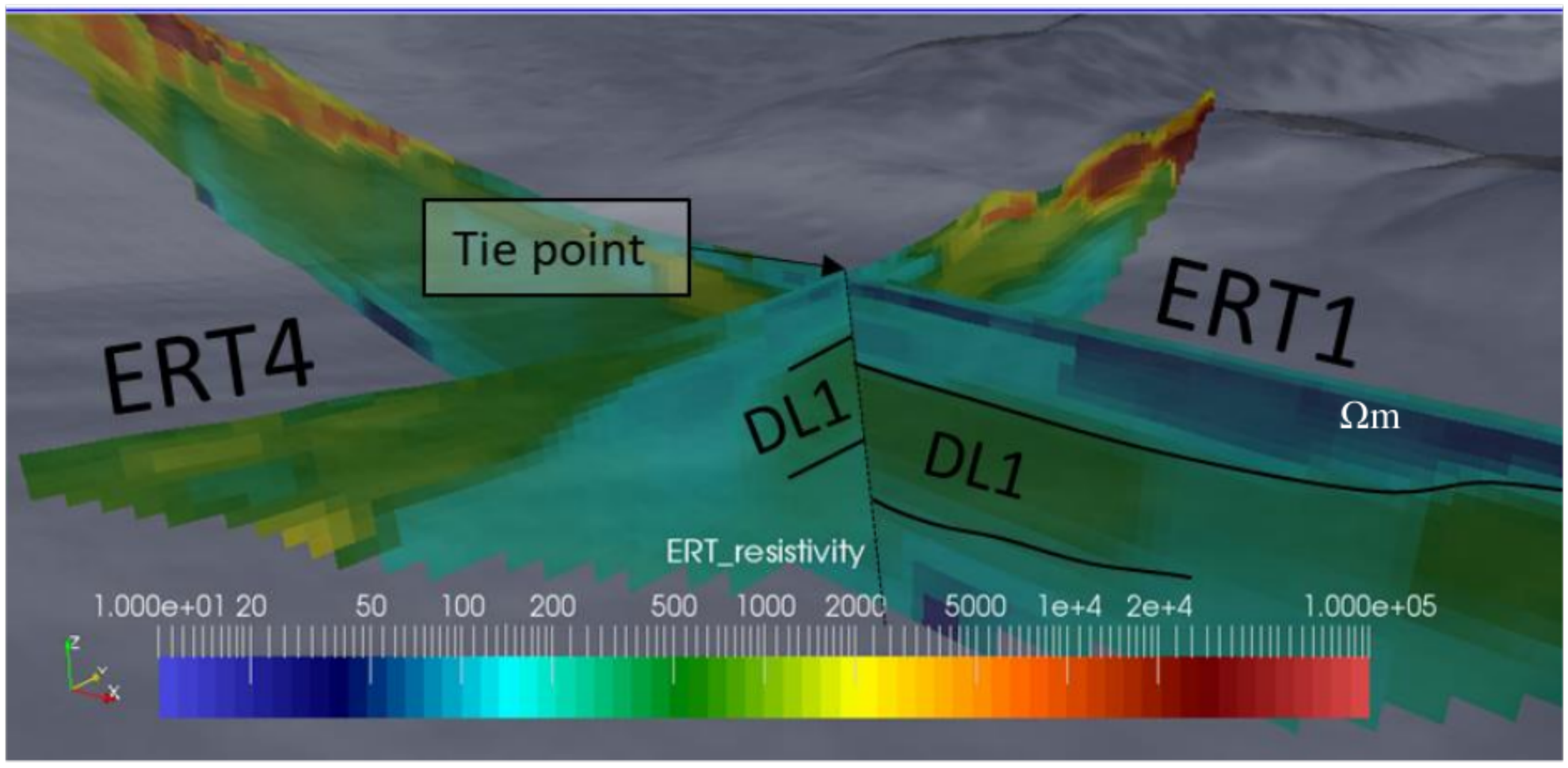

Figure 5-14: Oblique view (facing northwest) focusing on the tie point between ERT1 and ERT4 where resistivity boundary depths of deeper layers differ by as much as 5 m.

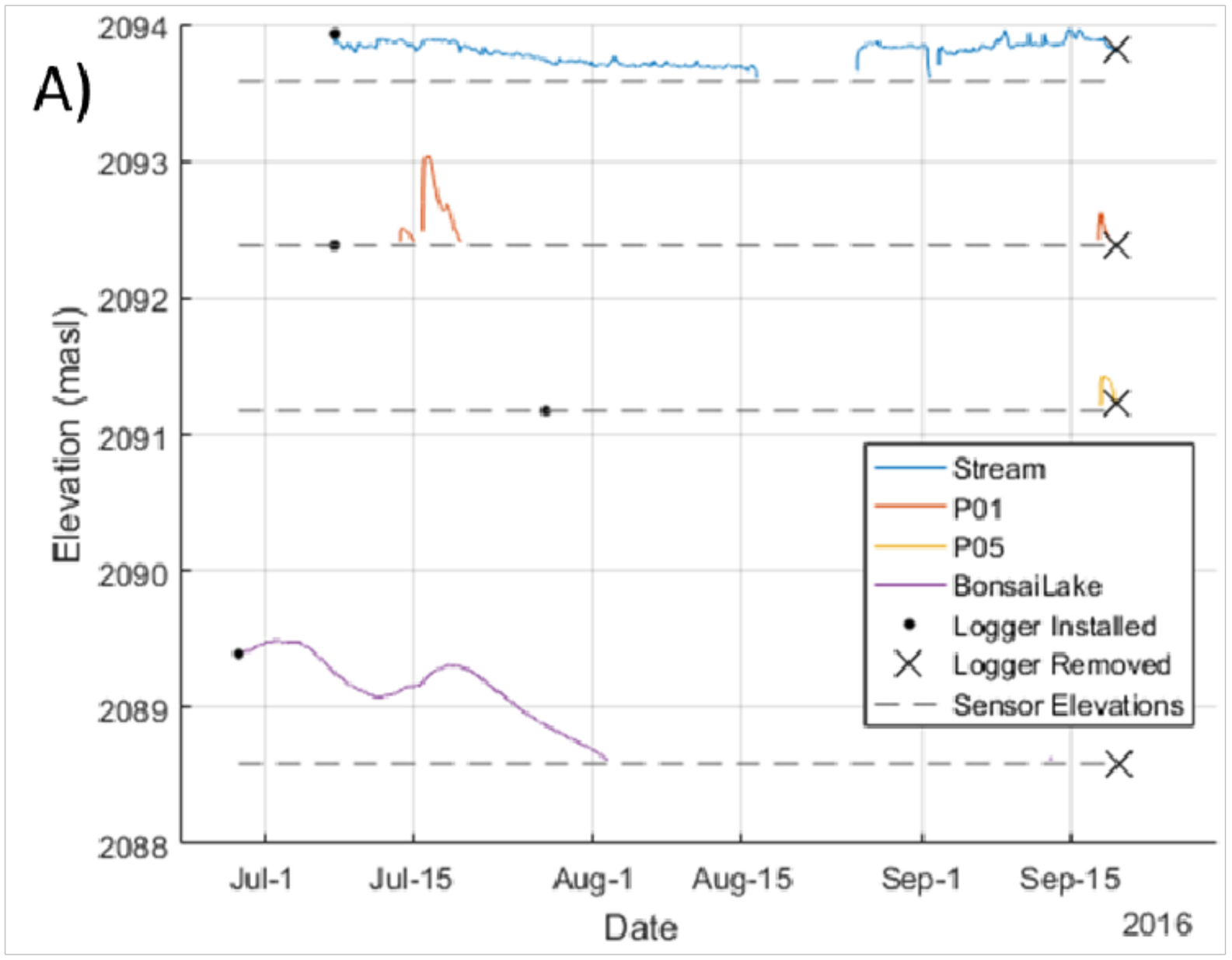

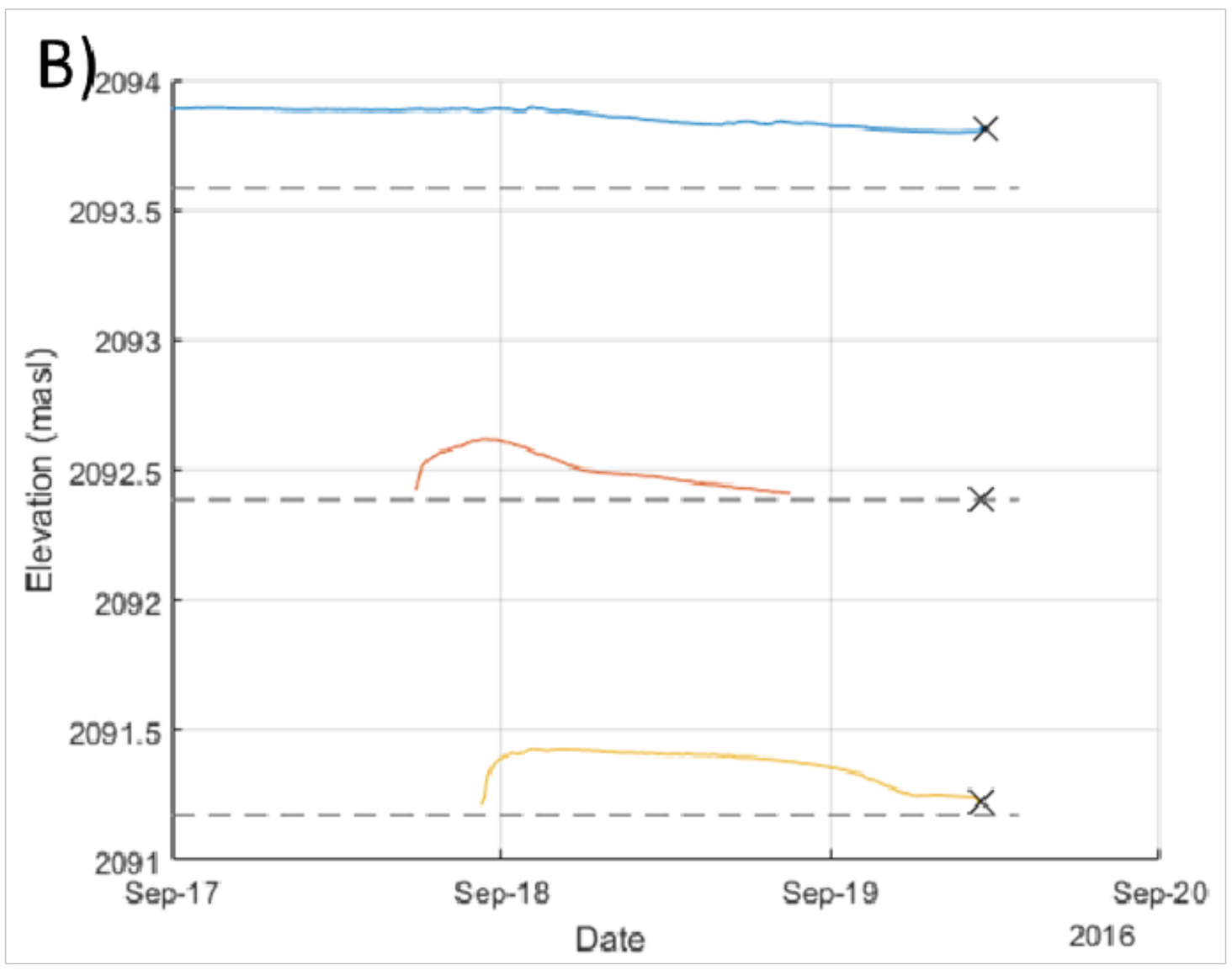

Figure 5-15: Piezometric data collected in the meadow and lake, shown over the whole field season (A) and during a short period in September 2016 (B). Dashed lines indicate the elevation of (and hence lower detection limit of) the sensors. The stream measurements are taken from the stilling well labelled "HWW" in Figure 3-5 and Figure 5-10.

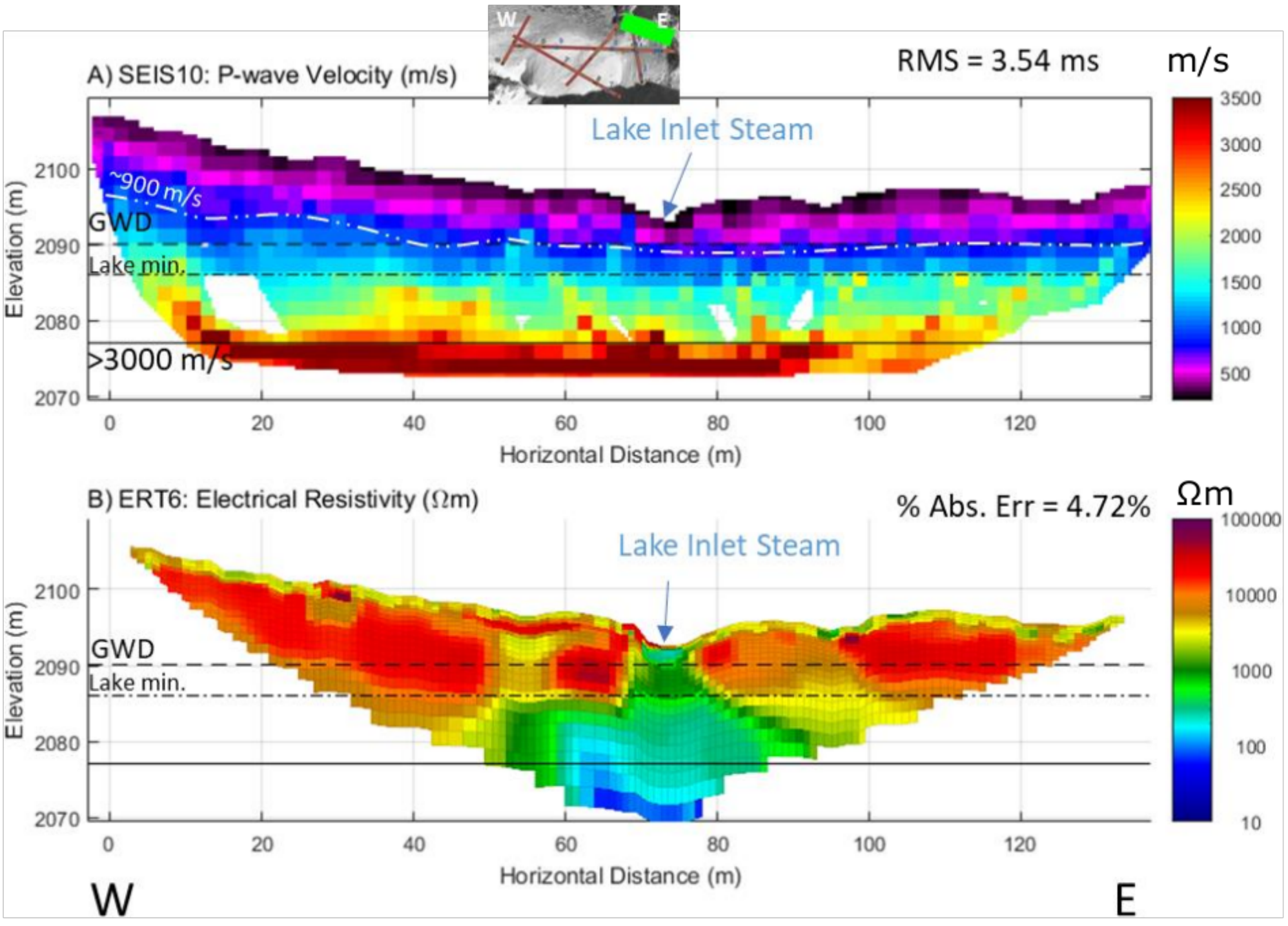

Figure 5-16: Geophysical models from the moraine along the south side of Bonsai Lake. Annotations note the elevation of GWD on the south shore of Bonsai Lake (dashed black line), the minimum elevation of the lakebed (dot-dashed line), the interpreted depth to bedrock (solid black line), and the location of the inlet stream from the meadow to the lake. See Figure 5-10 for the location of this line.

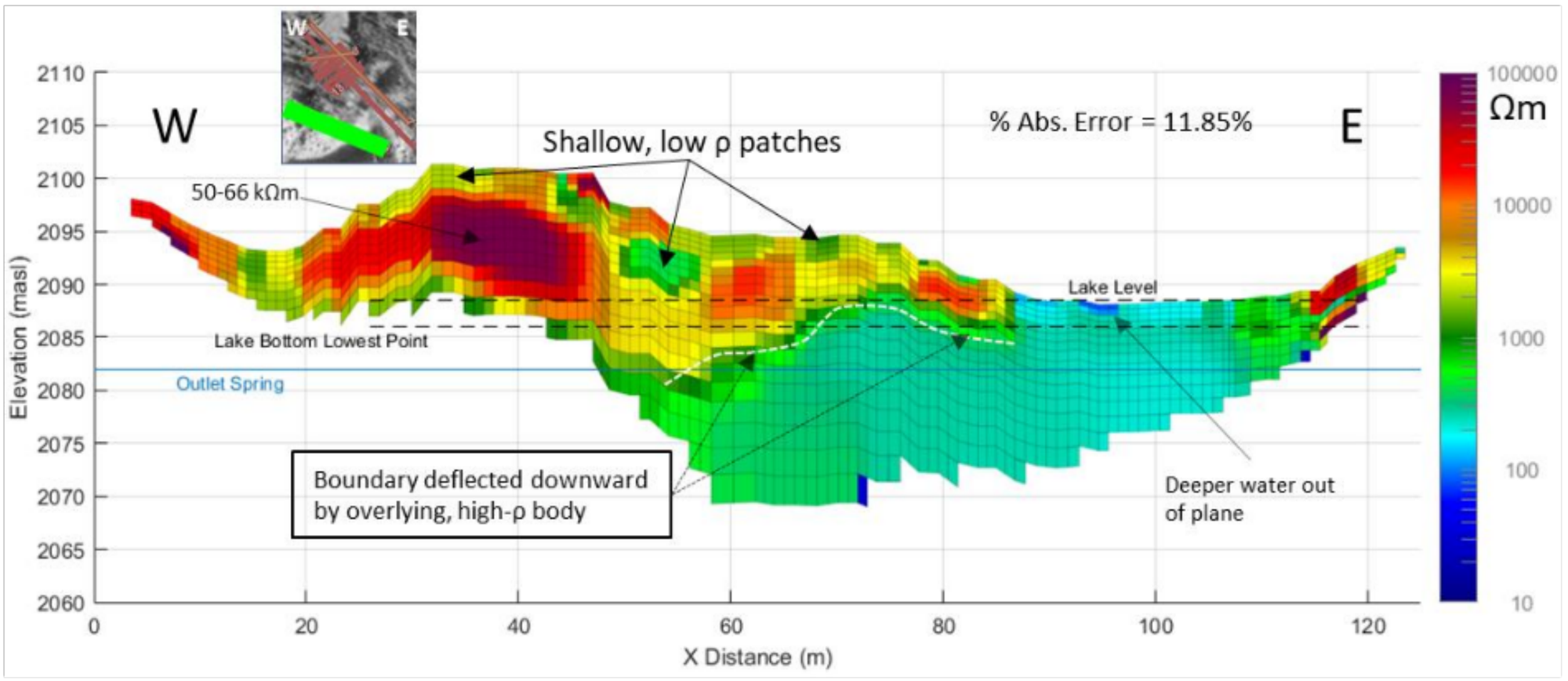

Figure 5-17: Resistivity image (in Ωm) along ERT9. The elevation of the lake at the time of survey (2088.5 masl), the lowest point in the lake (2086 masl), and outlet springs SP6 and SP7 (2082 masl), and indicated with horizontal lines. See Figure 5-10 for the location of this line.

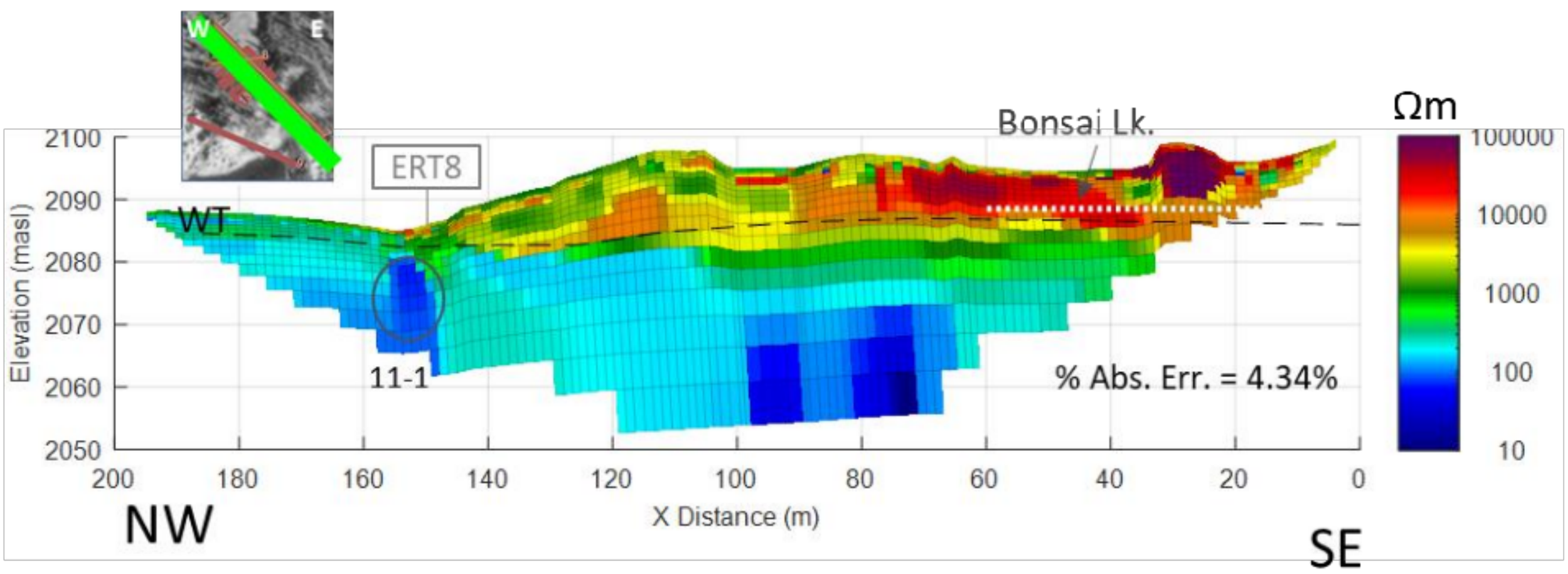

Figure 5-18: Geophysical models near the northern outlet spring along ERT11. Annotations note the elevation of the interpreted depth to saturation (WT, dashed line), the intersection with ERT8 (grey box), a low-resistivity anomaly at depth (black ellipse), and the elevation of Bonsai Lake (2088.5 masl) at the time of survey. See Figure 5-10 for the location of this line.

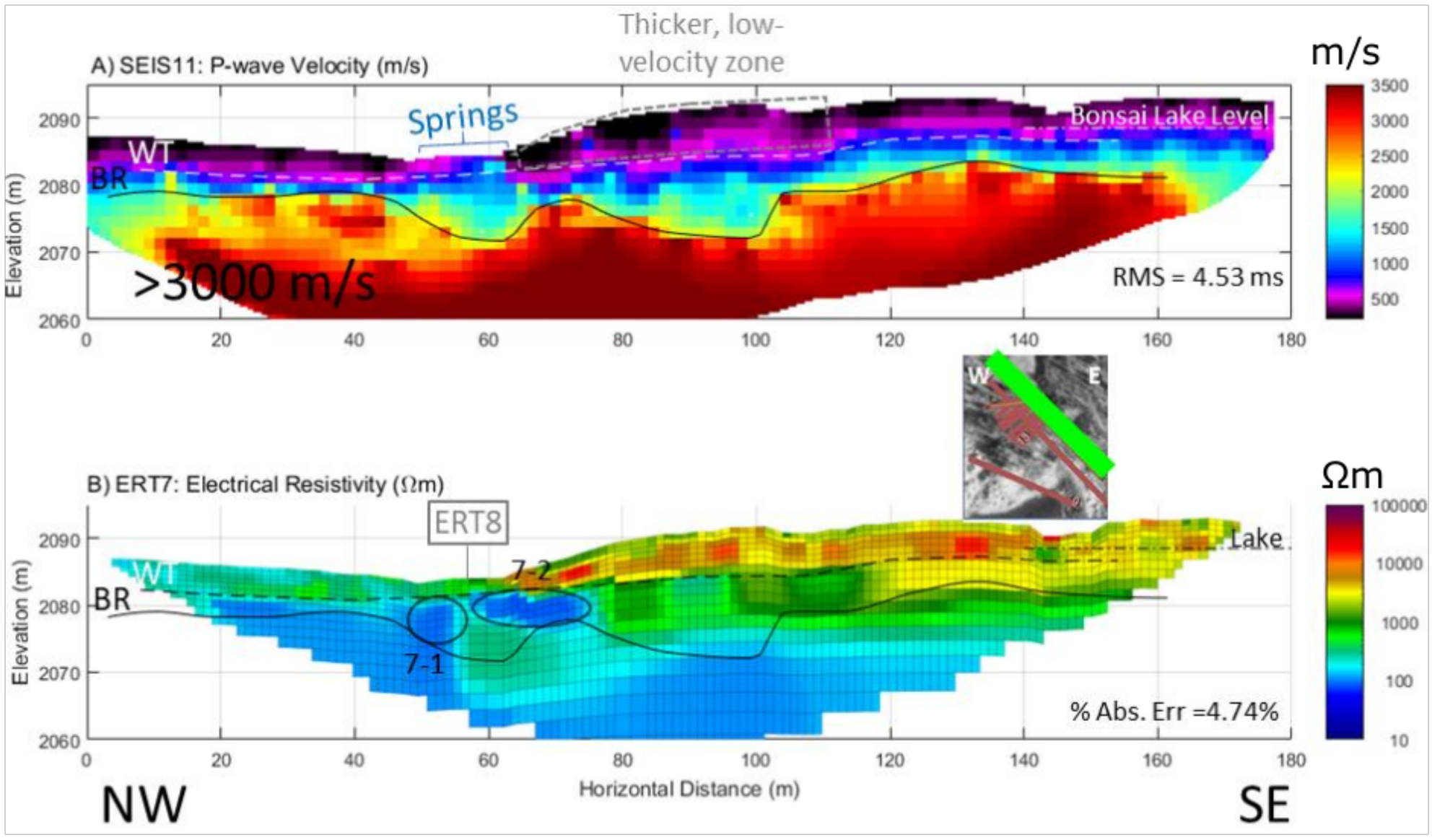

Figure 5-19: Geophysical models near the northern outlet spring along ERT7. Annotations note the elevation of the interpreted depth to bedrock (BR, solid black line), the interpreted depth to saturation (WT, dashed line), the location of the outlet springs SP6 and SP7, the intersection with ERT8 (grey box), low-resistivity anomalies at depth (black ellipses), and the elevation of Bonsai Lake (2088.5 masl) at the time of survey (dot-dash line). See Figure 5-10 for the location of this line.

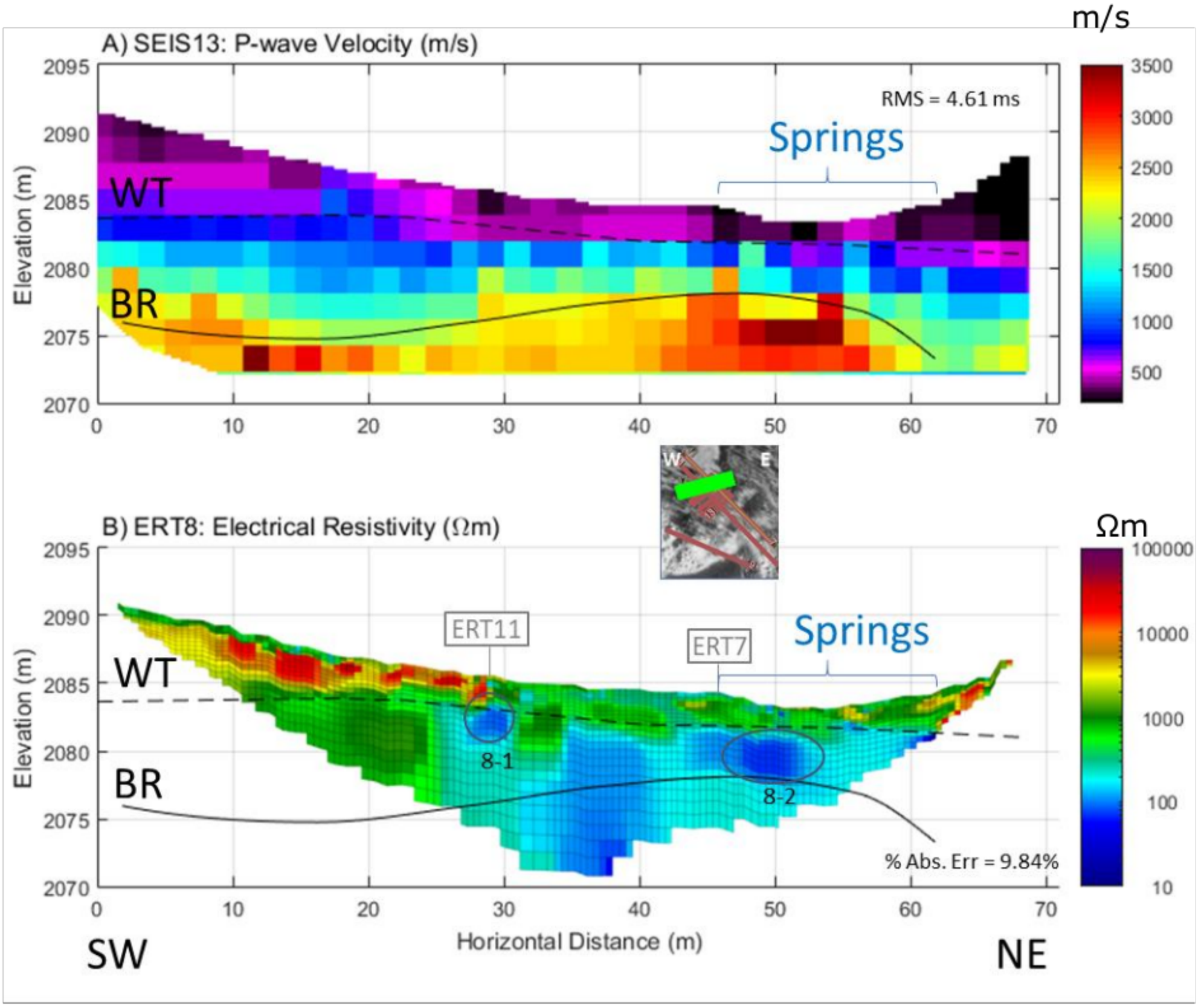

Figure 5-20: Geophysical models near the northern outlet spring along ERT8. Annotations note the elevation of the interpreted depth to bedrock (BR, solid black line), the interpreted depth to saturation (WT, dashed line), the location of the outlet springs SP6 and SP7, the intersection with ERT7 and ERT11, (grey boxes) and low-resistivity anomalies at depth (black ellipses). See Figure 5-10 for the location of this line.

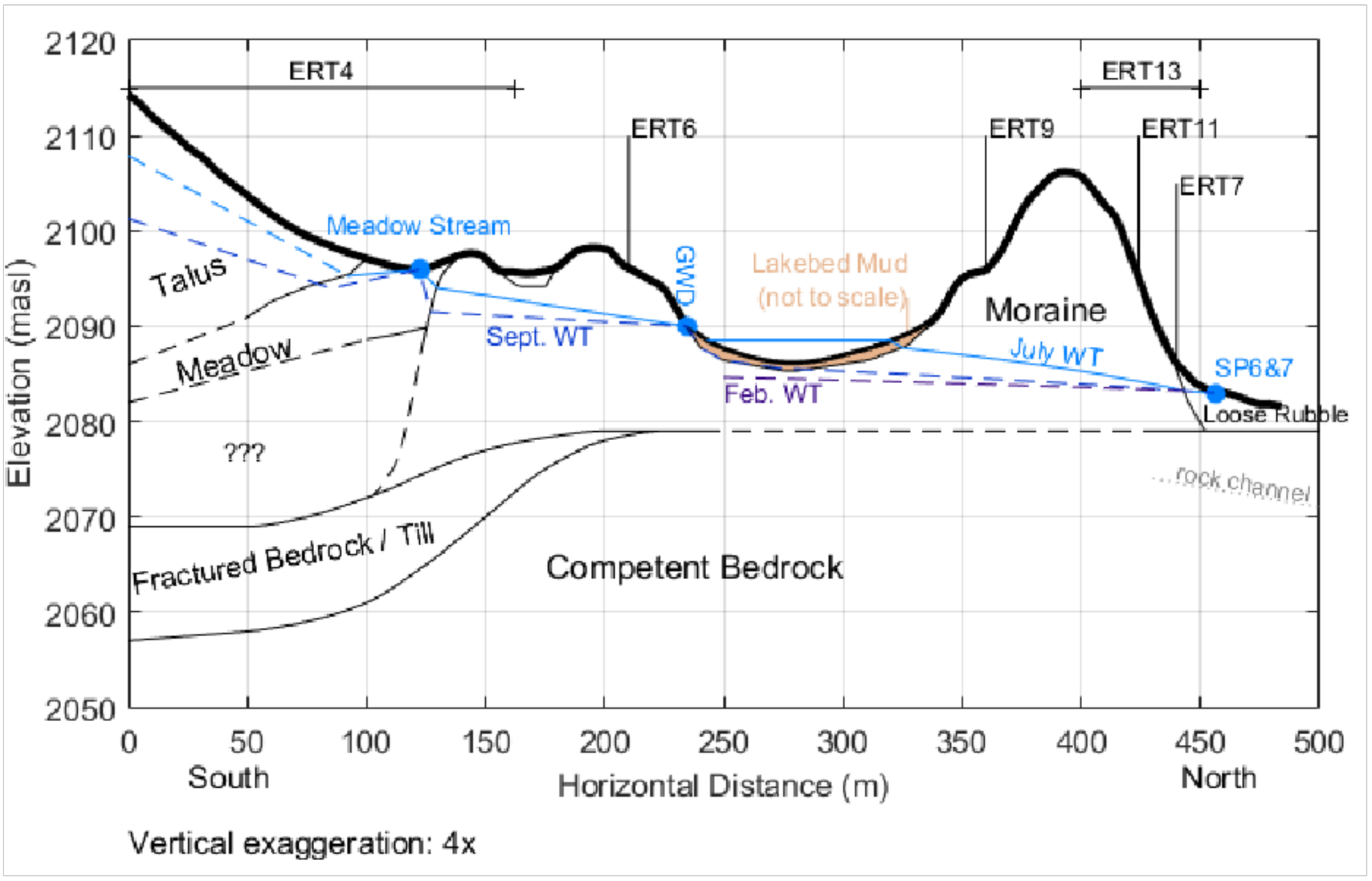

Figure 5-21: A conceptual model showing the geology and water table fluctuations of the study site. Geophysical survey lines parallel to (ERT4) or perpendicular to (ERT1, 6, 9, and 7) this cross-section are noted above. See Figure 5-10 for the alignment of this cross-section.

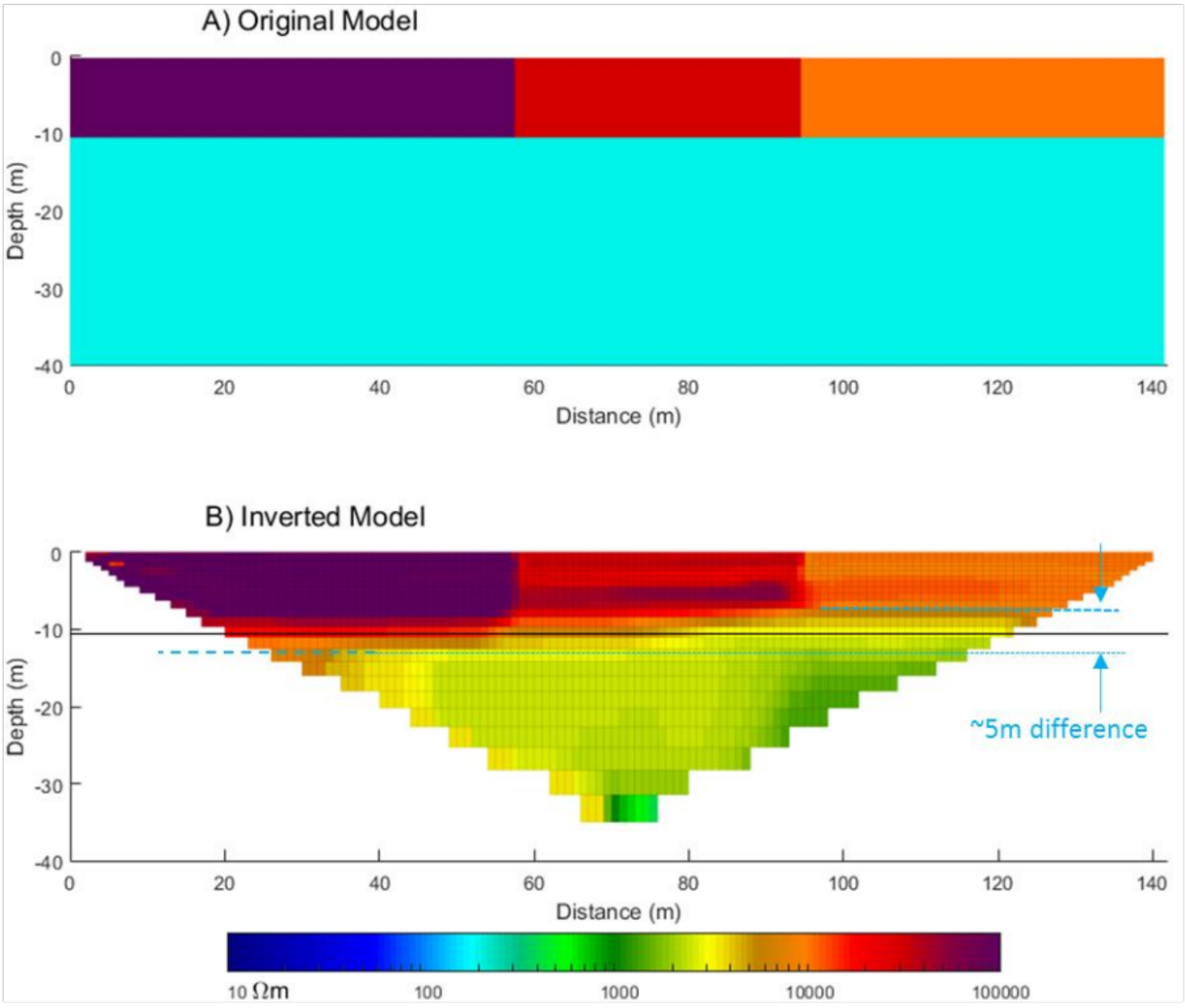

Figure 5-22: Forward modeling exercise with the aim of showing how resistivity of overburden material may affects the interpreted depth to the saturated zone: (A) the known resistivity distribution; (B) the inverted resistivity model based on simulated surface measurements of the known resistivity distribution.

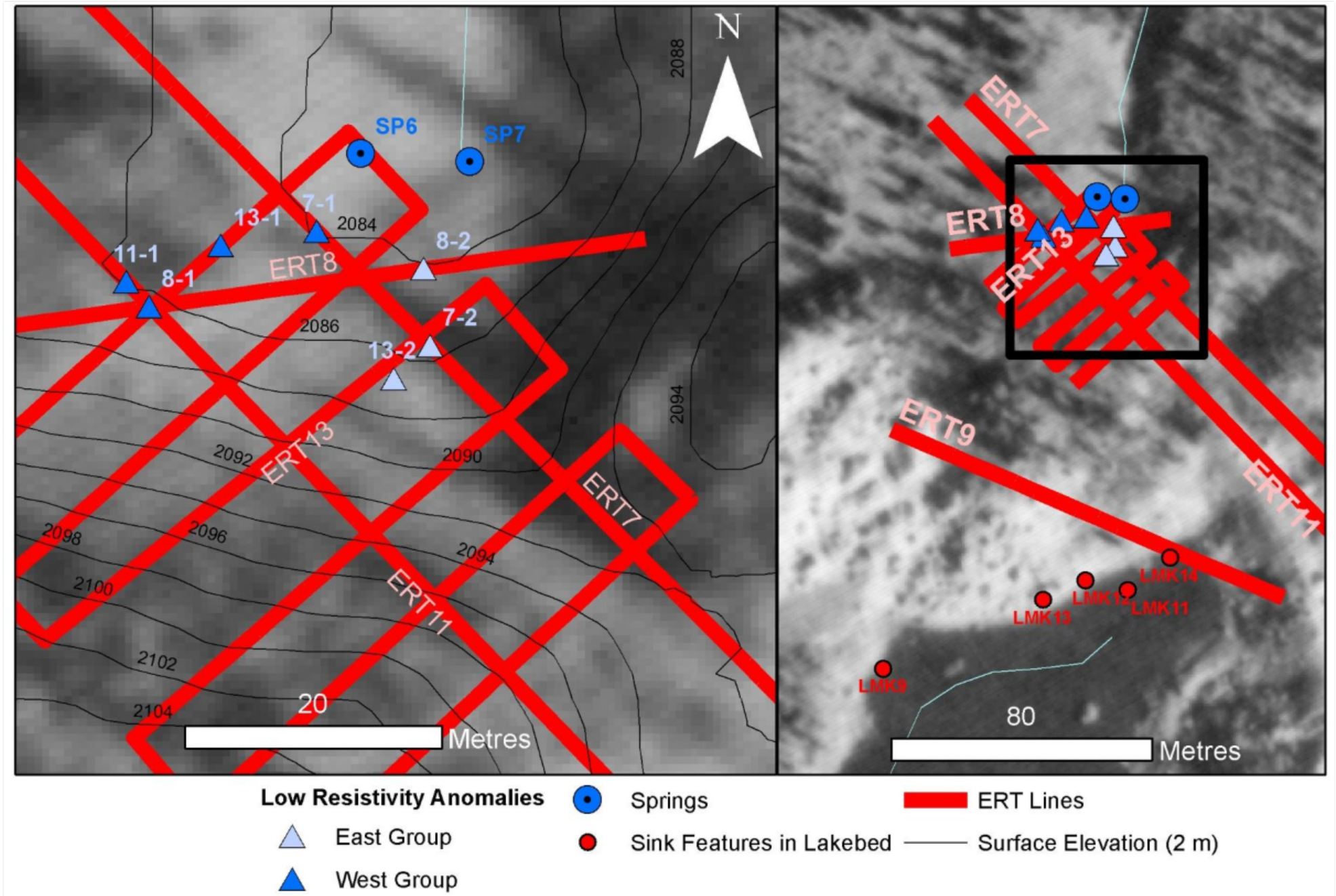

Figure 5-23: Map showing all the low-resistivity anomalies (triangle symbols) imaged around the outlet springs in ERT surveys (Figure 5-18B, Figure 5-19B, and Figure 5-20B).

Chapter 6 **Synthesis**

6.1 Streamflow Comparisons with Nearby Headwater Basins

As discussed in Chapter 4 and Chapter 5, the geophysical images revealed several important subsurface structures that may all plausibly contribute to maintaining wintertime flow at the northern outlet spring. To gauge the relative importance these structures may have, stream temperature and baseflow measurements from other alpine headwater basins in the southwestern Canadian Rocky Mountains are compared in this subsection. These data, many of which are unpublished records provided courtesy of collaborators at the University of Saskatchewan, are summarized in Table 6-1. The data come from three different sites. The Marmot Creek Basin, located approximately 15 km NNE of Bonsai Lake, is primarily tree-covered in lower elevations and talus-covered in its upper sections. A full description is available in Pomeroy et al. (2016). Second, a prominent groundwater spring near Lake O'Hara in the Opabin sub-basin is included. The spring, which is the largest source of stream discharge in the sub-basin, has a contributing area dominated by bedrock and a proglacial moraine that is between 5-30 m thick (Paznekas 2016). The final site included is the groundwater spring at Helen Lake Rock Glacier. Located in the Main Ranges approximately 125 km northwest of Bonsai Lake and 32 km north of Lake Louise, this active rock glacier was studied by Mozil (2016) and Harrington (2017).

There are some uncertainties in computing normalized discharge from the outlet spring at Bonsai. The total annual discharge from the northern outlet spring, as computed from data in Figure 5-9, is 1.7×10^6 to 1.9×10^6 m^3, which equates to 1900-2100 mm of area-normalized discharge over the Bonsai Lake basin (0.92 km^2). This is roughly double the total precipitation measured in the basin (Table 6-1). The discrepancy likely occurs because the surface topography-derived catchment area (0.92 km^2) is not the full area contributing to the spring. This is common problem in alpine hydrology because bedrock topography does not necessarily match surface topography (Langston et al. 2011). As Figure 6-1 shows, there is an area up to 2.9 km^2 (including the Bonsai Lake basin) that drains into the stream confluence below the northern outlet spring and which also is of a greater elevation than the outlet spring ($\geq$ 2082 masl). However, there is another stream with a similar magnitude of flow that drains the northwest portion of the cirque. A conservative, minimum estimate of the area that drains into the other stream instead of the Northern Outlet Spring is 0.6 km^2. Hence, the area contributing to the Northern Outlet Spring is

probably at most 2.3 km^2, and area-normalized winter baseflow from the spring is between 0.4 and 1 mm day^{-1}.

Even when accounting for these uncertainties, area-normalized winter baseflows are anomalously high at Bonsai Lake compared to these other sites listed in Table 6-1. Only Marmot Creek Basin has a range that overlaps (0.2 to 0.7 mm day^{-1}). Paznekas and Hayashi's (2016) compilation of winter baseflow averages for basins 21 to 3873 km^2 ranged between 0.1 and 0.4 mm day^{-1}. Hence, winter baseflow at Bonsai is slightly higher than one other nearby headwater basin in the Kananaskis Valley, and 2-4 times higher than most basins observed in the southeastern Canadian Rocky Mountains.

The data also indicate that the northern outlet spring at the Bonsai Lake basin has rather low amplitude seasonal temperature fluctuations. The springs from the Opabin proglacial moraine and Helen Lake rock glacier reach a maximum of 1.8 °C and 2.2 °C respectively and flow year-round (Table 6-1). This is a bit lower than the maximum 3.0 °C observed at Bonsai (Figure 5-6), though the actual maximum may be slightly higher given that a continuous log of temperature is not available. However, considering the locally defined near-surface lapse rate of mean annual temperature of -4 to -5 °C km^{-1} (Cullen and Marshall 2011), this 1 °C difference in spring temperatures can largely be attributed to differences in elevation (Smerdon et al. 2006; Taylor and Stefan 2009; Benz et al 2016). Hence, it seems that the groundwater system at Bonsai Lake can dampen surface water temperature fluctuations to a similar degree as those at other high-elevation sites.

Attributing these higher winter baseflows and dampened stream temperatures to the subsurface structures imaged by the geophysics is an interpretation consistent with past studies. Both field and modeling studies have shown that the dimensions of an aquifer strongly influence its thermal response, with temperatures of deeper groundwater sources fluctuating less than shallow ones (Kurylyk et la. 2014; Briggs et al 2017). Multiple authors have also argued that bedrock depressions, fracture flow, and thin layers of fine-grain material are important storage mechanisms for maintaining winter baseflow in headwaters (e.g. Paznekas 2016; Winkler et al. 2016; Harrington 2017). Compared to the sites compiled in Table 6-1, Bonsai has an anomalously large bedrock depression, a thick package of unconsolidated material filling it, weaker bedrock that may have a thick fracture zone, and a larger fraction of fine-grained

sediment in talus slopes, all of which can enhance long-term storage. Hence, it is plausible that the temperatures and winter baseflow observed can be explained by the geologic characteristics observed.

However, there are several sources of uncertainty that weaken this hypothesized connection between geology and streamflow at Bonsai Lake. Unlike other sites, meteorological data has only been recorded for two years, so the influence of differences in mean annual precipitation are unknown. There may be microclimatic effects that may also affect stream temperature and total discharge. This includes thermal insulation by deep snowpack, shading from the cliff, and redistribution of snow from other parts of the catchment. Hence, while these data support the notion than subsurface structures play an important role in water storage and temperature regulation, a more complete hydrogeological numerical model is necessary to establish a stronger causal link.

6.2 Physiographic Controls on Groundwater Processes

The next question is: if this causal relationship between the geologic structures observed and streamflow holds true, are there possible spatial patterns where basins will have longer groundwater residence times and less variable stream temperatures? This section discusses possible links between topographic variables and alpine hydrogeology.

This synthesis relies on a comparison of talus deposits at the Opabin sub-basin versus those at Bonsai Lake basin, all of which have been studied in detail with geophysics. Results from this synthesis are summarized in the conceptual map shown in Figure 6-2. On the right side, in blue, are the hydrogeological conditions that the Bonsai Lake basin appears to have: lower hydraulic conductivities and a higher than average groundwater storage potential that maintains winter baseflow. As Section 6.1 elaborates, this hydrogeological characteristic appears to be related to structures present at Bonsai Lake listed in red in Figure 6-2 under “Geomorphic Result”. The following two subsections discusses the rationale behind the left half of Figure 6-2. Specifically, the Bonsai Lake basin and the Opabin sub-basin at Lake O’Hara are compared in terms of geology and topography with the aim of identifying geomorphic processes (orange in Figure 6-2) that may have led to contrasts in structure.

6.2.1 Comparison of Talus Slopes Opabin Versus Bonsai Lake Basins

The hydrogeology and geomorphology of talus deposits at the Bonsai Lake basin differ significantly from those studied by McClymont et al. 2010 and Muir et al. 2011 in the Opabin Sub-Basin of Lake O'Hara. These are discussed in Sections 4.4.1 and 4.4.2 but are summarized here again briefly. Talus deposits at Opabin are generally thinner (no more than 20 m thick), are coarse and open-work, and exhibit less heterogeneity in grain-size distribution. Groundwater flow in those deposits is limited to a thin saturated zone above bedrock. Moreover, they presumably have a lower storage potential because they lack fines except in a thin layer right above bedrock surface. In a larger, global context, Opabin talus slopes seem thinner, are less heterogeneous, and play a less dominant role in overall water balance than most other talus slopes in headwater basins studied elsewhere (Clow et al. 2003; Sass and Krautblatter 2007; Götz et al. 2013; Baraer et al. 2015; Brody et al. 2015). This makes Opabin rather distinct and more of an "end-member" case. Hence, these two detailed case studies from the southeastern Canadian Rocky Mountains, which show a wide divergence in geomorphology and hydrological regimes of talus slopes, provide an opportunity to examine the potential genetic origins of these differences.

6.2.2 Emplacement of Fines in Talus Deposits

First, the fine-grained content of talus, which has a strong control on hydrological properties (Sections 4.1 and 4.4.2), may be explained by differences in bedrock characteristics. At Opabin, the source material from the adjoining headwalls is largely carbonate and quartzite rock with rather sparse joint spacing (Price et al. 1980; Hislop 2008; Muir et al. 2011). In contrast, the headwall at Bonsai Lake has both competent carbonates from the Palliser Formation but also weaker and more recessive shales from the Banff and Exshaw Formations that are weathered into smaller pieces. As Figure 6-2 indicates, this heterogeneous bedrock leads to poorly-sorted talus deposits (e.g. Figure 4-8C), lower porosity due to denser packing, and consequently lower hydraulic conductivity.

The fine-grained content of talus may also be related to the formation process of the deposit. White (1981) observed that alluvial talus in general has more fines content because small grains are washed in to pore spaces between larger boulders. Similarly, de Scally and Owens (2005) showed that for alluvial fans whose areal extents were similar to the talus cones of the present

study, the smallest grain sizes occurred in alluvial deposits, the largest in avalanche-dominated deposits, and intermediate particle sizes in debris-flow deposits. Even within the talus cones surveyed in the present study, areas directly downslope of the waterfall on the Central Cone have a greater proportion of fine grains. Moreover, fluvial redistribution appears to play a minimal role in sediment redistribution at Opabin compared to rockfall and avalanche processes (Muir et al. 2011). Hence, as Figure 6-2 shows, talus cones with *increased fluvial redistribution* are expected to have a lower hydraulic conductivity.

Fluvial erosion may play a bigger role at Bonsai because of the relief of the headwall areas above the talus. First, the contributing area above talus cones is greater at Bonsai. As Figure 6-3A and B show, the lowermost, main cliff face extends approximately 400 m horizontally in front of the drainage divide at Bonsai, but only by approximately 300 m at Opabin. Its headwall has a northerly aspect compared to Opabin's NW orientation, and it has a less steep and more stepped topographic profile that may support a thicker snowpack that helps sustain flow in the waterfalls through the summer (Figure 6-3C and D). Moreover, unlike Opabin, Bonsai has a deeply incised headwall where couloirs concentrate flow into streams (Figure 4-1). This leads to an increased erosive potential and hence more fluvial redistribution within the talus (Fryxell and Horberg 1943; van Steijn 1995; Sass and Krautblatter 2007). Hence, in Figure 6-2 , headwall aspect, headwall slope, headwall catchment area, and presence of couloirs are all linked to increased fluvial redistribution.

6.2.3 Thickness of Talus Deposit

Several factors are known to affect erosion rates of cliff faces. First, cliff faces associated with fault scarps, high-curvature folds, and newly exposed cirque walls are more susceptible to large-volume rockfall (Butler et al. 1986; Coe and Harp 2007; Melzner et al. 2013). Thapa's (2017) study of talus slopes in Kananaskis headwater basins near Bonsai Lake found that talus deposits were more likely to be present and thicker where these three features are present. Beyond the presence of faults, folds, and cirques, studies in both the Canadian Rocky Mountains (Gardner 1983) and European Alps (Sass and Wollny 2001; Sass 2007) have shown that north-facing rock walls weather more quickly due to enhanced frost cracking (i.e. mechanical weathering from ice). Lastly, rockmass properties also influence weathering rates of alpine cliffs. Moore et al. (2009) showed that lower intact rock strength, smaller joint spacing, more heavily altered joint surfaces,

and certain joint orientations are correlated to higher rates of cliff erosion. Rockmass properties of the upper slopes were not directly observed, but many aspects of rockmass rating systems (specifically intact rock strength and joint condition) do correlate with lithology and mineralogy. Generally, siliciclastic sedimentary rocks have a lower unconfined compressive strength compared to igneous and high-grade metamorphic rocks (Bieniawski 1974), and quartz-rich rocks are not as easily chemically altered as pelagic rocks (Bieniawski 1989). Hence, alpine cliffs with shaded aspect, highly-altered and jointed rock, softer, young sedimentary rock, and geologic structures that weaken rock should expect higher rates of erosion and hence thicker talus deposits.

A comparison of Bonsai Lake and Opabin is consistent with this theory. The headwall at Bonsai is north-facing, is coincident with the Sulphur Mountain Thrust Fault, is the headwall of a glacial cirque, and is within 1 km of where McMechan (2012) mapped the hinge zone of a major syncline. In contrast, no major folds or faults are present in the headwall above the talus slopes studied at Opabin (Price et al. 1980; Hislop 2008), and the slope is more northwest-facing. Furthermore, Bonsai Lake, which has a carbonate and shale headwall, should expect higher rockfall rates than Opabin, where the headwall is of limestone and quartzite. While it is not clear which of these inter-basin differences may be the most important determinant(s) of weathering rates, this comparison suggests that lithology, structure, and topography indeed affect talus deposit thickness and may therefore affect groundwater storage potential of a basin. Hence, in Figure 6-2, “Shaded aspect,” “Weaker bedrock,” and “Fault scarps, cirques, folds” on the left side of the figure have all been linked to “Higher rockfall rates.”

6.2.4 Comparison to Previous Studies and Upscaling of Results

This comparison of Opabin and Bonsai and the resulting conceptual model put forth in Figure 6-2 is consistent with Paznekas and Hayashi’s (2016) statistical analysis comparing winter baseflow in alpine watersheds and builds on their results. They saw a correlation between baseflow and age of bedrock, which was used as a proxy for rock strength. This agrees with Figure 6-2, which shows that softer bedrock leads to increased rockfall rates and hence thicker talus deposits. Their study also found a significant correlation between mean annual precipitation and baseflow. The precipitation contrast between Opabin and Bonsai was minimal, but given that increased precipitation leads to increased fluvial erosion and lower-porosity rockfall deposits (Sass and Krautblatter 2007), this second correlation is also consistent with the geomorphic

process shown in Figure 6-2. The comparison suggests that other physiographic variables may affect alpine headwater hydrogeology beyond the ones Paznekas and Hayashi (2016) found to be statistically significant. They studied watersheds ranging from 21 to 3873 km^2, but none of those compared in this thesis (Section 6.1) were greater than 14 km^2. Hence, variables that vary on smaller spatial scales (e.g. average slope, hypsometric integral) would have been averaged out in Paznekas and Hayashi's (2016) analysis, while differences in aspect, headwall characteristics, etc. are more prominent in the present study.

However, without a more well-defined statistical relationship between these topographic and hydrogeological parameters, it is still difficult to precisely predict where alpine groundwater storage will be enhanced. At a regional scale in the southeastern Canadian Rocky Mountains, pre-Mesozoic rocks, which make up the Main Ranges, are more resistant to weathering than the Mesozoic rocks of the Front Ranges (Osborn et al 2006). This should lead to generally lower hydraulic conductivity and increased storage potential in talus slopes in the Front Ranges. Yet, mean annual precipitation generally decreases from the Main Ranges going east (Government of Canada et al. 2010), so one might expect more low-porosity, fluvial talus in Main Ranges. Without an understanding of the relative magnitude of either effect, one cannot generalize about regional patterns in groundwater storage at this point. The same is true when comparing smaller (<15 km^2) basins because the strength of the link between hydrologic parameters and topographic variables that vary on small spatial scales is unknown. Thus, while the causal links in Figure 6-2 are backed by both the comparison of two small watersheds in this study and by previous studies in alpine geomorphology, a quantitative understanding remains elusive.

Nonetheless, the present study does contribute two new important insights. First, it provides some evidence for the geomorphic processes that link topographic variables and groundwater dynamics at a regional scale suggested by authors like Paznekas and Hayashi (2016). Second, it points to characteristics of headwater basins that may have an important control on groundwater dynamics at small spatial scales (i.e. <15 km^2) and that are worthy of further investigation.

6.3 Implications for Alpine Hydrology

While this study falls short of defining statistical relationships between topographic variables and hydrogeologic parameters, it provides some important lessons for hydrogeological modelling of mountain areas. First, it provides a cautionary note for a common approach for constructing

conceptual models. Modellers often divide alpine watersheds into "hydrologic response units," (e.g. Pomeroy et al. 2007), areas that are grouped together based on similar features such as land cover, slope angle, aspect and elevation. Often, this involves grouping different landscape units such moraines, meadows, and talus slopes together, and this method is valid in basins where vertical variations in hydraulic parameters are minimal and overburden is thin (e.g. Fang et al. 2013; Paznekas 2016). However, the geophysical images at Bonsai Lake demonstrate that simply taking an inventory of sedimentary units seen at surface can lead to an erroneous conceptual model because there may be hydrologically significant layers at depth. Moreover, this study demonstrates that though two basins may have a type of landform in common, the hydrologic regimes of the unit may differ significantly between basins. For instance, talus is present at both Opabin and Bonsai, but the dominant groundwater flow paths were different: bedrock interface flow was most important at Opabin, while grain size heterogeneity was the dominant control at Bonsai. This demonstrates that for larger, process-based hydrologic models, it is invalid to assume that similar landscape units in different basins can always be modeled in the same manner.

Furthermore, while regional trends remain unknown, this study points to which alpine headwaters may be of higher priority for conservation. The topographic variables listed in Figure 6-2 are almost all available through public data sets, allowing one to identify basins that are more likely to have greater groundwater storage potential, more consistent stream flow temperatures, and higher winter baseflows. These insights would assist water resource and ecosystem managers in identifying headwaters that may be more resilient or more vulnerable to climate change and hence have water resources and aquatic habitat that require more urgent conservation efforts. While the proposed model is only qualitative, it is a tool that may help managers to narrow down potential sites that warrant more detailed field study.

6.4 Other Limitations

The spatial and temporal resolution of the geophysical methods are limited. There is simply insufficient resolution or petrophysical contrast to image processes like creep, dry grain flow, supranival sliding, meteoric diagenesis, etc. in talus slopes (Sass and Krautblatter 2007; Sanders et al. 2010a, 2010b). The talus and meadow areas are often inaccessible due to avalanche risk. Hence, this study cannot comment on geomorphic and hydrologic phenomena occurring at small spatial scales or in winter. Moreover, geophysical methods cannot directly measure

hydrogeological parameters like porosity or hydraulic conductivity, so source areas and relative contribution of different landscape units remain unknown.

Moreover, only a fraction of the Bonsai Lake basin has dense data coverage. Given the complex geometry of the landscape units studied, the 2D cross section (Figure 5-21) may not necessarily be representative for the whole drainage basin. Similarly, the full extent of the ice body is not known and may play a more significant role in stream temperature moderation than this first set of geophysical surveys suggests. As Table 5-1 shows, the resistivity of the water emerging from SP5 (70 Ωm; 140 µS/cm) is much higher than that sourced from SP4 (10-30 Ωm; 1000-330 µS/cm). Temperature measurements from Figure 5-9 show that SP5 was much colder (<0.5°C) than other springs measured in July 2015. A large body of permafrost in the East Talus Slopes might contribute to these contrasts. While mapping the extent of permafrost might be feasible with surface temperature measurements, mapping bedrock topography would require more geophysical data. This is important not only for finding other topographic lows like that under the meadow, but also critical for better delineating the true area that contributes to the northern outlet spring. A tool like the horizontal-to-vertical spectral ratio (HVSR) seismic method has been used to quickly map bedrock depth in alpine zones (e.g. Briggs et al. 2017) and may be a faster alternative to SRT.

Lastly, the geophysical methods used may have issues with accurately imaging water content that does not monotonically increase with depth. GPR consistently had issues with signal penetration in saturated zones, shallow conductive zones are known to mask higher resistivity layers below (Langston et al. 2011), and the problem of imaging alternating low- and high-velocity layers is well known in seismic refraction. Hence, alternative conceptual models, such as separate perched and deep flow systems in the meadow, would be difficult to detect.

6.5 Priorities for Future Study

At Fortress Mountain, some aspects of the geological model remain poorly constrained. Now that a preliminary conceptual model is now in place, targeted ground truth data in a few key locations can help address the weaknesses of the geophysical methods. The layers between the meadow and bedrock is one such location where a borehole may be needed to identify deeper layers. Further BTS or geophysical data should also be used to map the full extent of permafrost in the Upper East Talus Cone and the Eastern Talus Slopes.

The hydrogeological conceptual model put forth in this study should be tested further. Geochemistry data, particularly ion analysis, isotopes, etc. would help constrain the relative contributions from different flow paths, particularly from deeper units like the bedrock that are not visible at surface. A numerical model of the site should also be included to test whether the geologic structures imaged indeed have a strong influence on streamflow. Some measure of hydraulic conductivity of the landscape units will thus be necessary to build this model, whether through grain size analysis, tracer tests, or pumping tests. Given the uncertainties in contributing area, mapping bedrock topography throughout the rest of the cirque would be valuable for constructing a more accurate simulation.

Other geophysical and hydrogeological data from different alpine headwater basins is needed to test the links between topographic variables and hydrogeologic parameters proposed in Figure 6-2. One option is to do case studies in basins that are like those in previous studies but different in only one or two key ways. For example, one could find a talus slope at base of a cliff formed by Sulphur Mountain Thrust Fault that lacks overlying shales and instead has only carbonate units. This could help confirm or refute the role of headwall rheology in talus hydrogeological properties. One such location in a neighbouring cirque fits these criteria (Figure 6-4). Moreover, a large body of literature exists that links topoclimatic variables with geomorphic properties of individual landscape units like talus and moraine. These studies, which are reviewed in Appendix G, hint at other links between topography and hydrogeology. More field studies, in the long run, should lead to an aggregate statistical analysis analyzing these links as Paznekas and Hayashi (2016) did, but on much smaller (< 15 km^2) basins or on individual landscape units.

6.6 Tables

Table 6-1: Summary of important hydrometric and climatic characteristics of alpine streams previously studied in the southeastern Canadian Rocky Mountains. Bracketed numbers indicate years measured

	Location (decimal latitude, longitude, WGS1984)	Gauging elevation (masl)	Catchment area (km^2)	Winter baseflow ($mm\ day^{-1}$)	Maximum stream temperature (°C)	Mean annual precipitation (mm)	Data sources
Bonsai Outlet Spring	50.820844, -115.21369	2082	>0.92*	0.4 to 1** (2015-2016)	*3.0*** (2015)	*890 to 1500* (2014-2016)	*J. Pomeroy, X. Fang, and H. Wu, personal communication*
Marmot Creek Basin	50.951454, -115.153979	1600	9.4	0.2 to 0.7 (2014-2016)	-	1100 (Storr 1967)	Pomeroy et al. 2016; *J. Pomeroy, personal communication*
Spring in Opabin Basin	51.341784, -116.32075	2234	2.9	~0.3 (2016)	1.8 (2005)	1000 to 1200 (2006-2015)	Roy and Hayashi (2009); Hood and Hayashi (2015); Paznekas (2016)
Lake O'Hara Outlet	51.358101, -116.338952	2021	14	0.14 (2013-2016)	-		
Helen Lake Rock Glacier Spring	51.678176, -116.41303	2320	0.4 to 0.5	0.09 (2015-2016)	2.2 (2015-2016)	-	Harrington (2017)

*See discussion of catchment area uncertainty in Section 6.1
**.5-1 $mm\ day^{-1}$ when using 1.8 km^2 area, but 0.4-0.8 $mm\ day^{-1}$ when using most conservative estimate of catchment area (2.3 km^2)
***Author's own measurements

6.7 Figures

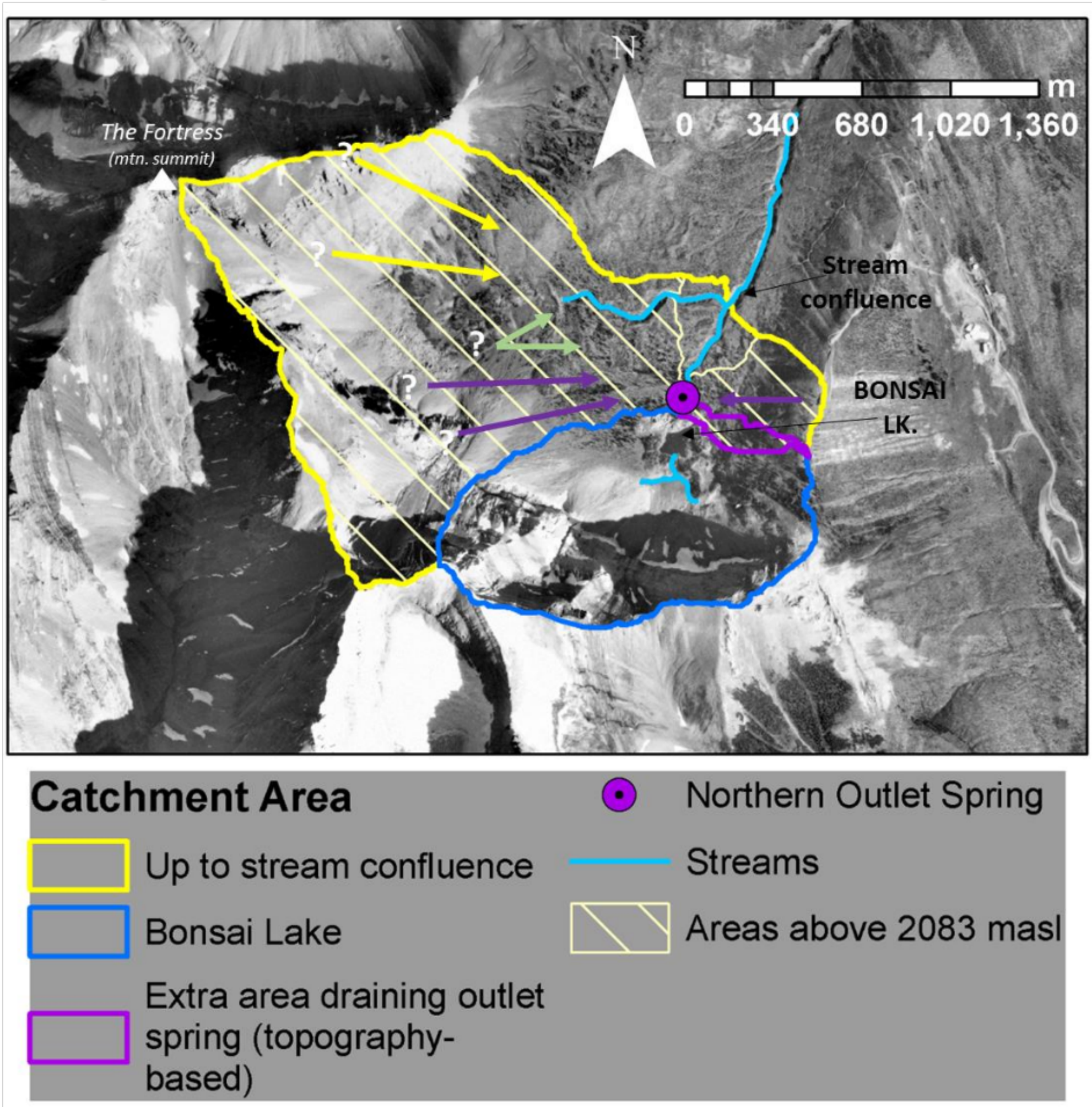

Figure 6-1: Map showing the whole cirque southwest of The Fortress. The yellow polygon indicates catchment area (as derived from surface topography) upstream of an important stream confluence. Thicker arrows indicate groundwater flow lines in areas that may plausibly drain into the Northern Outlet Spring (purple) or the northwestern stream branch (yellow) due to unknown bedrock topography. The exact demarcation between the two zones is not exactly known, as suggested by the green arrows.

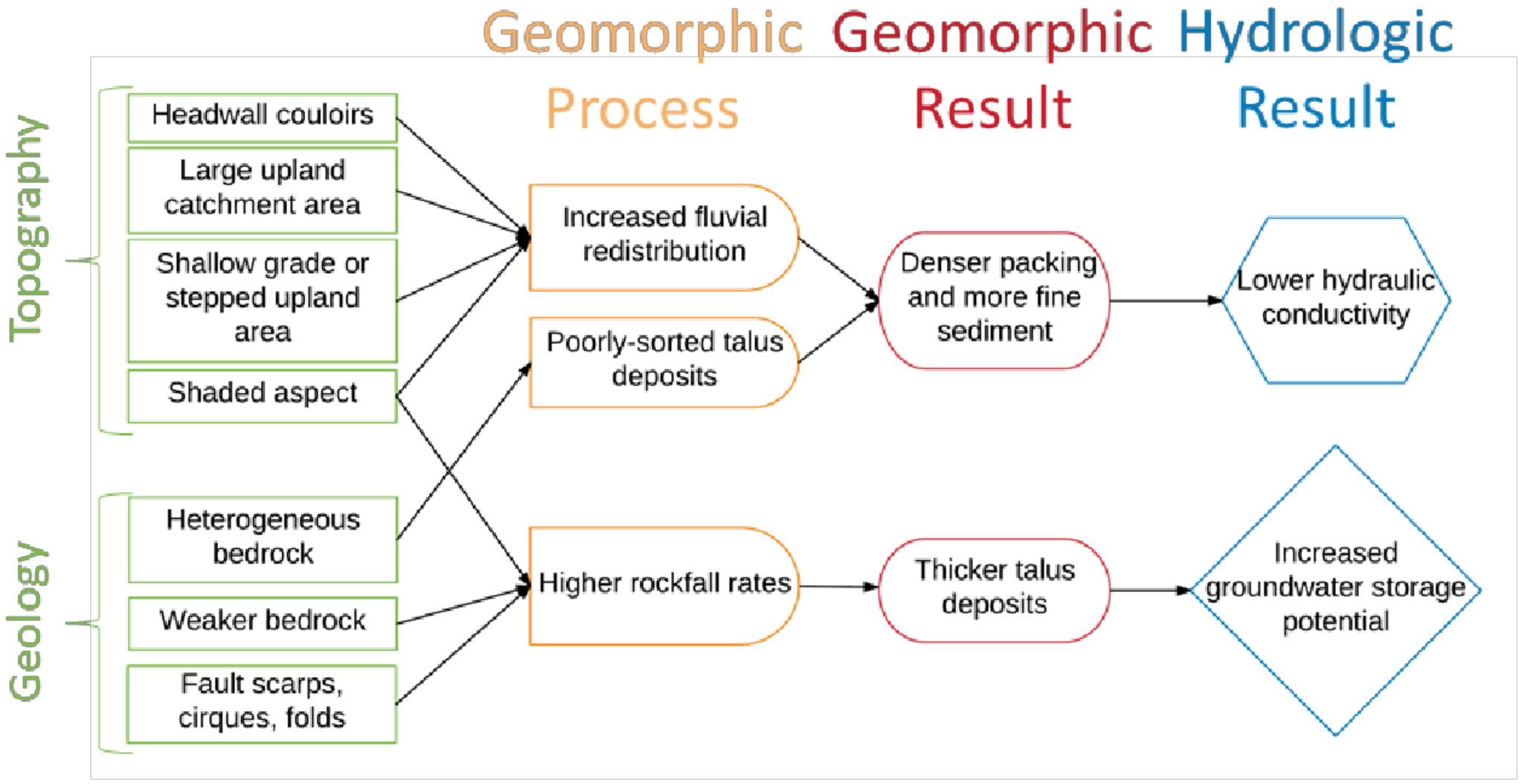

Figure 6-2: A model summarizing how topographic and geologic variables (in green) affect the geomorphologic processes (orange) and hence the geomorphology of talus deposits (red) and in turn their hydrogeological characteristics (blue).

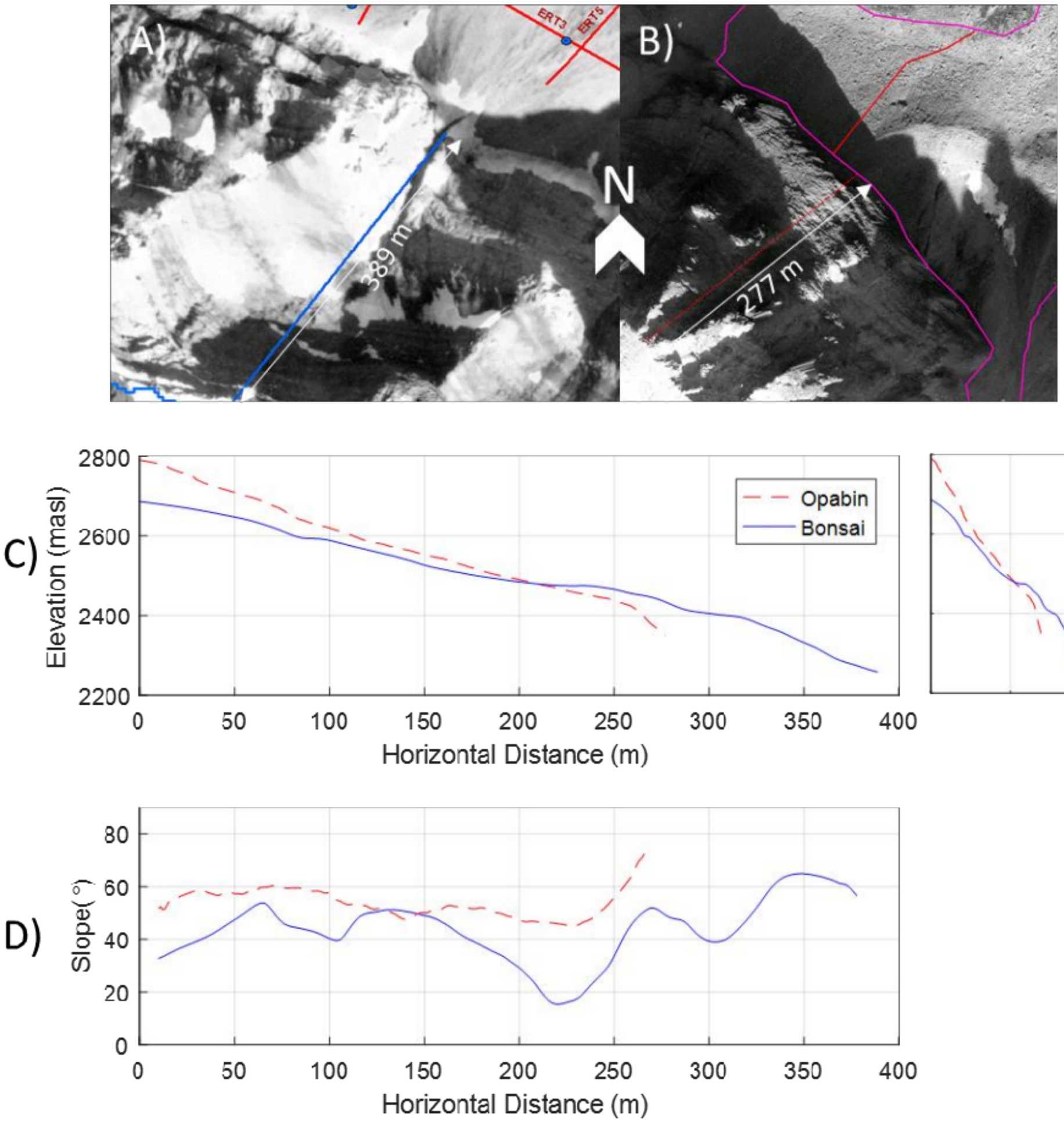

Figure 6-3: Comparisons of the headwall characteristics at Bonsai Lake (A) above the Central Cone, and Opabin (B) above the talus studied by Muir et al. (2011). Elevation profiles (C) and calculated slopes (D) are shown along the solid blue and dashed red lines in in A) and B). The second panel on the right in C) shows the same data but with a 1:1 horizontal to vertical aspect ratio.

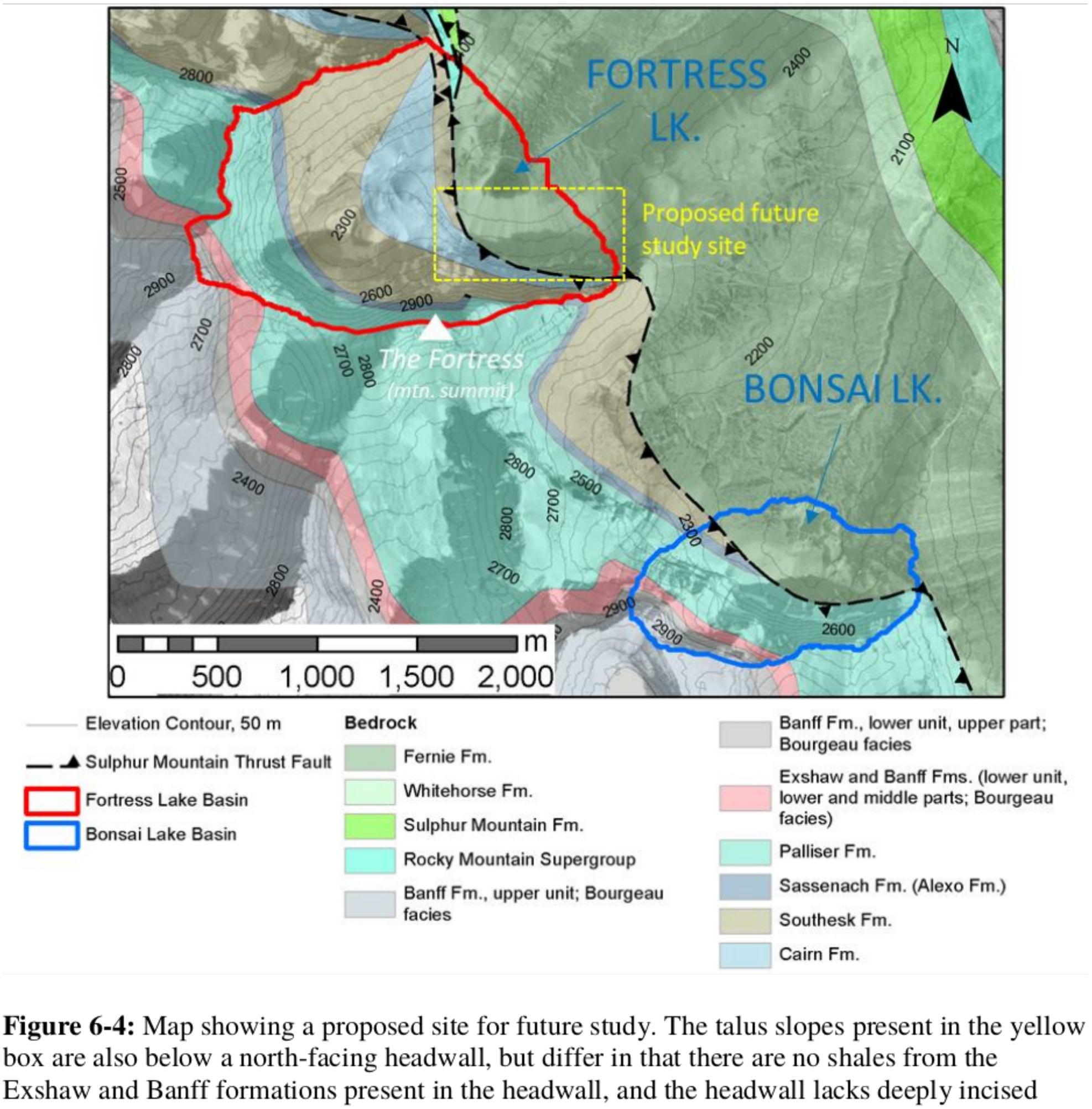

Figure 6-4: Map showing a proposed site for future study. The talus slopes present in the yellow box are also below a north-facing headwall, but differ in that there are no shales from the Exshaw and Banff formations present in the headwall, and the headwall lacks deeply incised gullies.

Chapter 7 **Conclusions**

Mountain regions are key sources of river flow both worldwide and specifically in the western Canadian Prairies. Groundwater is critical for maintaining streamflow in alpine zones, but detailed studies have been limited to only a few locations. This study aimed to identify the controls on groundwater storage and flow processes at a new study site: a headwater basin herein referred to as the Bonsai Lake basin located in the Front Ranges of the southeastern Canadian Rocky Mountains. This was accomplished by imaging major subsurface structures with geophysical methods. By comparing results to earlier studies, the overreaching goal was to identify possible trends linking geomorphology and groundwater dynamics at a larger scale.

Geophysical surveys showed that the talus deposits are generally 20-40 m thick, and as thick as 60 m in places. There are strong lateral and vertical variations of grain size distribution related to which sediment redistribution process dominates: recent, coarse rockfall being coarser and more openwork, and areas with fluvial redistribution having more fine-grained content. These heterogeneities are the most important controls on flow paths, leading to perched water tables and fast, convergent flow paths, explaining the presence of springs on the surface of these talus slopes. In addition, a large permafrost body was detected in a shaded portion of the talus at an elevation 2120 masl, but its full extent remains unknown

In low-lying areas of the basin, a thick zone of unconsolidated material up to approximately 35 m thick lies below the alpine meadow. The combination of an overdeepened subglacial basin and large moraines seems to have contributed to the formation of this large deposit of sediment. The data suggest that the deep bedrock basin, the thick package of sediments, and talus slopes upland help regulate streamflow at the northern outlet stream. Near this outlet spring, heterogeneities in overburden porosity and anomalous bedrock topography both play a role in controlling flow paths.

These results contrast with some hydrological studies of alpine headwaters but corroborate the findings of others. Bedrock interface flow is not as important in talus slopes here as it was in studies of similar coarse-grained deposits at the Opabin Sub-basin at Lake O'Hara. Yet, earlier studies agree that thick packages of unconsolidated material, including large bedrock depressions under meadows and moraine-dammed basins, can help regulate streamflow. Moreover, while

previous hydrological studies have indirectly inferred that bedrock topography and heterogeneity of grain sizes and porosity in overburden material lead to fast, convergent flow paths, this is one of the first hydrogeological studies to image such features with geophysics.

A comparison of streamflow data between Bonsai Lake basin and nearby basins shows that area-normalized winter baseflow is slightly higher than another headwater basin in the Kananaskis Valley, and 2-4 times greater than other alpine headwaters observed in the southeastern Canadian Rocky Mountains. Moreover, the temperature of the outlet spring has seasonal temperature fluctuations comparable to springs at previously studied site in the Main Ranges. Detailed numerical modeling is needed to more firmly establish a causal link between the structures observed and these anomalous features of the outlet spring.

Yet, assuming that this hypothesized link holds true, this study points to physiographic variables that may be used to identify basins with that may have anomalously high storage potential and a capacity for buffering stream temperature. These links between physiographic variables, geomorphic processes, and hydrologic processes are summarized as a conceptual model in Figure 6-2. This model is based on physiographic comparison of talus slopes at Opabin and Bonsai Lake, as well as by a review of relevant alpine geomorphology literature. While this analysis does not offer a quantitative, statistical link between topographic and hydrogeological parameters, it does accomplish three main things. First, it suggests mechanisms linking regional variables like rheology and faults to hydrologic variables like winter baseflow that previous aggregate statistical studies lacked. Second, it points to basin characteristics that may have an important control on groundwater dynamics in small (i.e. <15 km^2) headwater basins. Furthermore, this model may help water resource managers and ecologists narrow down which headwater basins may be more resilient or vulnerable to climate change and prioritize areas for future field work and conservation efforts.

In a broader sense, this study has two main implications for the discipline of alpine hydrology, specifically on how to set up numerical models. Dividing a basin in hydrologic response units based only on the landscape units at surface is insufficient because overburden may be surprisingly thick in alpine zones and hydrologic properties may vary significantly with depth. Also, the contrast in dominant flow processes in similar landscape units (i.e. talus cones) may

differ between basins, and hence ought not necessarily be treated the same in process-based hydrogeological models.

A key limitation of this study is the low resolution and ambiguity of certain parts of the geophysical images. Future studies at this study site can reduce this ambiguity by collecting additional data. This includes drilling to identify unknown layers below the meadow, mapping the full extent of permafrost, and using HSVR seismic methods to map depth to bedrock over a wider area. Additional geochemical data would help assess the relative contribution of different flow paths, especially through deeper layers like fractured bedrock. Integrating this new information, along with measurements of hydraulic conductivity, into a numerical model would help develop a more detailed understanding of the hydrogeology of the basin.

Moreover, further case studies of new alpine headwaters should be collected to test the hypothesized links between geomorphological and hydrogeological processes. As a first step, this may take the form of finding basins or individual landscape units that are like those in the present study but which vary in a limited number of ways. After building a sufficient inventory of such case studies, an aggregate statistical analysis, which would be akin to Paznekas and Hayashi (2016) but focusing on smaller basins or individual landscape units, may be used to assess the relative importance of the physiographic variables identified in Figure 6-2.

References

AMEC. 2009. South Saskatchewan River Basin in Alberta Water Supply Study. Lethbridge, Alberta. [accessed 2017 May 03] http://www1.agric.gov.ab.ca/$Department/deptdocs.nsf/all/irr13053/$FILE/ssrb_main_report.pdf

Alberta Agriculture and Forestry. 2017. Alberta Climate Information Service: Interpolated weather data since 1961 for Alberta Townships. [accessed 2017 July 05] http://agriculture.alberta.ca/acis/township-data-viewer.jsp .

Alberta Agriculture, Food, and Rural Development. 2003a. Mean wind speed and prevailing direction (September, October and November): 1971 to 2000. [accessed 2017 May 30] http://www1.agric.gov.ab.ca/$department/deptdocs.nsf/all/sag6453. Agroclimatic Atlas of Alberta: Maps.

Alberta Agriculture, Food, and Rural Development. 2003b. Mean wind speed and prevailing direction (December, January and February): 1971 to 2000. [accessed 2017 May 30] http://www1.agric.gov.ab.ca/$department/deptdocs.nsf/all/sag6450. Agroclimatic Atlas of Alberta: Maps.

Alberta Agriculture, Food, and Rural Development. 2003c. Mean wind speed and prevailing direction (March, April and May): 1971 to 2000. [accessed 2017 May 30] http://www1.agric.gov.ab.ca/$department/deptdocs.nsf/all/sag6451. Agroclimatic Atlas of Alberta: Maps.

Alberta Energy and Natural Resources. 1976. Panchromatic aerial photography of the Kananaskis region of Alberta. Edmonton, AB, Canada: Alberta Energy and Natural Resources. 68 black and white 26 x 26 cm images.

Alberta Environment and Parks. Air Photos [general information website]. [accessed 2017 May 08] http://aep.alberta.ca/forms-maps-services/air-photos/default.aspx.

Alberta Sustainable Resource Development (Air Photo Distribution). 2008. Kananaskis Improvement District colour aerial photographs. Edmonton, AB, Canada: Alberta Sustainable Resource Development. 187 colour 26 x 26 cm remote sensing images.

Ammon CJ, Vidale JE. 1993. Tomography without rays. Bulletin of the Seismological Society of America. 83:509-528.

Anderson RS. 2000. A model of ablation-dominated medial moraines and the generation of debris-mantled glacier snouts. Journal of Glaciology. 46:459-469. DOI: 10.3189/172756500781833025.

Andrews JT. 1972. Glacier power, mass balance, velocities and erosion potential. Zeitschrift für Geomorphologie. 13:1-17.

Ashmore P, Church M. 2001. The impact of climate change on rivers and river processes in Canada. Geological Survey of Canada Bulletin 555. Ottawa: Natural Resources Canada. DOI: 10.4095/211891.

Ballantyne CK. 2002. Paraglacial geomorphology. Quaternary Science Reviews. 21:1935-2017. DOI: 10.1016/S0277-3791(02)00005-7.

Bandyopadhyay J, Kraemr D, Kattelmann R, Kundzewicz Z. 1997. Highland waters: a resource of global significance. In: Messerli B, Ives J, editors. Mountains of the world: a global priority. New York: Parthenon. p. 131-151.

Baraer M, McKenzie J, Mark BG, Gordon R, Bury J, Condom T, Gomez J, Knox S, Fortner SK. 2015. Contribution of groundwater to the outflow from ungauged glacierized catchments: a multi-site study in the tropical Cordillera Blanca, Peru. Hydrological Processes. 29:2561-2581. DOI: 10.1002/hyp.10386.

Barnett TP, Adam JC, Lettenmaier DP. 2005. Potential impacts of a warming climate on water availability in snow-dominated regions. Nature. 438:303-309. DOI: 10.1038/nature04141.

Barr ID, Lovell H. 2014. A review of topographic controls on moraine distribution. Geomorphology. 226:44-64. DOI: 10.1016/j.geomorph.2014.07.030.

Bash EA, Marshall SJ. 2014. Estimation of glacial melt contributions to the Bow River, Alberta, Canada, using a radiation-temperature melt model. Annals of Glaciology. 55:138-152. DOI: 10.3189/2014AoG66A226.

Benn DI, Lehmkuhl F. 2000. Mass balance and equilibrium-line altitudes of glaciers in high-mountain environments. Quaternary International. 65-66:15-29. DOI: 10.1016/S1040-6182(99)00034-8.

Bentley LR, Gharibi M. 2004. Two- and three-dimensional electrical resistivity imaging at a heterogeneous remediation site. Geophysics. 69:674–680. DOI: 10.1190/1.1759453.

Benz SA, Bayer P, Goettsche FM, Olesen FS, Blum P. 2016. Linking surface urban heat islands with groundwater temperatures. Environmental Science and Technology. 50:70-78. DOI: 10.1021/acs.est.5b03672.

Berthling I, Etzelmüller B, Isaksen K, Sollid JL. 2000. Rock Glaciers on Prins Karls Forland. II: GPR Soundings and the Development of Internal Structures. Permafrost and Periglacial Processes. 11:357–369. DOI: 10.1002/1099-1530(200012)11:4<357::AID-PPP366>3.0.CO;2-6.

Berthling I, Etzelmüller B, Wåle M, Sollid JL. 2003. Use of Ground Penetrating Radar (GPR) soundings for investigating internal structures in rock glaciers. Examples from Prins Karls Forland, Svalbard. Zeitschrift für Geomophologie. Supplement 132:103-121.

Bertran P, Francou B, Pech P. 1993. Stratogenèse associée à la dynamique des coulées à front pierreux en milieu alpin, La Mortice, Alpes méridionales, France = Bedding Associated to the Dynamics of Stone-Banked Sheets in an Alpine Environment (La Mortice, Southern Alpes, France). Géographie Physique et Quaternaire. 47:93. DOI: 10.7202/032933ar. French, English.

Bieniawski ZT. 1989. Engineering rock mass classification: A complete manual for engineer and geologists in mining, civil, and petroleum engineering. New York: Joh Wiley and Sons.

Bieniawski, ZT. 1974. Estimating the strength of rock materials. International Journal of Rock Mechanics and Mining Sciences & Geomechanics Abstracts. 11:A160. DOI: 10.1016/0148-9062(74)91782-3.

Bonsal B, Shabbar A. 2008. Impacts of large-scale circulation variability on low streamflows over Canada: a review. Canadian Water Resources Journal. 33:137-154. DOI: 10.4296/cwrj3302137.

Briggs MA, Lane JW, Snyder CD, White EA, Johnson ZC, Nelms DL, Hitt NP. 2017. Shallow bedrock limits groundwater seepage-based headwater climate refugia. Limnologica - Ecology and Management of Inland Waters. [In Press] DOI: 10.1016/j.limno.2017.02.005.

Brody AG, Pluhar CJ, Stock GM, Greenwood WJ. 2015. Near-Surface Geophysical Imaging of a Talus Deposit in Yosemite Valley, California. Environmental & Engineering Geoscience. 21:111-127. DOI: 10.2113/gseegeosci.21.2.111.

Brown LE, Hannah DM, Milner AM. 2009. ARISE: a classification tool for Alpine RIver and Stream Ecosystems. Freshwater Biology. 54:1357-1369. DOI: 10.1111/j.1365-2427.2008.02161.x.

Brückl E, Brückl J, Chwatal W, Ullrich C. 2010. Deep alpine valleys: examples of geophysical explorations in Austria. Swiss Journal of Geosciences. 103:329-344. DOI: 10.1007/s00015-010-0045-x.

Burn DH, Fan L, Bell G. 2008. Identification and quantification of streamflow trends on the Canadian Prairies. Hydrological Sciences Journal. 53:538-549. DOI: 10.1623/hysj.53.3.538.

Butler DR, Oelfke JG, Oelfke LA. 1986. Historic Rockfall Avalanches, Northeastern Glacier National Park, Montana, U.S.A. Mountain Research and Development. 6:261. DOI: 10.2307/3673396.

Caballero Y, Jomelli V, Chevallier P, Ribstein P. 2002. Hydrological characteristics of slope deposits in high tropical mountains (Cordillera Real, Bolivia). Catena. 47:101-116. DOI: 10.1016/S0341-8162(01)00179-5.

Caine N. 2010. Recent hydrologic change in a Colorado alpine basin: an indicator of permafrost thaw? Annals of Glaciology. 51:130-134. DOI: 10.3189/172756411795932074.

Campbell DH, Clow DW, Ingersoll GP, Mast MA, Spahr NE, Turk JT. 1995. Processes Controlling the Chemistry of Two Snowmelt-Dominated Streams in the Rocky Mountains. Water Resources Research. 31:2811-2821. DOI: 10.1029/95WR02037.

Carrivick JL, Tweed FS. 2013. Proglacial lakes: character, behaviour and geological importance. Quaternary Science Reviews. 78:34-52. DOI: 10.1016/j.quascirev.2013.07.028.

Christensen CW, Hayashi M, Bentley LR. 2017. Scanning Calgary's 'water towers': applications of hydrogeophysics in challenging mountain terrain. CSEG Recorder. 42(3), 28-35.

Clauge JJ. 1989. Quaternary geology of the Canadian Cordillera. In: Fulton RJ, editor. Quaternary Geology of Canada and Greenland. Ottawa, Canada: Geological Survey of Canada. Geology of Canada Seies no. 1. DOI: 10.4095/127905.

Clow DW, Schrott L, Webb R, Campbell DH, Torizzo A, Dornblaser M. 2003. Ground Water Occurrence and Contributions to Streamflow in an Alpine Catchment, Colorado Front Range. Ground Water. 41:937-950. DOI: 10.1111/j.1745-6584.2003.tb02436.x.

Coe JA, Harp EL. 2007. Influence of tectonic folding on rockfall susceptibility, American Fork Canyon, Utah, USA. Natural Hazards and Earth System Science. 7:1-14. DOI: 10.5194/nhess-7-1-2007.

Cook SJ, Swift DA. 2012. Subglacial basins: Their origin and importance in glacial systems and landscapes. Earth-Science Reviews. 115:332-372. DOI: 10.1016/j.earscirev.2012.09.009.

Cullen RM, Marshall SJ. 2011. Mesoscale Temperature Patterns in the Rocky Mountains and Foothills Region of Southern Alberta. Atmosphere-Ocean. 49:189-205. DOI: 10.1080/07055900.2011.592130.

Dahl SO, Nesje A, Øvstedal J. 2008. Cirque glaciers as morphological evidence for a thin Younger Dryas ice sheet in east-central southern Norway. Boreas. 26:161-180. DOI: 10.1111/j.1502-3885.1997.tb00850.x.

Davinroy TC. 2000. Hydrological and biogeochemical characteristics of alpine talus, Colorado Front Range [PhD Thesis]. Boulder, Colorado, USA: University of Colorado.

de Scally FA, Owens IF. 2005. Depositional processes and particle characteristics on fans in the Southern Alps, New Zealand. Geomorphology. 69:46-56. DOI: 10.1016/j.geomorph.2004.11.021.

DeBeer CM, Wheater HS, Carey SK, Chun KP. 2016. Recent climatic, cryospheric, and hydrological changes over the interior of western Canada: a review and synthesis. Hydrology and Earth System Sciences. 20:1573-1598. DOI: 10.5194/hess-20-1573-2016.

deGroot-Hedlin C, Constable S. 1990. Occam's inversion to generate smooth, two-dimensional models from magnetotelluric data. Geophysics. 55:1613–1624. DOI: 10.1190/1.1442813.

Detty JM, McGuire KJ. 2010. Topographic controls on shallow groundwater dynamics: implications of hydrologic connectivity between hillslopes and riparian zones in a till mantled catchment. Hydrological Processes. 24:2222-2236. DOI: 10.1002/hyp.7656.

Dingman SL. 2002. Physical Hydrology. 2nd edition.Long Grove, Illinois: Waveland Press. p.646.

Environment and Climate Change Canada. 2017. Historical Climate Data. [accessed 2017 July 05] http://climate.weather.gc.ca/index_e.html .

Evans IS. 1990. Climatic effects on glacier distribution across the southern Coast Mountains, B.C. Annals of Glaciology. 14:58-64.

Evans IS. 2004. Cirque. In: Goudie A, editor. Encyclopedia of geomorphology. 1st ed. New York: Routledge. p. 154-158.

Fang X, Pomeroy JW, Ellis CR, MacDonald MK, DeBeer CM, Brown T. 2013. Multi-variable evaluation of hydrological model predictions for a headwater basin in the Canadian Rocky Mountains. Hydrology and Earth System Sciences. 17:1635-1659. DOI: 10.5194/hess-17-1635-2013.

Farquharson CG, Oldenburg DW. 1998. Non-linear inversion using general measures of data misfit and model structure. Geophysical Journal International. 134:213-227. DOI: 10.1046/j.1365-246x.1998.00555.x.

Fernandes R, Korolevych V, Wang S. 2007. Trends in Land Evapotranspiration over Canada for the Period 1960–2000 Based on In Situ Climate Observations and a Land Surface Model. Journal of Hydrometeorology. 8:1016–1030. DOI: 10.1175/JHM619.1.

Finn DS, Khamis K, Milner AM. 2013. Loss of small glaciers will diminish beta diversity in Pyrenean streams at two levels of biological organization. Global Ecology and Biogeography. 22:40-51. DOI: 10.1111/j.1466-8238.2012.00766.x.

Fischer BMC, Rinderer M, Schneider P, Ewen T, Seibert J. 2015. Contributing sources to baseflow in pre-alpine headwaters using spatial snapshot sampling. Hydrological Processes. 29:5321-5336. DOI: 10.1002/hyp.10529.

Ford KR, Ettinger AK, Lundquist JD, Raleigh MS, Hille Ris Lambers J. 2013. Spatial heterogeneity in ecologically important climate variables at coarse and fine scales in a

high-snow mountain landscape. PLoS ONE. 8:e65008. DOI: 10.1371/journal.pone.0065008.

Freer J, McDonnell JJ, Beven KJ, Peters NE, Burns DA, Hooper RP, Aulenbach B, Kendall C. 2002. The role of bedrock topography on subsurface storm flow. Water Resources Research. 38:5-1-5-16. DOI: 10.1029/2001WR000872.

Fryxell FM, Horberg L. 1943. Alpine mudflows in Grand Teton National Park, Wyoming. Geological Society of America Bulletin. 54:457–472. DOI: 10.1130/GSAB-54-457.

Gardner J. 1970. Geomorphic Significance of Avalanches in the Lake Louise Area, Alberta, Canada. Arctic and Alpine Research 2:135. DOI: 10.2307/1550348.

Gardner J. 1983. Rockfall frequency and distribution in the Highwood Pass Area, Canadian Rocky Mountains. Zeitschrift für Geomorphologie. 27:311-324.

Geotomo Software. 2012a. RES2DINVx64 [computer software]. Version 4.01.06. Gelugor, Penang, Malaysia: Geotomo Software. Operated on a system with: Windows Server 2008 R2 Enterprise Service Pack 1, Intel Xenon CPU (two E5645 processers at 2.40 GHz, 64-bit architecture), 48.0 GB RAM.

Geotomo Software. 2012b. RES3DINVx64 [computer software]. Version 3.06.21. Gelugor, Penang, Malaysia: Geotomo Software. Operated on a system with: Windows Server 2008 R2 Enterprise Service Pack 1, Intel Xenon CPU (two E5645 processers at 2.40 GHz, 64-bit architecture), 48.0 GB RAM.

Geotomo Software. 2014. RES2DMOD [computer software]. Version 3.01. Gelugor, Penang, Malaysia: Geotomo Software. Operated on a system with: Windows 10 Home operating system, Intel Core i5-6300 HW CPU (2.30 GHz, 64-bit architecture), 8.00 GB RAM.

Gordon RP, Lautz LK, McKenzie JM, Mark BG, Chavez D, Baraer M. 2015. Sources and pathways of stream generation in tropical proglacial valleys of the Cordillera Blanca, Peru. Journal of Hydrology. 522:628-644. DOI: 10.1016/j.jhydrol.2015.01.013.

Government of Canada; Natural Resources Canada; Earth Sciences Sector; Atlas of Canada. 2010. Annual mean total precipitation. [accessed 2017 May 03] http://geogratis.gc.ca/api/en/nrcan-rncan/ess-sst/d8fb41f0-8893-11e0-92bb-6cf049291510.html. Atlas of Canada, 6th edition, issue 6350.

Gray DM, Landine PG. 1988. An energy-budget snowmelt model for the Canadian Prairies. Canadian Journal of Earth Sciences. 25:1292-1303. DOI: 10.1139/e88-124.

Götz J, Otto J-C, Schrott L. 2013. Postglacial sediment storage and rockwall retreat in a semi-closed inner-alpine sedimentary basin (Gradenmoos, Hohe Tauern, Austria). Geografia Fisica E Dinamica Quaternaria. 36:63-80. DOI: 10.4461/GFDQ.2013.36.5.

Haeberli W, Linsbauer A, Cochachin A, Salazar C, Fischer UH. 2016. On the morphological characteristics of overdeepenings in high-mountain glacier beds. Earth Surface Processes and Landforms. 41:1980-1990. DOI: 10.1002/esp.3966.

Hales TC, Roering JJ. 2007. Climatic controls on frost cracking and implications for the evolution of bedrock landscapes. Journal of Geophysical Research. 112:F02033. DOI: 10.1029/2006JF000616.

Hannah DM, Brown LE, Milner AM, Gurnell AM, McGregor GR, Petts GE, Smith BPG, Snook DL. 2007. Integrating climate-hydrology-ecology for alpine river systems. Aquatic Conservation: Marine and Freshwater Ecosystems. 17:636-656. DOI: 10.1002/aqc.800.

Harrington JS. 2017. The Hydrogeology of a Rock Glacier and Its Effect on Stream Temperature [MSc Thesis]. Calgary, Alberta, Canada: University of Calgary; [accessed 2017 May 02] http://hdl.handle.net/11023/3592.

Harris SA, Pedersen DE. 1998. Thermal regimes beneath coarse blocky materials. Permafrost and Periglacial Processes. 9:107-120. DOI: 10.1002/(SICI)1099-1530(199804/06)9:2<107::AID-PPP277>3.0.CO;2-G.

Hasselström B. 1969. Water prospecting and rock-investigation by the seismic refraction method. Geoexploration. 7:113-132. DOI: 10.1016/0016-7142(69)90026-X.

Hauck C, Kneisel C. 2008. Applied geophysics in periglacial environments. Cambridge, UK: Cambridge University Press.

Haynes VM. 1968. The influence of glacial erosion and rock structure on corries in Scotland. Geografiska Annaler. Series A, Physical Geography. 50:221-234. DOI: 10.2307/520780.

Hijmans RJ, Cameron SE, Parra JL, Jones PG, Jarvis A. 2005. Very high resolution interpolated climate surfaces for global land areas. International Journal of Climatology. 25:1965-1978. DOI: 10.1002/joc.1276.

Hislop A. 2008. Structural Geology of the Opabin Plateau. [BSc Honours Thesis]. Calgary, Alberta, Canada: University of Calgary.

Hoelzle M, Wegmann M, Krummenacher B. 1999. Miniature temperature dataloggers for mapping and monitoring of permafrost in high mountain areas: first experience from the Swiss Alps. Permafrost and Periglacial Processes. 10:113-124. DOI: 10.1002/(SICI)1099-1530(199904/06)10:2<113::AID-PPP317>3.0.CO;2-A.

Hoffmann T, Müller T, Johnson EA, Martin YE. 2013. Postglacial adjustment of steep, low-order drainage basins, Canadian Rocky Mountains. Journal of Geophysical Research: Earth Surface. 118:2568-2584. DOI: 10.1002/2013JF002846.

Hood JL, Hayashi M. 2015. Characterization of snowmelt flux and groundwater storage in an alpine headwater basin. Journal of Hydrology. 521:482-497. DOI: 10.1016/j.jhydrol.2014.12.041.

Hood JL, Roy JW, Hayashi M. 2006. Importance of groundwater in the water balance of an alpine headwater lake. Geophysical Research Letters. 33:L13405. DOI: 10.1029/2006GL026611.

Isaak DJ, Young MK, Luce CH, Hostetler SW, Wenger SJ, Peterson EE, Ver Hoef JM, Groce MC, Horan DL, Nagel DE. 2016. Slow climate velocities of mountain streams portend their role as refugia for cold-water biodiversity. Proceedings of the National Academy of Sciences. 113:4374-4379. DOI: 10.1073/pnas.1522429113.

Jackson LE Jr, Pawson M. 1984. Alberta radiocarbon dates: Geological Survey of Canada, Paper 83-25. Ottawa: Geological Survey of Canada. 27 pages. DOI: 10.4095/119743.

Jasechko S, Wassenaar LI, Mayer B. 2017. Isotopic evidence for widespread cold-season-biased groundwater recharge and young streamflow across central Canada. Hydrological Processes. [In Press] DOI: 10.1002/hyp.11175.

Jordan P. 2010. Analysis of overdeepened valleys using the digital elevation model of the bedrock surface of Northern Switzerland. Swiss Journal of Geosciences. 103:375-384. DOI: 10.1007/s00015-010-0043-z.

Kirkbride MP, Warren CR. 1999. Tasman Glacier, New Zealand: 20th-century thinning and predicted calving retreat. Global and Planetary Change. 22:11-28. DOI: 10.1016/S0921-8181(99)00021-1.

Kirkbride MP, Winkler S. 2012. Correlation of Late Quaternary moraines: impact of climate variability, glacier response, and chronological resolution. Quaternary Science Reviews. 46:1-29. DOI: 10.1016/j.quascirev.2012.04.002.

Kirsch R. 2006. Petrophysical properties of permeable and low-permeable rocks. In: Kirsch R, editor. Groundwater geophysics. Berlin: Springer. p. 1-22.

Knight PG. 2004. Moraine. In: Goudie A, editor. Encyclopedia of geomorphology. 1st ed. New York: Routledge. p. 691-694.

Kurylyk BL, MacQuarrie KTB, Voss CI. 2014. Climate change impacts on the temperature and magnitude of groundwater discharge from shallow, unconfined aquifers. Water Resources Research. 50:3253-3274. DOI: 10.1002/2013WR014588.

Langston G, Bentley LR, Hayashi M, McClymont A, Pidlisecky A. 2011. Internal structure and hydrological functions of an alpine proglacial moraine. Hydrological Processes. 25:2967-2982. DOI: 10.1002/hyp.8144.

Langston G, Hayashi M, Roy JW. 2013. Quantifying groundwater-surface water interactions in a proglacial moraine using heat and solute tracers. Water Resources Research. 49:5411-5426. DOI: 10.1002/wrcr.20372.

Lanz E, Maurer H, Green AG. 1998. Refraction tomography over a buried waste disposal site. Geophysics. 63:1414-1433. DOI: 10.1190/1.1444443.

Lehmann-Horn JA, Walbrecker JO, Hertrich M, Langston G, McClymont AF, Green AG. 2011. Imaging groundwater beneath a rugged proglacial moraine. Geophysics. 76:B165-B172. DOI: 10.1190/geo2011-0095.1.

Linde N. 2014. Falsification and corroboration of conceptual hydrological models using geophysical data. Wiley Interdisciplinary Reviews: Water. 1:151-171. DOI: 10.1002/wat2.1011.

Loke MH, Acworth I, Dahlin T. 2003. A comparison of smooth and blocky inversion methods in 2D electrical imaging surveys. Exploration Geophysics. 34:182. DOI: 10.1071/EG03182.

Lowe DR. 1976. Grain flow and grain flow deposits. Journal of Sedimentary Petrology. 46:188-199. DOI: 10.1306/212F6EF1-2B24-11D7-8648000102C1865D.

Lowrie W. 1997. Fundamentals of Geophysics. 1st ed. Cambridge, UK: Cambridge University Press.

Luckman BH. 2000. The little ice age in the Canadian Rockies. Geomorphology. 32:357-384. DOI: 10.1016/S0169-555X(99)00104-X.

Luckman BH. 2004. Scree. In: Goudie A, editor. Encyclopedia of geomorphology. 1st ed. New York: Routledge. p. 915-917.

Mallamo MP. 1995. Paleoceanography of the upper Devonian Fairholme carbonate complex [PhD Thesis]. Montréal, Québec, Canada: McGill University; [accessed 2017 May 02] http://digitool.library.mcgill.ca/R/-?func=dbin-jump-full&object_id=39958&silo_library=GEN01

Martz LW, Bruneau JF, Rolfe JT. 2007. Climate Change and Water: South Saskatchewan River Basin Final Technical Report. Regina: Prairie Adaptation Research Collaborative. [accessed 2017 May 03] http://www.parc.ca/ssrb/.

Mast MA, Kendall C, Campbell D, Clow DW, Back J. 1995. Determination of hydrologic pathways in an alpine-subalpine basin using isotopic and chemical tracers, Loch Vale Watershed, Colorado, USA. In: Tonnessen KA, Williams MW, Tranter M, editors. Biogeochemistry of seasonally snow-covered catchments. Wallingford, Oxfordshire, UK: International Association of Hydrological Sciences. p. 263-270. IAHS Publication no. 228.

McClymont AF, Hayashi M, Bentley LR, Liard J. 2012. Locating and characterising groundwater storage areas within an alpine watershed using time-lapse gravity, GPR and seismic refraction methods. Hydrological Processes. 26:1792-1804. DOI: 10.1002/hyp.9316.

McClymont AF, Hayashi M, Bentley LR, Muir D, Ernst E. 2010. Groundwater flow and storage within an alpine meadow-talus complex. Hydrology and Earth System Sciences. 14:859-872. DOI: 10.5194/hess-14-859-2010.

McClymont AF, Roy JW, Hayashi M, Bentley LR, Maurer H, Langston G. 2011. Investigating groundwater flow paths within proglacial moraine using multiple geophysical methods. Journal of Hydrology. 399:57-69. DOI: 10.1016/j.jhydrol.2010.12.036.

McMechan ME. 2012. Geology, Spray Lakes Reservoir, Alberta - British Columbia: Geological Survey of Canada, Canadian Geoscience Map 14. Ottawa: Natural Resources Canada. 1 sheet. DOI: 10.4095/288954.

Melzner S, Lotter M, Linner M, Pestal G, Kociu A. 2013. Rockfall occurrence in the southern border of the Tauern Window – structural, lithological and geomorphologic aspects [poster]. Emile Argand Conference on Alpine Geological Studies; 2013 Jun 9-12; Schladming, Austria; European Geosciences Union. [accessed 2017 May 03] https://www.geologie.ac.at/fileadmin/user_upload/dokumente/pdf/poster/poster_2013_eacags_melzner_etal.pdf.

Menounos B, Osborn G, Clague JJ, Luckman BH. 2009. Latest Pleistocene and Holocene glacier fluctuations in western Canada. Quaternary Science Reviews. 28:2049-2074. DOI: 10.1016/j.quascirev.2008.10.018.

Meybeck M, Green P, Vörösmarty C. 2001. A new typology for mountains and other relief classes. Mountain Research and Development. 21:34-45. DOI: 10.1659/0276-4741(2001)021[0034:ANTFMA]2.0.CO;2.

Moore JR, Sanders JW, Dietrich WE, Glaser SD. 2009. Influence of rock mass strength on the erosion rate of alpine cliffs. Earth Surface Processes and Landforms. 34:1339-1352. DOI: 10.1002/esp.1821.

Mote PW, Hamlet AF, Clark MP, Lettenmaier DP. 2005. Declining mountain snowpack in western North America. Bulletin of the American Meteorological Society. 86:39-49. DOI: 10.1175/BAMS-86-1-39.

Mozil A. 2016. A geophysical investigation of a rock glacier in the Canadian Rockies [MSc Thesis]. Calgary, Alberta, Canada: University of Calgary; [accessed 2017 May 02] http://hdl.handle.net/11023/2756.

Muir DL, Hayashi M, McClymont AF. 2011. Hydrological storage and transmission characteristics of an alpine talus. Hydrological Processes. 25:2954-2966. DOI: 10.1002/hyp.8060.

Musil M, Maurer H, Green AG, Horstmeyer H, Nitsche FO, Mühll DV, Springman S. 2002. Shallow seismic surveying of an Alpine rock glacier. Geophysics. 67:1701-1710. DOI: 10.1190/1.1527071.

National Air Photo Library (Canada). 1947 Panchromatic aerial photography covering the northern section of 82 J from the Windermere Lake region of British Columbia to the Kananaskis region of Alberta. Ottawa, ON, Canada: Department of Energy, Mines and Resources. 555 black and white 23 x 23 cm or 26 x 26 cm remote-sensing images.

Natural Resources Canada. 2016. CanVec [cartographic reference product]. [accessed 2017 May 03] http://geogratis.gc.ca/api/en/nrcan-rncan/ess-sst/23387971-b6d3-4ded-a40b-c8e832b4ea08.html.

Oldenburg DW, Li Y. 1999. Estimating depth of investigation in dc resistivity and IP surveys. Geophysics. 64:403-416. DOI: 10.1190/1.1444545.

Onaca A, Ardelean AC, Urdea P, Ardelean F, Ărăşan AS. 2016. Genetic typologies of talus deposits derived from GPR measurements in the alpine environment of the Făgăraş Mountains. Carpathian Journal of Earth and Environmental Sciences. 11:609-616.

Onda Y, Tsujimura M, Tabuchi H. 2004. The role of subsurface water flow paths on hillslope hydrological processes, landslides and landform development in steep mountains of Japan. Hydrological Processes. 18:637-650. DOI: 10.1002/hyp.1362.

Osborn G, Luckman B. 1988. Holocene glacier fluctuations in the Canadian Cordillera (Alberta and British Columbia). Quaternary Science Reviews. 7:115-128. DOI: 10.1016/0277-3791(88)90002-9.

Osborn G, Stockmal G, Haspel R. 2006. Emergence of the Canadian Rockies and adjacent plains: A comparison of physiography between end-of-Laramide time and the present day. Geomorphology. 75:450-477. DOI: 10.1016/j.geomorph.2005.07.032.

Outcalt SI, Nelson FE, Hinkel KM. 1990. The zero-curtain effect: Heat and mass transfer across an isothermal region in freezing soil. Water Resources Research. 26:1509–1516. DOI: 10.1029/WR026i007p01509.

PFRA (Prairie Farm Rehabilitation Administration); Agriculture and Agri-Food Canada. 2008. PFRA Watershed Project - Environment Canada Sub-Basins [spatial dataset]. Regina (SK): Agriculture and Agri-Food Canada.

Paznekas A, Hayashi M. 2016. Groundwater contribution to winter streamflow in the Canadian Rockies. Canadian Water Resources Journal. 41:484-499. DOI: 10.1080/07011784.2015.1060870.

Paznekas A. 2016. Groundwater contribution to winter streamflows in alpine watersheds [MSc Thesis]. Calgary, Alberta, Canada: University of Calgary; [accessed 2017 May 02] http://hdl.handle.net/11023/2957.

Pérez FL. 1998. Conservation of soil moisture by different stone covers on alpine talus slopes (Lassen, California). Catena. 33:155-177. DOI: 10.1016/S0341-8162(98)00091-5.

Permafrost Subcommittee, Associate Commitee on Geotechnical Research. 1998. Glossary of Permafrost and Related Ground-ice Terms. Ottawa.

Pierson TC. 1982. Classification and hydrological characteristics of scree slope deposits in the Northern Craigieburn Range, New Zealand. Journal of Hydrology. (New Zealand) 21:34-60.

Pomeroy JW, Fang X, Marks DG. 2016. The cold rain-on-snow event of June 2013 in the Canadian Rockies - characteristics and diagnosis. Hydrological Processes. 30:2899-2914. DOI: 10.1002/hyp.10905.

Pomeroy JW, Gray DM, Brown T, Hedstrom NR, Quinton WL, Granger RJ, Carey SK. 2007. The cold regions hydrological model: a platform for basing process representation and model structure on physical evidence. Hydrological Processes. 21:2650-2667. DOI: 10.1002/hyp.6787.

Potter N. 1969 Jan 1. Tree-Ring Dating of Snow Avalanche Tracks and the Geomorphic Activity of Avalanches, Northern Absaroka Mountains, Wyoming. Geological Society of America Special Papers 123:141–166. DOI: 10.1130/SPE123-p141.

Preusser F, Reitner JM, Schlüchter C. 2010. Distribution, geometry, age and origin of overdeepened valleys and basins in the Alps and their foreland. Swiss Journal of Geosciences. 103:407-426. DOI: 10.1007/s00015-010-0044-y.

Price RA, Cook DG, Aitken JD, Mountjoy EW. 1980. Geology, Lake Louise (west half), west of fifth meridian, British Columbia-Alberta: Geological Survey of Canada, “A” Series Map 1483A. Ottawa: Geological Survey of Canada. 2 sheets. DOI: 10.4095/108873.

Rood SB, Pan J, Gill KM, Franks CG, Samuelson GM, Shepherd A. 2008. Declining summer flows of Rocky Mountain rivers: Changing seasonal hydrology and probable impacts on floodplain forests. Journal of Hydrology. 349:397-410. DOI: 10.1016/j.jhydrol.2007.11.012.

Roy JW, Hayashi M. 2007. Groundwater - surface water exchange in alpine and subalpine watersheds : a review of recent field studies. In: Ginot P, Sicart J-E, editors. Glacier mass

balance changes and meltwater discharge. Wallingford, Oxfordshire, UK: International Association of Hydrological Sciences. p. 3-16. IAHS Publication no. 318.

Roy JW, Hayashi M. 2008. Groundwater exchange with two small alpine lakes in the Canadian Rockies. Hydrological Processes. 22:2838-2846. DOI: 10.1002/hyp.6995.

Roy JW, Hayashi M. 2009. Multiple, distinct groundwater flow systems of a single moraine-talus feature in an alpine watershed. Journal of Hydrology. 373:139-150. DOI: 10.1016/j.jhydrol.2009.04.018.

Rödder T, Kneisel C. 2012. Influence of snow cover and grain size on the ground thermal regime in the discontinuous permafrost zone, Swiss Alps. Geomorphology. 175-176:176-189. DOI: 10.1016/j.geomorph.2012.07.008.

Sanders D, Ostermann M, Brandner R, Prager C. 2010. Meteoric lithification of catastrophic rockslide deposits: Diagenesis and significance. Sedimentary Geology. 223:150-161. DOI: 10.1016/j.sedgeo.2009.11.007.

Sanders DG, Ostermann M, Kramers J. 2010. Meteoric diagenesis of Quaternary carbonate-rocky talus slope successions (Northern Calcareous Alps, Austria). Facies. 56:27-46. DOI: 10.1007/s10347-009-0194-4.

Sandmeier Software. 2005. Reflex-Win [computer software]. Version 4.0. Karlsruhe, Germany: Sandmeier Software. Operated on a system with: Windows 10 Home operating system, Intel Core i5-6300 HW CPU (2.30 GHz, 64-bit architecture), 8.00 GB RAM.

Sass O, Krautblatter M. 2007. Debris flow-dominated and rockfall-dominated talus slopes: Genetic models derived from GPR measurements. Geomorphology. 86:176-192. DOI: 10.1016/j.geomorph.2006.08.012.

Sass O, Wollny K. 2001. Investigations regarding Alpine talus slopes using ground-penetrating radar (GPR) in the Bavarian Alps, Germany. Earth Surface Processes and Landforms. 26:1071-1086. DOI: 10.1002/esp.254.

Sass O. 2006. Determination of the internal structure of alpine talus deposits using different geophysical methods (Lechtaler Alps, Austria). Geomorphology. 80:45-58. DOI: 10.1016/j.geomorph.2005.09.006.

Sass O. 2007. Bedrock detection and talus thickness assessment in the European Alps using geophysical methods. Journal of Applied Geophysics. 62:254-269. DOI: 10.1016/j.jappgeo.2006.12.003.

Sauchyn DJ, Barrow EM, Hopkinson RF, Leavitt PR. 2002. Aridity on the Canadian Plains. Géographie Physique et Quaternaire. 56:247. DOI: 10.7202/009109ar.

Scherler D, Bookhagen B, Strecker MR. 2011. Spatially variable response of Himalayan glaciers to climate change affected by debris cover. Nature Geoscience. 4:156-159. DOI: 10.1038/ngeo1068.

Schwartz FW, Zhang H. 2003. Fundamentals of Groundwater. New York: John Wiley and Sons.

Seed HB. 1964. Fundamental aspects of the Atterberg limits. Journal of the Soil Mechanics and Foundations Division. 90(6): 75-106.

Seiler KP. 1990. Groundwater balance and flow pattern in overdeepened sections of valleys in the Bavarian Alps. In: Molnár Ľ, editor. Hydrology of mountainous areas. Wallingford, Oxfordshire, UK: International Association of Hydrological Sciences. p. 329-337. IAHS Publication no. 190.

Selby MJ. 1982. Hillslope materials & processes. Oxford: Oxford University Press.

Smerdon JE, Pollack HN, Cermak V, Enz JW, Kresl M, Safanda J, Wehmiller JF. 2006. Daily, seasonal, and annual relationships between air and subsurface temperatures. Journal of Geophysical Research. 111:D07101. DOI: 10.1029/2004JD005578.

Smith DJ, Mccarthy DP, Colenutt ME. 1995. Little Ice Age glacial activity in Peter Lougheed and Elk Lakes provincial parks, Canadian Rocky Mountains. Canadian Journal of Earth Sciences. 32:579-589. DOI: 10.1139/e95-049.

Sosedov S. 1974. Investigation of the hydrologic characteristics of talus. Soviet Hydrology. 6:414-424.

Spedding N, Evans DJ. 2002. Sediments and landforms at Kviárjökull, southeast Iceland: a reappraisal of the glaciated valley landsystem. Sedimentary Geology. 149:21-42. DOI: 10.1016/S0037-0738(01)00242-1.

Spence C, Woo M. 2003. Hydrology of subarctic Canadian shield: soil-filled valleys. Journal of Hydrology. 279:151-166. DOI: 10.1016/S0022-1694(03)00175-6.

Staub B, Marmy A, Hauck C, Hilbich C, Delaloye R. 2015. Ground temperature variations in a talus slope influenced by permafrost: a comparison of field observations and model simulations. Geographica Helvetica. 70:45–62. DOI: 10.5194/gh-70-45-2015.

Statistics Canada. Data tables, 2016 Census: 1 - age (in single years) and average age (127) and sex (3) for the population: Canada, provinces, and territories, census divisions and census subdivisions. [accessed 2017 May 08] http://www12.statcan.gc.ca/census-recensement/2016/dp-pd/dt-td/Lp-eng.cfm?LANG=E&APATH=3&DETAIL=0&DIM=0&FL=A&FREE=0&GC=0&GID=0&GK=0&GRP=1&PID=0&PRID=10&PTYPE=109445&S=0&SHOWALL=0&SUB=0&Temporal=2016&THEME=115&VID=0&VNAMEE=&VNAMEF. Catalogue number: 98-400-X2016004.

Steinbauer MJ, Field R, Grytnes J-A, Trigas P, Ah-Peng C, Attorre F, Birks HJB, Borges PA V, Cardoso P, Chou C-H, et al. 2016. Topography-driven isolation, speciation and a global increase of endemism with elevation. Global Ecology and Biogeography. 25:1097-1107. DOI: 10.1111/geb.12469.

Stiegler C, Rode M, Sass O, Otto J-C. 2014. An undercooled scree slope detected by geophysical investigations in sporadic permafrost below 1000 M ASL, Central Austria. Permafrost and Periglacial Processes. 25:194–207. DOI: 10.1002/ppp.1813.

Stockmal GS. 1979. Structural geology of the northern termination of the Lewis Thrust, Front Ranges, southern Canadian Rocky Mountains [MSc Thesis]. Calgary, Alberta, Canada: University of Calgary.

Stroeve JC, Markus T, Boisvert L, Miller J, Barrett A. 2014. Changes in Arctic melt season and implications for sea ice loss. Geophysical Research Letters. 41:1216-1225. DOI: 10.1002/2013GL058951.

Swift DA, Nienow PW, Spedding N, Hoey TB. 2002. Geomorphic implications of subglacial drainage configuration: rates of basal sediment evacuation controlled by seasonal drainage system evolution. Sedimentary Geology. 149:5-19. DOI: 10.1016/S0037-0738(01)00241-X.

Tanzeeba S, Gan TY. 2012. Potential impact of climate change on the water availability of South Saskatchewan River Basin. Climatic Change. 112:355-386. DOI: 10.1007/s10584-011-0221-7.

Taylor CA, Stefan HG. 2009. Shallow groundwater temperature response to climate change and urbanization. Journal of Hydrology. 375:601-612. DOI: 10.1016/j.jhydrol.2009.07.009.

Thapa P. 2017. Controls on rockfall-talus process-response systems, Kananaskis, Canadian Rockies [MSc Thesis]. Calgary, Alberta, Canada: University of Calgary; [accessed 2017 May 02] http://hdl.handle.net/11023/3551.

Tromp-van Meerveld HJ, McDonnell JJ. 2006. Threshold relations in subsurface stormflow: 2. The fill and spill hypothesis. Water Resources Research. 42:1–11. DOI: 10.1029/2004WR003800.

van Steijn H, Bertran P, Francou B, Texier J-P, Hétu B. 1995. Models for the genetic and environmental interpretation of stratified slope deposits: Review. Permafrost and Periglacial Processes. 6:125-146. DOI: 10.1002/ppp.3430060210.

Viviroli D, Dürr HH, Messerli B, Meybeck M, Weingartner R. 2007. Mountains of the world, water towers for humanity: Typology, mapping, and global significance. Water Resources Research. 43:1-13. DOI: 10.1029/2006WR005653.

Viviroli D, Weingartner R. 2004. The hydrological significance of mountains: from regional to global scale. Hydrology and Earth System Sciences. 8:1017-1030. DOI: 10.5194/hess-8-1017-2004.

Watson DB, Doll WE, Jeffrey Gamey T, Sheehan JR, Jardine PM. 2005. Plume and lithologic profiling with surface resistivity and seismic tomography. Ground Water. 43:169-177. DOI: 10.1111/j.1745-6584.2005.0017.x.

Weekes AA, Torgersen CE, Montgomery DR, Woodward A, Bolton SM. 2015. Hydrologic response to valley-scale structure in alpine headwaters. Hydrological Processes. 29:356-372. DOI: 10.1002/hyp.10141.

White SE. 1981. Alpine mass movement forms (noncatastrophic): classification, description, and significance. Arctic and Alpine Research. 13:127-137.

Williams MW, Hood E, Molotch NP, Caine N, Cowie R, Liu F. 2015. The “teflon basin” myth: hydrology and hydrochemistry of a seasonally snow-covered catchment. Plant Ecology & Diversity. 8:639-661. DOI: 10.1080/17550874.2015.1123318.

Winkler G, Wagner T, Pauritsch M, Birk S, Kellerer-Pirklbauer A, Benischke R, Leis A, Morawetz R, Schreilechner MG, Hergarten S. 2016. Identification and assessment of groundwater flow and storage components of the relict Schöneben Rock Glacier, Niedere Tauern Range, Eastern Alps (Austria). Hydrogeology Journal. 24:937-953. DOI: 10.1007/s10040-015-1348-9.

Zelt CA, Azaria A, Levander A. 2006. 3D seismic refraction traveltime tomography at a groundwater contamination site. Geophysics. 71:H67-H78. DOI: 10.1190/1.2258094.

Zhi L. 2013. Geophysical characterizations of the Paskapoo Formation [MSc Thesis]. Calgary, Alberta, Canada: University of Calgary; [accessed 2017 May 02] http://hdl.handle.net/11023/1014.

Appendix A List of Field Site Visits

Date	Accompanying Personnel	Main goals/observations
2015-05-01	John Pomeroy	First introduction to field site and University of Saskatchewan activity on site
2015-06-18	Gerald Osborn, May Guan, Hongye Wu	Observe moraines and major surficial structures, get tour of hydrology from H. Wu and her instrumentation, follow up of initial desktop study
2015-06-28	Masaki Hayashi, Larry Bentley	Learn more about hydrology of the field site based on analysis of elevation data
2015-07-08	Masaki Hayashi	Explore for springs on talus slopes, make final plans for geophysics survey, stream gauging of Bonsai Creek
2015-07-13 to 2015-07-31	Feodora Ivaniuk, Calista Yim, Andrius Paznekas, Scarlett (Si Jia) Zhu, Ben Stevenson, Saskia Schaelicke, Matthew Lennon, Jordan Harrington, Jesse He, Shelby Snow, Polina Adbrakhimova, Masaki Hayashi, Brandon Hill, Laurence Bentley, Jenna Christensen, Barret Kurylyk, Yu Hu, Kim Sena	Primary geophysics field campaign (GPR, ERT, SRT)
2015-09-04	Brandon Hill	collect samples of Fernie Fm., retrieve failed level logger at Fortress Lake
2015-10-22	Chris Jackson	Deploy temperature sensors at possible ice locations, collect Fernie Fm. samples for Rn experiments
2016-06-14	Masaki Hayashi, Anna Pekinasova	Retrieval of temperature sensors, hand auger samples from meadow, install time-lapse cameras, hydro measurements (temperature and EC)
2016-06-24	Brandon Hill, Luke Kary	Install piezometers, hydro measurements, meadow soil samples
2016-06-28	Laura Beamish, Luke Kary	Install more piezometers and lake stilling well, download piezometer data, hydro measurements
2016-07-07	Laura Beamish	Scout locations for additional geophysical lines, collect rock samples of Palliser and Fernie Formations.

2016-07-19 to 2016-07-23	Cody Good, Jesse He, Brandon Hill, Anna Pekinasova, Kelsey Tillapaugh, Masaki Hayashi, Jenna Trofin, Rachel Lauer, Feodora Ivaniuk, Kristina Kublik	Supplementary geophysics campaign (GPR, ERT, SRT)
2016-07-27	Luke Kary	Survey piezometer elevations with DGPS, install nested pair of wells (P05 and P06)
2016-09-19	Polina Abdrakhimova, Jennifer Hanlon	Attempted unsuccessfully to auger to a shallow target on ERT1 (60 m), retrieve piezometers and time-lapse photos, survey features in the dry lakebed.
2017-02-21	Masaki Hayashi	Measure discharge from northern outlet spring, general reconnaissance of winter condition of site

Appendix B Petrophysics of Alpine Deposits

Deposit type	Velocity ($m\ s^{-1}$)	Resistivity (Ωm)	GPR velocity ($m\ ns^{-1}$)	Source*	Comments
Bedrock	2000 to 4000	5000 to 20,000	0.12	1	lower values near the rubble/bedrock interface
Bedrock	>2500	<20,000	0.13	6	Lower resistivity in shallow bedrock, where water is presumably in fractures. Deeper bedrock means lower fracture aperture and increased resistivity
Bedrock	-	7,000 to 15,000	-	4	Generally 10,000 Ωm
Bedrock	>3000	>10,000	-	3	lower resistivity in shallow bedrock, where water is presumably in fractures. Deeper bedrock means lower fracture aperture and increased resistivity
Bedrock (limestone/dolomite)	2000 to 6000	-	-	2	
Bedrock (metamorphic)	3000 to 5800	100 to 10,000	-	2	
Ice	3000 to 4000	$>10^6$	-	3	
Ice	3100 to 4500	10^6 to 10^8	0.168	2	
Meadow	300 to 700	2000 to 5000	0.065	1	poor GPR signal penetration
Moraine	<1500	5,000 to 10,000	0.13	6	
Moraine	500 to 1500	2000 to 5000	-	3	
Moraine	-	10,000 to 30,000	-	2	

Moraine (wet)	-	<3000	-	6	
Moraine (wet)	500 to 1500	300	-	3	
Overburden (loose)	400 to 550	1000 to >20,000	0.11 to .14	5	
Overburden (wet and compacted)	700 to 1800	1000 to 15,000	0.07 to 0.11	5	
Permafrost	-	>20,000	-	3	
Permafrost	-	1000 to 1,000,000	-	2	
Talus	<1000	>20,000	0.12	1	
Talus	-	20,000 to 75,000	-	4	
Talus	550 to 2500	10,000 to 100,000	-	2	range is 1000-4400 m/s when frozen
Talus (wet material at base)	-	750 to 5000	-	4	poor GPR signal penetration
Till	1500 to 2700	-	-	2	
Till	600 to 1050	500 to 3000	0.09 to 0.10	5	

*Source codes:

1	McClymont et al. 2010	4	Muir et al. 2011
2	Hauck and Kneisel 2008, Tables A2, A3, A4	5	Sass 2006
3	Langston et al. 2011	6	McClymont et al. 2011

Appendix C Optimization Equations for Geophysical Inversion

C.1 Electrical Resistivity Tomography

The optimisation equation used in RES2DINV is (Loke et al. 2003):

$$\left(\mathbf{J}_i^{\mathrm{T}}\mathbf{R}_d\mathbf{J}_i + \lambda_i \boldsymbol{W}^{\mathrm{T}}\mathbf{R}_m\boldsymbol{W}\right)\Delta\mathbf{r}_i = \mathbf{J}_i^{\mathrm{T}}\mathbf{R}_d\mathbf{g}_i - \lambda_i \boldsymbol{W}^{\mathrm{T}}\mathbf{R}_m\boldsymbol{W}\mathbf{r}_{i-1} \quad \text{(C-1)}$$

where

i	iteration number,
$\Delta\mathbf{r}_i$	change in model parameters (resistivity values)
$\mathbf{r}_{i-1}$	model resistivity values from the previous iteration
$\mathbf{g}_i$	data misfit vector
J	Jacobian matrix of partial derivatives
W	roughness filter (in this case, a first-order finite difference operator based on deGroot - Hedlin and Constable (1990))
λ_i	dampening factor for weighing the relative importance of the smoothness constraint.

The matrices $\mathbf{R}_d$ and $\mathbf{R}_m$, which are unused in the L_2-norm case, are added to ensure the elements of $\mathbf{g}_i$ and **W** have roughly equal weights during the optimization (Loke et al. 2003).

Res2dinv incorporates a reference model by modifying Equation C-1:

$$\left(\mathbf{J}_i^{\mathrm{T}}\mathbf{R}_d\mathbf{J}_i + \lambda_i \boldsymbol{W}^{\mathrm{T}}\mathbf{R}_m\boldsymbol{W}\right)\Delta\mathbf{r}_i = \mathbf{J}_i^{\mathrm{T}}\mathbf{R}_d\mathbf{g}_i - \lambda_i \boldsymbol{W}^{\mathrm{T}}\mathbf{R}_m\boldsymbol{W}\mathbf{r}_{i-1} - \lambda_i\mu(\boldsymbol{r}_i - \boldsymbol{r}_m) \quad \text{(C-2)}$$

where

$\mathbf{r}_m$	reference model resistivity
μ	dampening factor controlling weight of deviations from the initial reference model

The value of μ was set to the maximum value allowed by the software during repeated inversions where the reference model was set to either 100 Ωm and 10,000 Ωm to test locations where the model was poorly constrained.

C.2 Seismic Refraction Tomography

In general terms, the travel time of a seismic wave along a ray path S in a 2D isotropic medium is:

$$t = \int_S u(\boldsymbol{r}(\boldsymbol{x},\boldsymbol{z}))dr \tag{C-3}$$

where

$\mathbf{r(x, z)}$ position vector

$\mathrm{u}(\mathbf{r})$ the slowness field

In the code developed by Lanz et al. (1998), the slowness field is approximated using a discrete, square grid with *m* cells, each with a constant slowness $\hat{u}_k$ (k = 1 ... m). Hence, the i^{th} travel time of *n* observations is:

$$t_i = \sum_{k=1}^{m} l_{ik}\hat{u}_k = \boldsymbol{L_i}\hat{\boldsymbol{u}} \tag{C-4}$$

where

l_{ik} portion of the i^{th} raypath in the k^{th} cell of *u*

The optimization equation is thus:

$$\begin{pmatrix} \boldsymbol{t} \\ \boldsymbol{h} \end{pmatrix} = \begin{pmatrix} \boldsymbol{L} \\ \boldsymbol{D} \end{pmatrix} \hat{\boldsymbol{u}} \tag{C-5}$$

where **h** and **D** represent the regularization parameters of the problem. These are used to (1) minimize the differences between the output slowness model and an input reference model $\hat{\boldsymbol{u}}_0$, and (2) impose smoothness constraints, wherein high spatial gradients in model slowness only appear where the data provide strong support for them. Mathematically, these are formulated as:

$$\begin{pmatrix} \lambda\beta\hat{\boldsymbol{u}}_0 \\ \mathbf{0} \end{pmatrix} = \begin{pmatrix} \lambda\beta\boldsymbol{I} \\ \lambda(1-\beta)\boldsymbol{S} \end{pmatrix} \hat{\boldsymbol{u}} \tag{C-6}$$

where

I the identity matrix

S a Laplacian smoothing matrix from Ammon and Vidale (1993)

λ parameter controlling the overall amount of regularization applied

β parameter controlling the relative amount reference model dampening to smoothing, with a range of $0 < \beta < 1$

Appendix D Electrical Resistivity Tomography Images

This appendix contains additional ERT images not used in the main body of the text. In all 2D lines (ERT1 to ERT12), pesudosections comparing measured and calculated apparent resistivity values are included. In addition, resistivity models where a different starting model was used for inversion are also shown. Images from, ERT13, are also included.

Two forward-modeling exercises that were carried out highlight aspects of the ERT images that may be spurious are also contained herein. Figure D-3A shows a resistivity distribution with structures similar to ERT 1 (Figure 5-11B) while Figure D-10A shows a resistivity distribution similar to that in ERT4 (Figure 5-12B). The resulting images were produced using the method described in Section 3.2.1. Figure D-3B shows that while the locations of shallow boundaries are well resolved, the absolute values of resistivity in the lower units are not accurate. This may be due to the low-resistivity meadow sediments which divert electrical current flow and reduce the sensitivity of ERT measurements to deeper layers. Figure D-10B shows false lateral variations in resistivity at the deepest part of the image that are not in the true resistivity distribution (Figure D-10A). This may be because the inversion algorithm prioritizes optimizing near-surface resistivities, which exhibit large variations over several orders of magnitude (Figure D-10A). These exercises underline the issues with sensitivity of the ERT measurements with regards to deeper structures.

Table D-1: Summary of error statistics of the inverted ERT images.

Line	% Absolute Error of Inverted Model	0 m starts at _____ end of line
ERT1	4.75	East
ERT2	3.24	South
ERT3	6.22	West
ERT4	3.33	South
ERT5	9.26	North
ERT6	4.72	East
ERT7	4.74	West
ERT8	9.84	West
ERT9	11.85	West
ERT10	2.57	Northeast
ERT11	4.34	East
ERT12	9.72	South
ERT13	12.1	N/A

D.1 ERT1

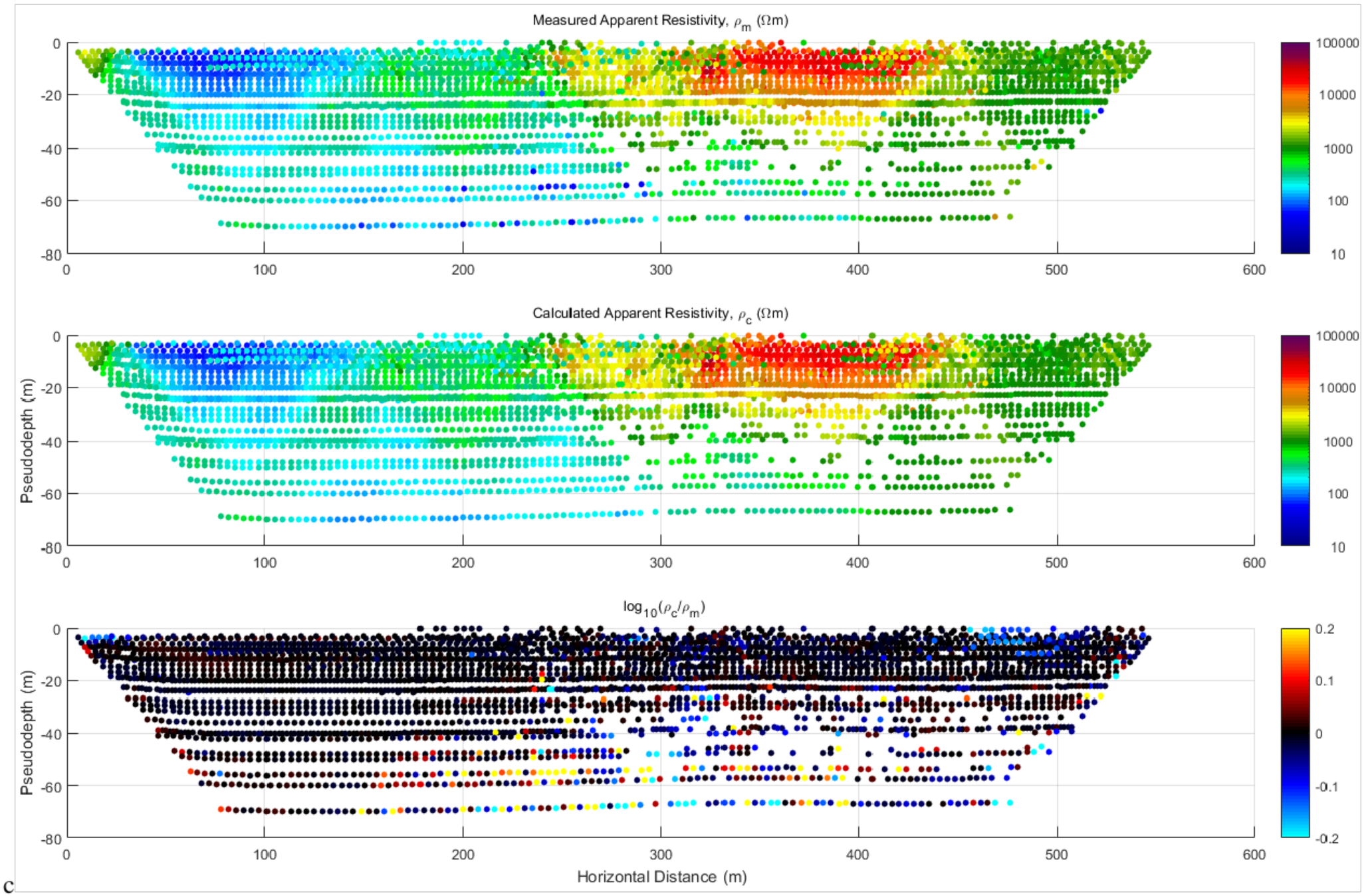

Figure D-1: Measured apparent resistivities (top) versus those calculated from the final resistivity model (middle) on ERT1.

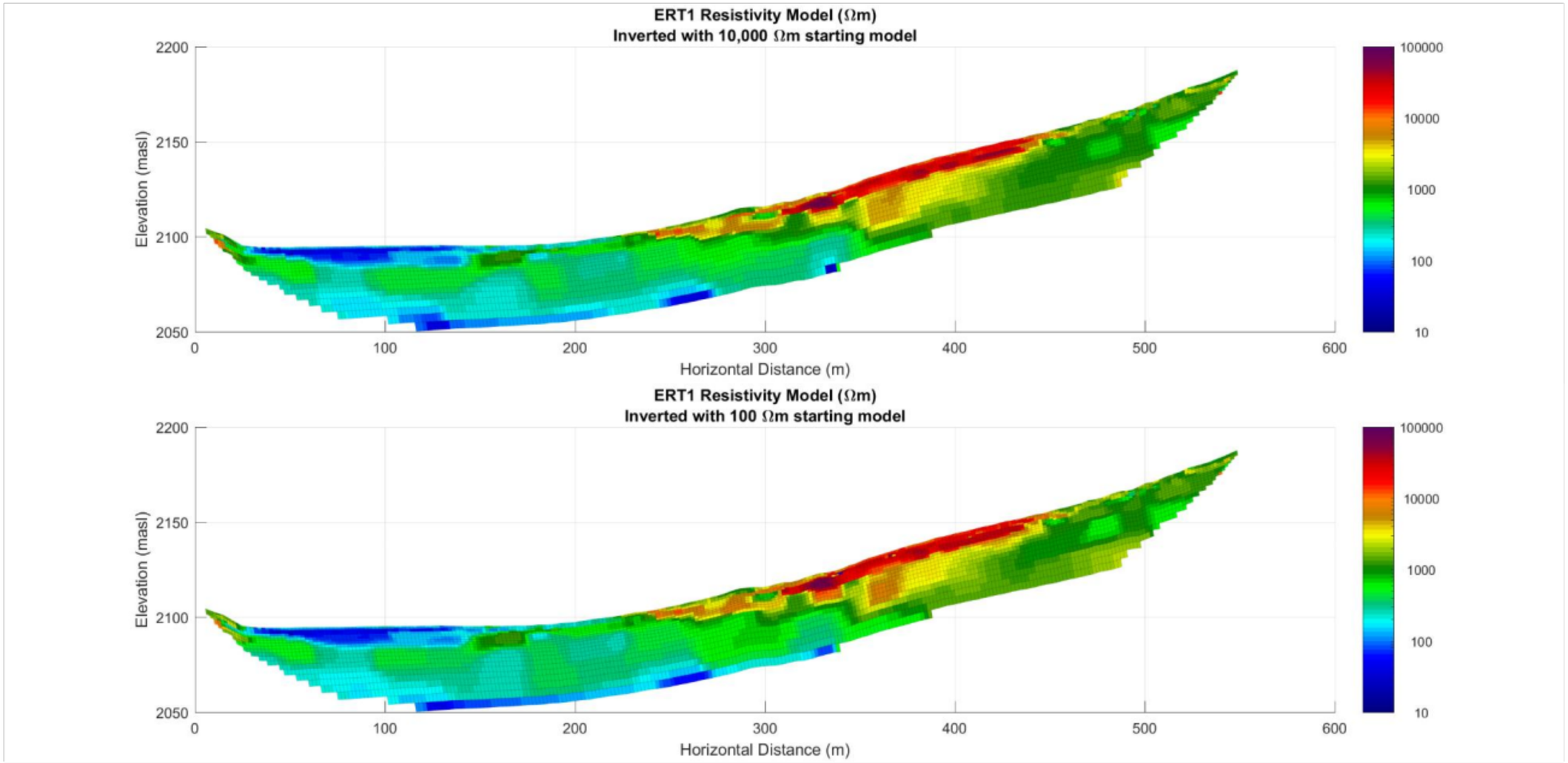

Figure D-2: Comparison of inverted models resulting from different starting models on ERT1.

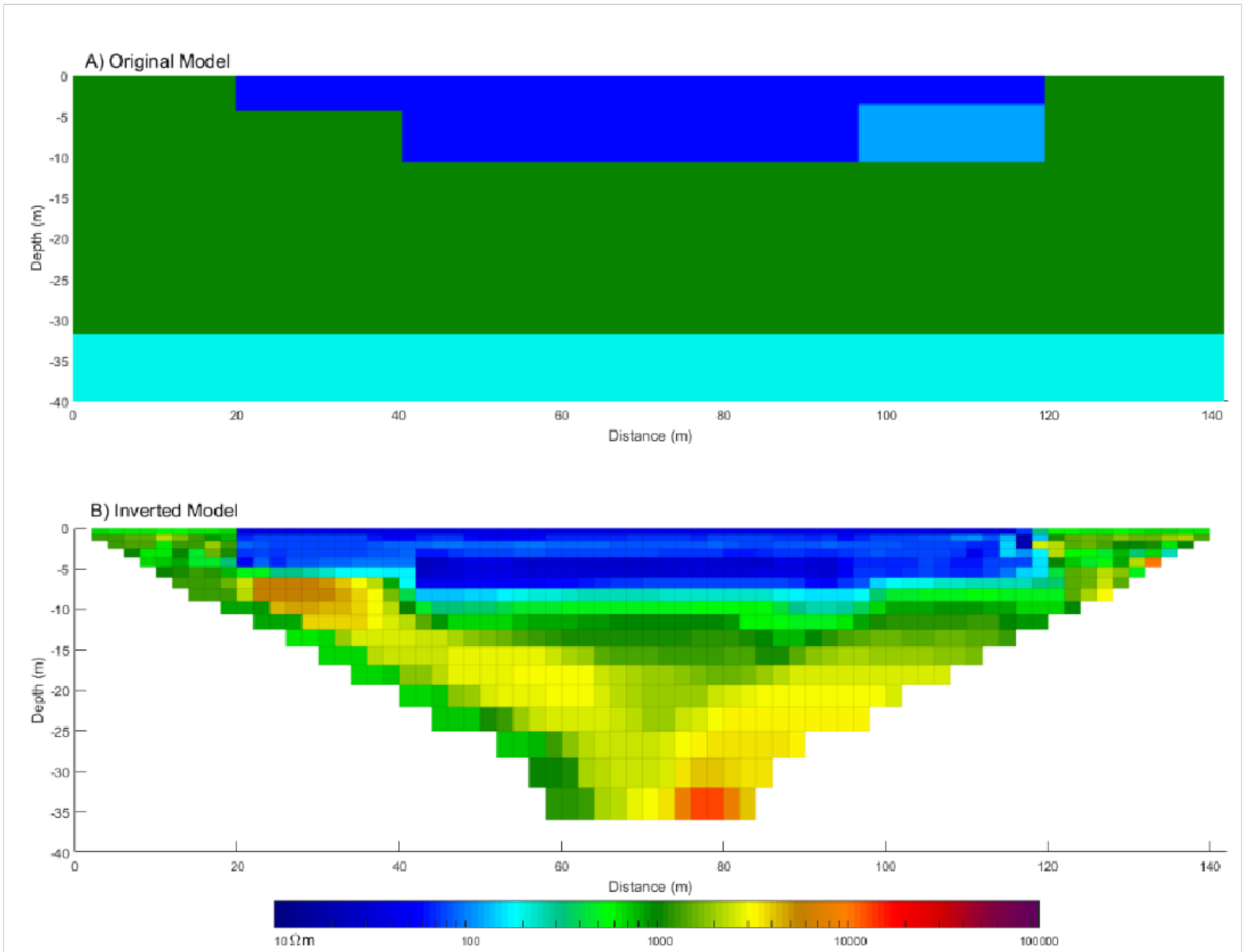

Figure D-3: Forward modeling exercise showing (A) a known resistivity distribution loosely based on the meadow section of ERT1 in Figure 5-11B and (B) the inverted resistivity model based on simulated surface measurements of the known resistivity distribution.

D.2 ERT2

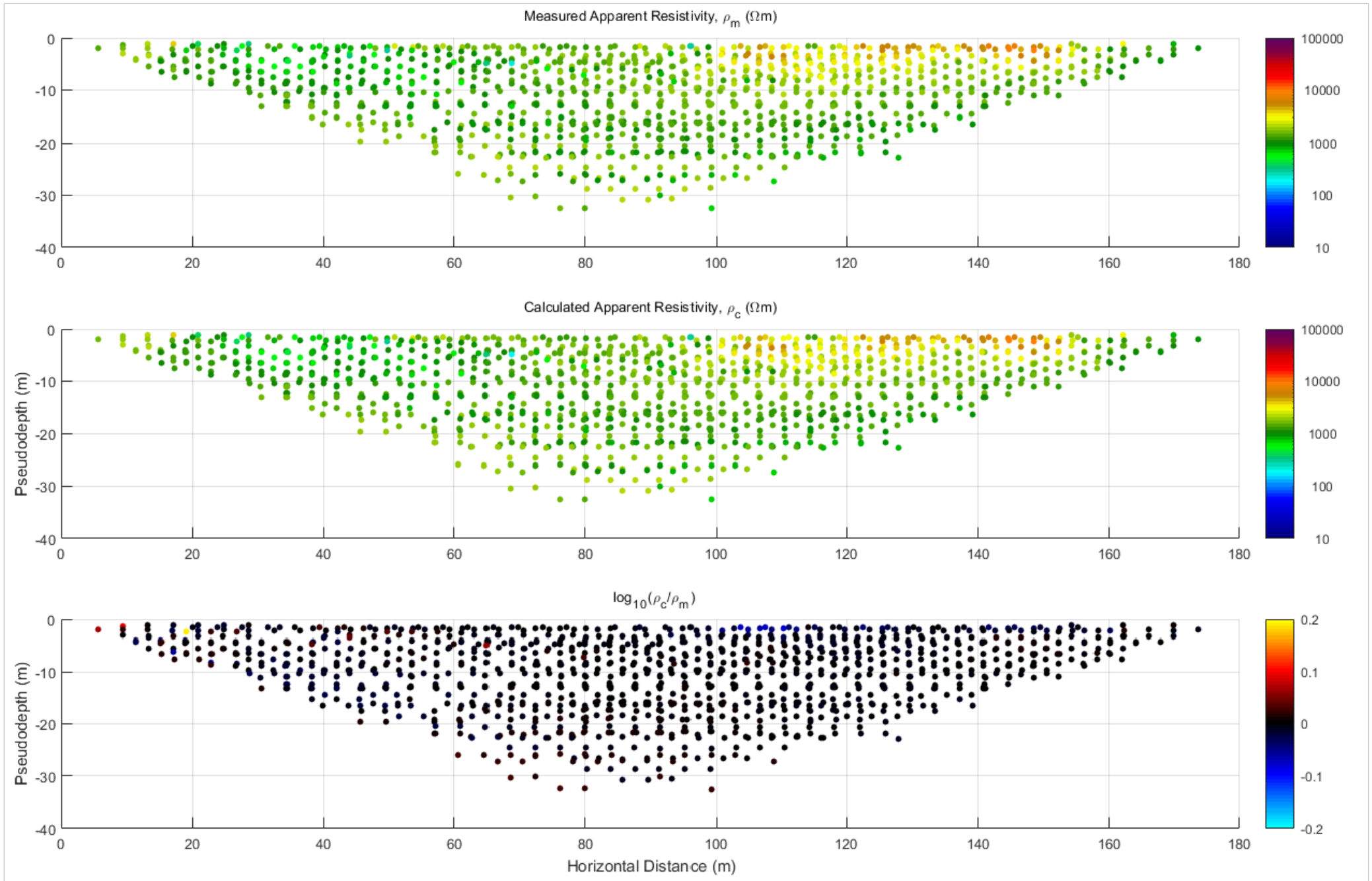

Figure D-4: Measured apparent resistivities (top) versus those calculated from the final resistivity model (middle) on ERT2.

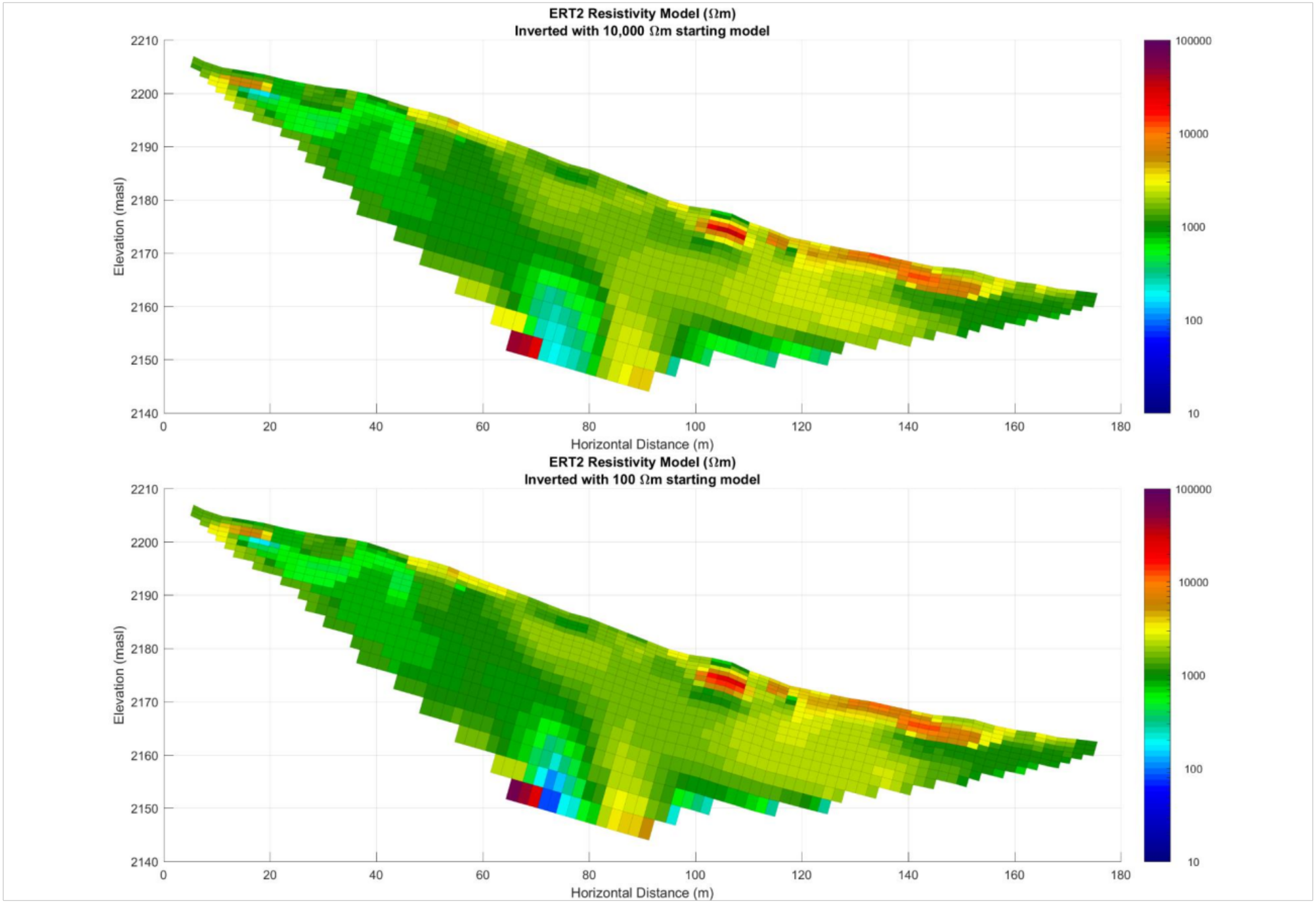

Figure D-5: Comparison of inverted models resulting from different starting models on ERT2.

D.3 ERT3

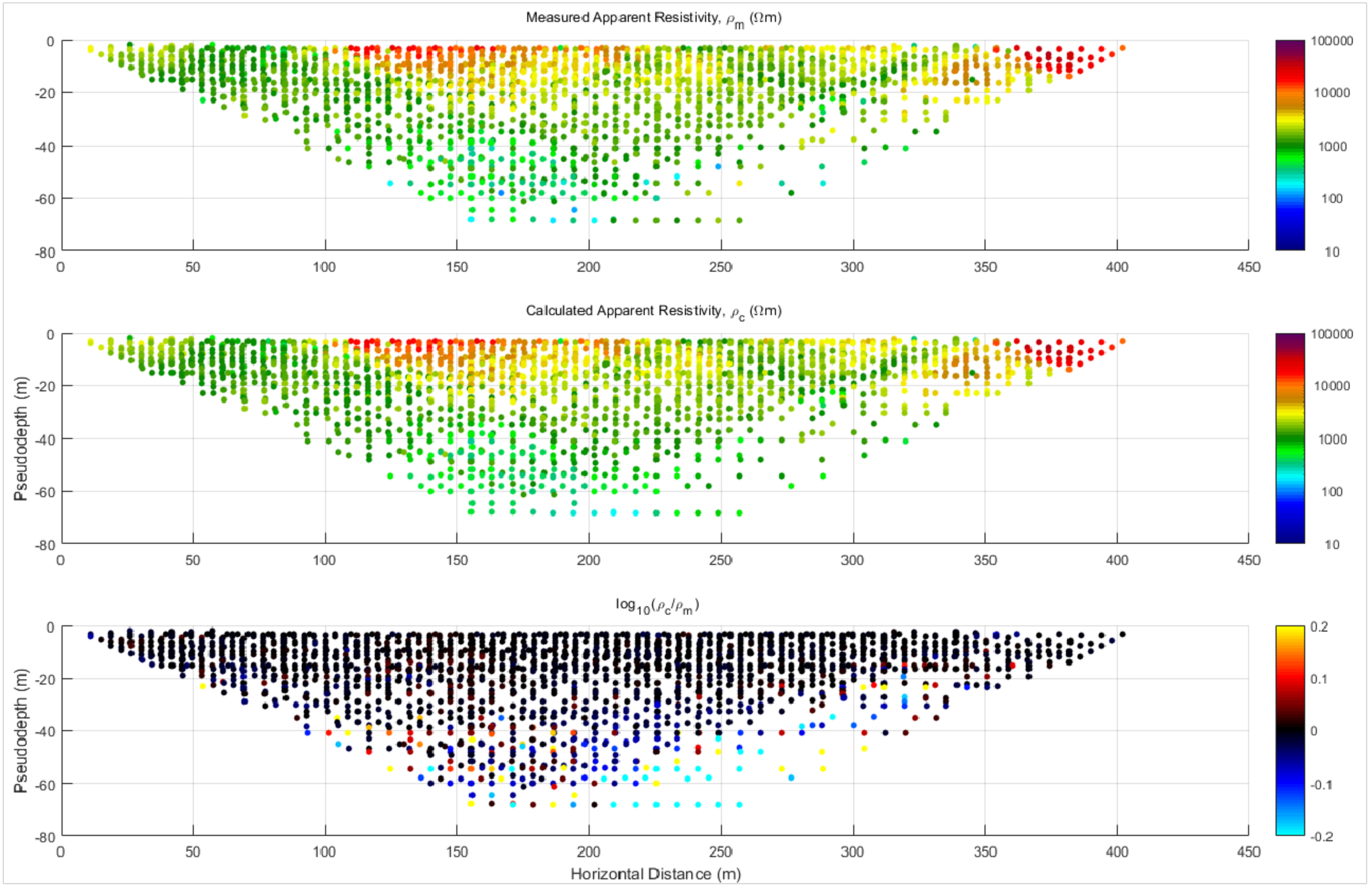

Figure D-6: Measured apparent resistivities (top) versus those calculated from the final resistivity model (middle) on ERT3.

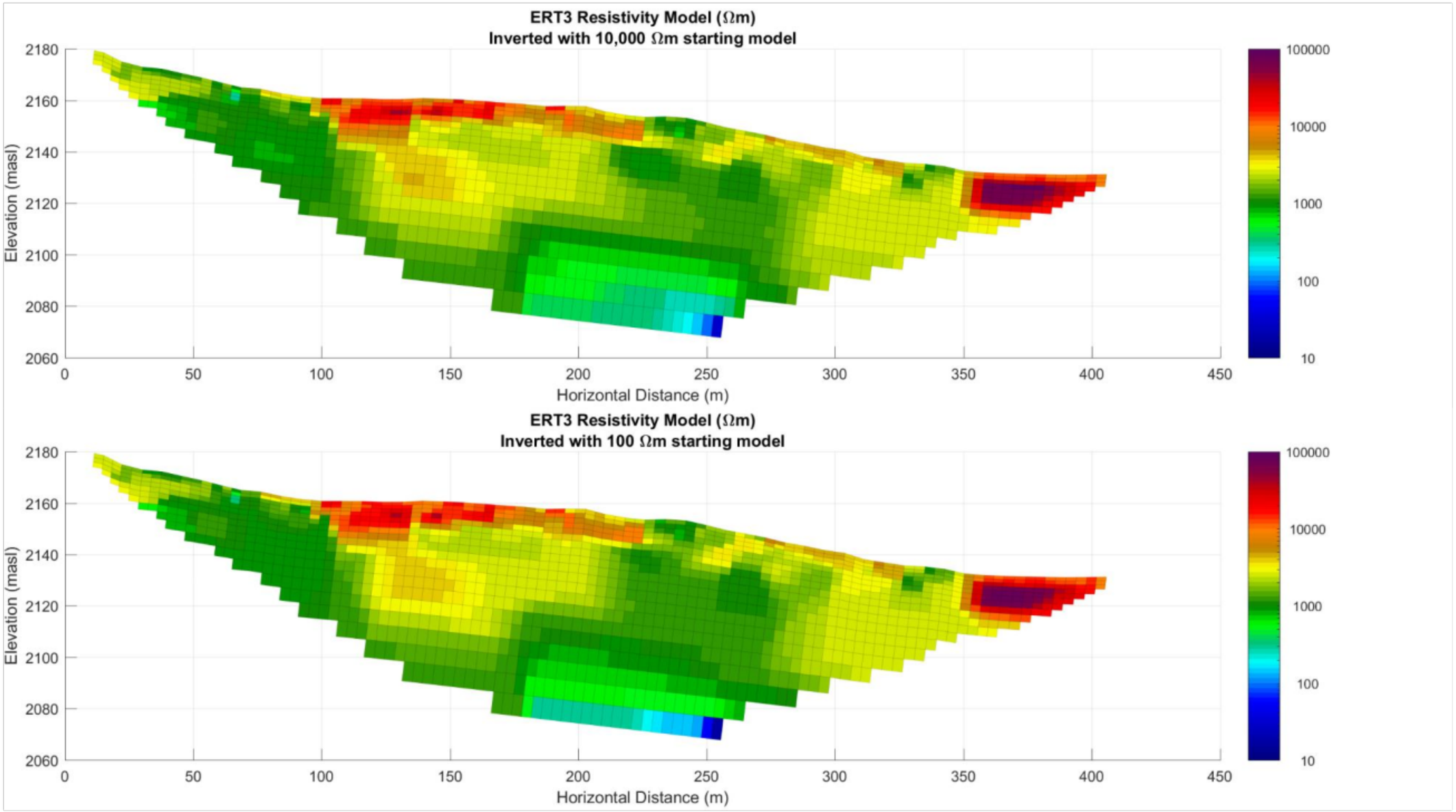

Figure D-7: Comparison of inverted models resulting from different starting models on ERT3.

D.4 ERT4

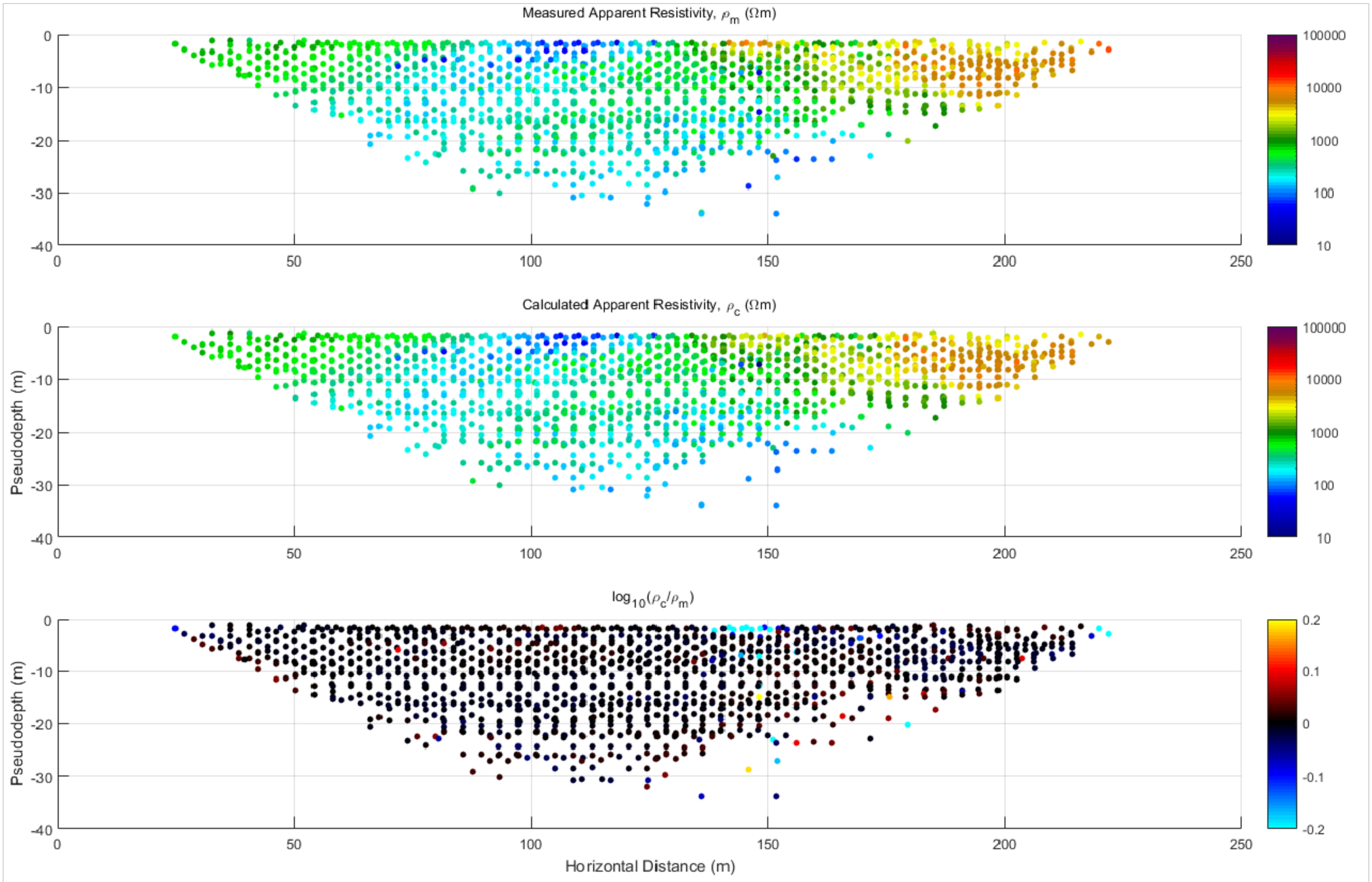

Figure D-8: Measured apparent resistivities (top) versus those calculated from the final resistivity model (middle) on ERT4.

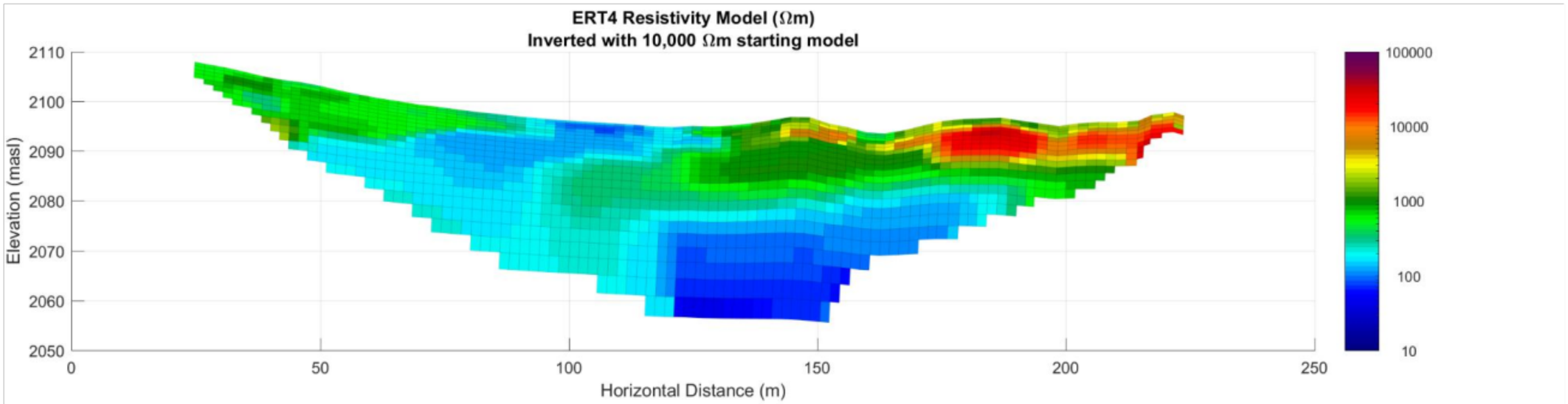

Figure D-9: Comparison of inverted models resulting from different starting models on ERT4.

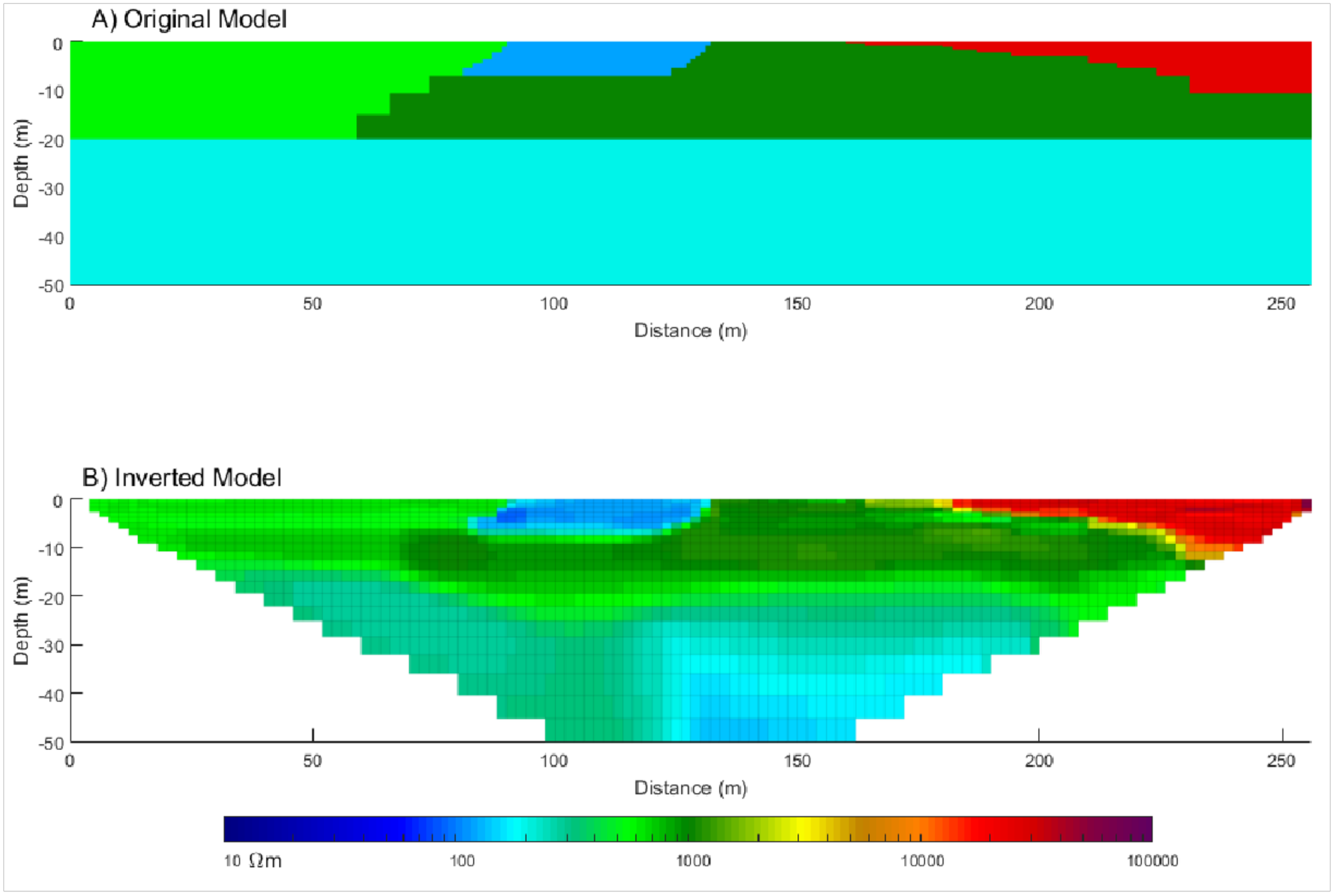

Figure D-10: Forward modeling exercise showing (A) a known resistivity distribution loosely based on ERT4 (Figure 5-12B), and (B) the inverted resistivity model based on simulated surface measurements of the known resistivity distribution.

D.5 ERT5

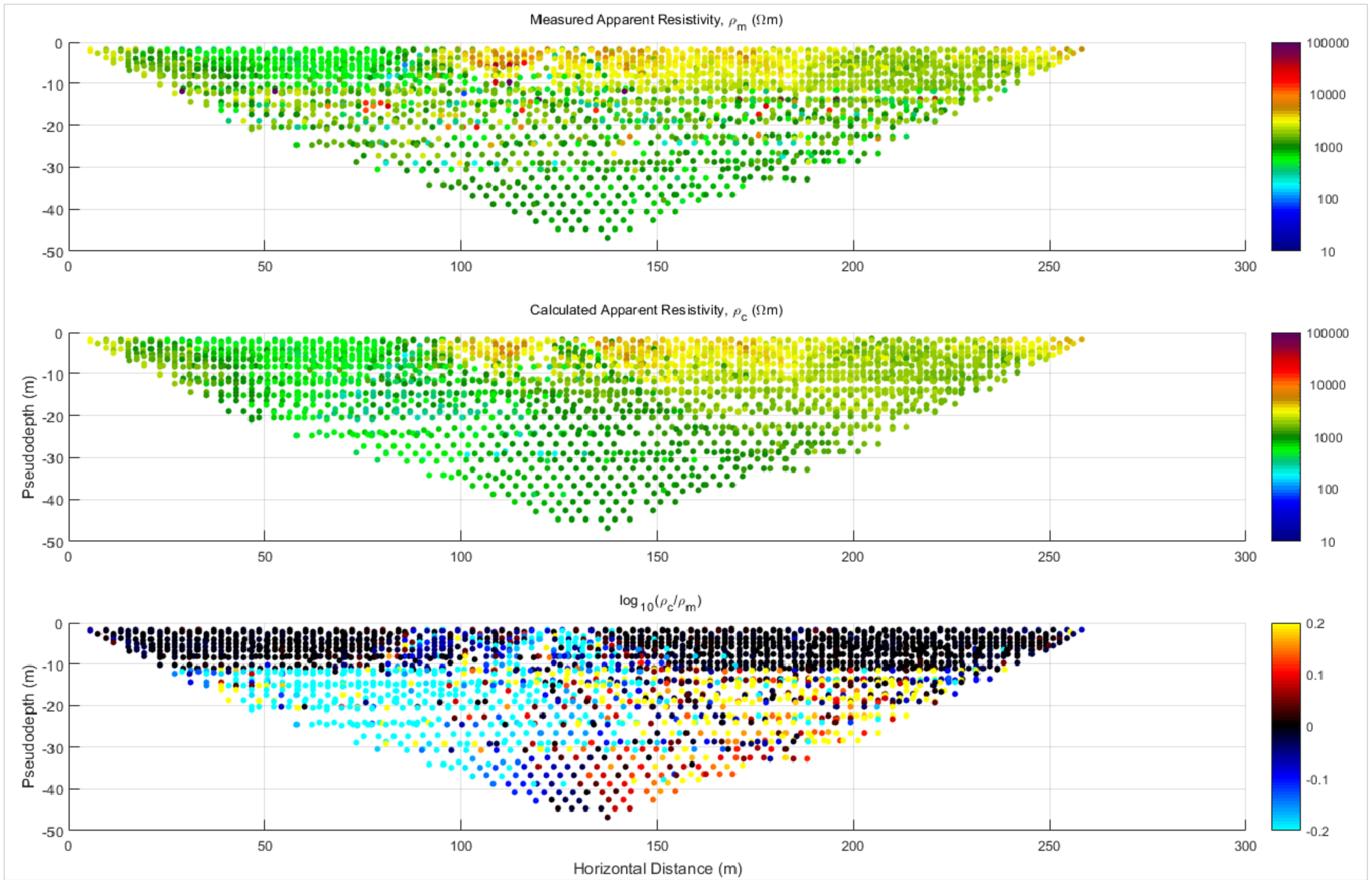

Figure D-11: Measured apparent resistivities (top) versus those calculated from the final resistivity model (middle) on ERT5.

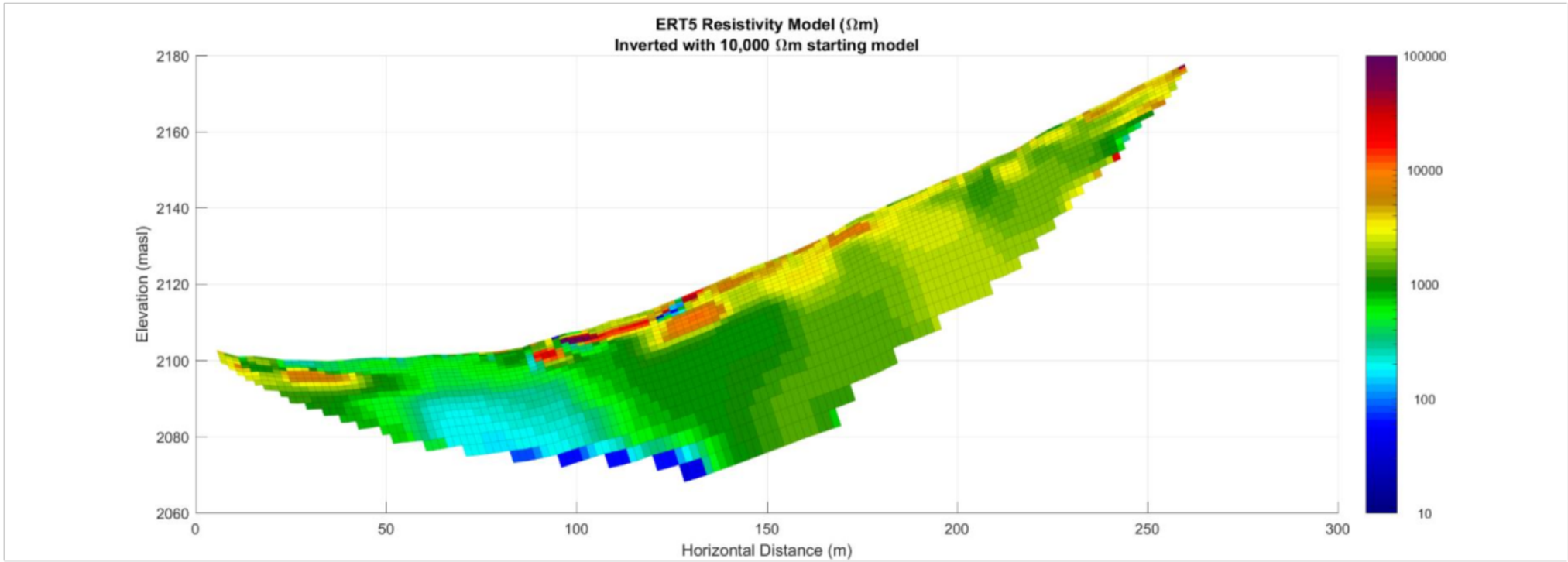

Figure D-12: Comparison of inverted models resulting from different starting models on ERT5

D.6 ERT6

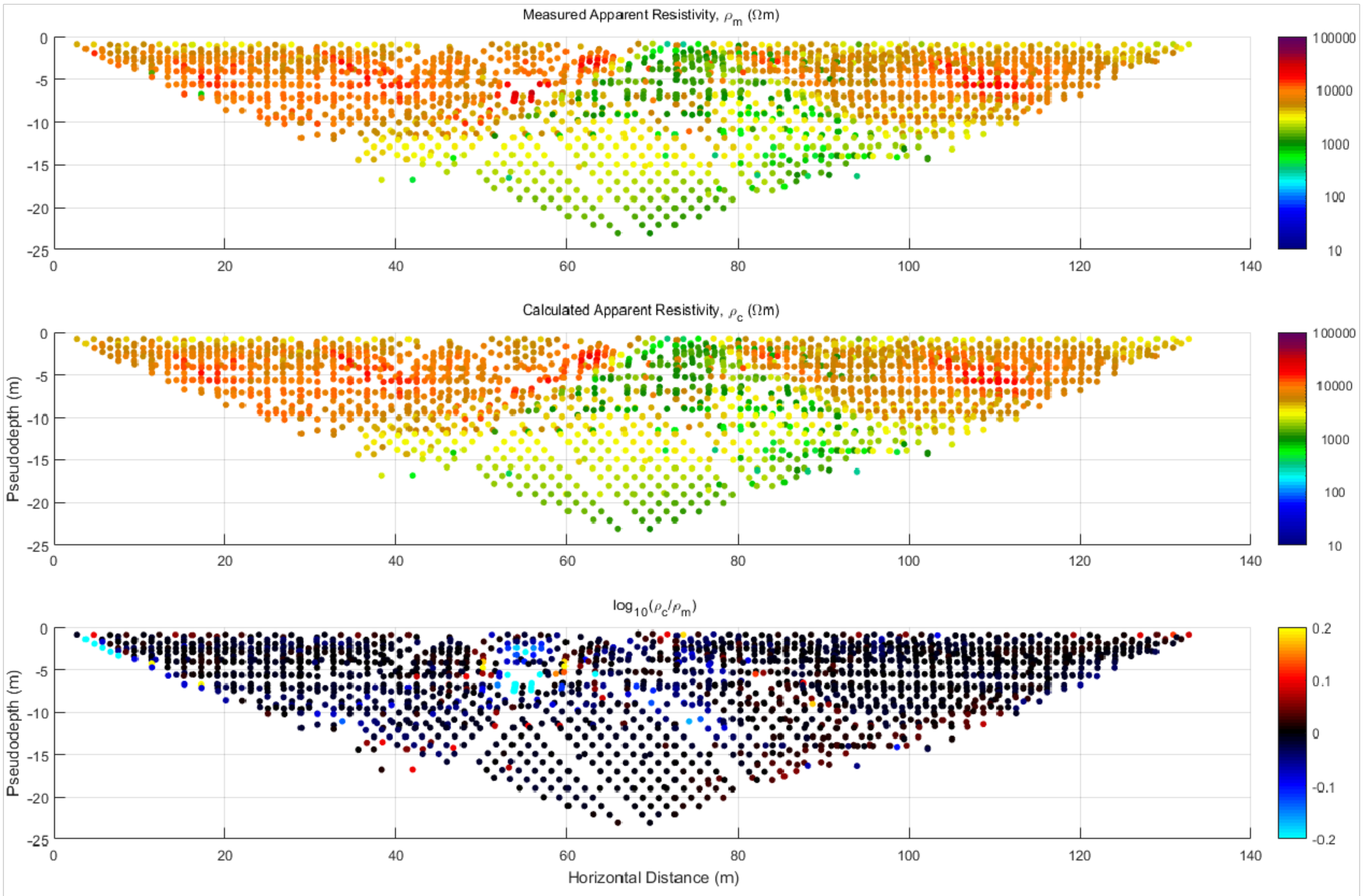

Figure D-13: Measured apparent resistivities (top) versus those calculated from the final resistivity model (middle) on ERT6.

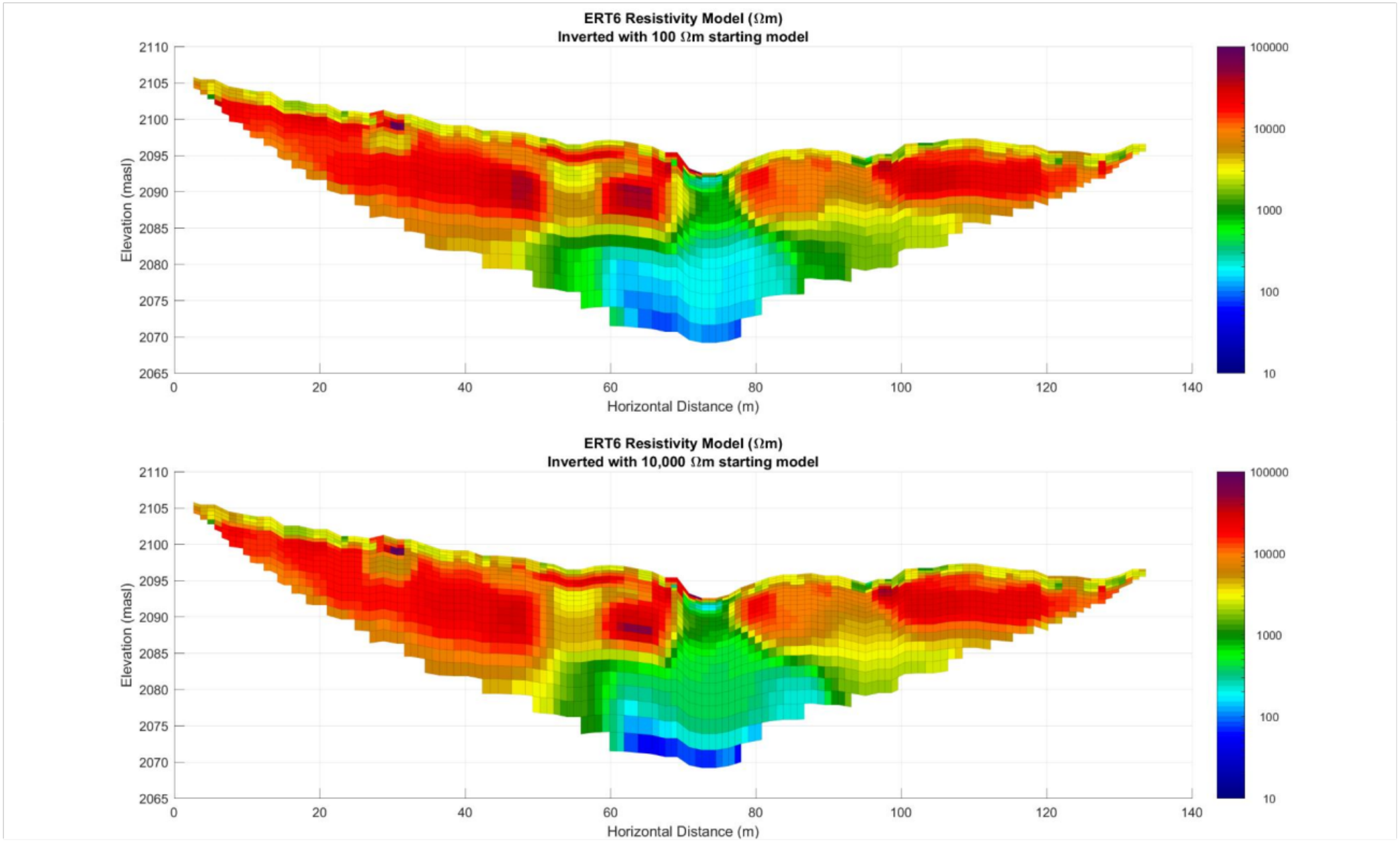

Figure D-14: Comparison of inverted models resulting from different starting models on ERT6.

D.7 ERT7

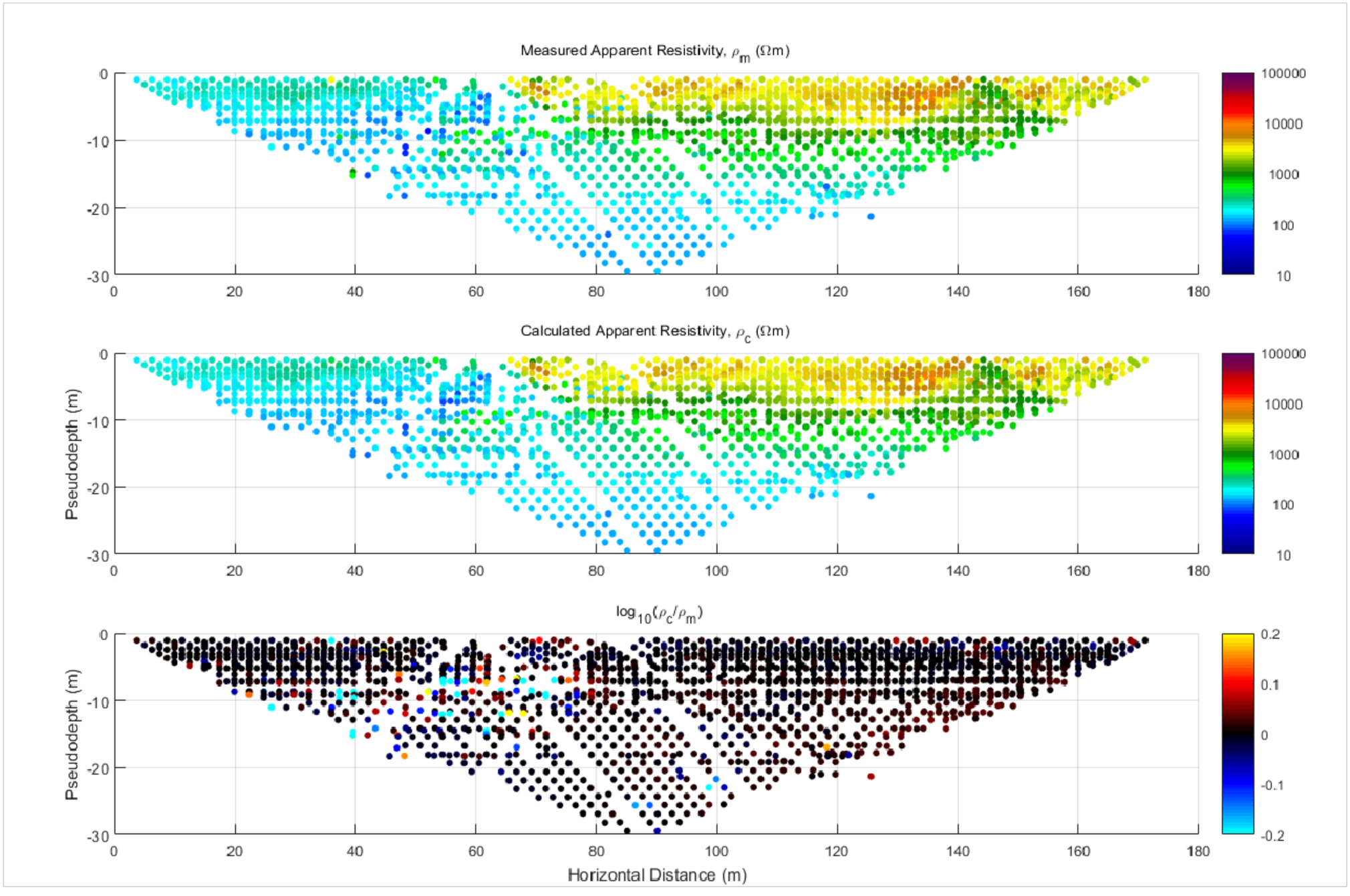

Figure D-15: Measured apparent resistivities (top) versus those calculated from the final resistivity model (middle) on ERT7.

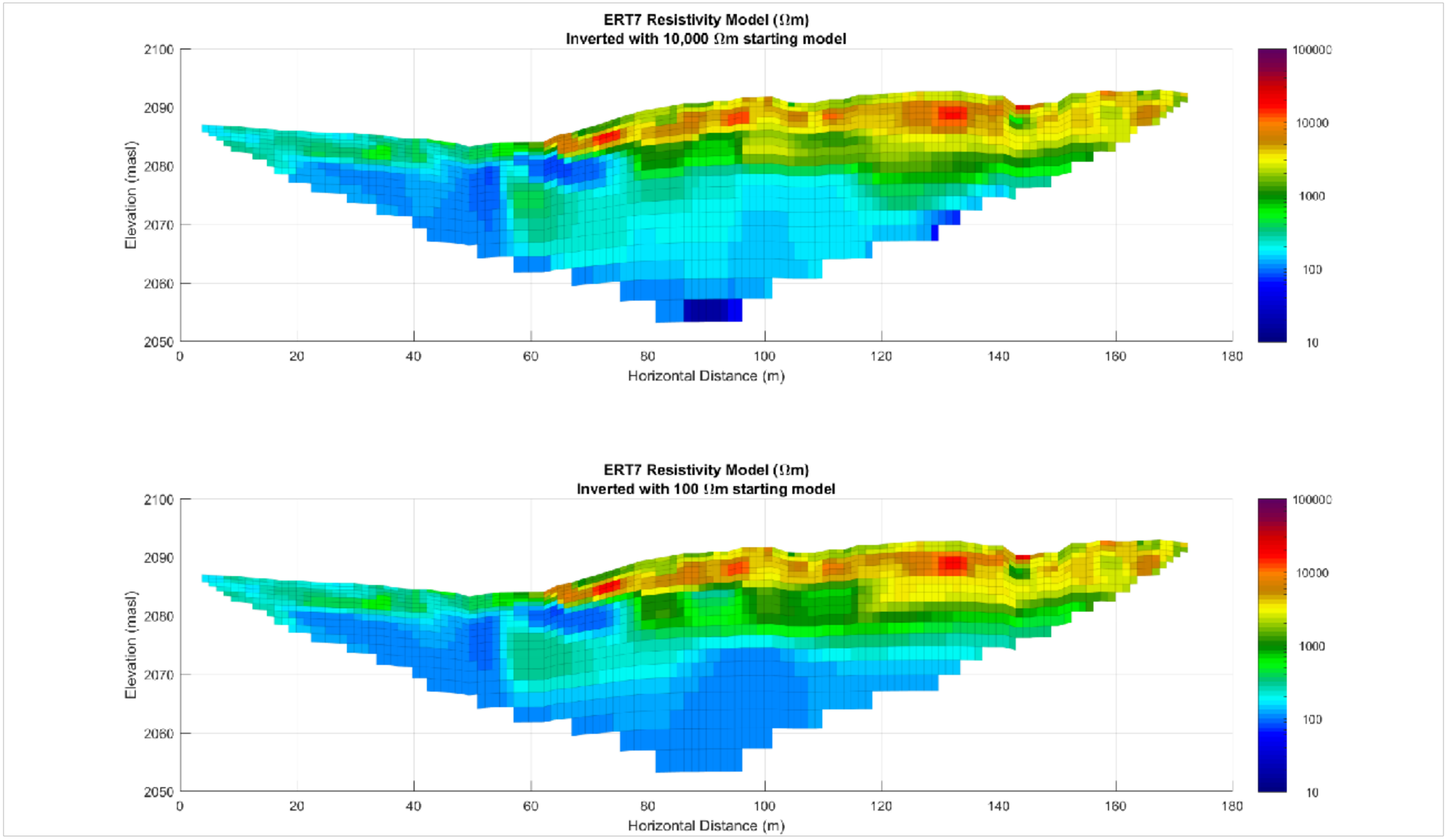

Figure D-16: Comparison of inverted models resulting from different starting models on ERT7.

D.8 ERT8

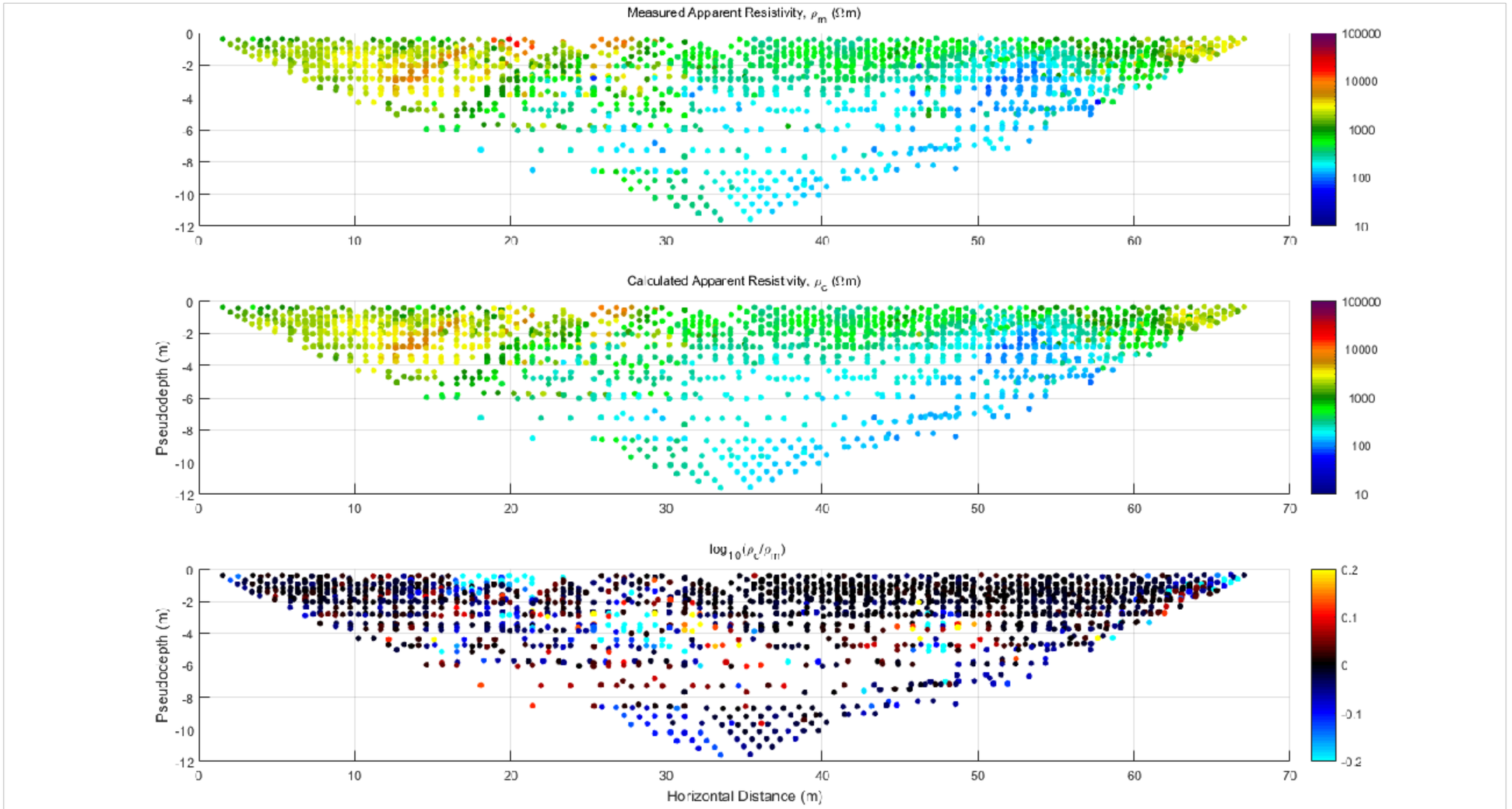

Figure D-17: Measured apparent resistivities (top) versus those calculated from the final resistivity model (middle) on ERT8.

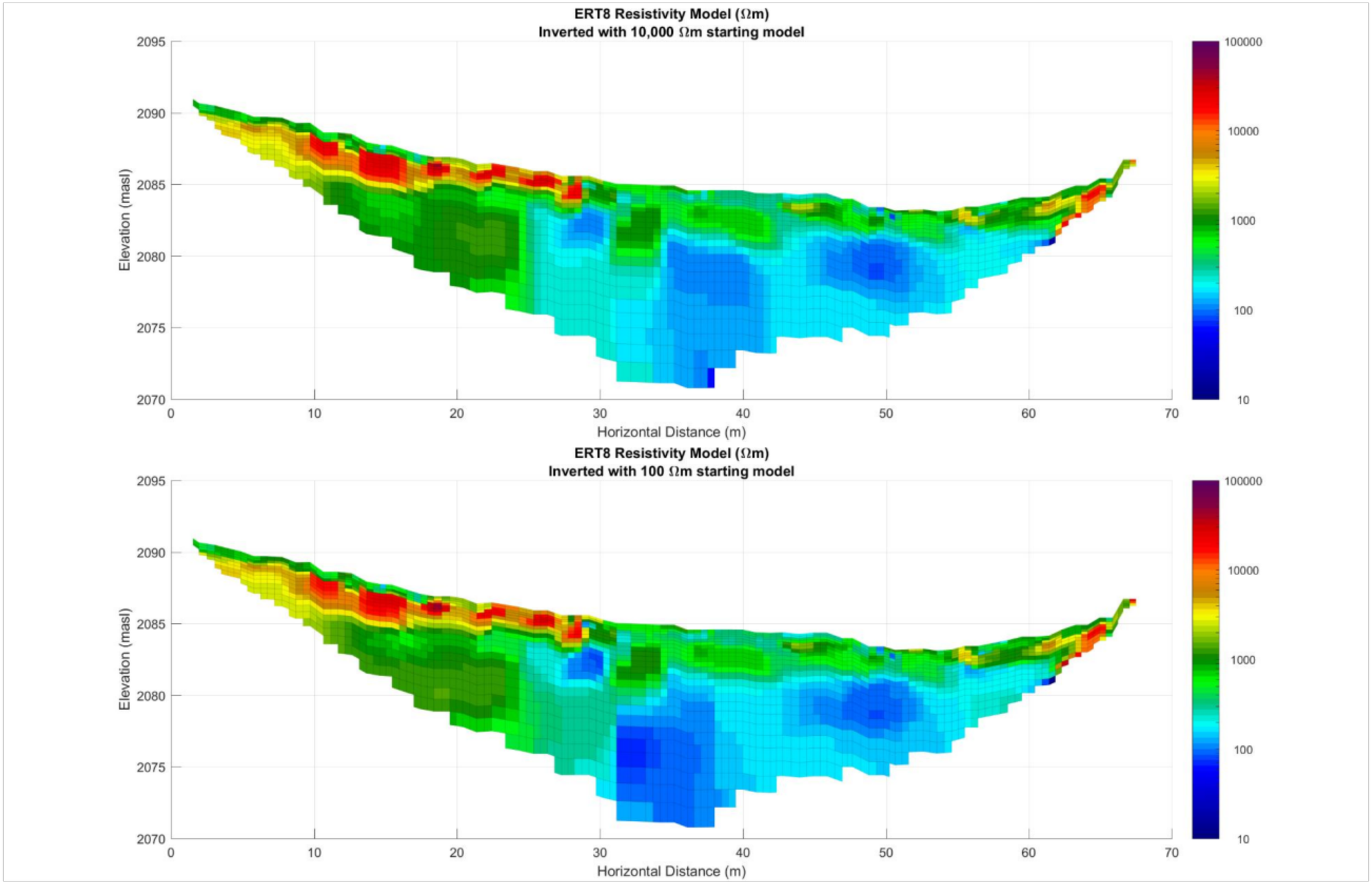

Figure D-18: Comparison of inverted models resulting from different starting models on ERT8.

D.9 ERT9

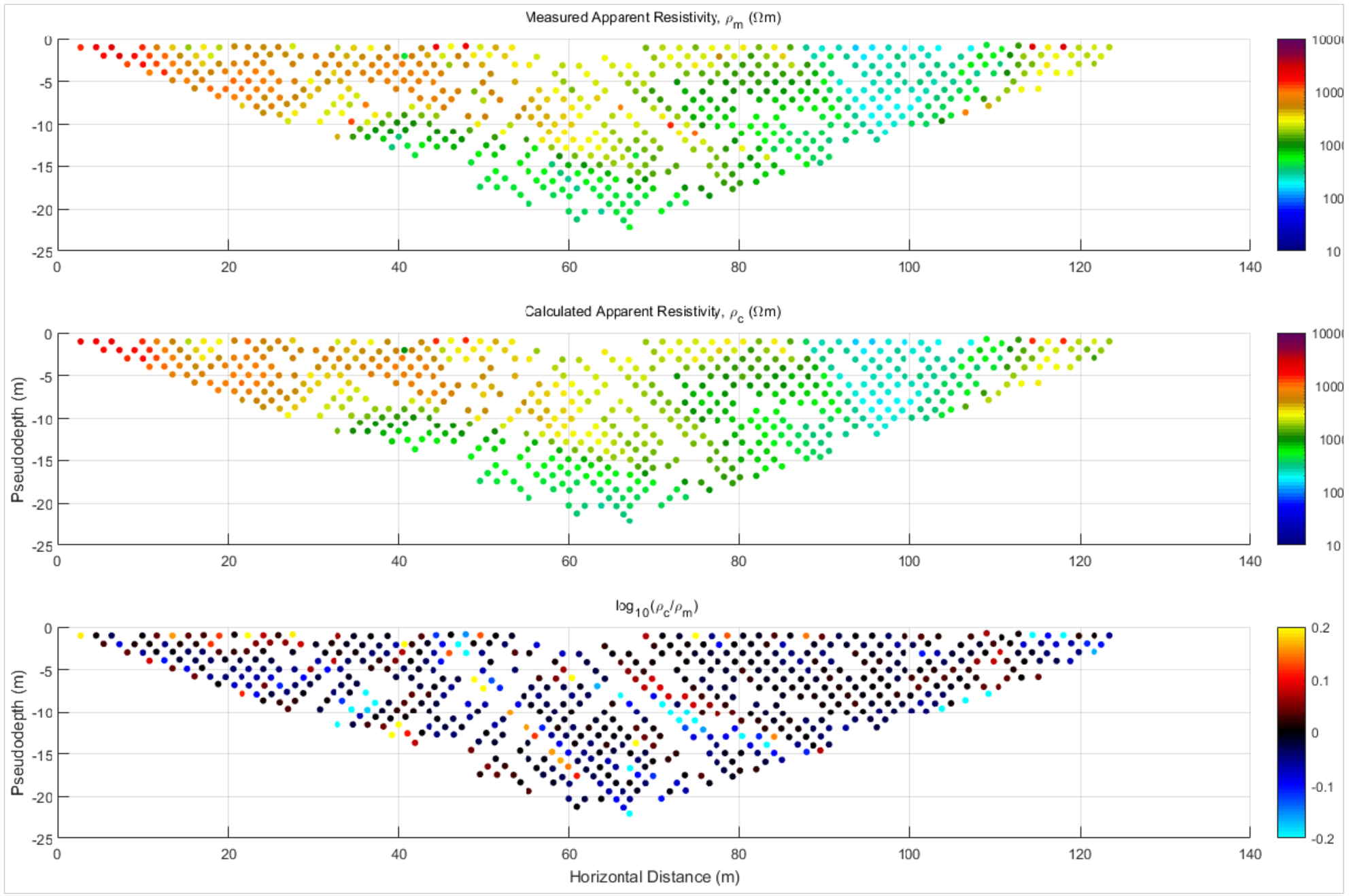

Figure D-19: Measured apparent resistivities (top) versus those calculated from the final resistivity model (middle) on ERT9.

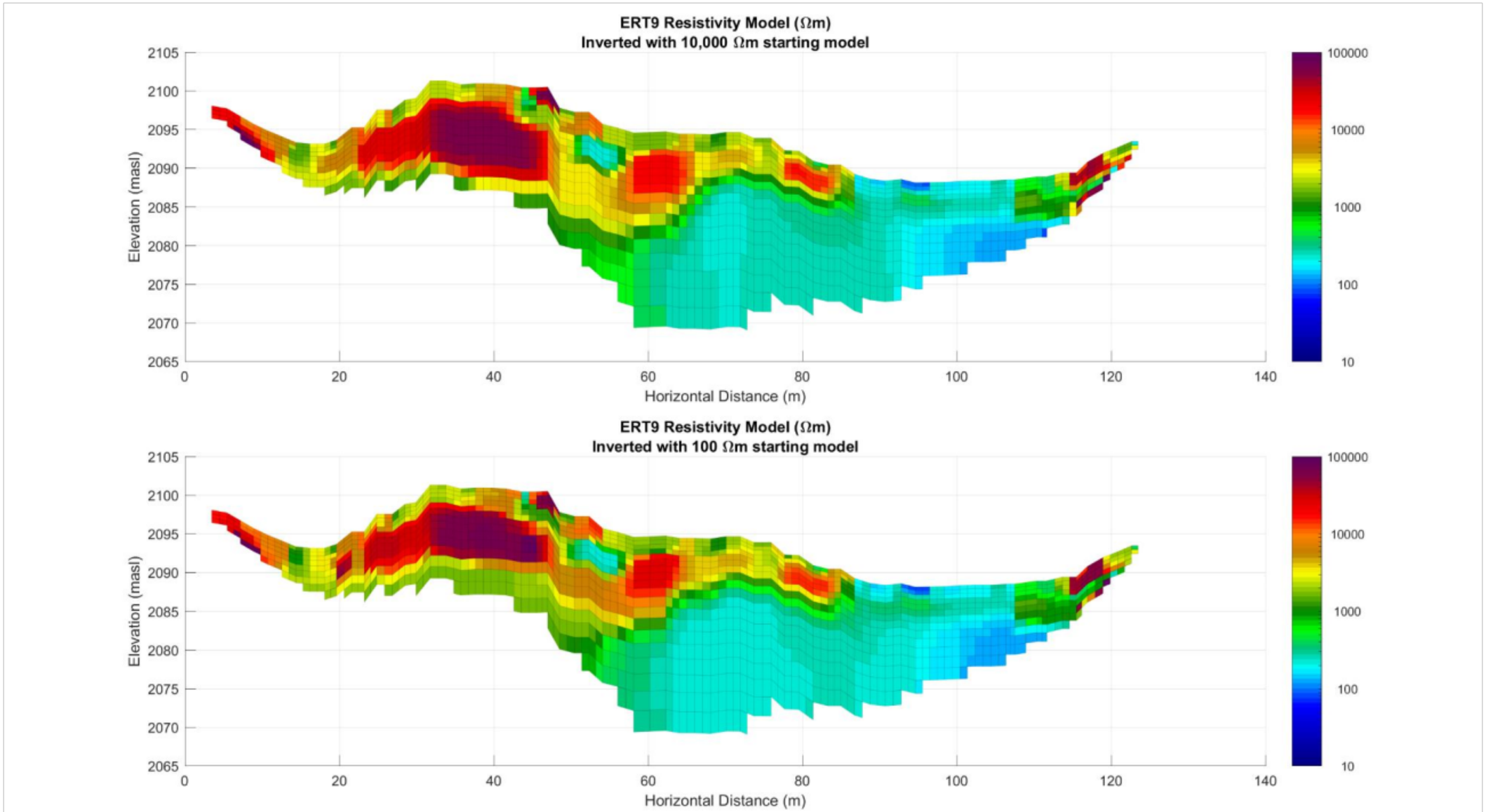

Figure D-20: Comparison of inverted models resulting from different starting models on ERT9.

D.10 ERT10

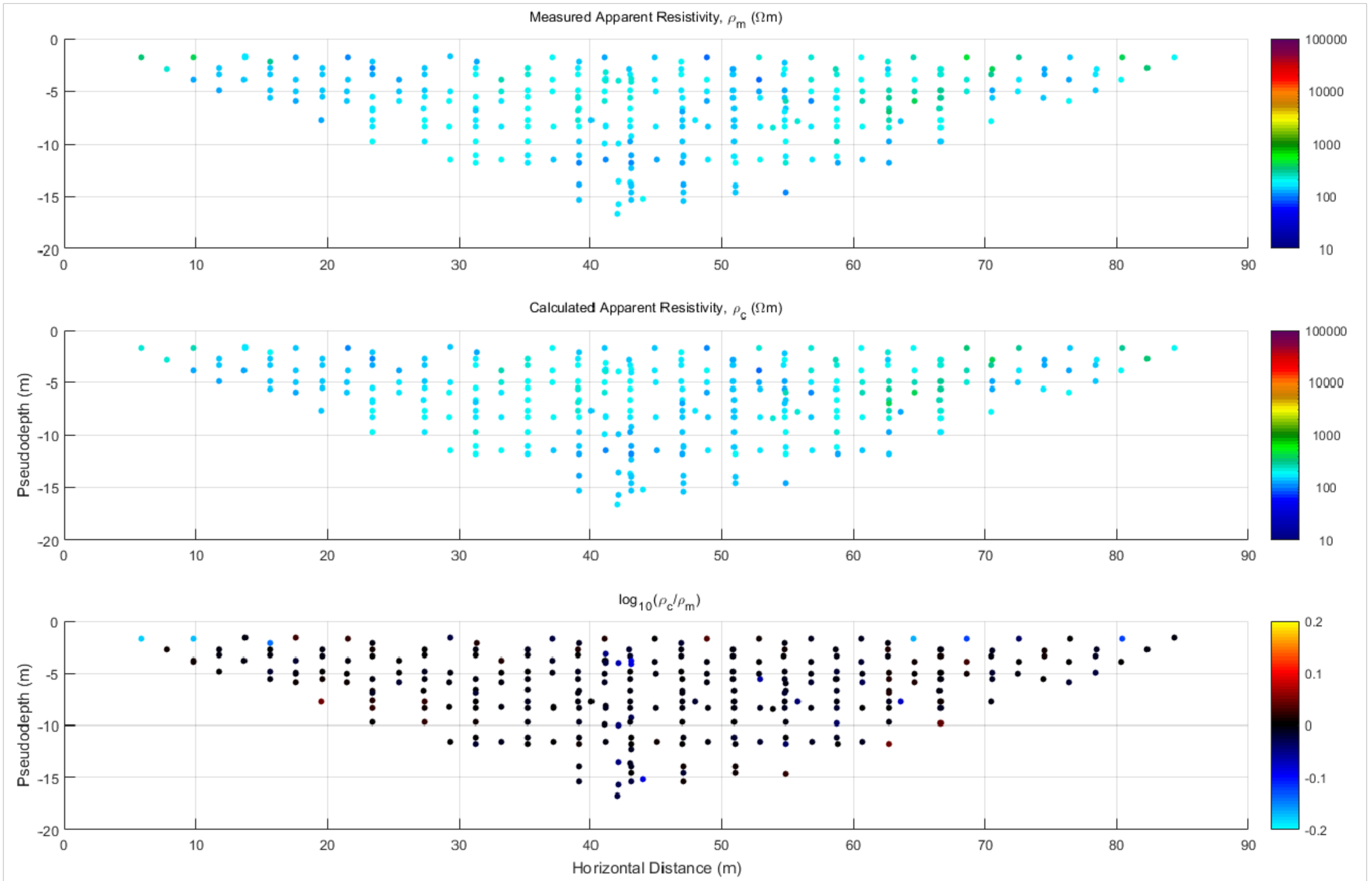

Figure D-21: Measured apparent resistivities (top) versus those calculated from the final resistivity model (middle) on ERT10.

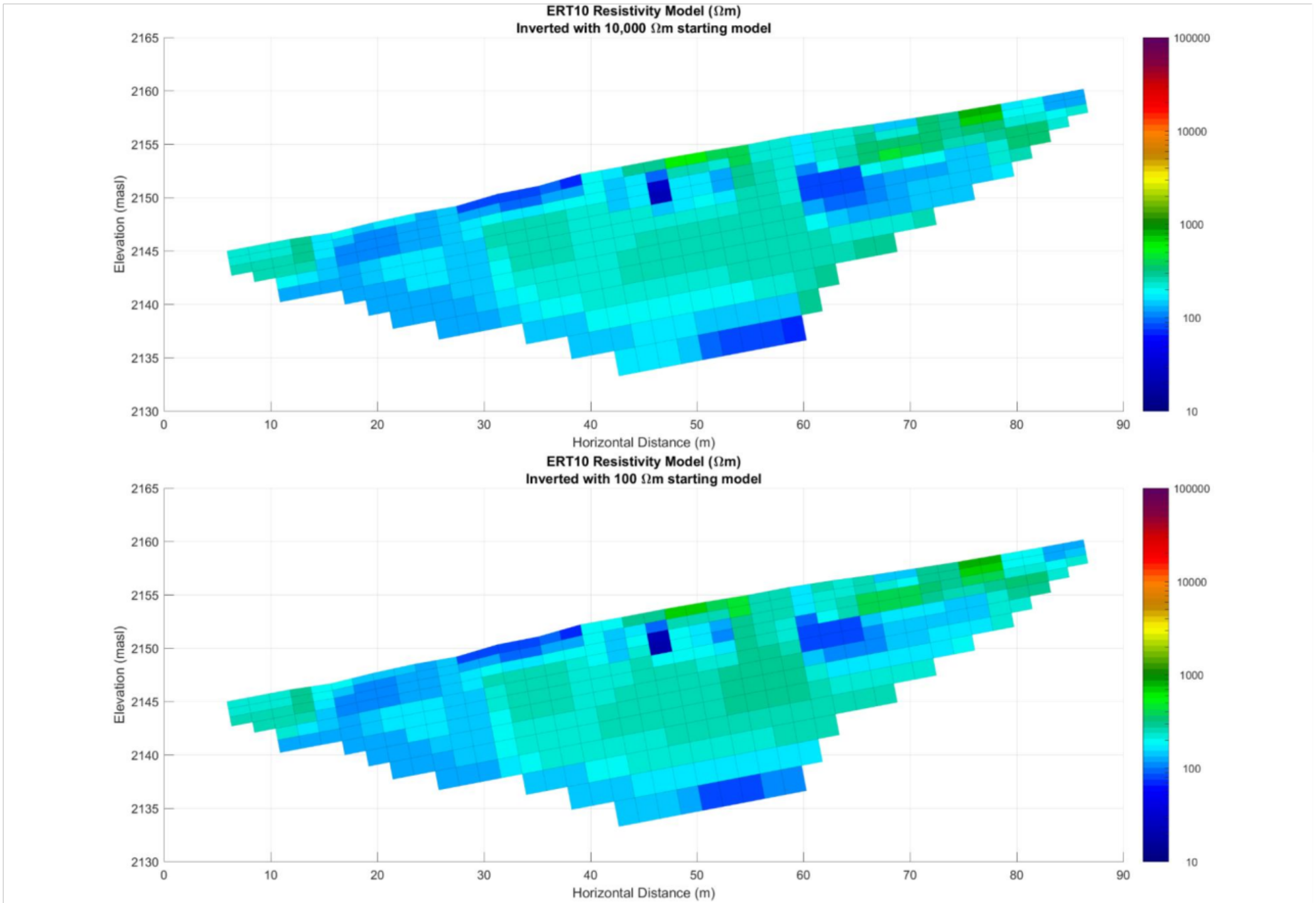

Figure D-22: Comparison of inverted models resulting from different starting models on ERT10.

D.11 ERT11

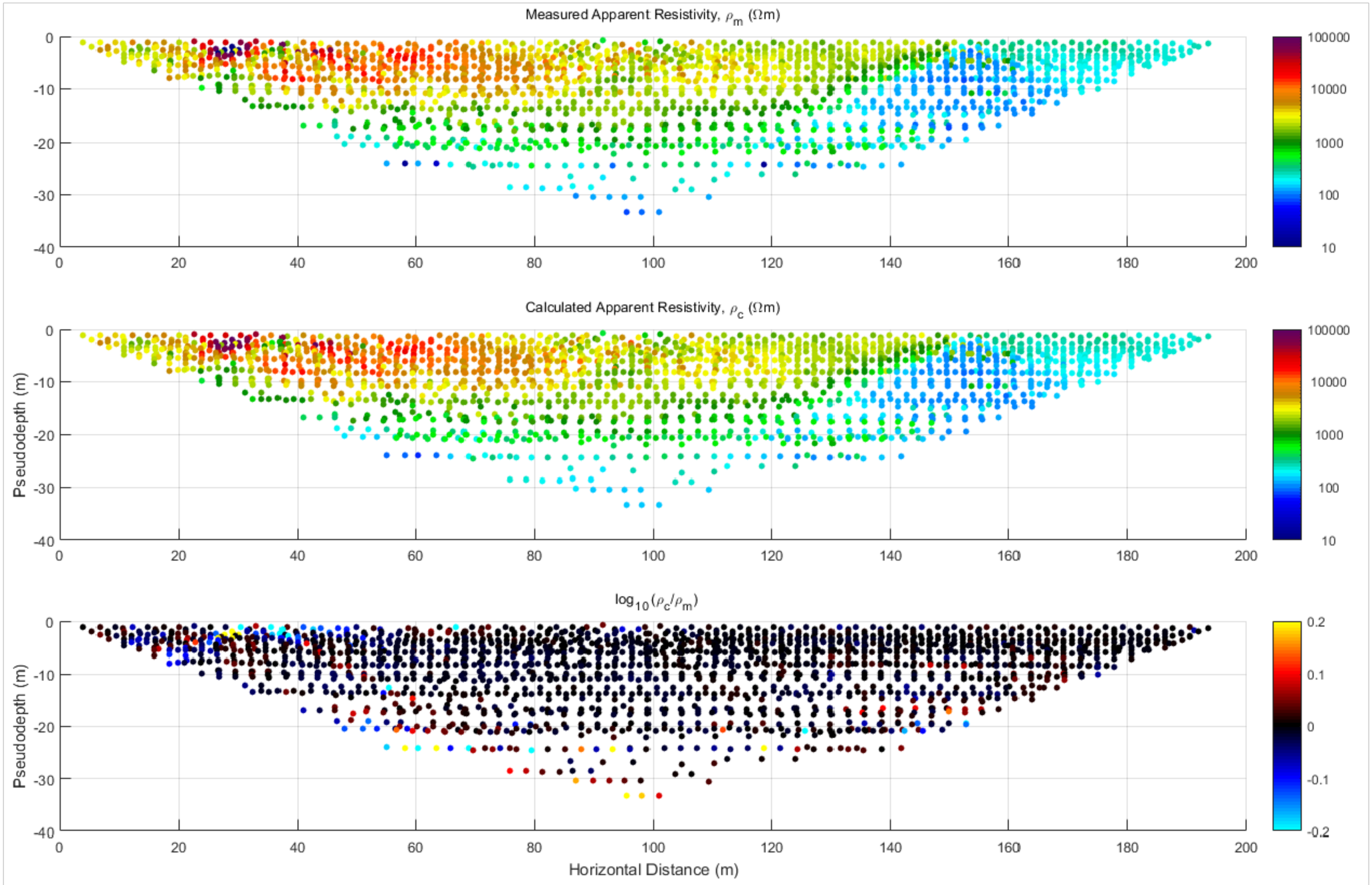

Figure D-23: Measured apparent resistivities (top) versus those calculated from the final resistivity model (middle) on ERT11.

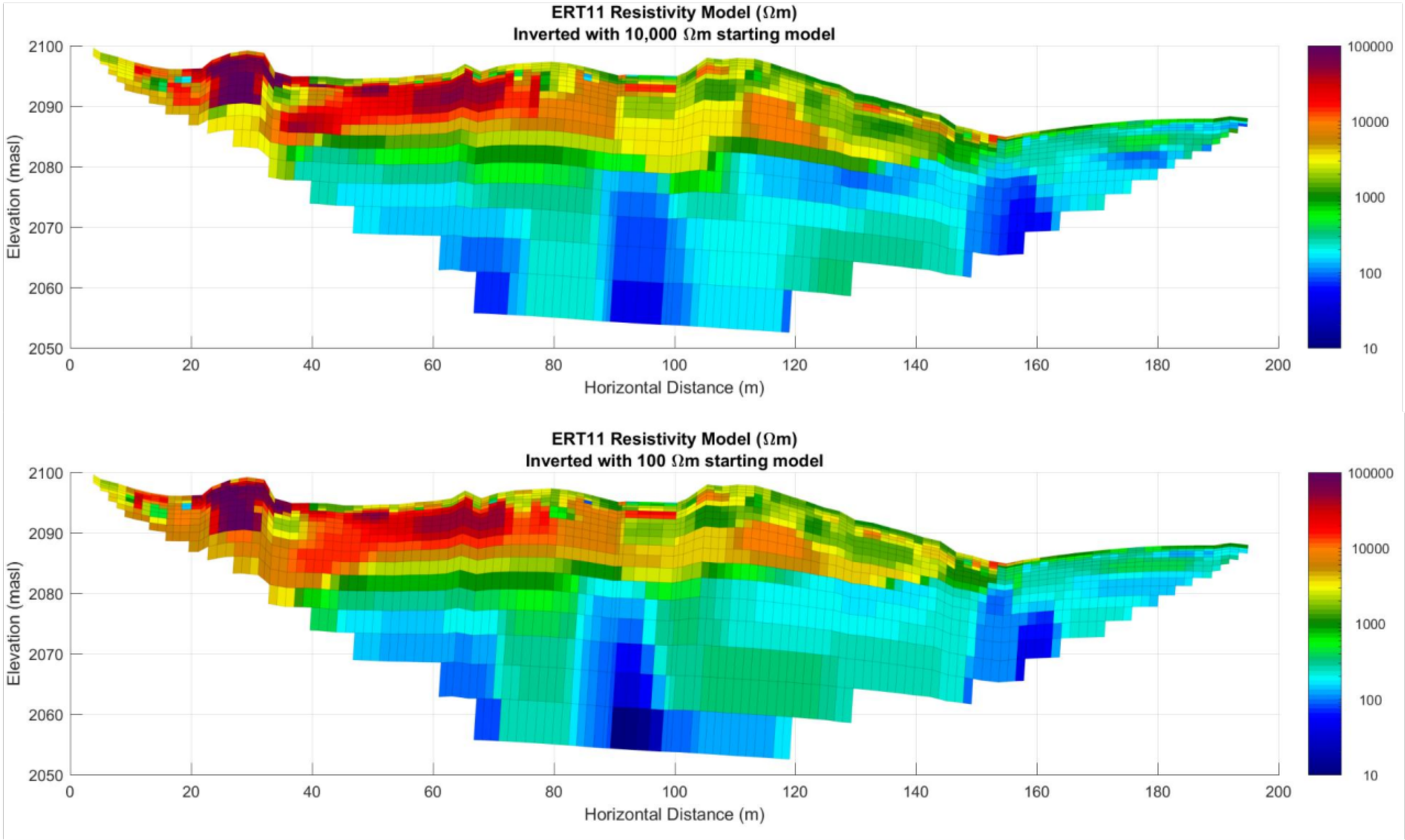

Figure D-24: Comparison of inverted models resulting from different starting models on ERT11.

D.12 ERT12

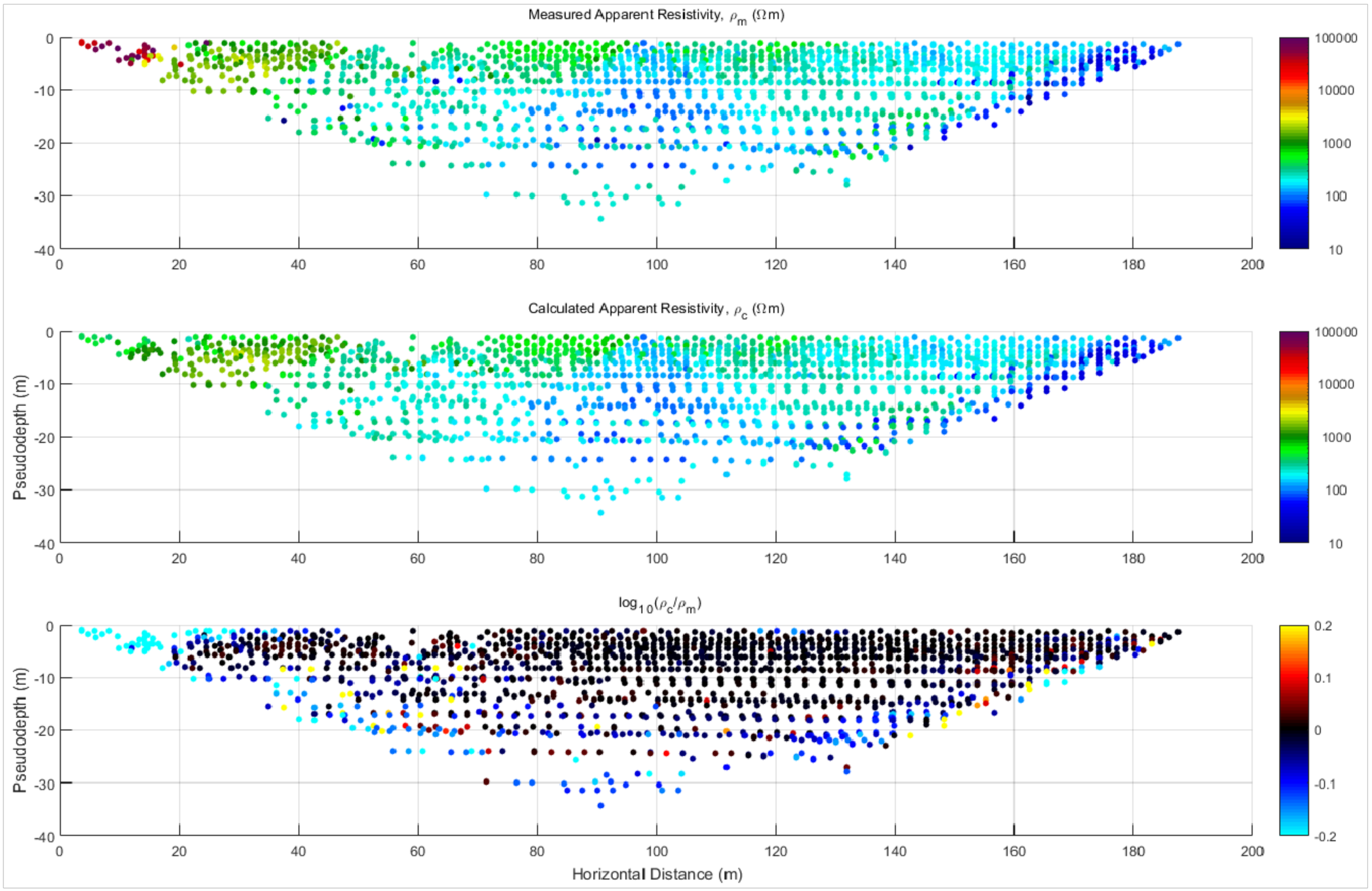

Figure D-25: Measured apparent resistivities (top) versus those calculated from the final resistivity model (middle) on ERT12

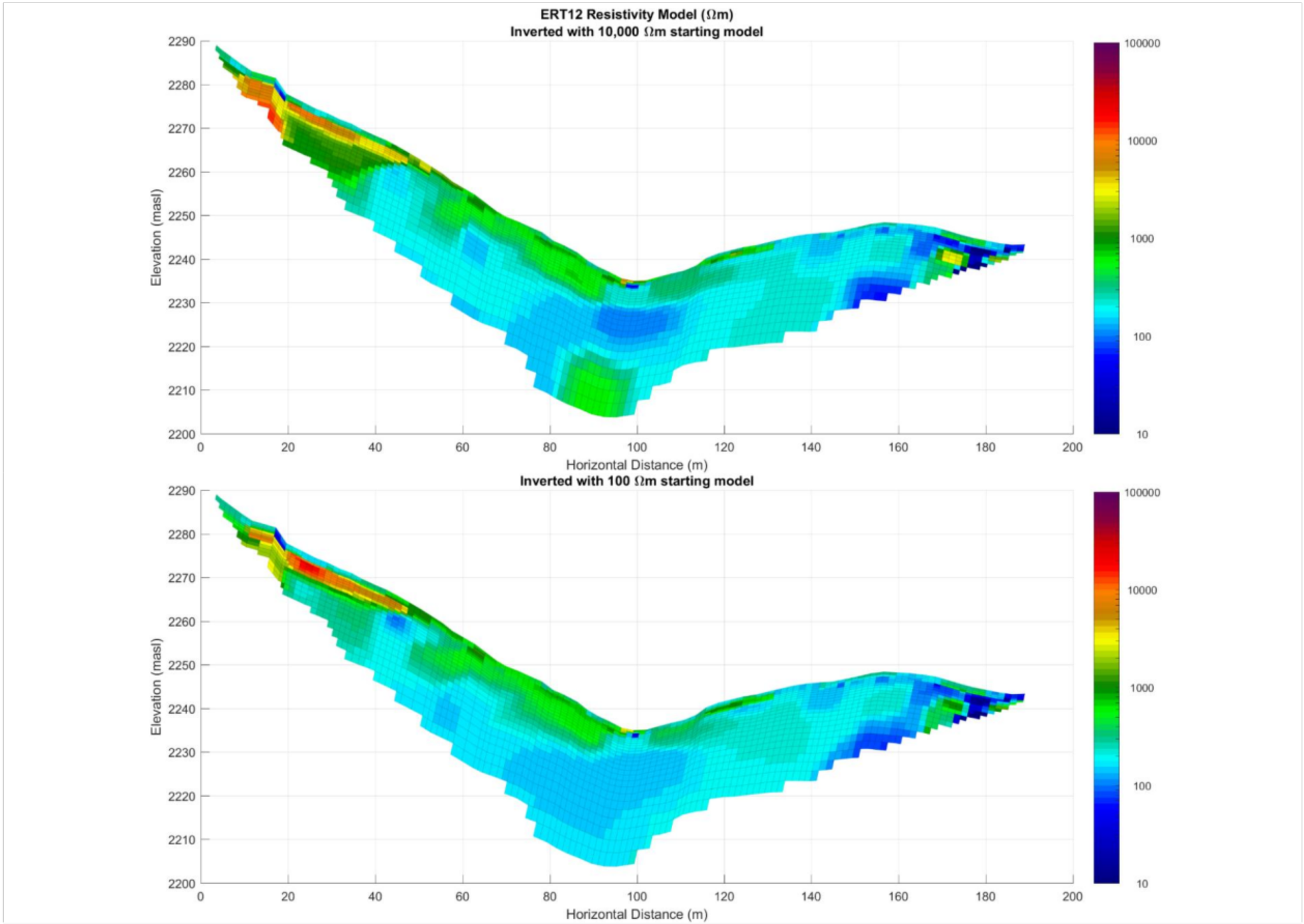

Figure D-26: Comparison of inverted models resulting from different starting models on ERT1.

D.13 ERT13

Table D-2: The depth range of each layer in the 3D resistivity model from ERT13.

Layer number	Depth range (m)
1	0.00 - 1.41
2	1.41 – 3.04
3	3.04 – 4.91
4	4.91 – 7.06
5	7.06 – 9.54
6	9.54 – 12.4
7	12.4 -15.7
8	15.7 - 19.4
9	19.4- 23.7

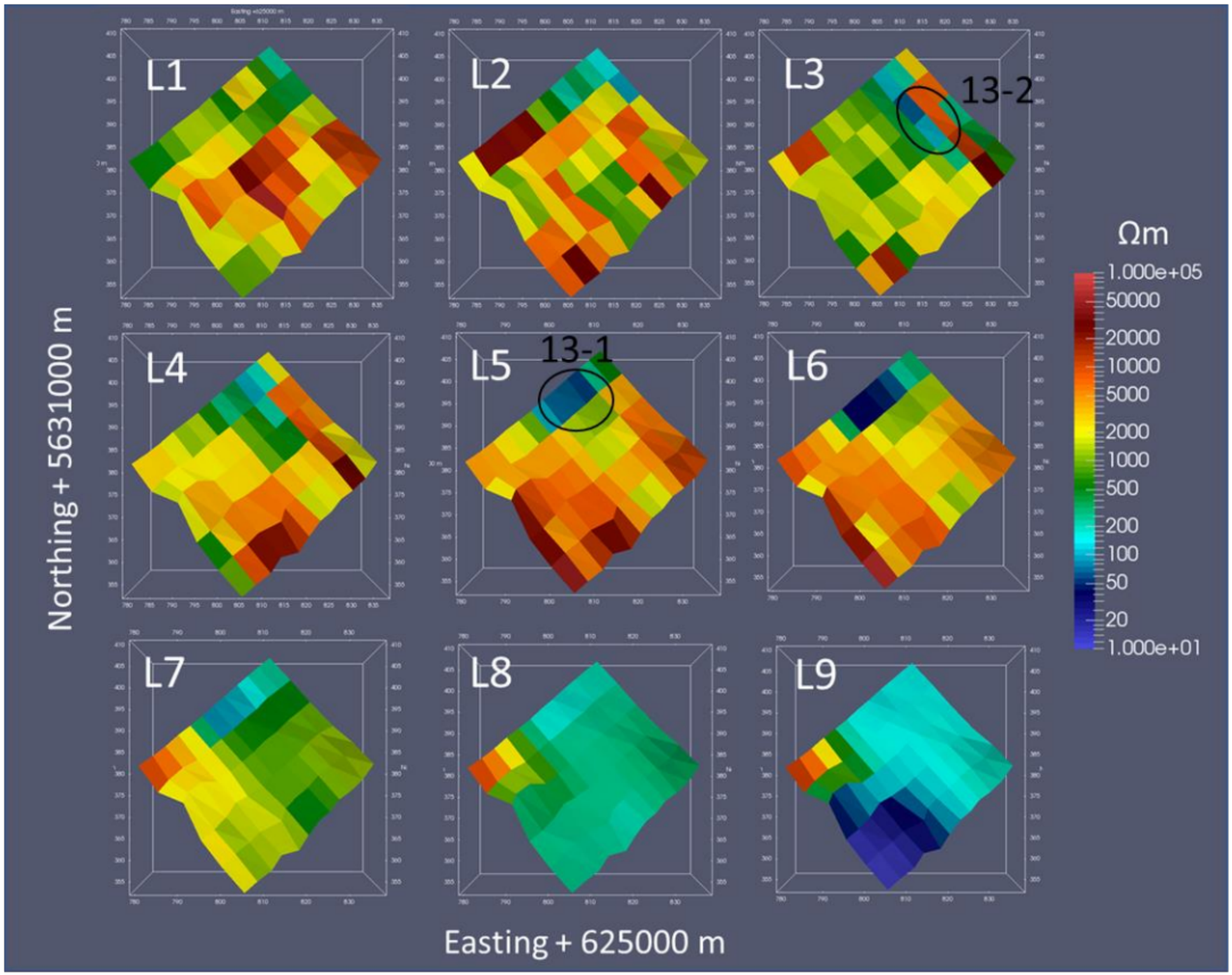

Figure D-27: Resistivity sections for each layer of the ERT13 resistivity model.

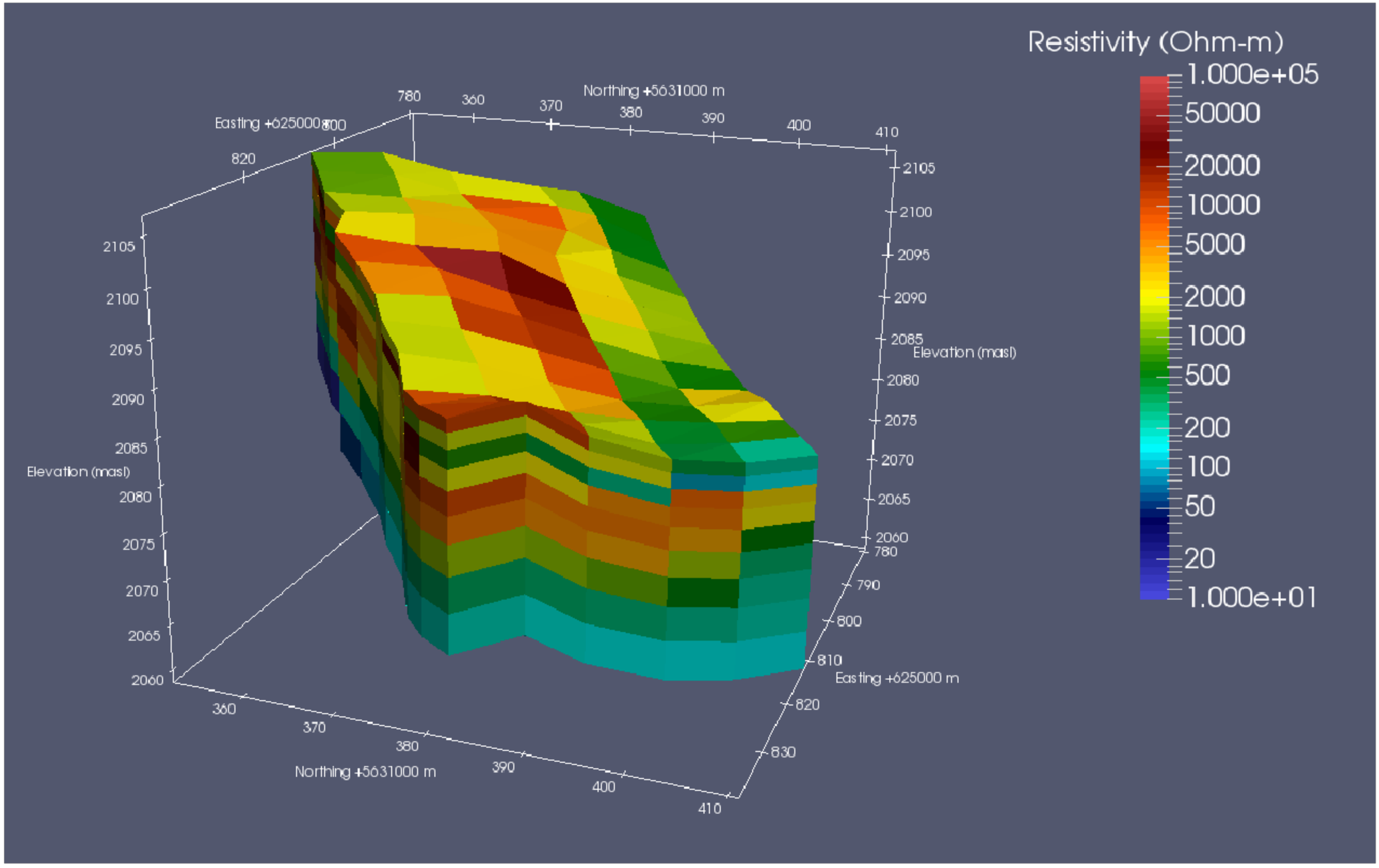

Figure D-28: Oblique view of the ERT13 resistivity model.

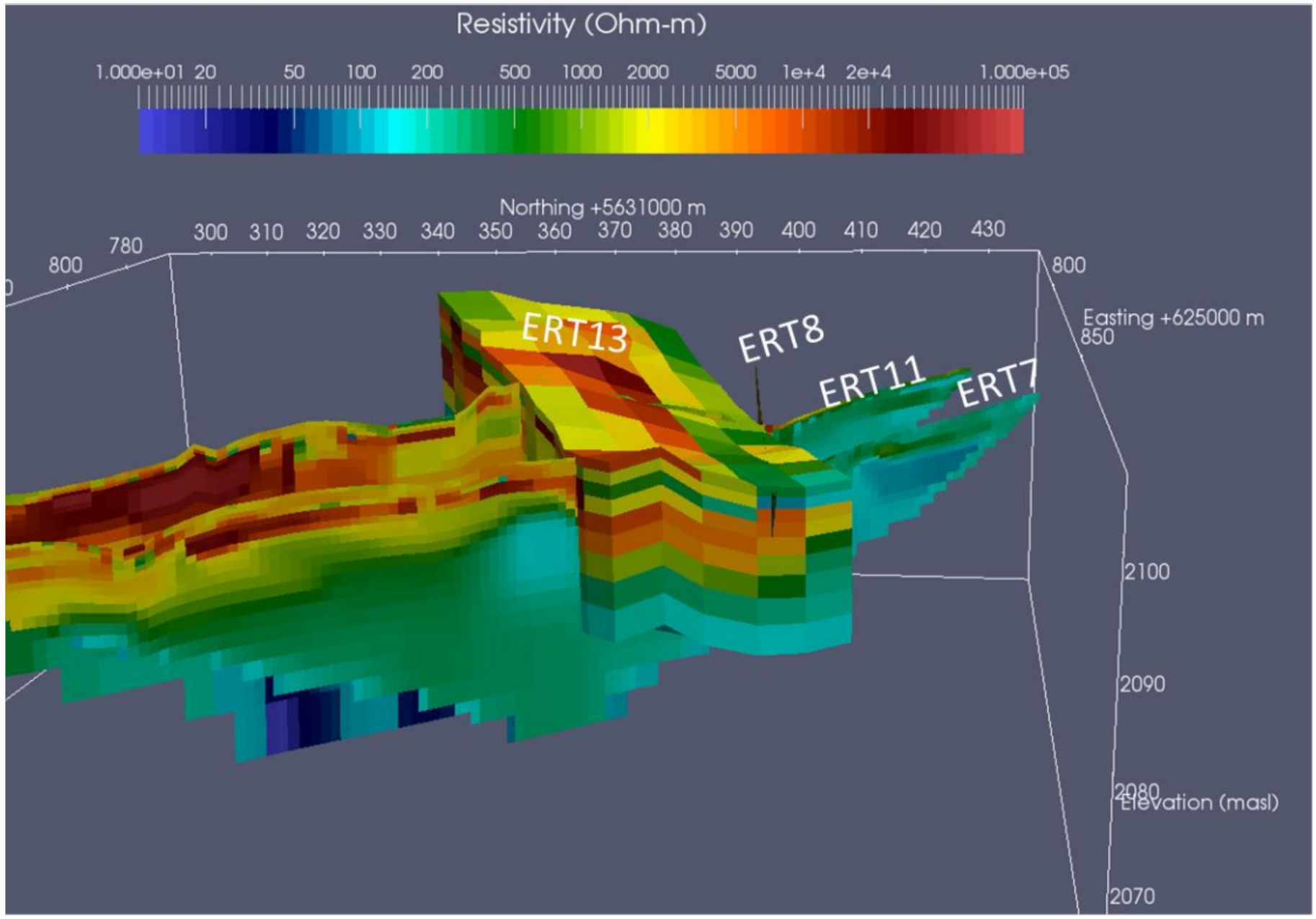

Figure D-29: Oblique view of the ERT13 resistivity model along with intersecting 2D models.

Appendix E Seismic Refraction Tomography Images

E.1 SEIS1-2-4

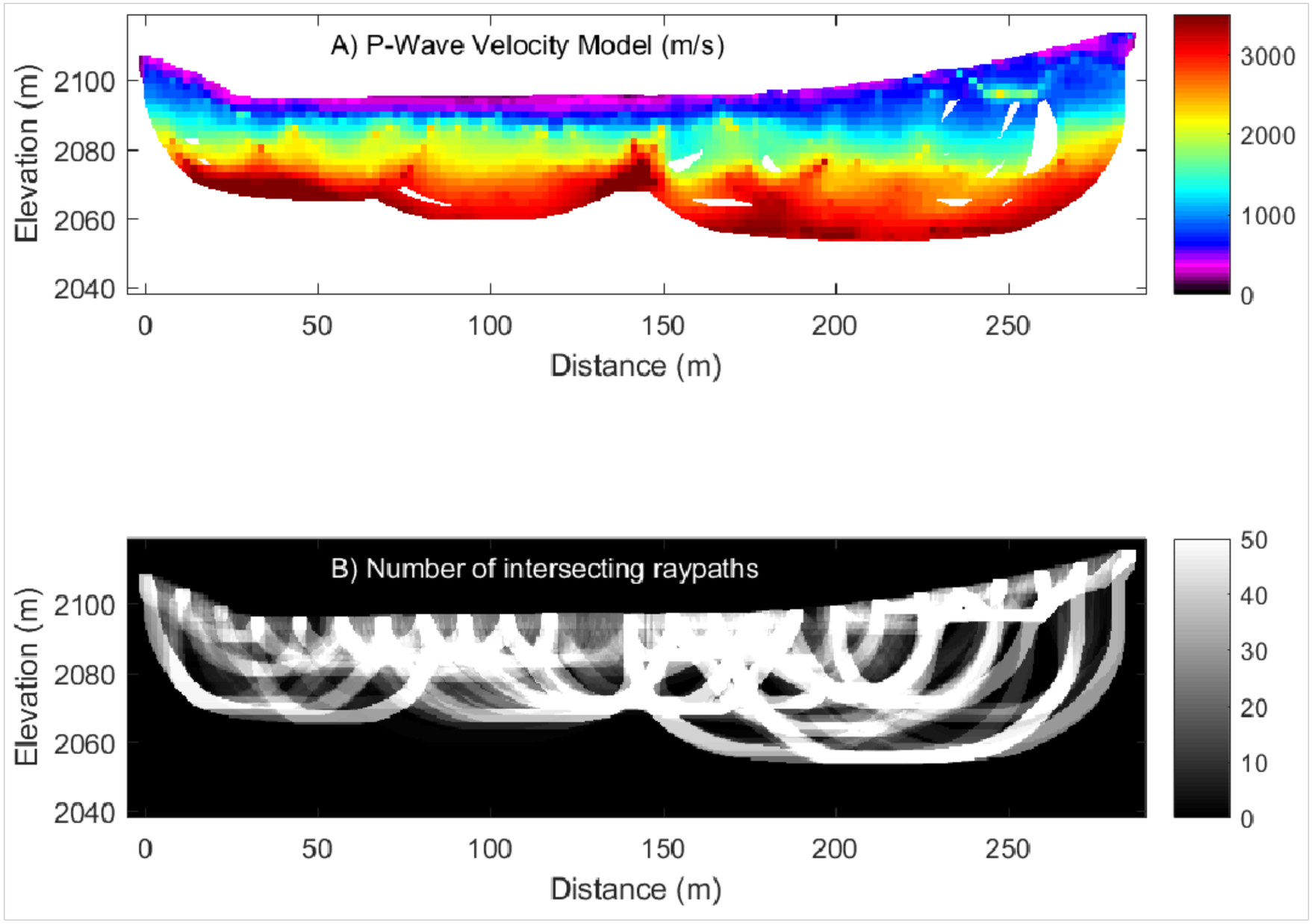

Figure E-1: P-wave velocity models (A) and ray path density (B) along SEIS1-2-4.

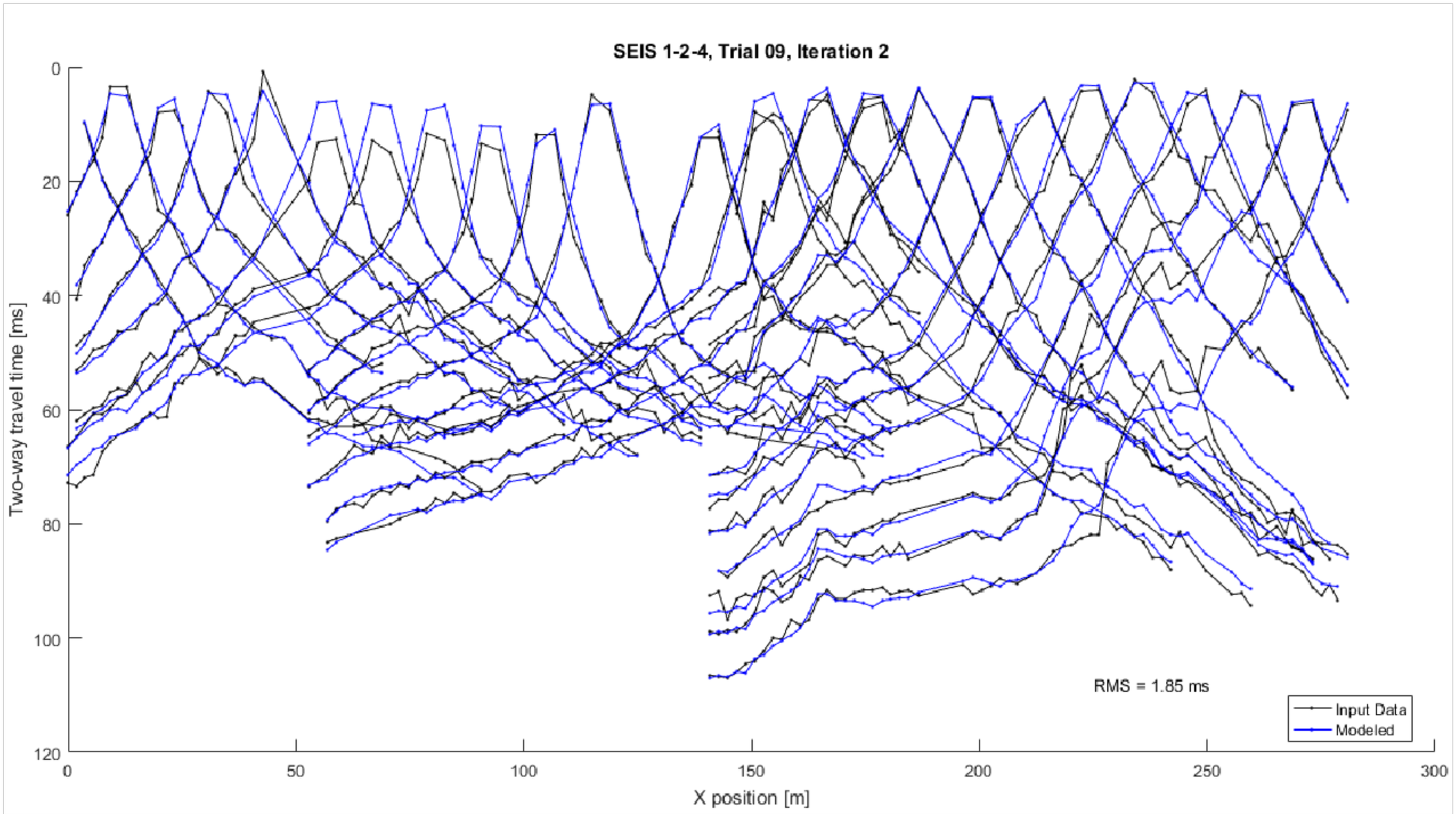

Figure E-2: Modeled versus measured first arrival times on SEIS1-2-4.

E.2 SIES3

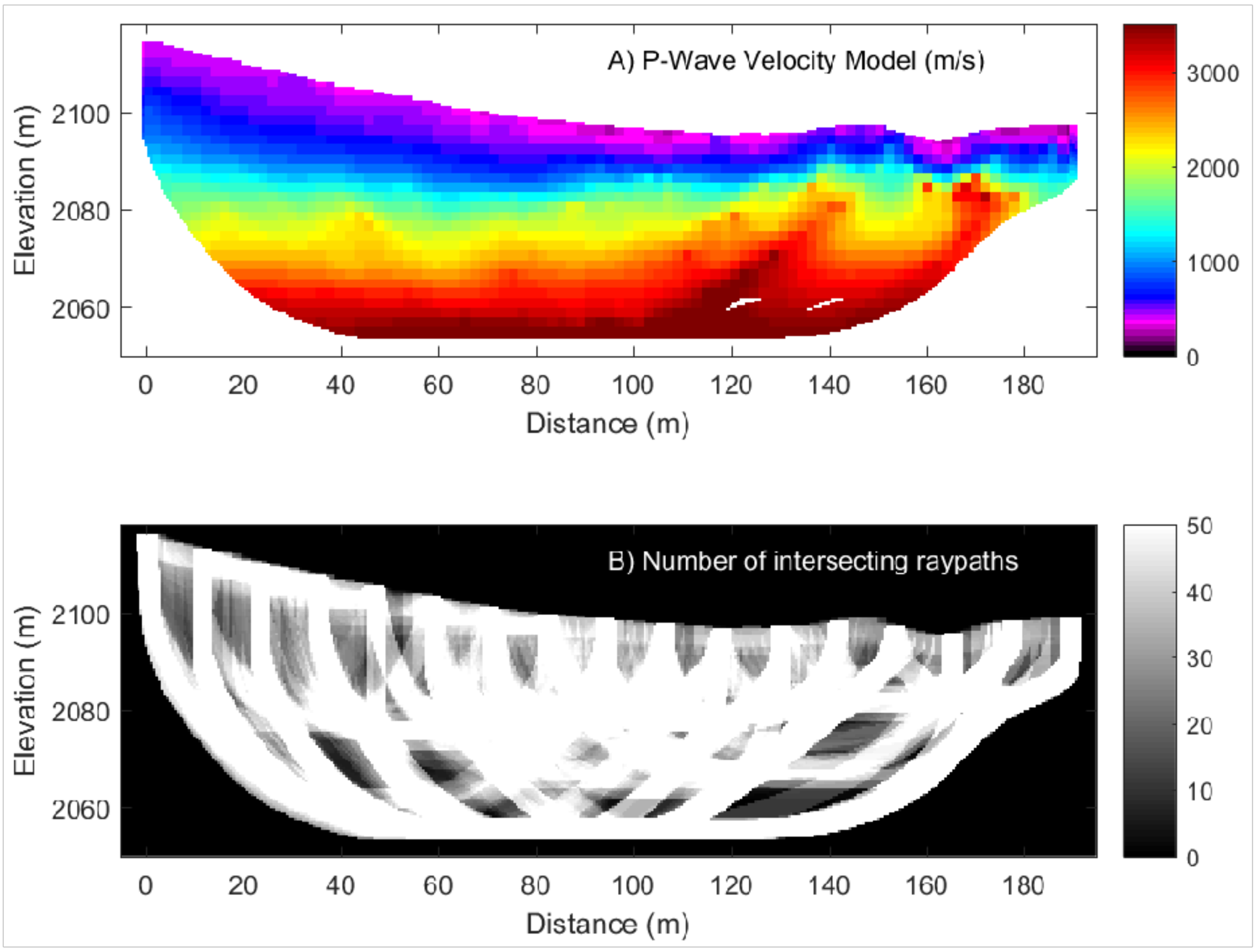

Figure E-3: P-wave velocity models (A) and ray path density (B) along SEIS3.

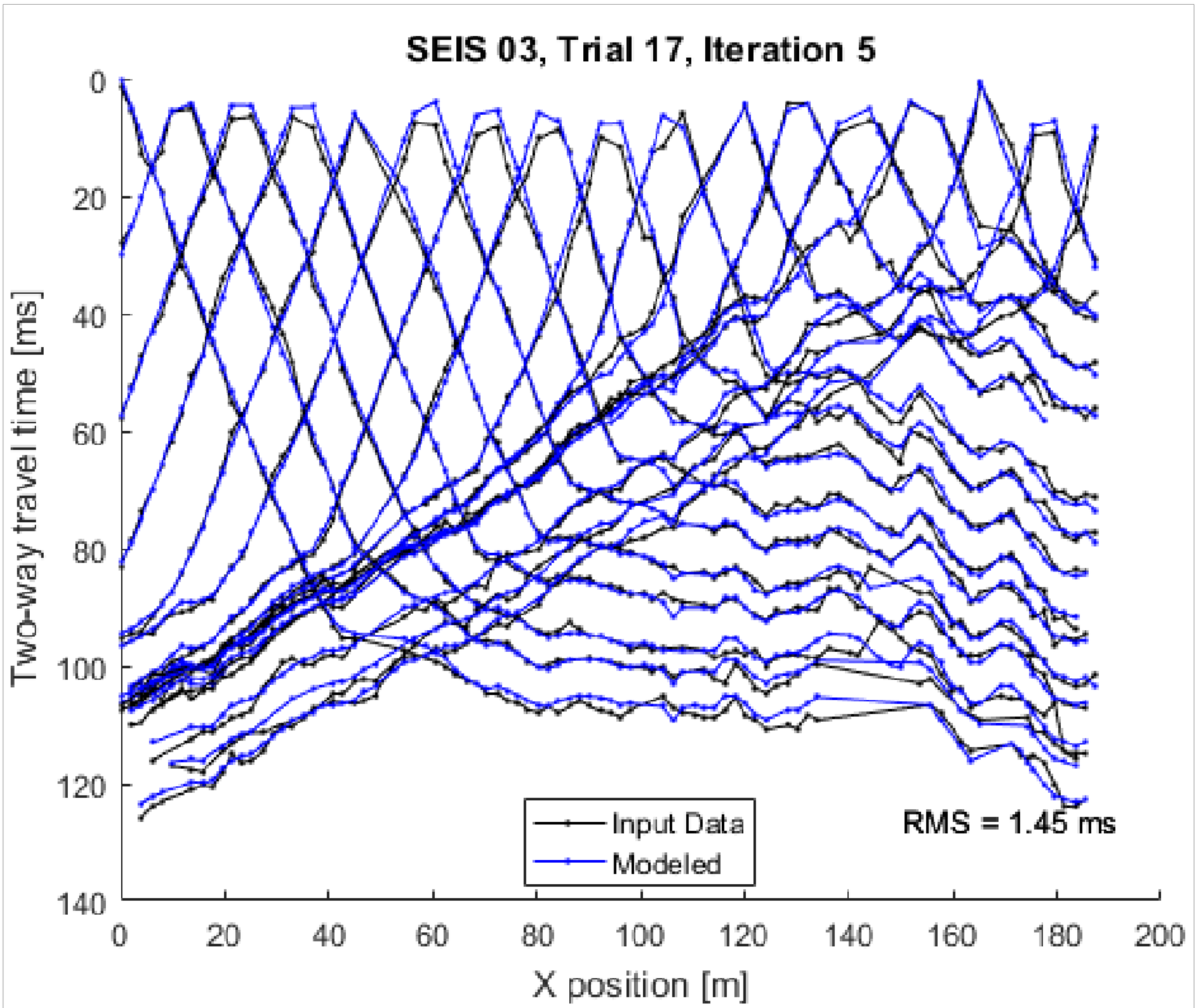

Figure E-4: Modeled versus measured first arrival times on SEIS3.

E.3 SEIS5

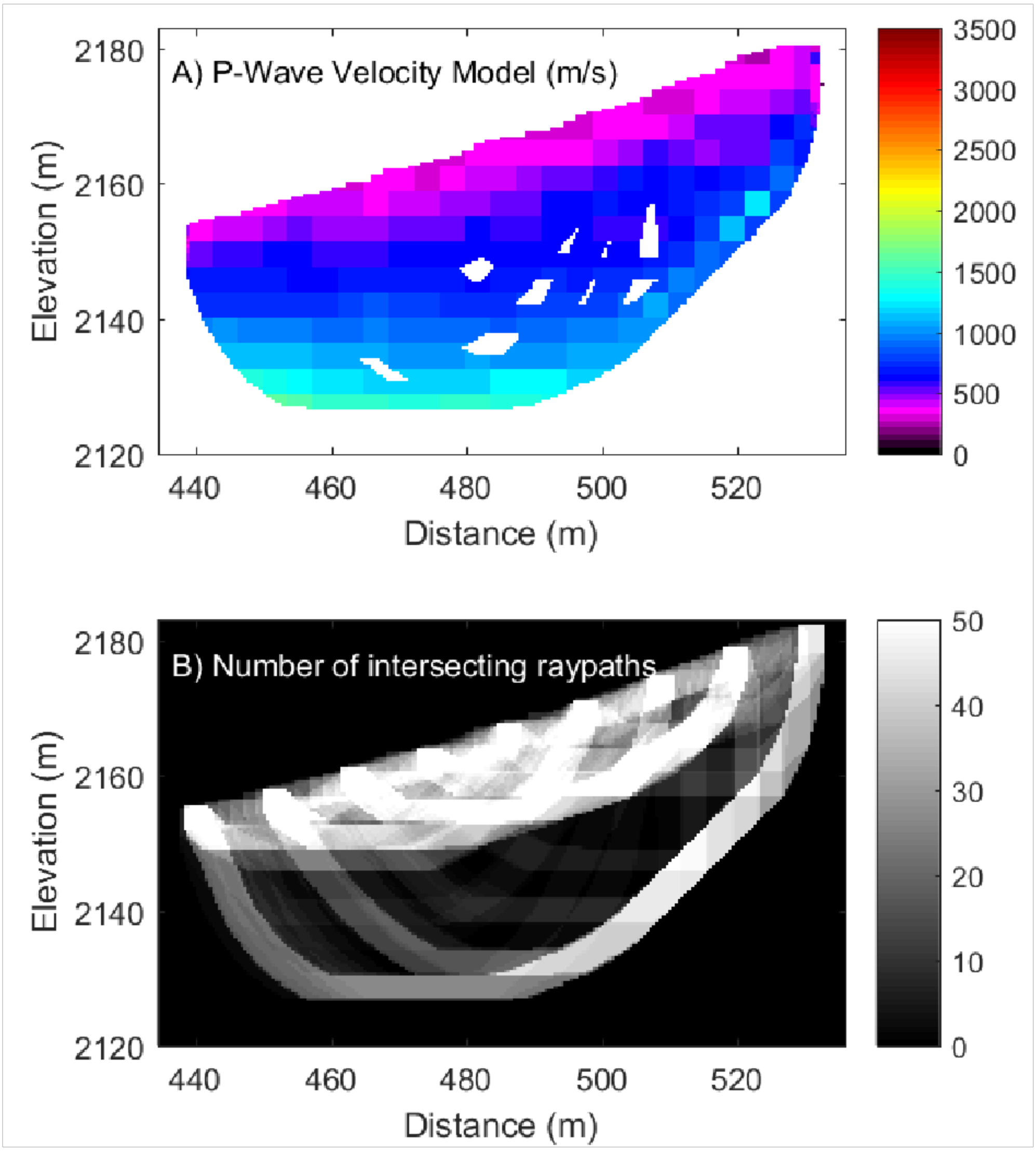

Figure E-5: P-wave velocity models (A) and ray path density (B) along SEIS5

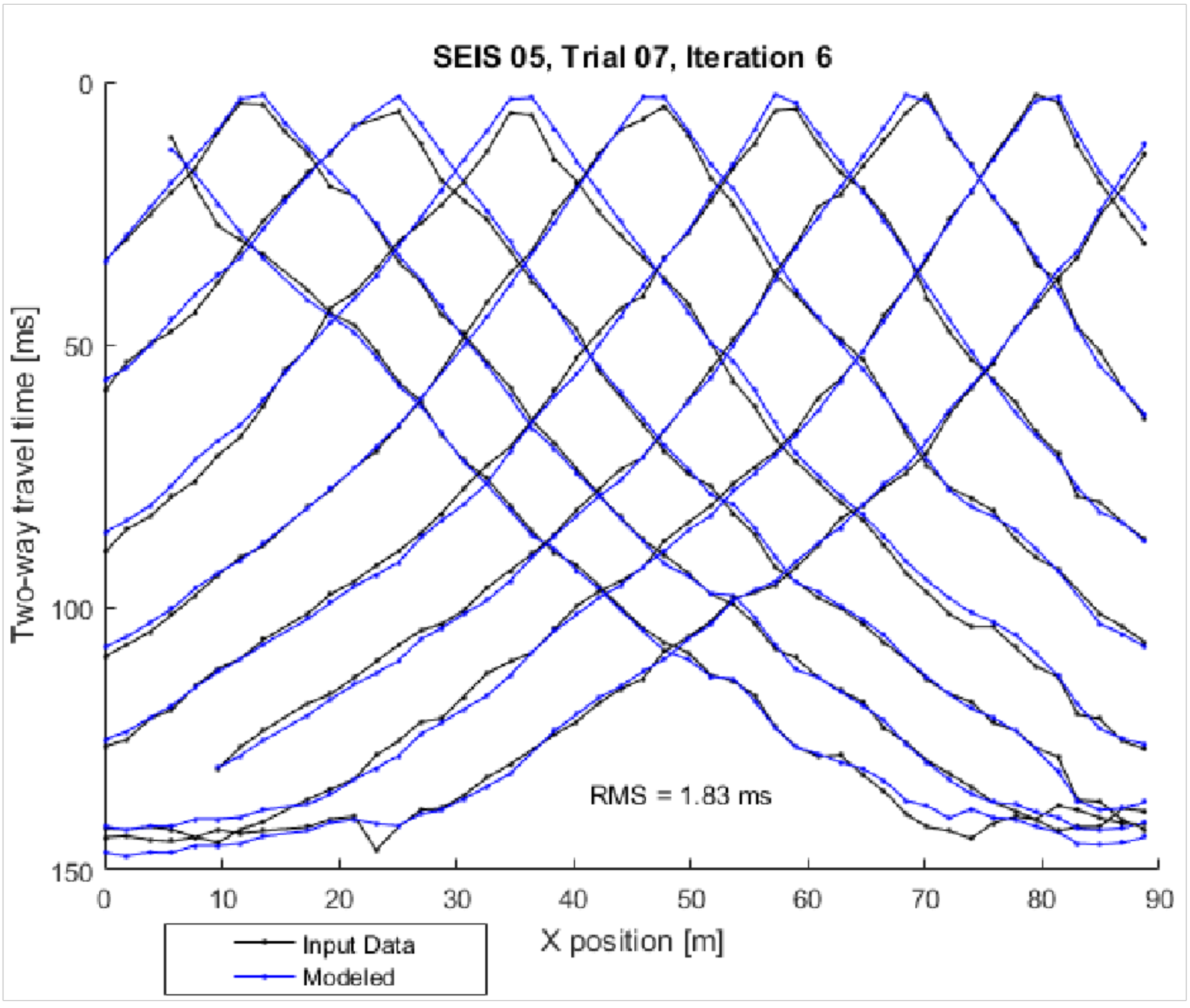

Figure E-6: Modeled versus measured first arrival times on SEIS5.

E.4 SEIS6

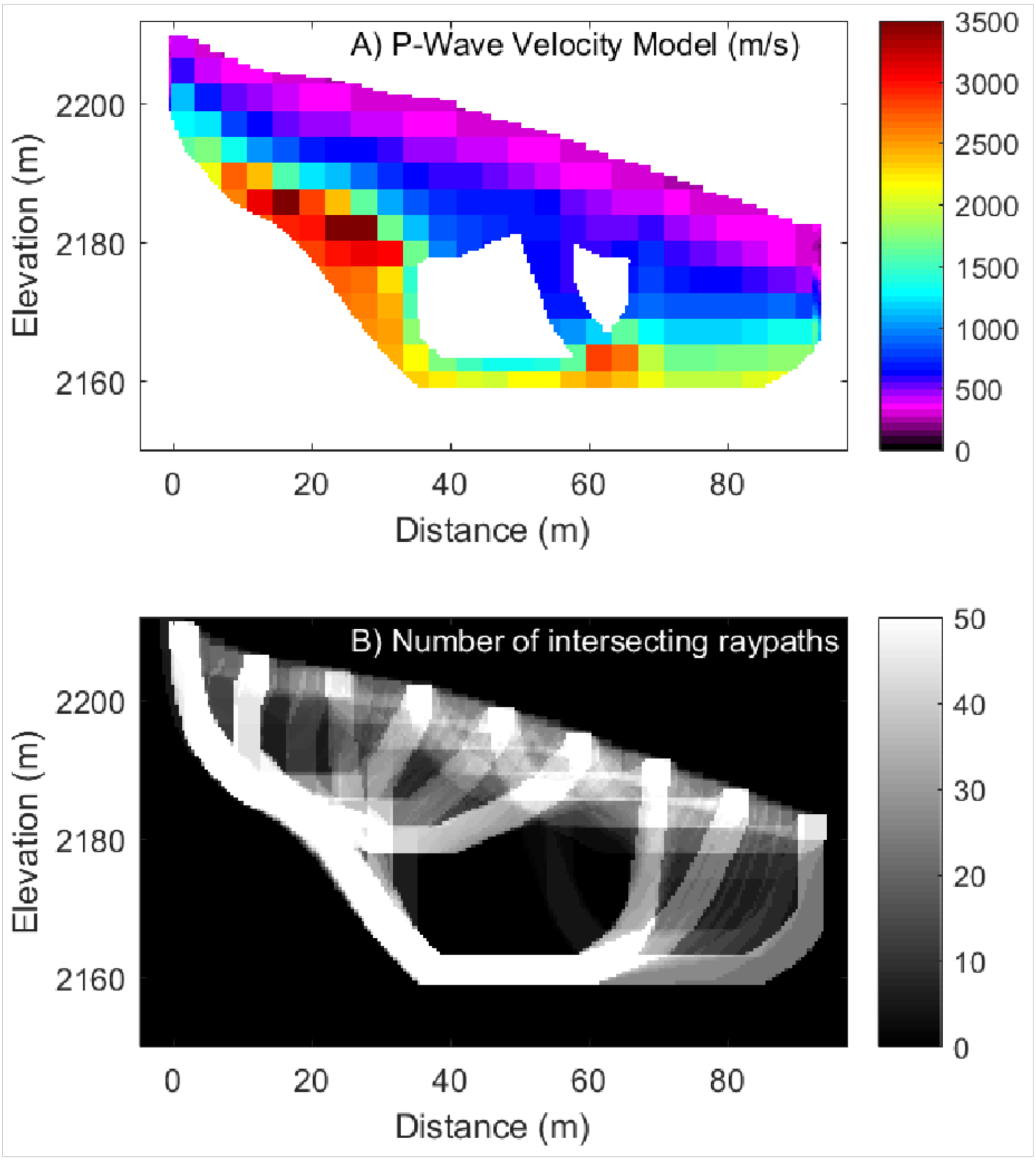

Figure E-7: P-wave velocity models (A) and ray path density (B) along SEIS6

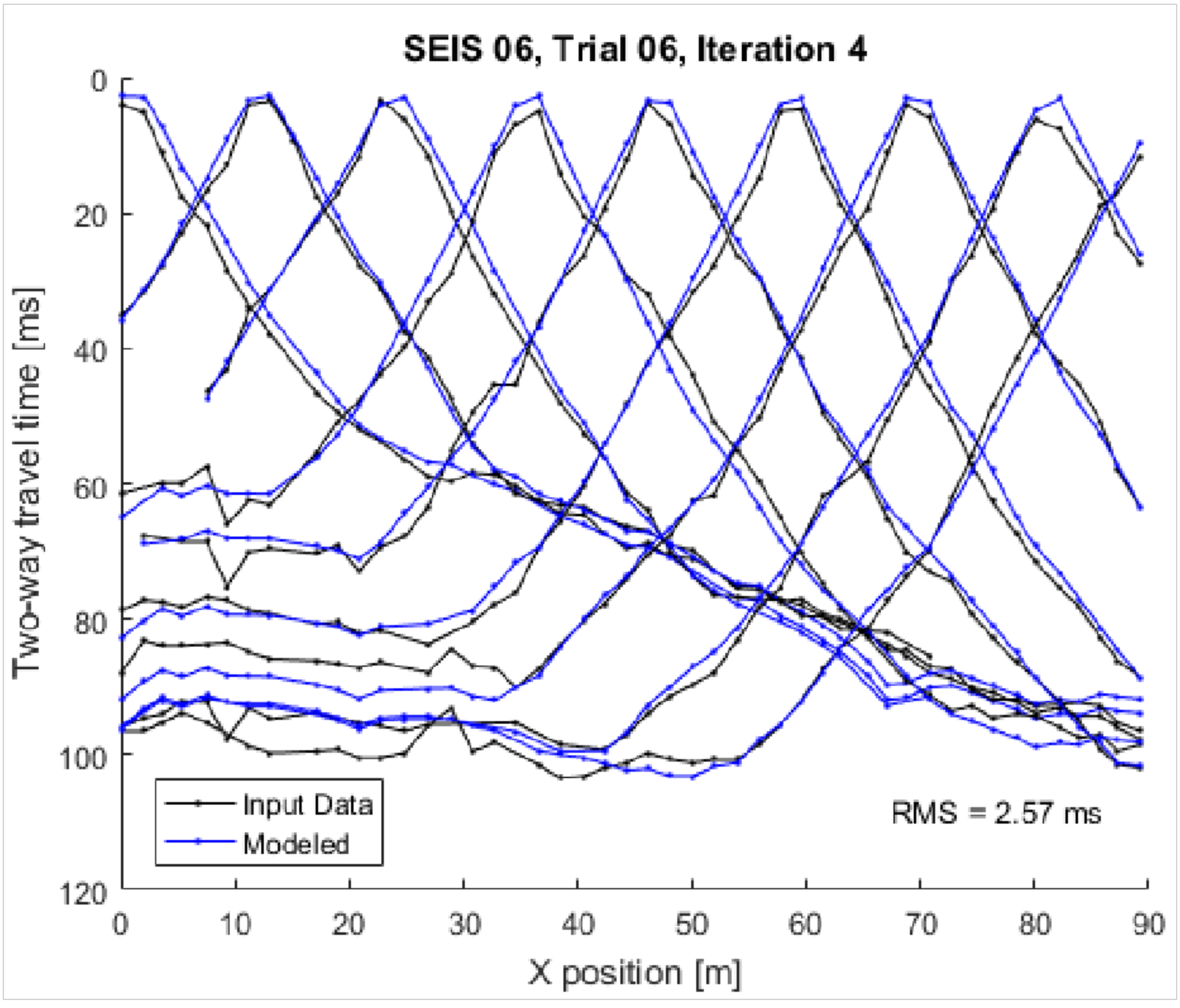

Figure E-8: Modeled versus measured first arrival times on SEIS6.

E.5 SEIS7-8

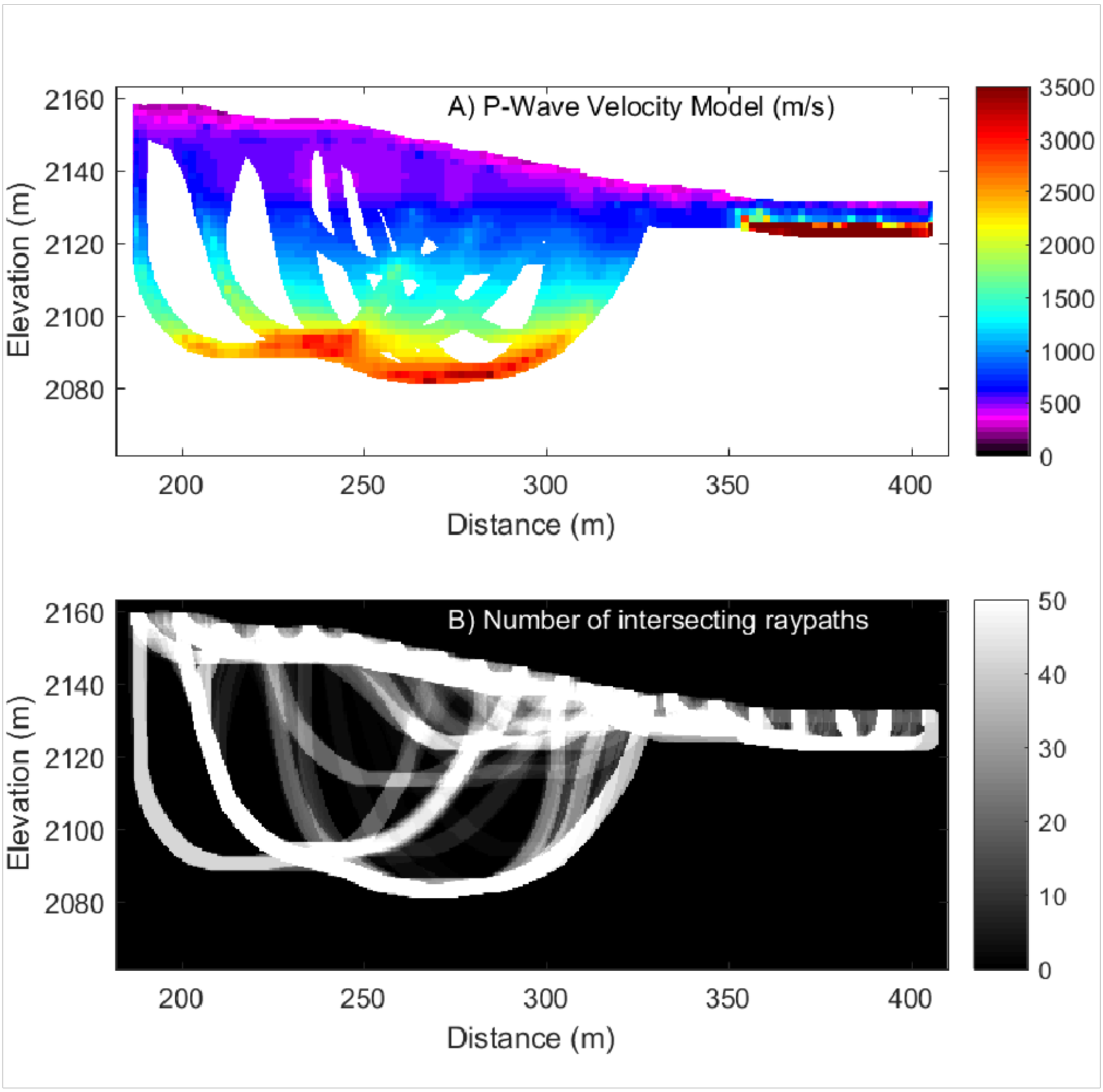

Figure E-9: P-wave velocity models (A) and ray path density (B) along SEIS7-8.

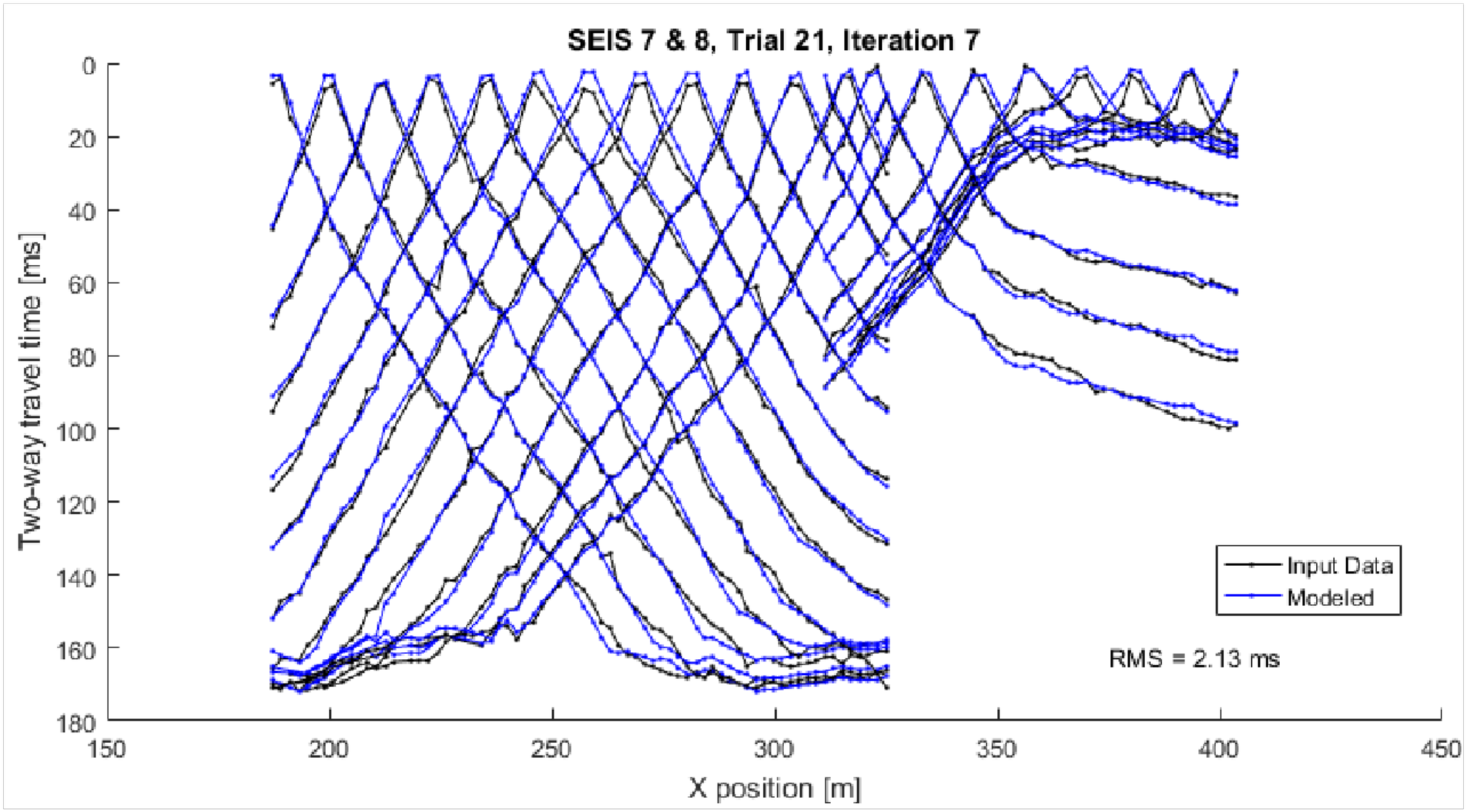

Figure E-10: Modeled versus measured first arrival times on SEIS7-8

E.6 SEIS9

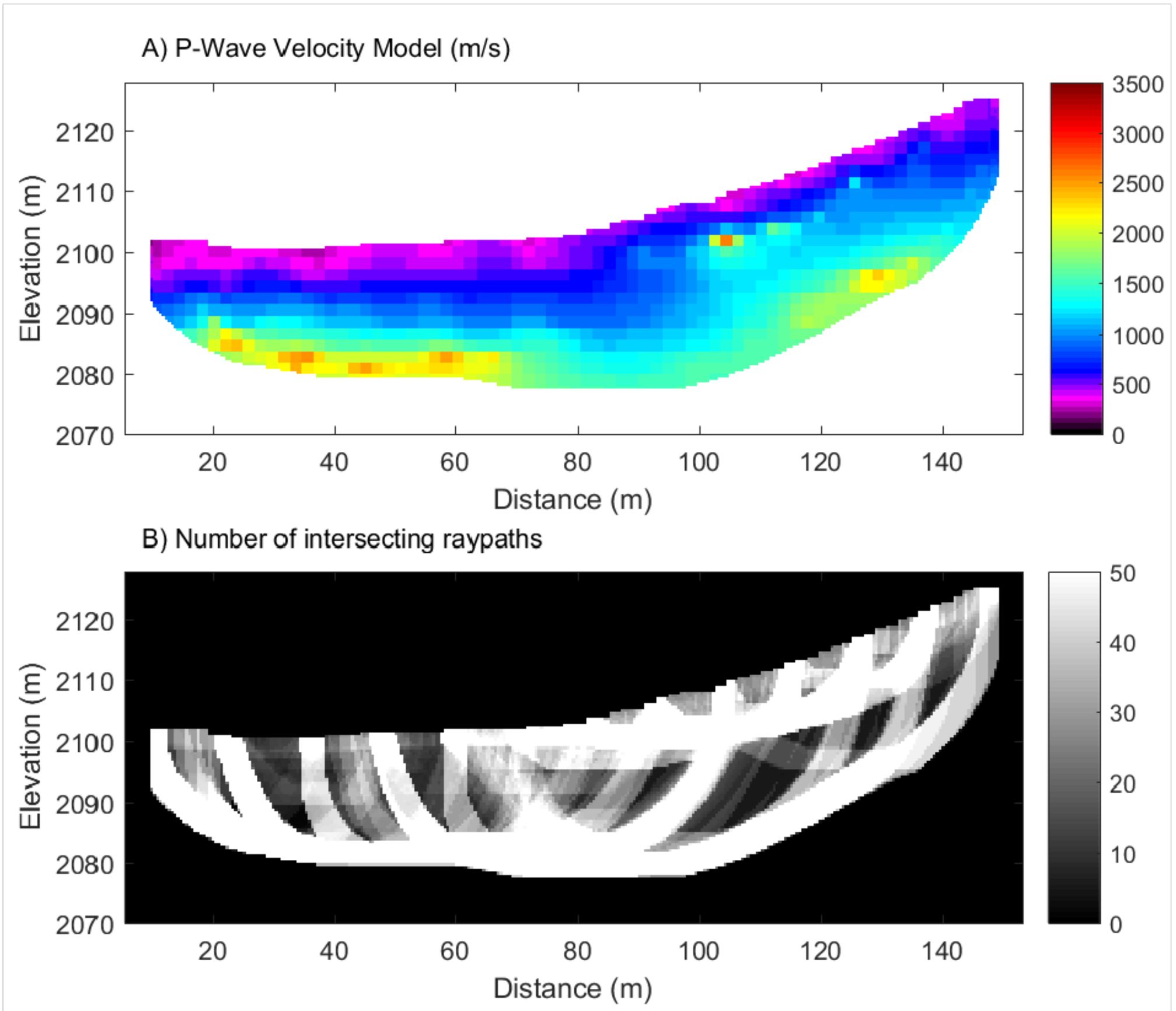

Figure E-11: P-wave velocity models (A) and ray path density (B) along SEIS9

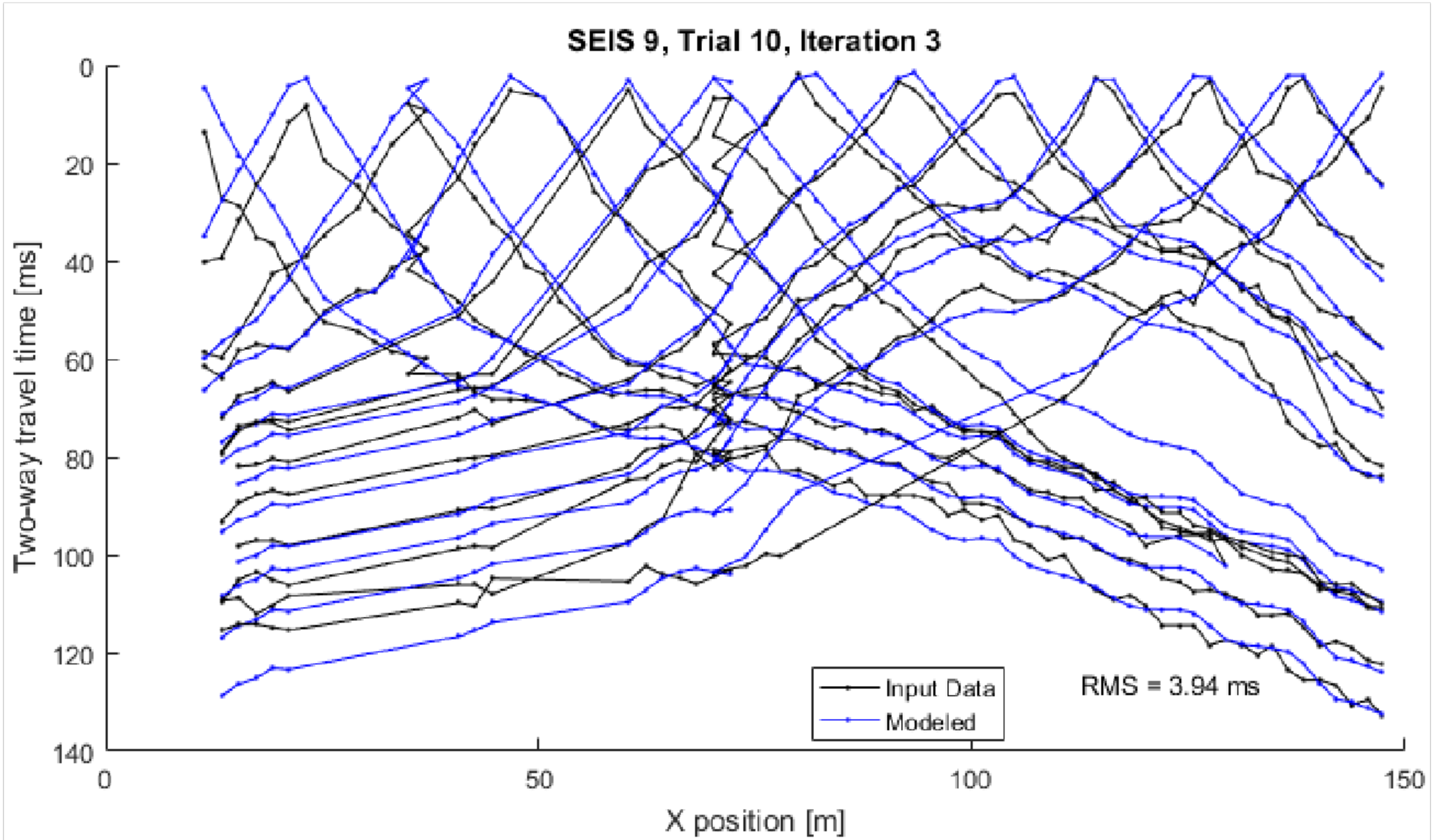

Figure E-12: Modeled versus measured first arrival times on SEIS9.

E.7 SEIS10

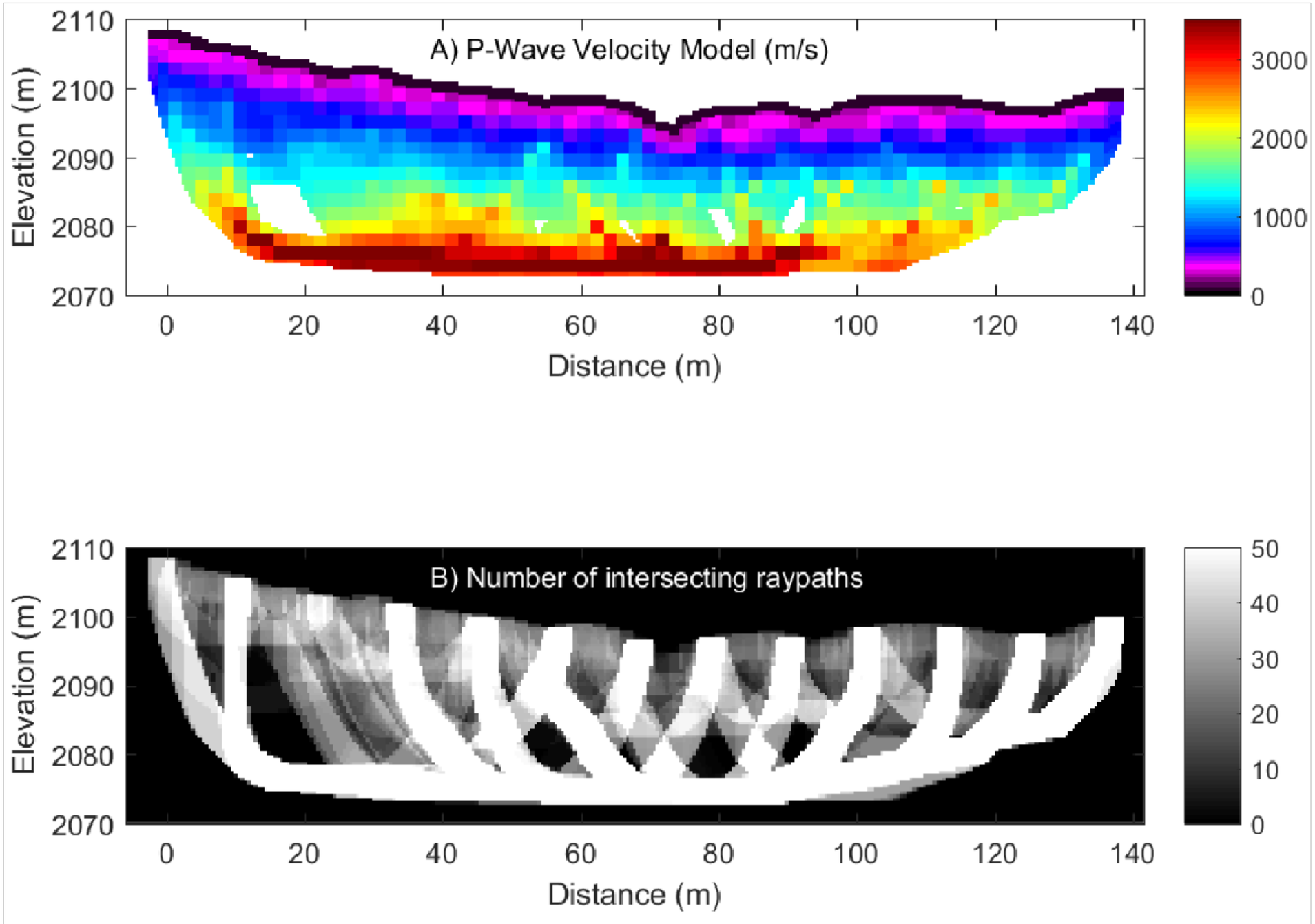

Figure E-13: P-wave velocity models (A) and ray path density (B) along SEIS10.

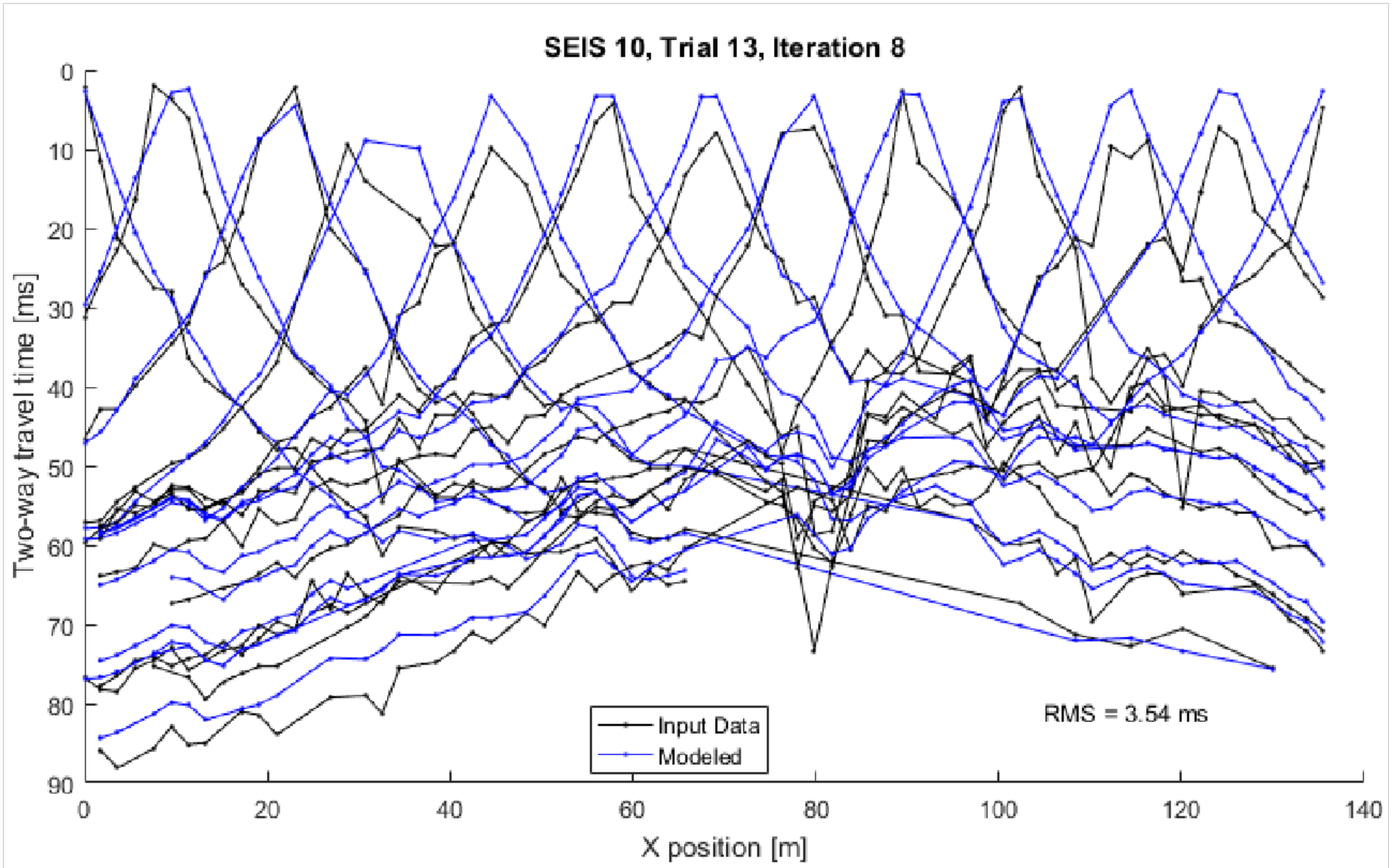

Figure E-14: Modeled versus measured first arrival times on SEIS10.

E.8 SEIS11

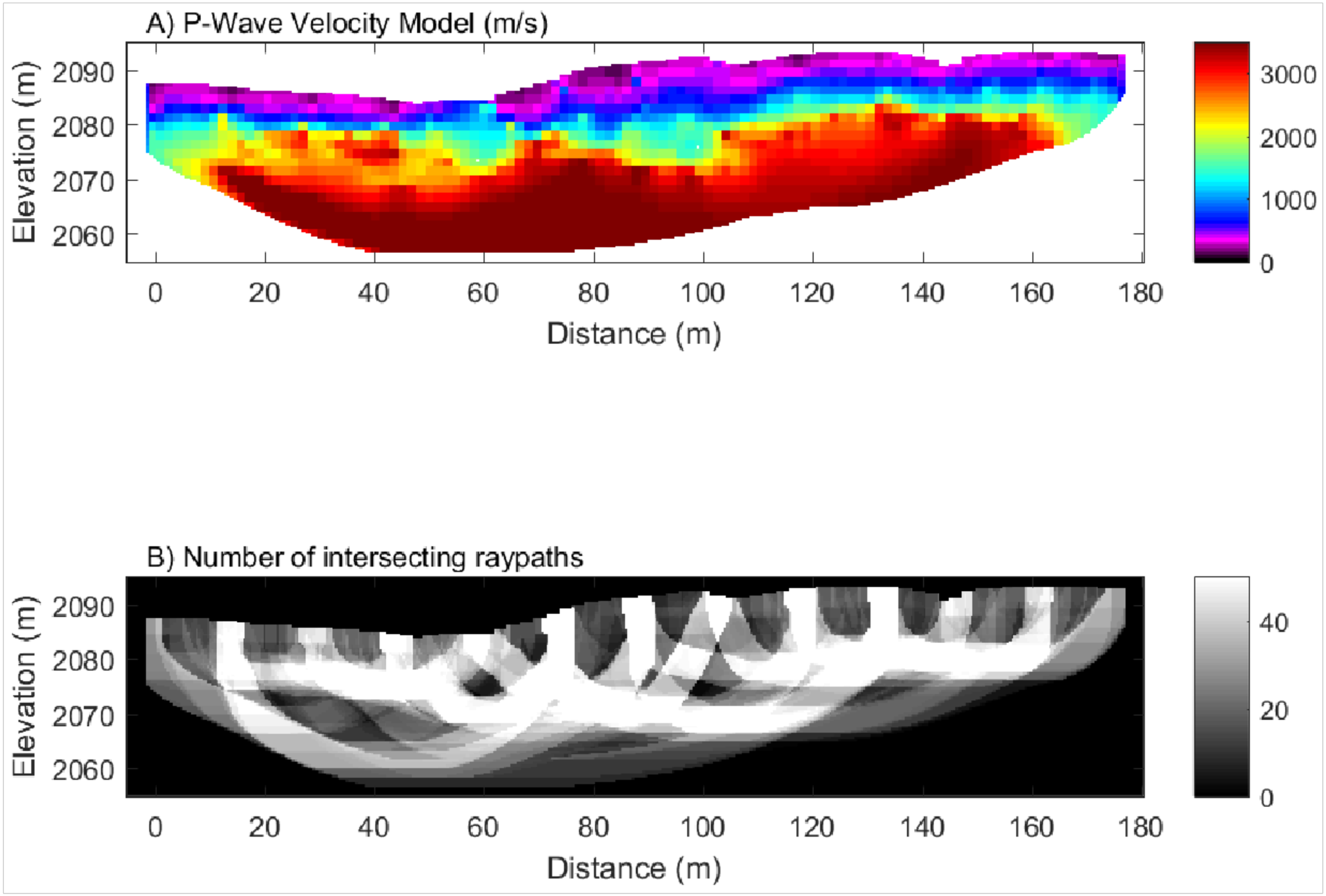

Figure E-15: P-wave velocity models (A) and ray path density (B) along SEIS11.

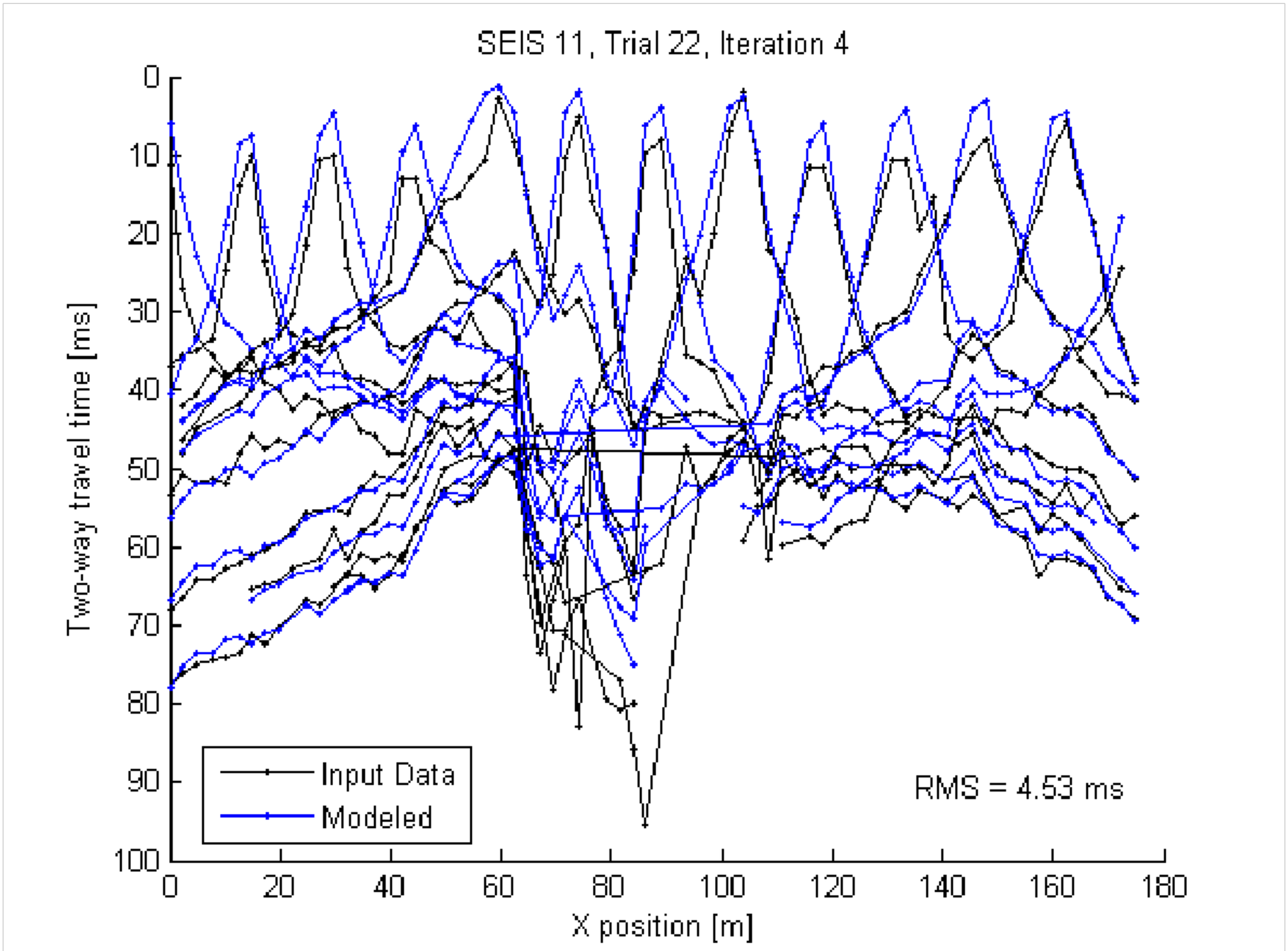

Figure E-16: Modeled versus measured first arrival times on SEIS11.

E.9 SEIS12

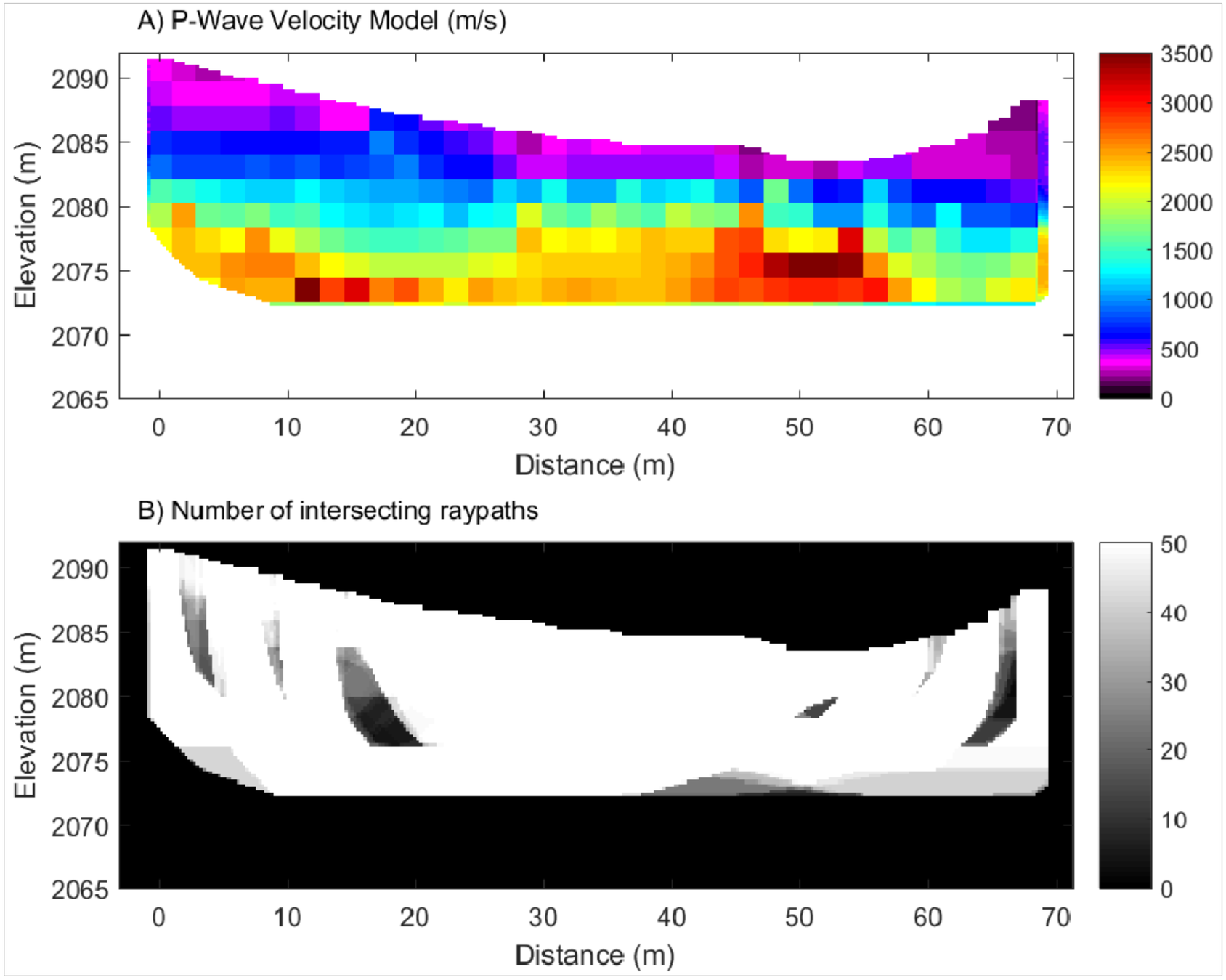

Figure E-17: P-wave velocity models (A) and ray path density (B) along SEIS12

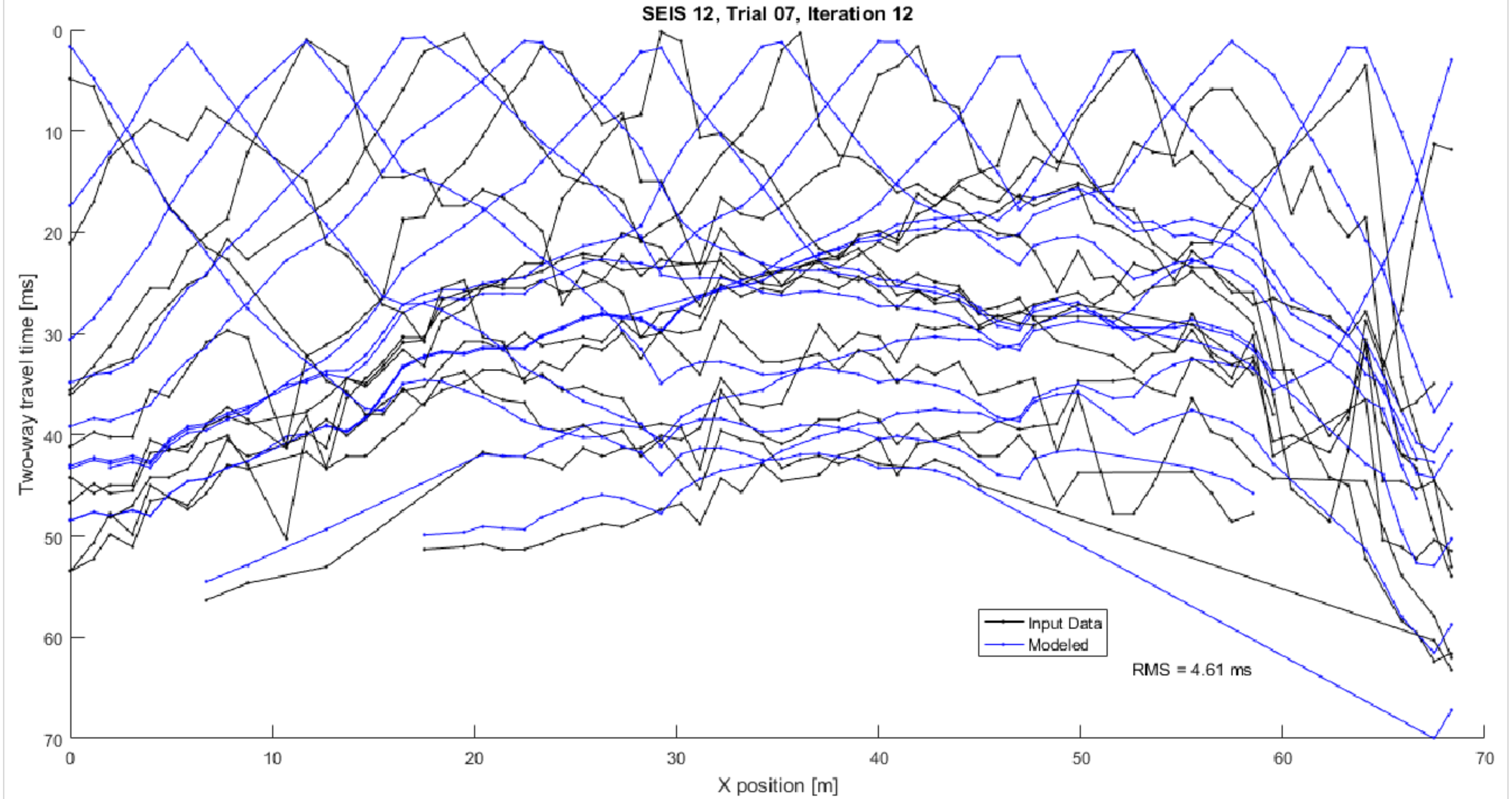

Figure E-18: Modeled versus measured first arrival times on SEIS12.

E.10 SEIS13

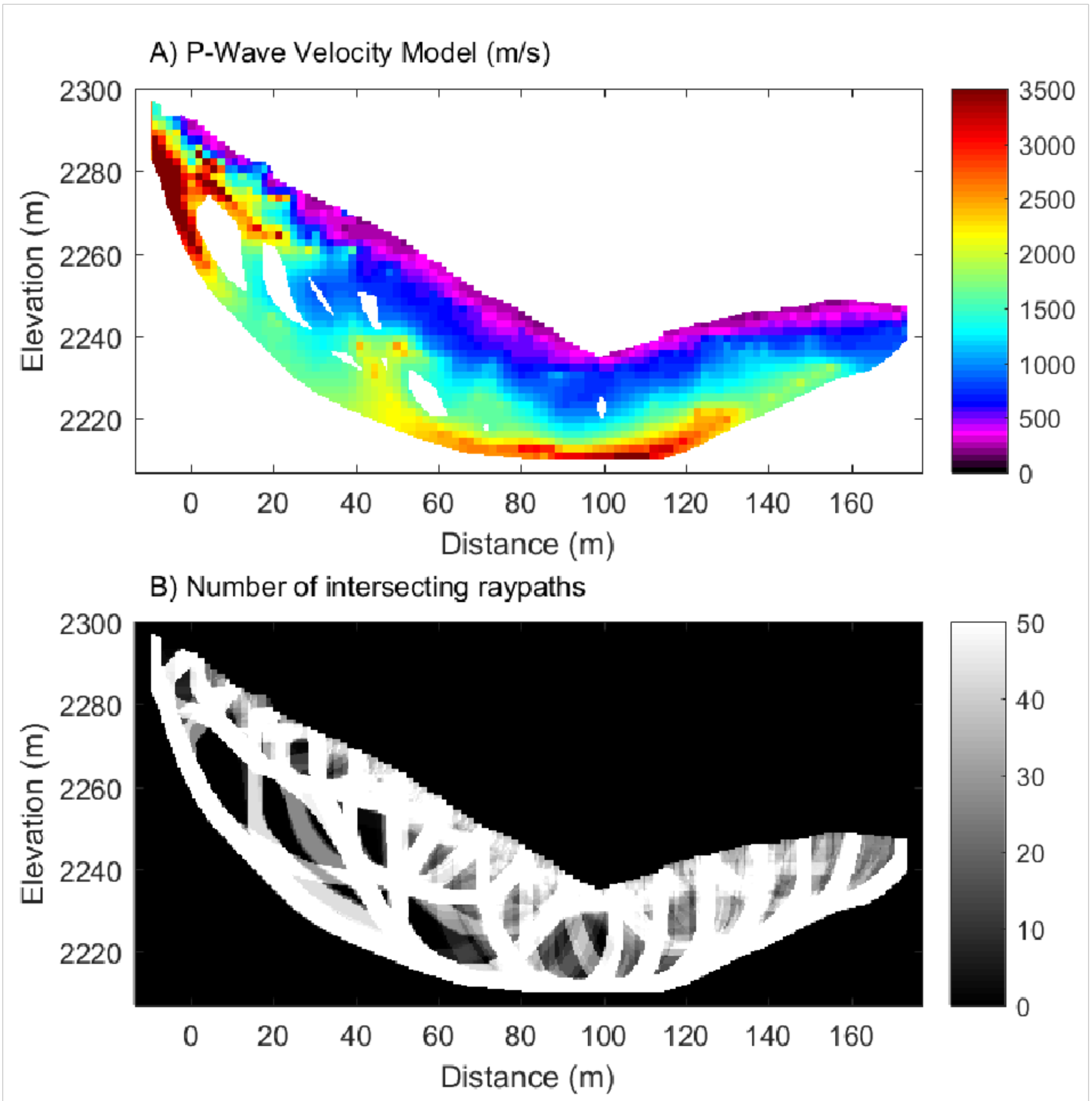

Figure E-19: P-wave velocity models (A) and ray path density (B) along SEIS13

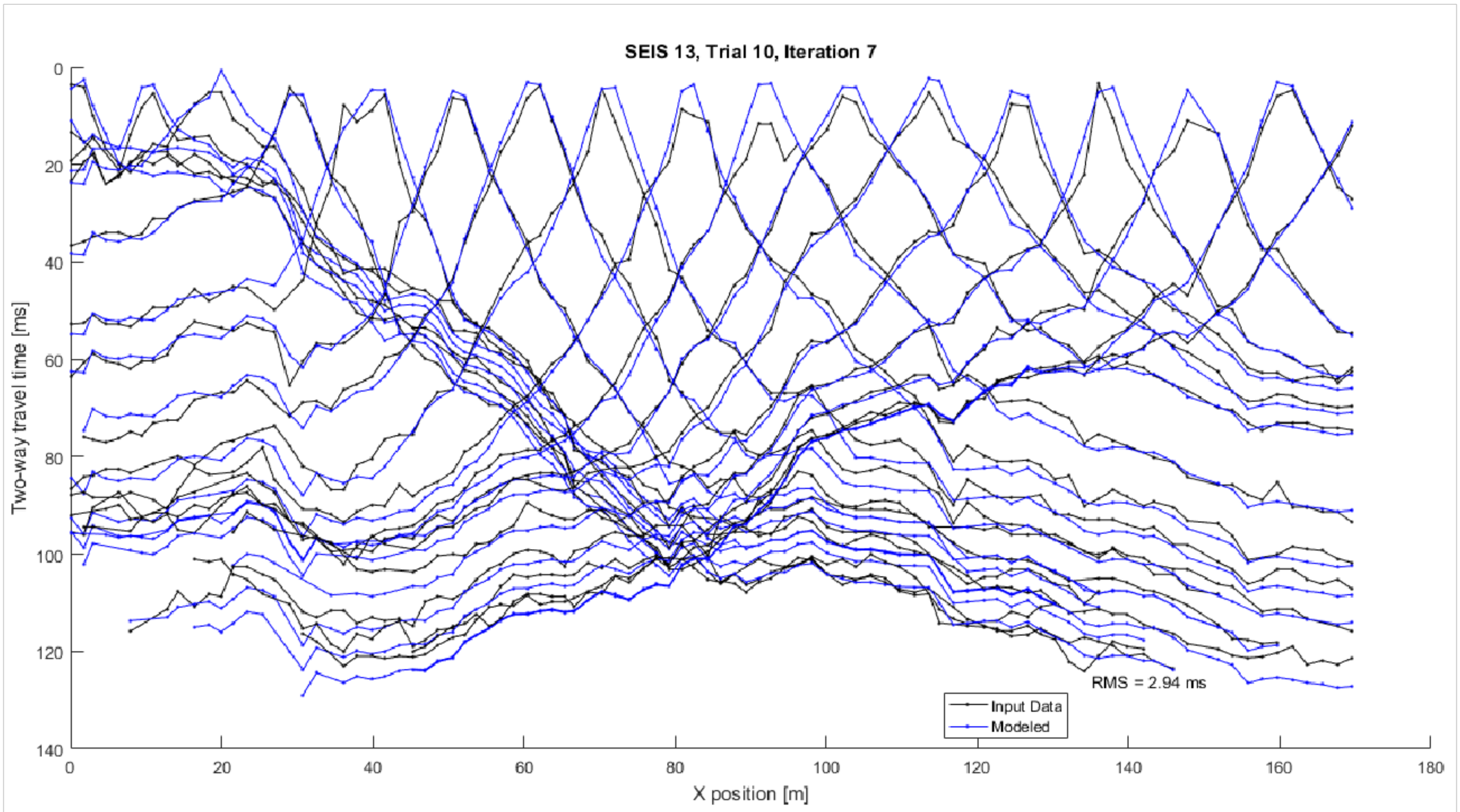

Figure E-20: Modeled versus measured first arrival times on SEIS13.

Appendix F Ground Penetrating Radar Images

F.1GPR1

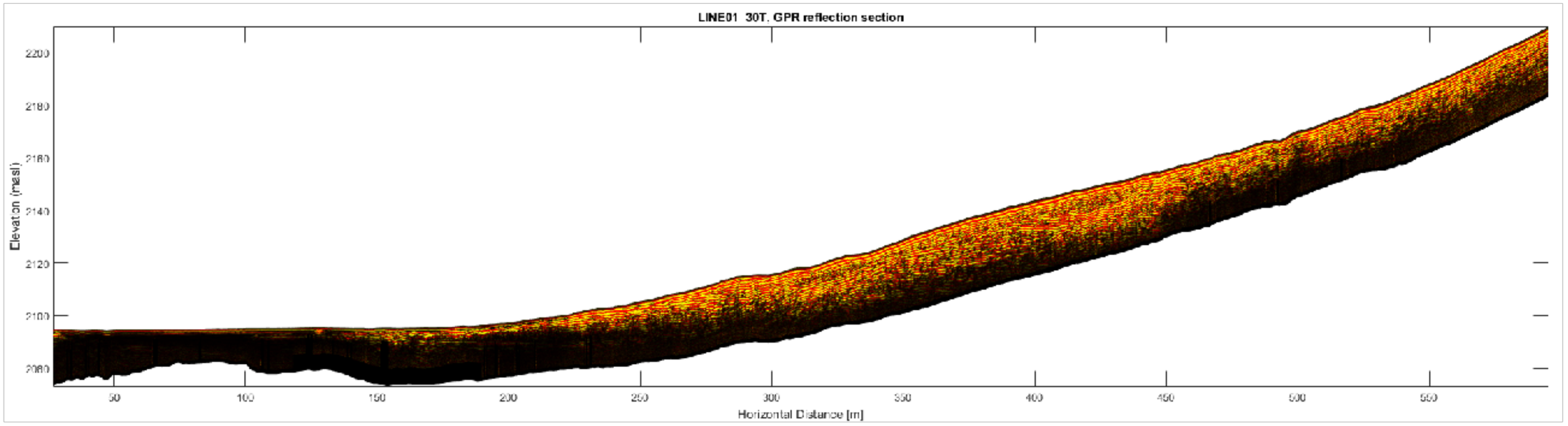

Figure F-1: Full view of GPR1.

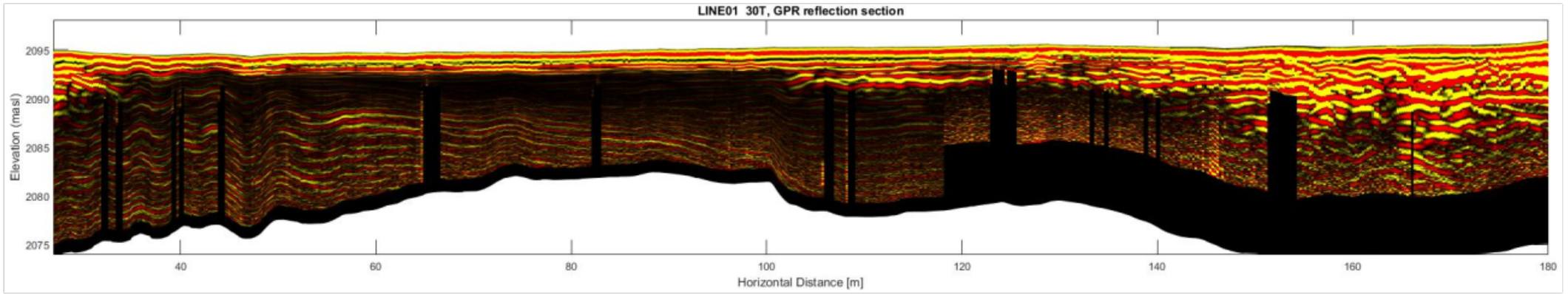

Figure F-2: Excerpt of GPR 1 from 28 to 180 m.

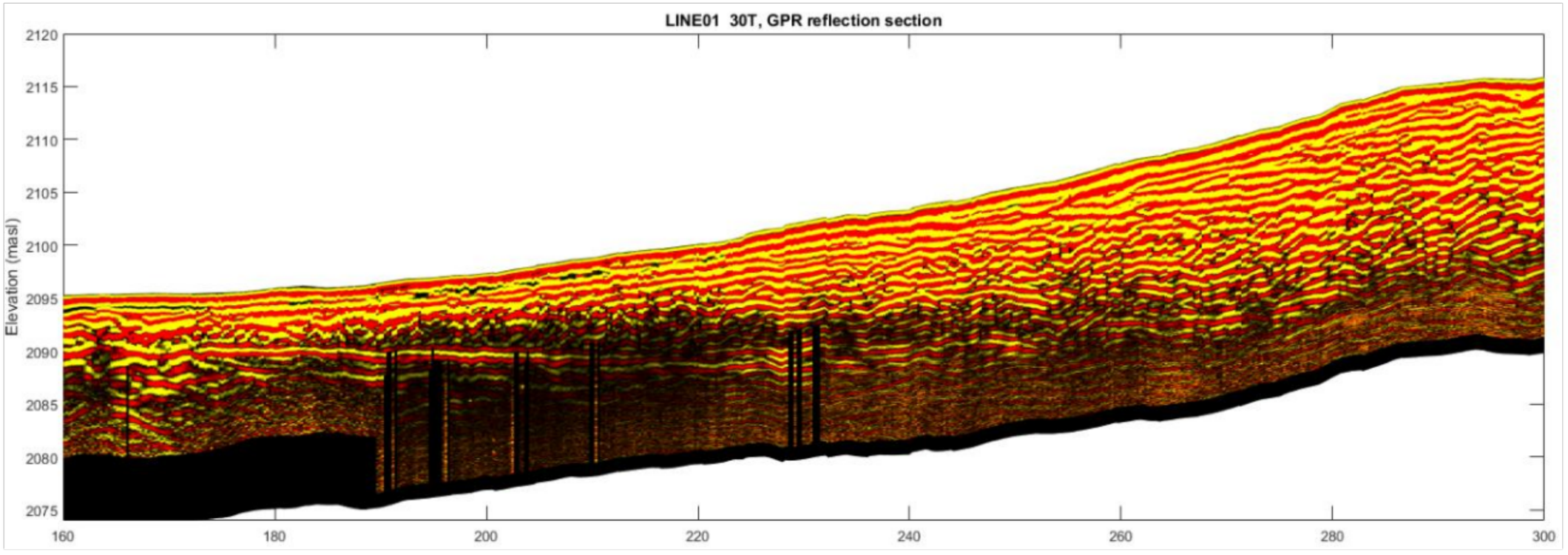

Figure F-3: Excerpt from GPR1 from 160 m to 300 m.

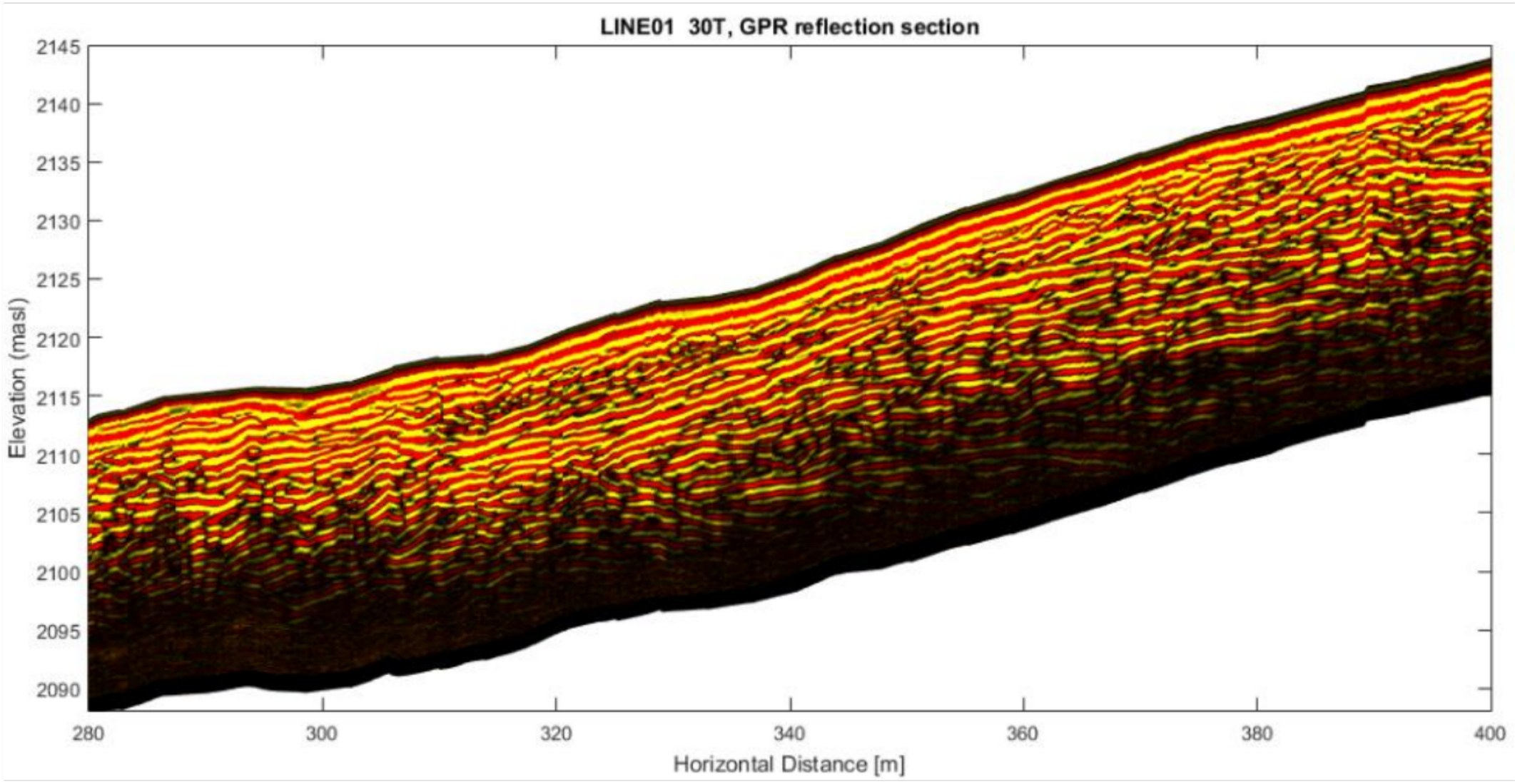

Figure F-4: Excerpt from GPR1 from 280 m to 400 m.

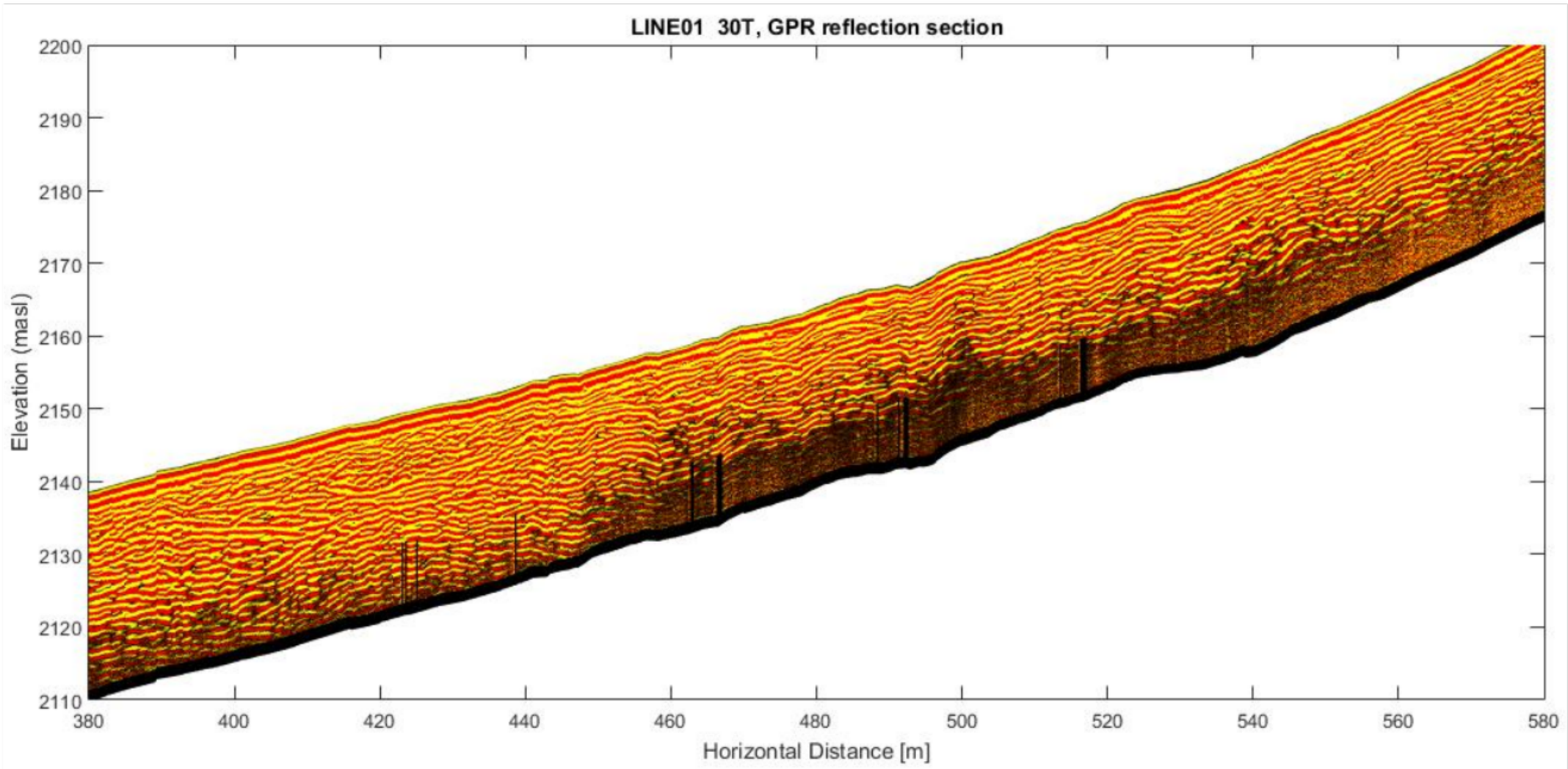

Figure F-5: Excerpt of GPR1 from 380 m to 580 m.

F.2GPR2

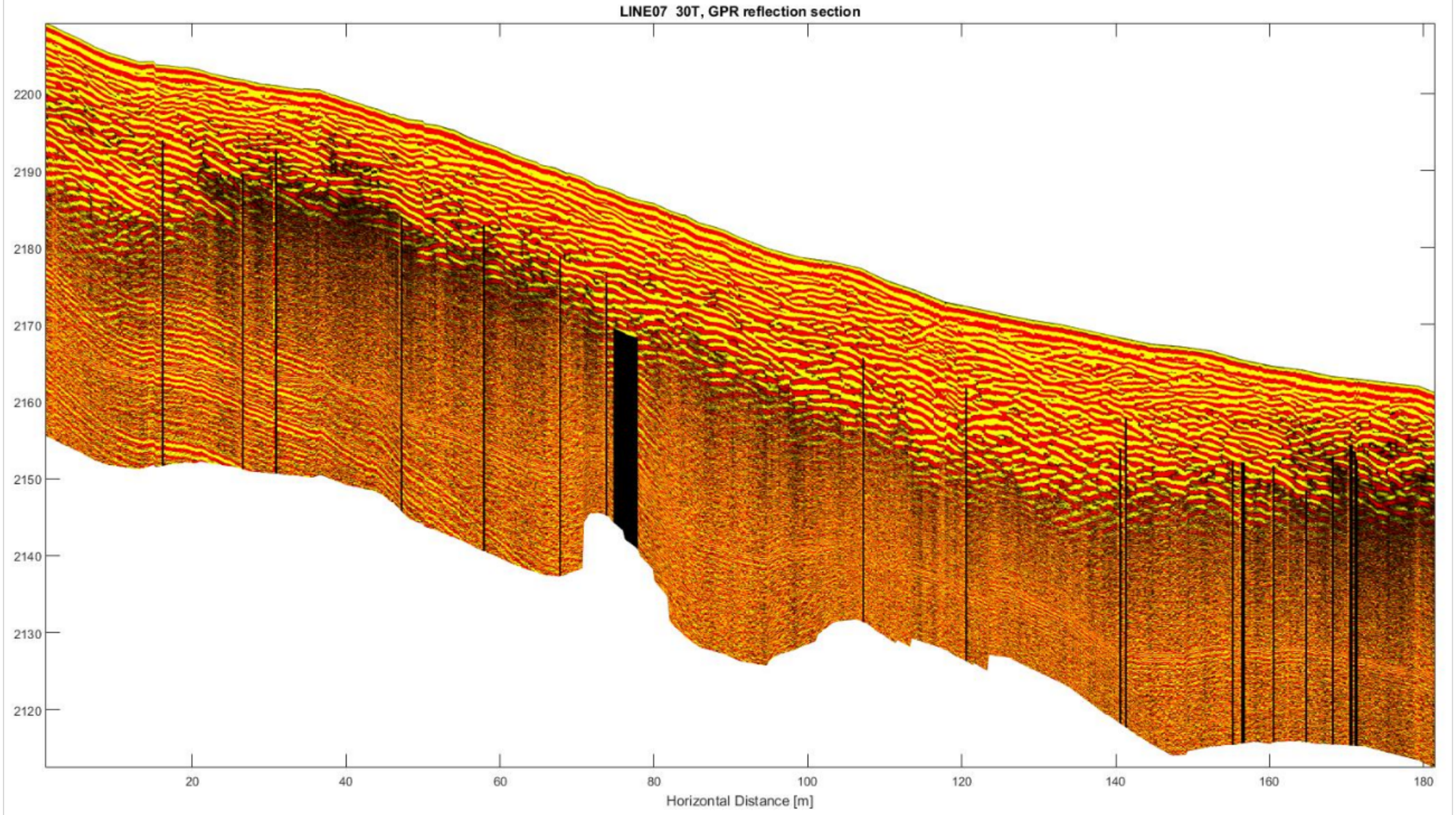

Figure F-6: Full view of GPR2.

F.3GPR3

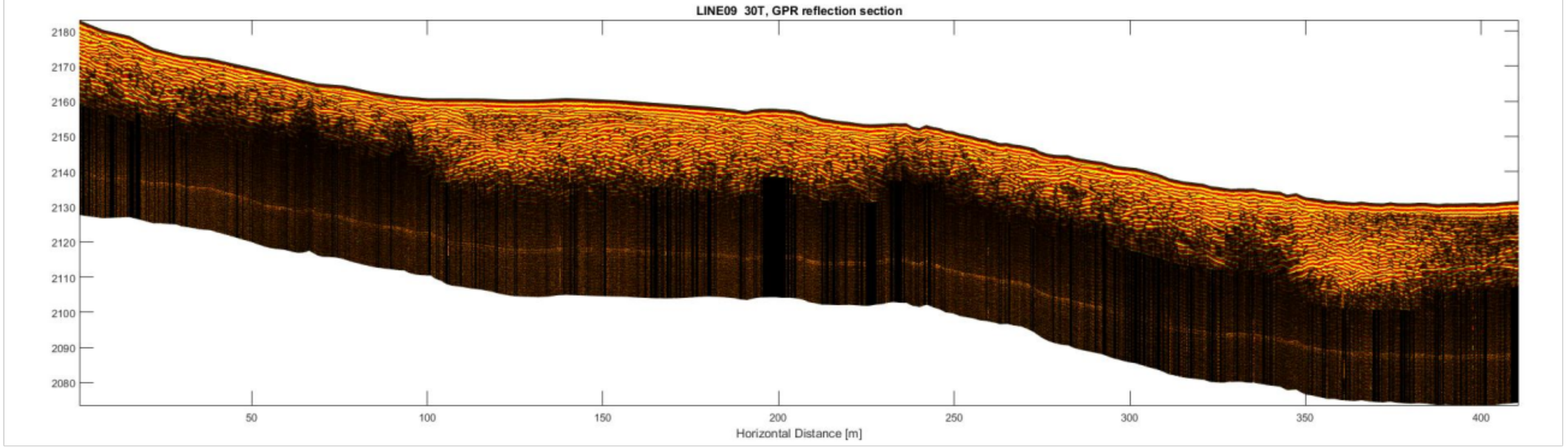

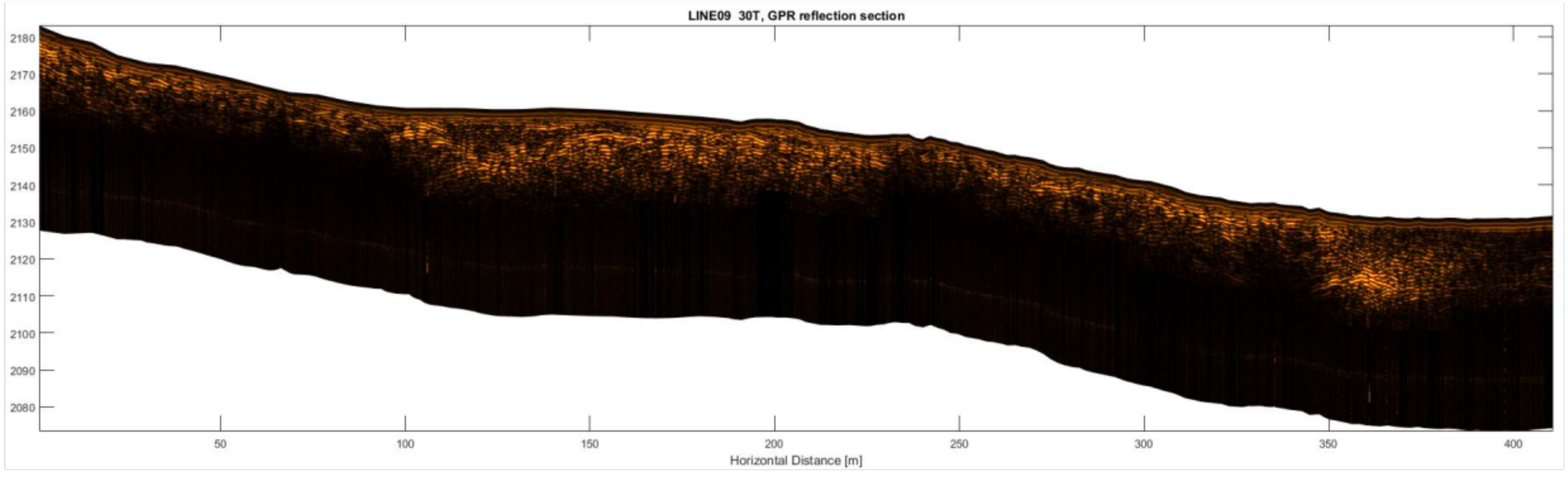

Figure F-7: Full view of GPR3 at rendered at two different illuminations.

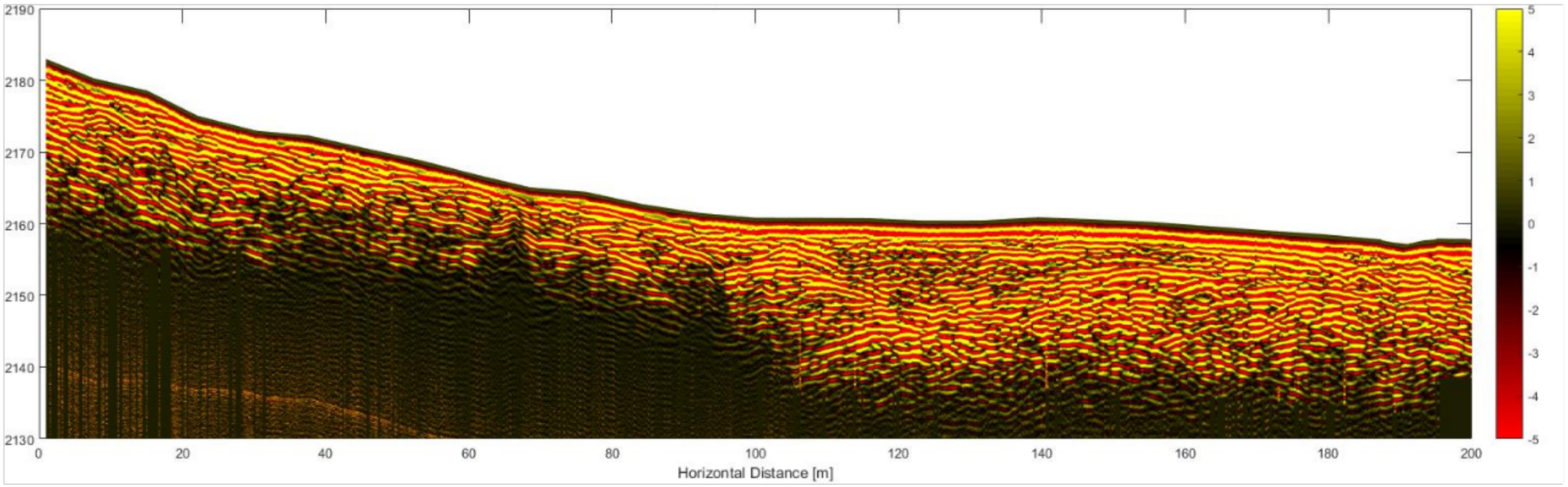

Figure F-8: Excerpt of GPR3 from 0 to 200 m

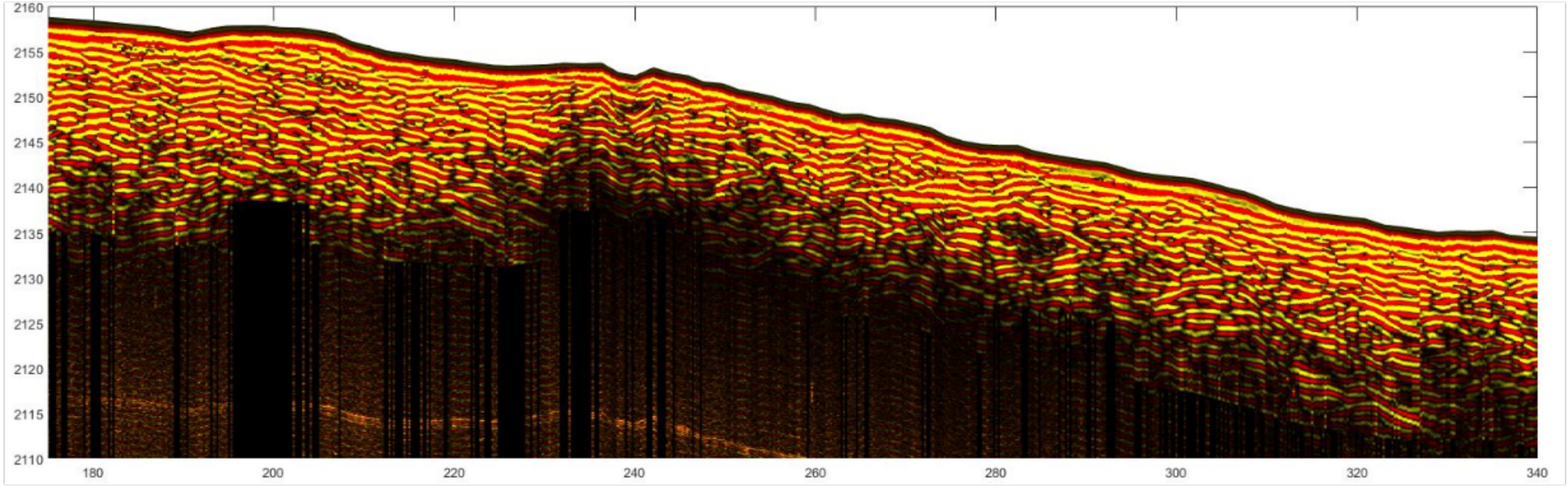

Figure F-9: Excerpt of GPR3 from 180 to 340 m.

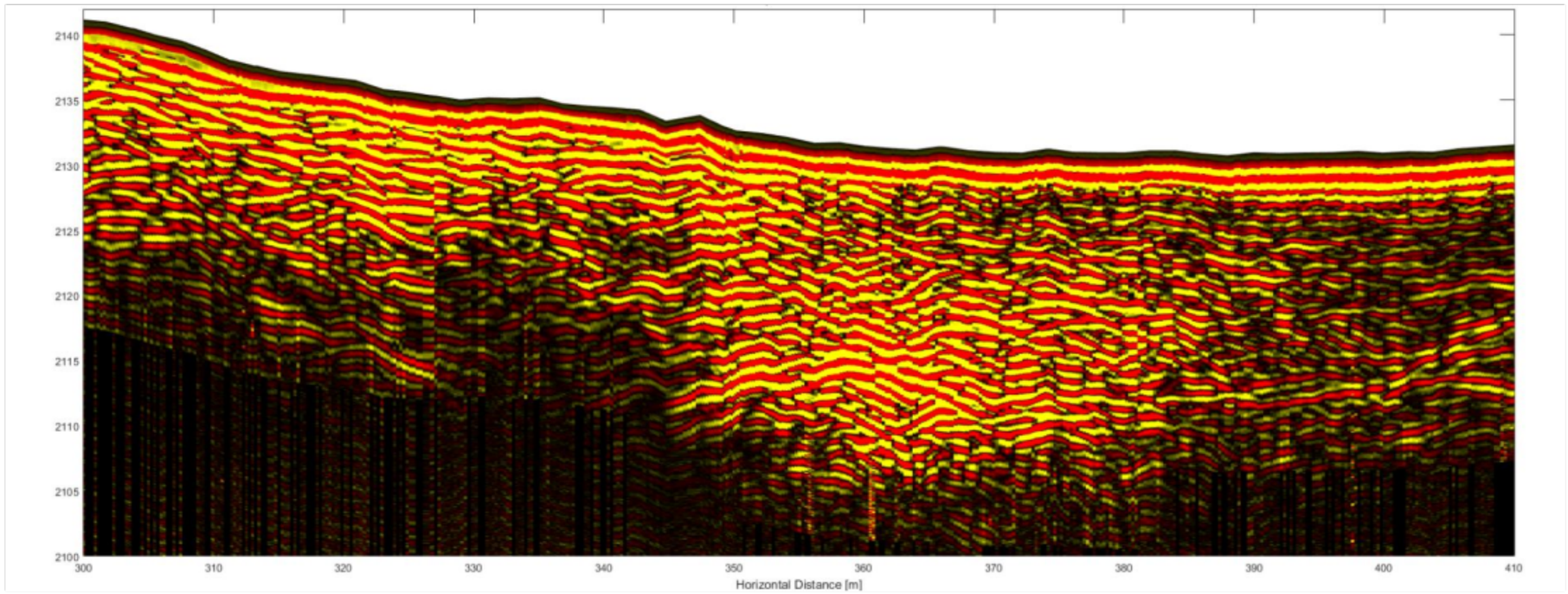

Figure F-10: Excerpt of GPR from 300 to 410 m.

F.4GPR4

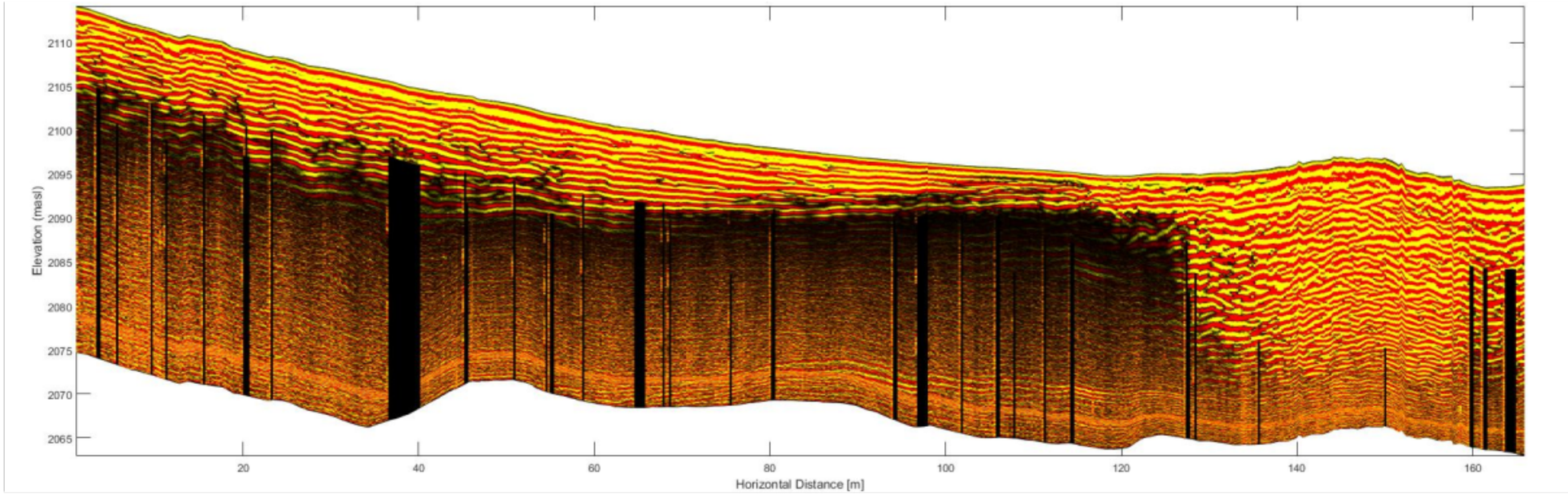

Figure F-11: Full view of GPR4.

F.5GPR5

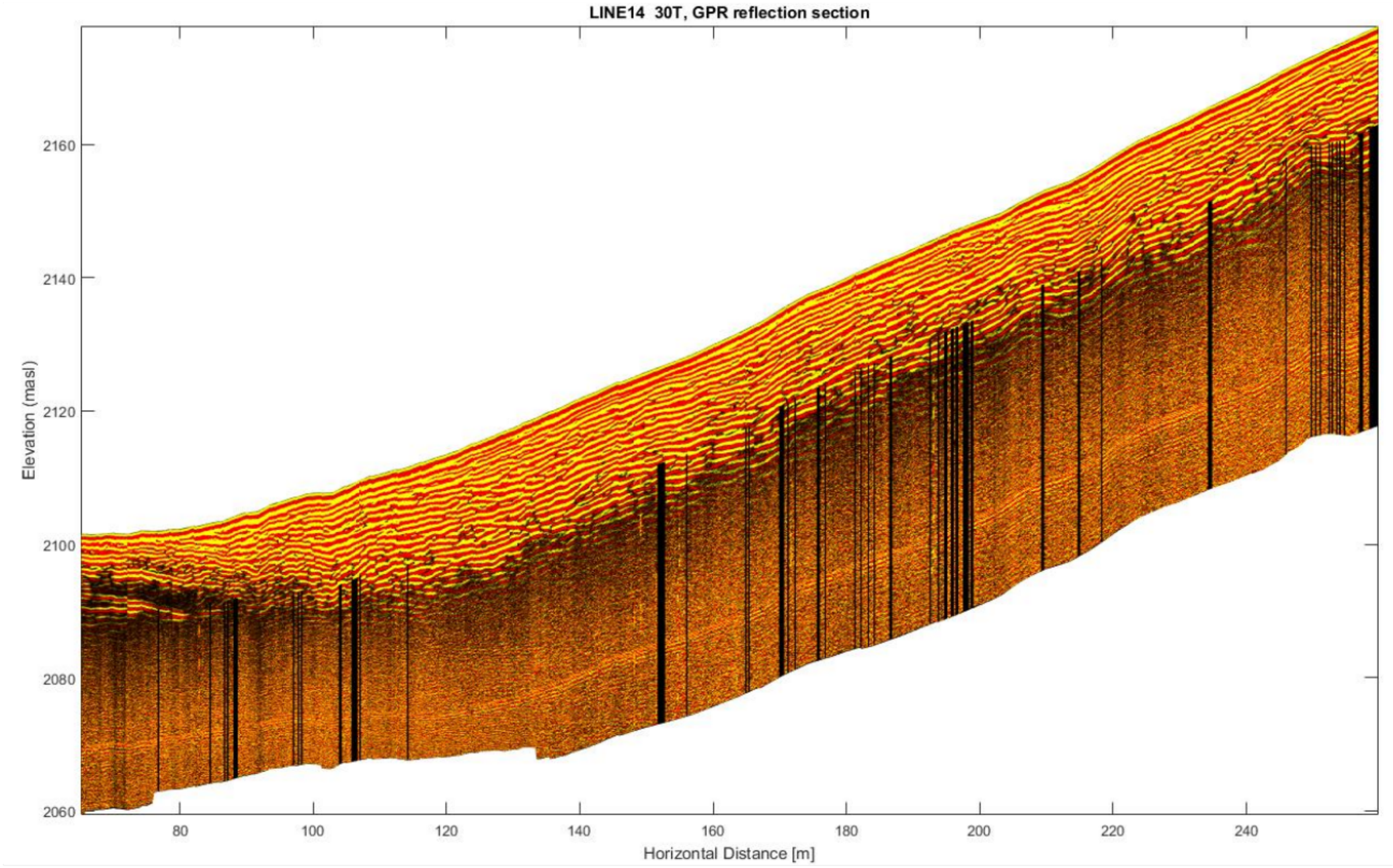

Figure F-12: Full view of GPR5

F.6GPR6

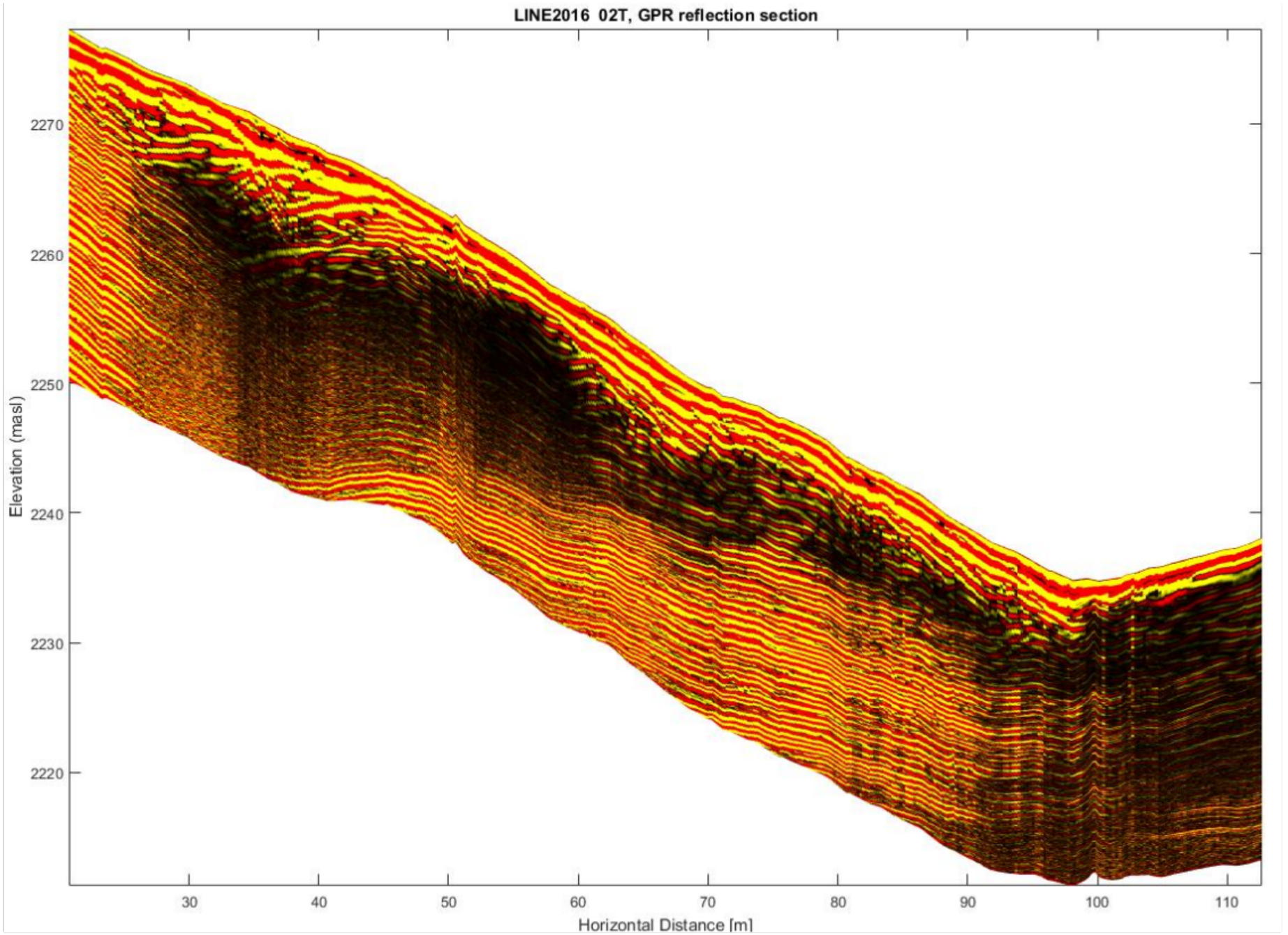

Figure F-13: Full view of GPR6

Appendix G Literature Review of Links Between Mountain Topography and Geomorphology of Mountain Landforms

While there is a large body of literature that links topographic and climatic variables to the geomorphology of mountain landforms, this study lacked the field data to test how these may in turn affect their hydrogeological characteristics. This appendix reviews known links between mountain topography and geomorphic processes that are suspected to affected landform hydrogeology. With more detailed field data, one can conduct a synthesis like that done with talus slopes at the Opabin sub-basin and the Bonsai Lake basin done in Section 6.2.

G.1 Climatic Controls on Glacier and Talus Development

While time since deglaciation and the optimal elevation for frost crack can affect rockfall rates in alpine zones (Hales and Roering 2007; Hoffmann et al. 2013; Thapa 2017), these do not differ significantly between the two basins compared in this study. Studies in basins at different latitudes and altitudes are needed to test the influence of these factors on hydrogeology. Moreover, as Figure G-1 illustrates, secular variations of rockfall rates of different rock formations may be a mechanism by which lithological heterogeneity in a headwall could affect talus hydrogeology. This hypothesis is difficult to test with field data given that the geometry of a headwall prior to glaciation is virtually unknowable, but it could be addressed with a numerical simulation.

Likewise, there are climatic factors that may play a role in controlling alpine geomorphology and hence hydrogeology, but there is a lack of data for comparing the Opabin sub-basin and the Bonsai Lake basin. For one, leeward slopes shielded from winds tend to accumulate more redistributed snow, leading to longer-persisting glaciers and hence larger moraines (Benn and Lehmkuhl 2000; Evans 2004). Also, more rainfall tends to lead to talus with a higher-proportion of fine-grained sediment (Sass and Krautblatter 2007), leading to a lower hydraulic-conductivity. While regional data on prevailing wind direction suggest that the headwall in the Bonsai Lake basin faces the lee side (Alberta Agriculture, Food, and Rural Development 2003a, 2003b, 2003c) and that precipitation generally decreases going east across the Rocky Mountains (Government of Canada et al. 2010), these figures may be misleading because climatic variables have strong, fine-scale heterogeneity in mountainous regions (Ford et al. 2013). Long-term weather records

are needed before a sound argument about climatic controls on geomorphology and hence hydrogeology can be made at the Opabin sub-basin and the Bonsai Lake basin.

G.2 Controls on Moraine and Overdeepening Geomorphology

Intuitively, larger inputs of debris ought to lead to higher moraine ridges (Andrews, 1972). More importantly, rockfall debris helps insulate the ice (Kirkbride and Warren 1999; Anderson 2000; Scherler et al. 2011), and hence makes it less likely that the ice margin will fluctuate due to climactic variations (Kirkbride and Winkler 2012). This stable margin is important for making tall moraine dams as opposed to complexes of short, wide moraines that would not form a closed basin to trap sediment (Spedding and Evans 2002; Swift et al. 2002; Cook and Swift 2012).

Similarly, in their review of topographic controls on moraine distribution, Barr and Lovell (2014) identify other conditions in which long-lasting glaciers (and hence large moraines) are more likely to form. Basins with lower temperatures due to a shaded aspect tend to persist longer (Evans 1990; Hijmans et al. 2005). Those where a large amount of redistributed snow is deposited also tend to have longer-lasting glaciers (Dahl et al. 1997). This can include basins where upland slopes can store and transfer snow through avalanching (Benn and Lehmkuhl 2000; Evans 2004). In addition, joints that dip towards a basin headwall favour the develop of alpine cirques (Haynes 1968).

Unlike moraines, mountain-scale patterns in overdeepenings are not well understood because their formation mechanism is unclear. Post-glacial overdeepenings are often filled with sediment, and syn-glacial ones are covered in ice, leading to this knowledge gap (Haeberli et al. 2016). Nevertheless, existing literatures shows that overdeepenings tend to be associated with areas with weaker bedrock and tectonic structures (e.g. faults) and lithological boundaries where there is a contrast in rock properties and with large moraine complexes (Spedding and Evans 2002; Preusser et al 2010; Brückl et al. 2010; Jordan 2010).

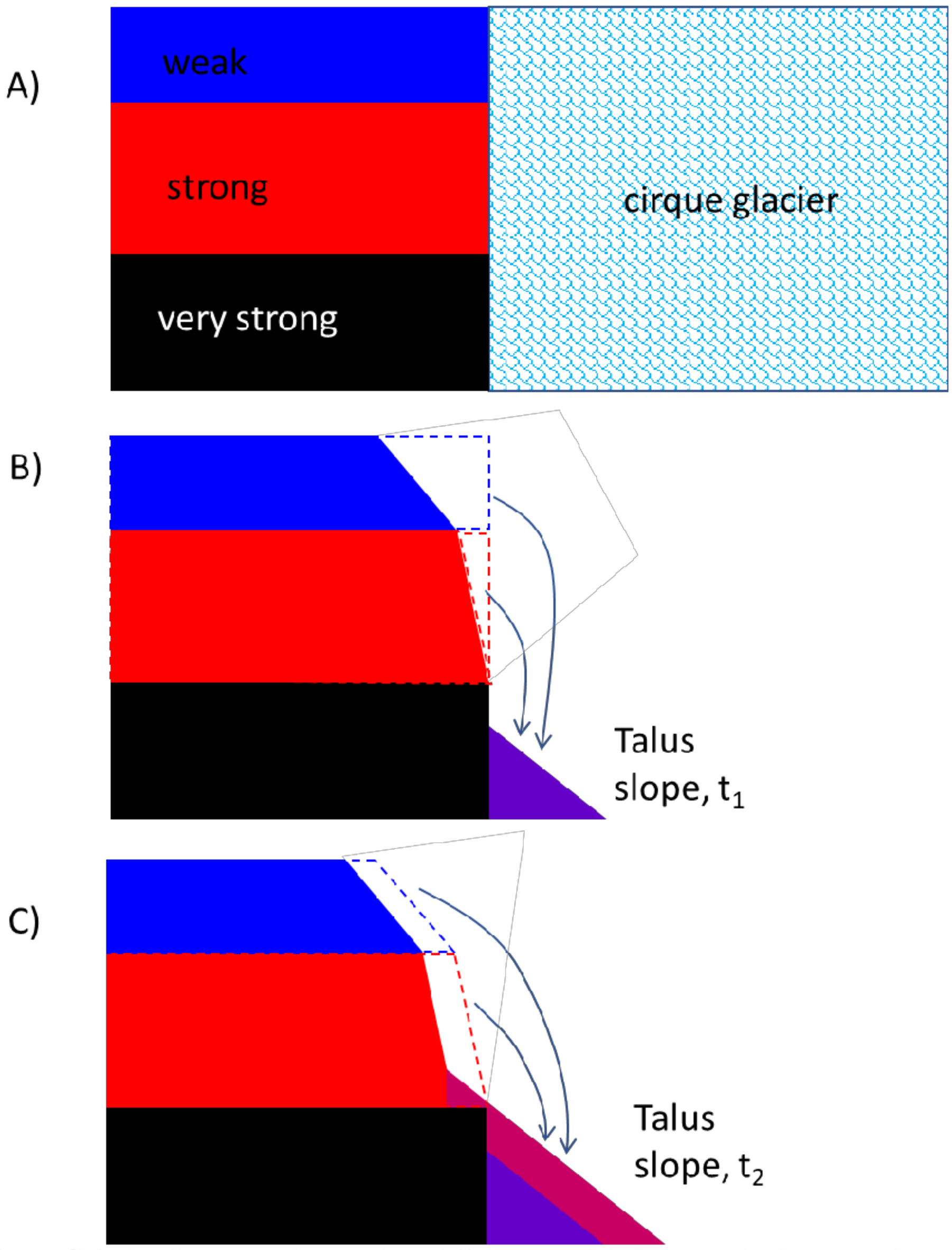

Figure G-1: An illustration showing how differences in lithology may lead to vertical heterogeneities in a paraglacial talus deposit. The cirque headwall has a uniform profile during glaciation (A), but the weaker rock unit recedes more quickly to a shallower equilibrium slope angle compared to the stronger one (B). After the units recede at a more uniform rate (C), the relative proportion of each unit in the talus (expressed as the weighted colour average between red and blue) changes, which may have implications for the hydrology of the deposit.

Appendix H Copyright Permission Letters

This appendix contains two letters of permission to include in this thesis materials from Christensen et al. (2017). (See the Preface for details). The first is an email from the chief editor of the CSEG Recorder. The second is a scanned copy of a letter of permission from other co-authors. Note that in either, sensitive personal information such as signatures and email addresses have been redacted.

H.1 Letter from Publisher of Christensen et al. (2017)

Copyright permission for including Figures from April 2017 Recorder Article

2 messages

Craig Christensen <[redacted]> Fri, Jun 23, 2017 at 10:16 AM
To: Nicole Willson <[redacted]>
Cc: ruth peach <[redacted]>

Hello Nicole,

I am submitting my thesis shortly. Some of the figures and tables used in the thesis are identical or very similar to those in the article I wrote for the April issue of your magazine, specifically:

Christensen, C., Hayashi, M., Bentley, L. 2017. Scanning Calgary's 'water towers': applications of hydrogeophysics in challenging mountain terrain. CSEG Recorder, 42(3), 28-35.

I am requesting written permission to use all nine (9) figures and the two (2) tables, and modified versions thereof, in my thesis. I am making this request because my thesis is to be included in the institutional repositories of the University of Calgary and the Library and Archives Canada. Here are links that you may access for further information:

University of Calgary Theses Repository – The Vault http://theses.ucalgary.ca/
Library and Archives Canada http://collectionscanada.gc.ca/obj/s4/f2/frm-nl59-2-e.pdf

I am also requesting to use all nine (9) figures and the two (2) tables in any future article that I or any of my two co-authors (Masaki Hayashi or Laurence Robert Bentley) may submit to a peer-reviewed scientific journal.

Do you, as magazine editor, have authorization to grant these permissions? If not, can you please forward this request to the appropriate person and copy me on that correspondence?

I do urge you to make a decision as soon as possible given that I plan to submit my thesis within two weeks' time.

If you do grant permissions, please specify the ISBN/ISSN of the April 2017. I have not been able to locate that number thus far.

Regards,

Craig W. Christensen
M.Sc. Candidate (Geoscience), University of Calgary
BSc.Eng. (Geological), Queen's University at Kingston

<[redacted]>

Nicole Willson <[redacted]> Sun, Jun 25, 2017 at 7:48 PM
To: Craig Christensen <[redacted]>

Hi Craig,

Yes you have permission to republish the images, tables, and photos in your thesis and future submissions to peer-reviewed journals. Thanks for asking. Please credit the CSEG Recorder.

I will verify the existence of the ISSN number next week. I'm fairly certain there isn't one.

Nicole Willson
CSEG Recorder
Chief Editor
[redacted]

H.2 Letter from Co-Authors of Christensen et al. (2017)

July 6, 2017

To whom it may concern,

We, the undersigned, co-authors to Mr. Craig William Christensen of the article listed below, consent to the inclusion of content therein in his Master of Science thesis titled "A geophysical study of alpine groundwater processes and their geologic controls in the southeastern Canadian Rocky Mountains."

The article in question is one we published in the April issue of Canadian Society of Exploration Geophysicists's (CSEG) industry magazine (the CSEG Recorder):

Christensen CW, Hayashi M, Bentley LR. 2017. Scanning Calgary's 'water towers': applications of hydrogeophysics in challenging mountain terrain. CSEG Recorder. 42(3), 28-35.

Signed,

[redacted]

Dr. Masaki Hayashi

July 6, 2017

Date

[redacted]

Dr. Laurence Robert Bentley

July 6, 2017

Date